

ULTRAFAST TIME RESOLVED EXCITATION DYNAMICS IN  
CONJUGATED DENDRIMERS

By

EV RIM ATAS

A DISSERTATION PRESENTED TO THE GRADUATE SCHOOL  
OF THE UNIVERSITY OF FLORIDA IN PARTIAL FULFILLMENT  
OF THE REQUIREMENTS FOR THE DEGREE OF  
DOCTOR OF PHILOSOPHY

UNIVERSITY OF FLORIDA

2006

Copyright 2006

by

Evrin Atas

To Selim, Avni, and my parents

## ACKNOWLEDGMENTS

As I look back upon the years that have led to this dissertation, I have been fortunate to have been surrounded by the help and influence of numerous exceptional people. I would like to extend my warmest thanks to my research advisor Professor Valeria D. Kleiman, for her inspiring, patient guidance and continuous motivation throughout this enjoyable, yet challenging journey. She has served as a great mentor and friend from whom I have learned plenty. It was her genuine understanding, unique enthusiasm and well-placed trust that has led this project to completion.

I wish to thank my supervisory committee members, Professors Jeff Krause and Kirk S. Schanze for their guidance, fruitful collaborations and valuable discussions throughout my graduate studies, and Professors Russ Bowers and David Reitze for accompanying me in the final stage of my graduate career. I extend my thanks to Prof. Adrian Roitberg for his contribution in the theoretical work and Prof. Nicó Omenetto for teaching me the basics of lasers. I also thank Prof. Zhonghua Peng from University of Missouri-Kansas for providing unsymmetrical dendrimers and Dr. Joseph S. Melinger for his contributions to the initial stage of this project.

Many friends as well as coworkers have had an important role during my graduate studies in Gainesville with their discussions and companionships. The members of Kleiman Group provide a fun work environment. Thanks go to Dr. Jürgen Müller for his ongoing friendship and working closely with me on the polymer project presented in Chapter 6 of this dissertation. I thank Daniel Kuroda for his contagious energy, personal

support and having an answer for my every question. I would like to thank Lindsay Hardison for being such a cool girl, for sharing both science and personal matters, and for her suffering to correct my English in this dissertation. I thank Chad Mair for his late night support and chats in the lab, and teaching me Matlab for data analysis. The newest member of our group, Aysun Altan, thanks for your hard work and contribution of low temperature data in Chapter 4. I would like to thank Dr. Chunyan Tan, my collaborator from Dr. Schanze's Group, for enjoyable discussions. I also thank Dr. Wilfredo Ortiz and Julio Palma for their contributions with the theoretical aspect of dendrimers. I especially thank Bob Letiecq from Spectra Physics who provided day and night technical support.

My time here would not have been the same without the social diversions provided by all my friends in Gainesville. I am particularly thankful to Meziyet-Enes family, Enes Çalik, Ece Ünür, Dilber and Yavuz for their continuous friendship. I would like to thank Özlem Demir for being a wonderful friend and great support since the day we met in Ankara ten years ago.

I thank my parents Reize and Akil for allowing me to make my own decisions since I was a little child. They always believed in me and supported me whatever I do. I thank my sisters Zehra, Eda, and Seda for sharing a very happy childhood together. I thank my Aunt Nazmiye for her directions and support whenever I needed.

Finally, I give my special thanks to my husband, Avni, for his true love and understanding me without words. You are my soul mate and you bring colors to my life.

## TABLE OF CONTENTS

	<u>page</u>
ACKNOWLEDGMENTS .....	iv
LIST OF TABLES .....	ix
LIST OF FIGURES .....	x
ABSTRACT .....	xv
CHAPTER	
1 INTRODUCTION .....	1
History of Dendrimers .....	1
Structural Properties .....	4
Light-Harvesting Dendrimers .....	8
Symmetrical PE Dendrimers .....	16
Unsymmetrical PE Dendrimers .....	23
Excitation Energy Transfer .....	28
Radiative Energy Transfer .....	29
Non-radiative Energy Transfer .....	30
Outline of the Dissertation .....	42
2 EXPERIMENTAL METHODS .....	45
Chemicals and Materials .....	45
Steady State Measurements .....	47
Why Time-Resolved Spectroscopy? .....	47
The Laser System .....	48
Ultrafast Time-Resolved Emission Spectroscopy .....	51
Time-Correlated Single Photon Counting .....	51
Fluorescence Upconversion Technique .....	53
Homemade Upconversion Apparatus .....	55
Ultrafast Transient Absorption Spectroscopy .....	58
Probe Characteristics and White Light Continuum Generation .....	62
Experimental Setup .....	63
Continuum generation .....	64
Time resolution of the experiment .....	69
Concentration and Pump Pulse Energy Dependence .....	71

3	ENERGY TRANSFER IN GENERATION 1 UNSYMMETRICAL PHENYLENE ETHYNYLENE DENDRIMERS .....	73
	Materials and Methods .....	77
	Steady State Spectroscopy .....	80
	Time-Resolved Emission Experiments.....	83
	Time-Resolved Broadband Transient Absorption Measurements.....	88
	Kinetic Model .....	93
	Energy Transfer via Weak Coupling .....	98
	Conclusions.....	100
4	ENERGY TRANSFER IN GENERATION 2 UNSYMMETRICAL PHENYLENE ETHYNYLENE DENDRIMERS .....	101
	Materials and Methods .....	102
	Steady State Spectroscopy of Phenylene Ethynylene Dendrimers.....	104
	Time-Resolved Emission Experiments.....	106
	Time-Resolved Broadband Transient Absorption Measurements.....	112
	Kinetic Model for Energy Transfer .....	116
	Energy Transfer in the Weak-Coupling Limit.....	121
	Vectorial Energy Transfer in Unsymmetrical PE Dendrimers .....	124
	Conclusions.....	128
5	ENERGY TRANSFER IN SYMMETRICAL PE DENDRIMER: NANOSTAR ...	130
	Materials and Methods .....	133
	Transient Absorption .....	134
	Time-resolved Emission.....	135
	Steady State Spectroscopy .....	136
	Transient Absorption Spectroscopy.....	137
	Model Compound DPA .....	139
	Model Compound Phenylethynylene Perylene .....	141
	Nanostar.....	143
	372 nm excitation.....	143
	352 nm excitation.....	145
	310 nm excitation.....	148
	Kinetic Model for Nanostar .....	151
	Model for 372 nm Excitation .....	152
	Model for 352 nm Excitation .....	154
	Model for 310 nm Excitation .....	156
	Time-Resolved Emission Experiments.....	158
	Energy Transfer .....	163
	Conclusions.....	169

6	THE ROLE OF EXCITON HOPPING AND DIRECT ENERGY TRANSFER IN THE CONJUGATED POLYELECTROLYTES .....	171
	Steady State Experiments .....	174
	Time Resolved Fluorescence Spectroscopy .....	176
	Comparison of Transient Fluorescence and Absorption Data .....	181
	Anisotropy and Ionic Complexes .....	185
	Loss of Anisotropy and the Absence of Quenching by Free Dye Molecules.....	188
	Comparison of TA- and PL-upconversion Dynamics .....	189
	Quenching Dynamics and the State Contribution .....	190
	Modeling.....	192
	Conclusions.....	201
7	SUMMARY AND PERSPECTIVE .....	204
APPENDIX		
A	THE FLUORESCENCE UP-CONVERSION TECHNIQUE.....	209
	The Excitation and Collection of Fluorescence .....	209
	Alignment of the Gate Beam and Upconversion Crystal Phase Matching.....	214
	Detection of Upconverted Fluorescence.....	216
	UV-Light Compression .....	217
B	DATA ANALYSIS .....	219
	Analysis of Transient Absorption Changes .....	219
	2G <sub>1</sub> -m-OH.....	223
	2G <sub>2</sub> -m-OH.....	227
	Nanostar Excited at 310 nm.....	231
	LIST OF REFERENCES.....	235
	BIOGRAPHICAL SKETCH .....	247

## LIST OF TABLES

<u>Table</u>	<u>page</u>
3-1. Fits for time-resolved fluorescence data.....	96
4-1. Lifetime measurements from TCSPC.....	107
4-2. Fits for time-resolved fluorescence data.....	119
5-1. Fits for transient absorption data .....	158
6-1. Parameters recovered from kinetic modeling of PPESO3 fluorescence decays with HMIDC in MeOH .....	176
6-2. Parameters and variables used in the numerical simulations and fitting of the time-resolved PL-upconversion and the transient absorption data. ....	194
6-3. Average distance between two acceptor molecules in complex with the PPESO3..	195

## LIST OF FIGURES

<u>Figure</u>	<u>page</u>
1-1 Representation of dendrimer growth by the divergent and convergent methods.....	3
1-2 Schematic representation of bacterial light-harvesting complexes. ....	9
1-3 The dendritic triad. ....	14
1-4 Poly(aryl ether) dendrimer functionalized with dyes.....	15
1-5 Nanostar dendrimer (a) Chemical structure (b) Energy level diagram. ....	20
1-6 Chemical structures of unsymmetrical PE dendrimers .....	24
1-7 Absorption and emission spectra of $G_nOH$ monodendrons. ....	25
1-8 Steady state spectra of $G_nPer$ monodendrons: absorption (a) and emission (b).....	26
1-9 Chemical structure of PE didendrons.....	28
1-10 Model picture for energy transfer showing resonant transitions of donor and acceptor, and spectral overlap of donor emission and acceptor absorption. ....	31
1-11 Schematic representation of energy transfer mechanism.....	32
1-12 Definition of the angles used to calculate the orientation factor between the dipoles. ....	35
1-13 Differences between strong, weak, and very weak coupling. ....	37
2-1 The laser system for the production of tunable femtosecond laser pulses with high energy per pulse. ....	49
2-2 Fluorescence up-conversion technique (a) Illustration of the upconversion principle (b) Up-converted fluorescence signal generated in a nonlinear crystal only while the delayed gate pulse is present .....	55
2-3 Fluorescence upconversion experimental setup.....	57
2-4 Basic principle of transient absorption experiment.....	59

2-5	The theoretical scheme of certain signals observed as transient absorption signals.....	61
2-6	Experimental setup for transient absorption experiment probing with white light continuum. UV pump pulses are obtained from the OPA.....	63
2-7	Spectrum of the white light continuum generated by CaF <sub>2</sub> . The probe (blue) and reference (red) beams used for transient absorption experiment. ....	65
2-8	The chirp of the white light continuum determined from the delay between the signals.....	68
2-9	Coherent artifact of hexane solvent excited at 310 nm, probed at 330 nm and 380 nm.....	70
3-1	Chemical structures of generation 1 phenylene ethynylene dendrimers: (a) 2G <sub>1</sub> -m-OH (b) 2G <sub>1</sub> -m-Per.....	77
3-2	Normalized absorption spectra of — 2G <sub>1</sub> -m-OH, — G <sub>1</sub> -OH, and — G <sub>2</sub> -OH in dichloromethane. Normalized emission spectrum of — 2G <sub>1</sub> -m-OH. ....	81
3-3	Normalized absorption spectra of ----2G <sub>1</sub> -m-OH, ...EPer, and —2G <sub>1</sub> -m-Per and fluorescence spectrum of —2G <sub>1</sub> -m-Per, excited at 315 nm. ....	82
3-4	2G <sub>1</sub> -m-OH in dichloromethane excited at a) 370 nm b) 315nm.....	85
3-5	Upconversion signal of 2G <sub>1</sub> -m-Per detected at 485 nm, excited at (a) 370 nm, (b) 315nm.....	87
3-6	2G <sub>1</sub> -m-Per Upconversion Signal. $\lambda_{\text{excitation}}=315$ nm, $\lambda_{\text{emission}} = 400$ nm.....	88
3-7	Transient absorption spectra of 2G <sub>1</sub> -m-OH molecule at different time delays, excited at 315 nm. ....	90
3-8	Transient absorption spectra of the 2G <sub>1</sub> -m-OH molecule at different delay times. Detailed display of the 350 nm-450 nm region.....	91
3-9	Transient absorption spectra of 2G <sub>1</sub> -m-Per at different time delays.....	92
4-1	Chemical structures of phenylene ethynylene dendrimers: (a) 2G <sub>2</sub> -m-OH (b) 2G <sub>2</sub> -m-Per and (c) 3D model of the 2G <sub>2</sub> -m-Per from a MD simulation. ....	103
4-2	Normalized absorption spectra of ----2G <sub>2</sub> -m-OH, —EPer and —2G <sub>2</sub> -m-Per and fluorescence spectrum of —2G <sub>2</sub> -m-Per , excited at 320 nm. ....	106
4-3	2G <sub>2</sub> -m-OH in dichloromethane excited at a) 415 nm b) 372nm and c) 330 nm... ..	108

4-4	Upconversion signal of 2G <sub>2</sub> -m-Per detected at 485 nm, excited at a) 465 nm, b) 420 nm, c)380 nm and d) 340 nm. ....	110
4-5	2G <sub>2</sub> -m-Per upconversion signal. $\lambda_{\text{excitation}}=320$ nm $\lambda_{\text{emission}} = 435$ nm. ....	112
4-6	Transient absorption spectra of 2G <sub>2</sub> -m-OH at different delay times.....	114
4-7	The excitation spectrum of 2G <sub>2</sub> -m-OH at 298 K (red) and 77 K (blue), emission detected at 450 nm (top). The excitation anisotropy of 2G <sub>2</sub> -m-OH at 77 K (bottom).....	116
4-8	Model describing the energy ladder. The intermediate state (I) is detected at 400 nm or 435 nm. Emission from trap is at 485 nm.....	125
4-9	Temporal evolution of the intermediate state population followed by fluorescence up-conversion. ....	127
5-1	Chemical structure of nanostar dendrimer (2 dimensional sketch .....	134
5-2	Absorption and emission spectrum of nanostar in DCM at room temperature.....	136
5-3	Normalized absorption spectrum of (a) 2-ring (black), 3-ring (green), and 4-ring (red) PE units (b) Nanostar absorption (red) and sum of rings' absorption at 298 K (c) nanostar absorption at 298 (blue) and 10 K (red). ....	138
5-4	Transient absorption spectrum of model compound DPA .....	140
5-5	Transient absorption spectrum of the model compound phenylethyne perylene.....	142
5-6	Transient absorption spectrum of nanostar after excitation at 372 nm. ....	144
5-7	Transient absorption signal as a function of time recorded at 340 nm (black), and 515 nm (blue) following excitation at 372 nm.....	145
5-8	Transient absorption spectrum of nanostar after excitation at 352 nm. (a) Short time window ( $\Delta t < 450$ fs). (b) Long time window (0.550-50 ps).....	147
5-9	Transient absorption signal as a function of time recorded at 360 nm (black), and 520 nm (red) following excitation at 352 nm.....	148
5-10	Transient absorption spectrum of nanostar after excitation at 310 nm. ....	149
5-11	Transient absorption signal as a function of time for three different excitation wavelengths.....	151
5-12	Kinetic model proposed for the dynamics of nanostar.....	153

5-13	Fluorescence upconversion signal detected at 485 nm (blue) and at 380 nm (red) following the 310 nm excitation.....	160
6-1	Conjugated polyelectrolytes PPESO3 (left) and cyanine dye HMIDC (right). ....	174
6-2	Absorption and emission spectra of PPESO3 and HMIDC in methanol .....	175
6-3	Time-resolved fluorescence of PPESO3 (34 $\mu$ M) in MeOH for different HMIDC concentrations.....	178
6-4	Normalized time-resolved fluorescence of HMIDC in MeOH.....	181
6-5	Transient absorption and up-conversion signal of PPESO3 in MeOH for different concentrations of added HMIDC.....	183
6-6	PL-upconversion and $\Delta A$ of a pure PPESO3 solution.....	184
6-7	Time dependent loss of anisotropy for pure PPESO3 and PPESO3 with HMIDC quencher. ....	186
6-8	The photoluminescence yield of samples containing HMIDC, divided by the photoluminescence of the pure PPESO3 solution.....	190
6-9	Stern-Volmer plot of the time-integrated photoluminescence and the instantaneous photoluminescence from the upconversion experiment.....	192
6-10	Average distance between quencher molecules complexed with the PPESO3 on a reciprocal scale as a function of the quencher concentration .....	195
6-11	Individual contributions to the integrated energy transfer, random walk mediated ( <i>a</i> ) direct Förster-transfer ( <i>b</i> ) versus time after excitation. ....	199
A-1	Diagram of off-axis aluminum parabolic mirrors used to collect and image the fluorescence of the sample. ....	210
A-2	Layout of the alignment beams and the collection by parabolic mirrors.....	211
B-1	Singular values .....	223
B-2	Transient spectra of SVD output.....	223
B-3	Dynamics of SVD output.....	224
B-4	Model fits for the relevant components with large singular values. ....	224
B-5	Reconstructed versus real $\Delta A$ as a function of wavelength.....	225
B-6	Reconstructed versus real $\Delta A$ as a function of time. ....	226

B-7	Singular values .....	227
B-8	Transient spectra of SVD output.....	227
B-9	Dynamics of SVD output.....	228
B-10	Model fits for the relevant components with large singular values. ....	228
B-11	Reconstructed versus real $\Delta A$ as a function of wavelength.....	229
B-12	Reconstructed versus real $\Delta A$ as a function of time. ....	230
B-13	Singular values .....	231
B-14	Transient spectra of SVD output.....	231
B-15	Dynamics of SVD output.....	232
B-16	Model fits for the relevant components with large singular values. ....	232
B-17	Reconstructed versus real $\Delta A$ as a function of wavelength.....	233
B-18	Reconstructed versus real $\Delta A$ as a function of time. ....	234

Abstract of Dissertation Presented to the Graduate School  
of the University of Florida in Partial Fulfillment of the  
Requirements for the Degree of Doctor of Philosophy

ULTRAFAST TIME RESOLVED EXCITATION DYNAMICS IN  
CONJUGATED DENDRIMERS.

By

Evrin Atas

May 2006

Chair: Valeria D. Kleiman  
Major Department: Chemistry

Light-matter interactions play an important role in light-harvesting processes such as photosynthesis, which has attracted much attention due to its major impact on the cycle of life. Understanding the fundamental principles of this energy transfer process is possible through the study of artificial light harvesting systems. Dendrimers are perfectly branched synthetic macromolecules having numerous peripheral chain-ends surrounding a single core. Incorporating suitable chromophore groups into their structure can create very efficient antenna systems. This PhD thesis details the dynamics of intramolecular energy transfer in conjugated phenylene ethynylene dendrimers. Built-in energy-gradients in the dendrimer structure enable a unidirectional energy transfer from the periphery to the core. Depending on the substitution pattern on the phenyl ring, symmetrical and unsymmetrical architectures are formed that yield different photophysical properties.

Ultrafast time-resolved fluorescence and absorbance techniques are utilized to study the fast dynamics of energy transfer. Our approach is based on a comparative study of symmetrical and unsymmetrical dendrimers with various  $\pi$ -conjugation and sizes. Dendrimer backbones are selectively excited at specific absorption wavelengths and the energy migration toward the acceptor is monitored. Time-resolved fluorescence measurements explore the population of intermediate states and the final energy acceptor, while broadband transient absorption (300 nm to 600 nm) probes the dynamics from the initially excited state to the final trap.

To understand the dynamics and mechanisms of energy transfer we propose kinetic models describing the time-resolved data as a function of dendrimer size, presence or absence of a trap and excitation wavelength. For unsymmetrical dendrimers, typical energy transfer times are in the range of 200-750 fs. While absorption is into delocalized exciton states, emission occurs from localized states. In the presence of attached perylene trap, excitation energy migrates through multiple channels. The calculated interaction energies (75-100  $\text{cm}^{-1}$ ) indicate that dendrimers and perylene are weakly coupled. The symmetrical phenyl ethynylene dendrimer, however, shows energy transfer times from 200 fs to 20 ps, much slower than the unsymmetrical molecule. Considering the broken  $\pi$ -conjugation due to the meta substitution, the subunits of the nanostar are investigated independently via transient absorption. The kinetic model analysis shows that there are both direct and indirect transfer (through the cascade) pathways. The experimental energy transfer rates are discussed within the Förster theory to understand the extent of the electronic coupling. In addition, an ultrafast study of exciton transport in a phenyl ethynylene polyelectrolyte is performed through quenching experiments.

## CHAPTER 1 INTRODUCTION

### **History of Dendrimers**

The synthesis of dendrimers is an important stage in the evolution of macromolecular chemistry. Dendrimers are hyperbranched, well-defined, three-dimensional, and perfectly monodisperse macromolecules.<sup>1-4</sup> Although Flory theoretically investigated the role of branched units in macromolecular architectures half a century ago,<sup>5,6</sup> the first successful synthesis of a dendritic structure did not occur until the late 1970s. The first example of an iterative cascade procedure toward well-defined branched structures, such as low molecular weight branched amines, has been reported by the Vögtle group.<sup>7</sup> However, not all regularly branched molecules are dendrimers. Important characteristics, which will be explained in detail later in this chapter, are reached when globularity is achieved at a certain generation and size threshold. The Vögtle group's cascade molecules are too small to exhibit the properties of dendrimers and are used as branched oligomeric building blocks in dendrimer construction.<sup>7</sup>

Optimization of the iterative method with Michael addition enabled the synthesis of the first globular dendrimers called PAMAM (polyamidoamine) by Tomalia et al. at Dow Chemical Research Laboratories.<sup>8-10</sup> PAMAM dendrimers are the first dendrimer family to be commercialized and they have been thoroughly investigated to date. Shortly after, Newkome et al.<sup>11</sup> reported the synthesis of arborols, another family of trisbranched polyamide dendrimers, and two research groups, Mülhaupt and Meijer, were able to improve the Vögtle's synthesis approach to enable the production of poly(propylene

imine) dendrimers.<sup>12,13</sup> These dendrimers were constructed divergently, implying that the synthesis starts with a functional core molecule and is expanded to the periphery. In 1990, Hawker and Fréchet introduced the convergent approach to produce aromatic polyether dendrimers.<sup>14,15</sup>

In contrast to polymers, dendrimers are core-shell structures possessing three basic architectural components: 1) a core, 2) repeating units in the interior of shells consisting of branching points (generations), 3) terminal functional groups (periphery).

Two complementary methods, the divergent and convergent synthesis, have been used to construct high-generation dendrimers.<sup>3,4,15,16</sup> Both methods consist of a repetition of reaction steps, accounting for the creation of an additional generation. Within each of these major approaches there may be variations in methodology. The features desired for the target molecule and specific building blocks justify the choice of the synthetic approach.

**Divergent approach.** Based on the work of Tomalia and Newkome, the growth starts at the core and proceeds radially outward toward the periphery.<sup>10,11</sup> The number of reactions that must be completed at each step of growth increases exponentially. Therefore, a large excess of reagents is required making it harder to maintain the purity and structural uniformity. However, this method is used widely for the preparation of high generation dendrimers and for the synthesis on large scale. The major drawback is the poor yield of defect-free dendrimers.

**Convergent approach.** This method, first reported by the Fréchet group, initiates growth at what will become the periphery of the molecule and proceeds inward towards the focal point.<sup>14</sup> This approach is best described as an “organic chemist” approach to

globular macromolecules, since it provides outstanding control over growth, structure, and functionality.<sup>17</sup> The inward growth allows for the reduction in the amount of synthetic steps and intermediate purification at each step of growth. The yield of defect-free dendrimers is about 80%. Figure 1-1 illustrates the dendrimer growth by both the divergent and the convergent methods.

Since the discovery of dendrimers, one of the controversial issues has been the purity of these structures. The quality of the final dendritic product is directly related to the chosen synthetic method. A variety of convergently synthesized dendrimers have been reported in the last decade, and these dendrimers have shown that the convergent approach provides greater structural control than the divergent approach; allowing purity, structural uniformity, and functional versatility. Another attractive feature of the convergent approach is its ability to selectively modify both the focal point and the chain ends. In addition, functional groups can be precisely placed throughout the structure. Overall, the organic nature of the convergent method results in defect-free dendrimers with appropriate purification.

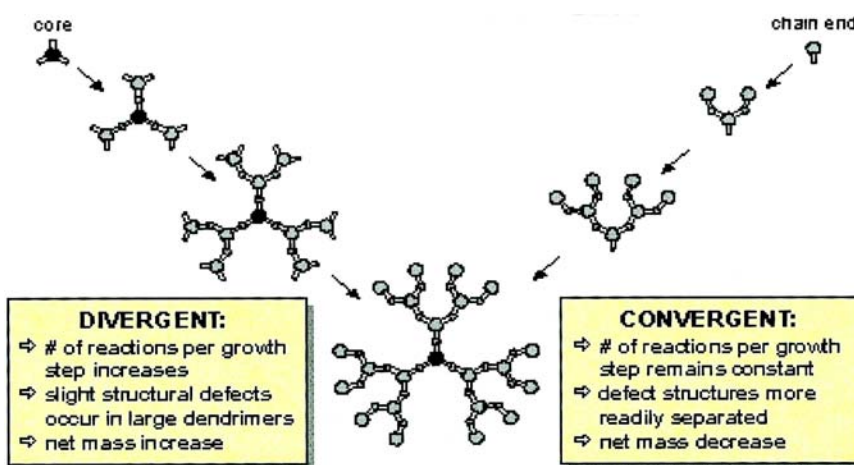


Figure 1-1. Representation of dendrimer growth by the divergent and convergent methods. Figure is adapted from Tomalia et al.<sup>18</sup>

## Structural Properties

Structural and conformational behavior of dendrimers is discussed in many books and publications. Several intriguing questions arise: Are dendrimers always globular or can their shape be highly distorted? How rigid are they? Can the end groups back-fold? Are there cavities present within dendrimers? How do the physical properties change with generation? What are the similarities with linear analogues?

The dendrimer structure can be divided into three distinct architectural regions: core or focal moiety, branched repeat units, and end groups on the outer layer. Their structural precision leads to an exact number of branching points or generations, which differentiates dendrimers from hyperbranched polymers. In contrast to linear polymer analogues, dendrimers have several sharp characteristic features.

- (i) A dendrimer will have size monodispersity due to its well-defined iterative synthesis, whereas most linear polymers are synthesized composing a range of molecular species differing in size and molecular weight.
- (ii) While the linear polymers contain only two end groups, the number of dendrimer end groups increases exponentially with generation. As the size of the dendrimer increases, the nature of end groups will determine important properties such as solubility, chemical reactivity, and glass transition temperature.
- (iii) In theory, polymers can grow as much as their solubility allows them, whereas dendritic growth is mathematically limited. The number of monomer units increases exponentially, but the volume available to the dendrimer grows proportionally to the cube of its radius. As a result of this physical limitation, dendrimers develop more globular conformation as the generation increases. In contrast to polymers, the intrinsic viscosity of dendrimers does not increase with molecular weight.

More extended arrangements for lower generation dendrimers will gradually transform into compact and globular shapes for higher generation dendrimers. In general, this gradual transition in overall shape results in the deviation in physical behavior of dendrimers from those of linear macromolecules.<sup>17</sup>

Dendrimers might be flexible or fairly rigid depending on the actual dendritic structure. Recent calculations and measurements have suggested backfolding of the chain ends. For example, the polyether dendrimers synthesized by the Fréchet group have been investigated in detail to verify the possibilities for backfolding.<sup>19</sup> The flexible nature of these dendrimers implies that the end groups are found throughout the dendrimer volume. However, when the end groups can communicate with each other with attractive secondary interactions such as  $\pi$ - $\pi$  interactions, electrostatic repulsions, and hydrogen bonding interactions, the terminal units will assemble at the periphery precluding back folding.<sup>20</sup>

One of the most studied rigid dendrimer family is phenylethynylene dendrimers, first synthesized by Moore et al.<sup>21</sup> These dendrimers are distinguished from other dendrimers by their rigidity and shape persistence as confirmed by various experimental measurements.<sup>22</sup> Another type of shape persistent dendrimers is based on polyphenylene units. Müllen and coworkers investigated these molecules and found that their rigidity originates from the very dense packing of benzene rings.<sup>23-25</sup>

Do cavities exist within the dendrimer? Indeed, unlike linear polymers, properly designed high generation dendrimers exhibit a distinct interior where molecules have been encapsulated in a noncovalent manner.<sup>26-28</sup> The encapsulation does not necessarily indicate the presence of a permanent and rigid cavity within the dendrimer. Especially, flexible dendrimers can accommodate guest molecules. When solvent molecules that freely penetrate dendrimers are removed, the volume collapses leaving the guest molecules trapped inside the dendrimer. For example, the well-designed and rigidified dendrimer structure called “dendritic box” can encapsulate various small organic

molecules and control their release by modifying the steric crowding of the dendritic periphery.<sup>29-31</sup>

The encapsulation of a functional core moiety creating specific site-isolated nanoenvironments leads to a variety of bio- and nanotechnology applications including light-harvesting, amplification, and drug delivery.<sup>32,33</sup> Having full control of the structure and architecture, researchers are able to place active sites that have photophysical, photochemical, electrochemical, or catalytic functional groups at the core of the dendrimers. One of the more elegant works on efficient, unidirectional energy transfer from a dendritic framework to a single chromophore was reported by Xu and Moore.<sup>34,35</sup> A gradient effect was created using a poly(phenylethynylene) dendrimer. The conjugation length of the repeat units of this dendrimer increases with generation from the periphery to the core. This is the so called “nanostar” molecule later discussed in Chapter 5 of this dissertation. The phenylethynylene units of Moore dendrimers can be used to create unsymmetrical dendrimer architectures, which are also investigated in this dissertation (Chapters 3 and 4).

Fréchet group’s poly(benzylether) dendrimers, functionalized with different dye chromophores at the periphery and core, are able to harvest light and transfer the energy efficiently to a chromophore located at the center of the dendrimer structure. It was shown that the core chromophore emission is significantly amplified compared to the same chromophore without the dendritic framework. As the size of the dendrimer increases, so does the number of peripheral units, therefore the energy transferred to the core increases due to a larger absorption cross-section.<sup>36-38</sup> Another application of the same dendrimer structure is in optical signal amplification. Luminescent lanthanide ions

are used as signal amplifiers for optical fiber communications. However, their self-quenching in the solid state greatly limits the effectiveness. Kawa et al. encapsulated individual lanthanide ions within poly(benzylether) dendrons leading to site-isolation, thereby decreasing the self-quenching effect. This antenna light-harvesting effect results in emission signal amplification.<sup>33</sup>

In another report, Jiang and Aida used azobenzene containing aryl ether dendrimers to study energy transfer.<sup>39</sup> They demonstrated that cis-trans isomerization of azobenzene moiety at the core accelerates for larger generation (e.g. G-4, G-5) dendrimers. The acceleration was observed via exciting a stretching mode of the aromatic rings with IR irradiation. However, UV excitation of the dendrons did also result in accelerated isomerization. Thus, it was proposed that the dendritic shell not only insulates the azobenzene core from collisional energy dissipation, but it acts as a photon harvesting antenna.

Müllen and coworkers reported polyphenylene dendrimers functionalized with different chromophores at the periphery and core, while the De Schryver group investigated this family of dendrimers and explored the energy transfer dynamics via time-resolved spectroscopy experiments.<sup>40,41</sup> The dendrimer rigid structure decorated with a unique selection and positioning of the chromophores allows a systematic study of possible energy transfer mechanisms.

A different type of encapsulation involves the formation of metal nanoparticles within dendrimers and it has been widely used to prepare organic-inorganic composite structures useful in catalytic applications.<sup>42</sup> Since dendrimers have nanoscopic dimensions and can be dissolved molecularly, catalytic active site can be placed at a

particular, isolated position resulting in beneficial interactions with the substrate.<sup>17</sup>

Brunner et al.<sup>43</sup> introduced the first branched molecules containing internal core catalytic sites, later called “dendrzymes.” In parallel to this work, the first dendritic catalyst with multiple catalytic sites at the periphery has been reported by Ford et al.<sup>44</sup> Both studies concluded that low-generation dendrimers are better catalytic supports than higher generation dendrimers. More recently, Crooks et al. have shown that substrates can penetrate the dendrimers to access the catalytic sites and undergo simple reactions such as hydrogenations.<sup>42</sup> The Crooks group also developed a system composed of PAMAM molecules covalently attached to a metallic surface and tested its function as a chemical sensor.<sup>45</sup>

Recently, a sequence of dendrimers containing Zn-porphyrin monomers situated on the surface were investigated by Sundström and coworkers.<sup>46,47</sup> The goal of this project was to study energy transfer between the individual Zn-porphyrins within a dendrimer, and to measure whether this process becomes more efficient with increasing dendrimer size. The molecules based on porphyrin chromophores are an example of compounds that can be used as a model for the bacteriochlorophyls (BChls) in the natural light-harvesting (LH2) complex.

Before going through the details of these specific structures, a brief summary of light-harvesting dendrimers and the role of an energy gradient within these dendrimers will be presented.

### **Light-Harvesting Dendrimers**

Photosynthesis is an extremely effective natural process for harvesting sunlight and converting sunlight into useful chemical energy stored in the form of ATP. Thus, it has been of vital importance to the evolution of life and it is essential for almost all life-

forms. Therefore, it is inevitable that the photochemistry of photosynthesis be the focus of considerable scientific research.

There are two key processes in photosynthesis. First is the absorption of photons by an antenna system, followed by a rapid and efficient transfer of excitation energy to the reaction center. Then, a sequence of charge transfer events from the excited state of the reaction center results in storage of chemical energy. To date, the most studied photosynthetic system is probably the purple bacteria.<sup>48</sup> The high resolution X-ray crystal structure of this bacteria? reveals a central reaction center surrounded by light harvesting complexes as shown in Figure 1-2. These chlorophyll containing assemblies are capable of absorbing photons from a broad spectral range of sunlight, which makes them a perfect light-harvesting antenna.

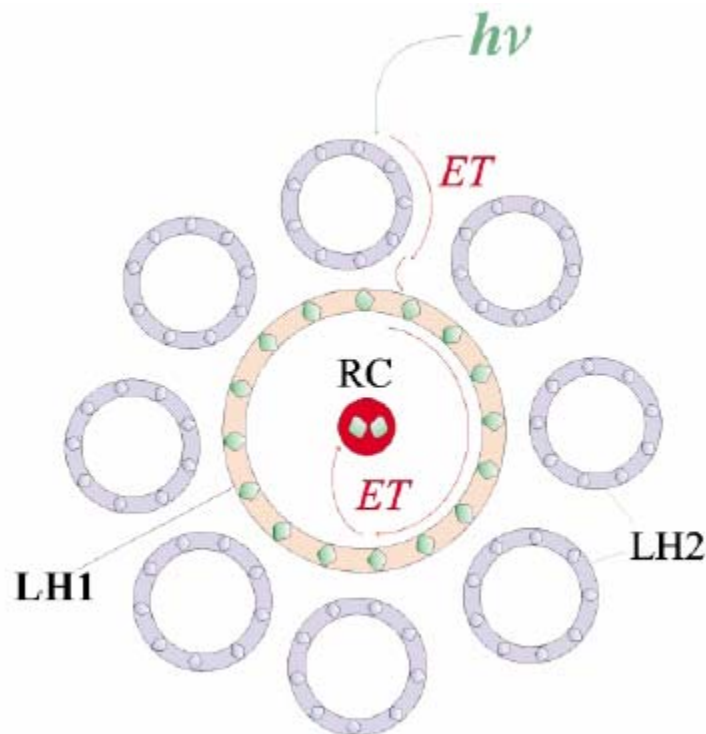


Figure 1-2. Schematic representation of bacterial light-harvesting complexes.

In the last decade, there has been great devotion to the design and synthesis of molecular or supramolecular species that can function as antennas in artificial systems. The first requirements to develop a light harvesting system are that its components must absorb in a substantial part of the visible spectral region and the light-absorbing units must be chemically and photochemically stable. In order to have high light-harvesting efficiency, the excitation energy must be delivered to a common acceptor component.

Several groups have tried to develop artificial light harvesting systems with custom-designed molecules such as small covalent arrays containing photoactive units, polymeric and supramolecular systems with multichromophores.<sup>17,20</sup> It has been concluded that linear-chain macromolecules do not have the most ideal architecture for efficient light harvesting.<sup>20</sup> First of all, it is difficult to make polymeric systems with an energy gradient, which is shown to be vital for vectorial energy transfer. Secondly, most polymeric chains are flexible enough to form aggregates or excimers which will act as energy traps. In this regard, dendrimers characterized by their high degree of order and the possibility to contain selected photoactive chemical units in predetermined sites are excellent candidates for light harvesting antenna. Proper choice and placement of chromophores enable the investigation of efficient energy transfer from the periphery to the core of the dendrimer.

Balzani and coworkers<sup>49</sup> have reported initial studies on multichromophoric dendrimers undergoing intramolecular energy transfer. They incorporated different metal and ligand combinations into low-generation dendrimers and found that energy transfer occurs from internal higher energy units to the external lower energy units. The concept of intramolecular energy transfer was clearly illustrated by these initial reports.<sup>50-55</sup>

However, these structures are not ideal photosynthetic mimics. As mentioned before, the optimum light harvesting system should have numerous peripheral chromophore channeling the absorbed energy in a unidirectional manner to a single and central energy acceptor molecule or complex. The first report of an efficient, unidirectional energy transfer from a dendrimer structure to a single core chromophore was published by Xu and Moore.<sup>34</sup> These systems and their properties will be explained in details in the symmetrical phenyl ethynylene dendrimers section.

The Fréchet group has then studied the lanthanide –cored poly(benzylether) dendrimer. In this study, it was shown that the excitation energy was channeled from a dendrimer shell to a single core unit.<sup>33</sup> Later, Jiang and Aida observed similar antenna effect utilizing a different luminescent core such as porphyrin.<sup>56</sup> A variety of structures were designed and studied differing in the number of poly(benzylether) dendrons attached to the central porphyrin as well as in the generation number of dendrons.<sup>56</sup> In a similar manner, Balzani et al. reported a polylysine dendrimer with chromophoric dansyl units in the periphery playing the role of a ligand for lanthanide ions with efficient conversion of UV light into light of different frequencies in the visible or near infrared region.<sup>52,53,57</sup> In another approach, also developed by the Fréchet group, the flexible poly(benzylether) dendrimer was functionalized with dye molecules at the periphery that served as the molecular antenna while the core functionalized with a proper dye molecule served as the energy acceptor. Both steady state and time-resolved experiments indicated that the energy migration from the periphery to the core was extremely efficient, thus most of the absorbed energy is concentrated at a single center.<sup>36,58,59</sup>

Inspired by natural photosynthetic systems including elegant light-harvesting antenna of photosynthetic bacteria, systems capable of directional energy transfer between several chromophores have gained much attention.<sup>60</sup> In the absence of a gradient, the exciton will randomly hop between neighboring localized states following the photoexcitation. The hopping probability is based on the separation distance between chromophores. Due to the branched structure, there is an entropic bias increasing the probability of energy dissipation outwards toward the molecular periphery rather than inwards toward the core. Recent theoretical investigations of dendrimers without an energy gradient have shown that the efficiency of exciton trapping at the core decreases with an increase in molecular size, even though larger number of absorbing units is present.<sup>61,62</sup> On the other hand, the presence of an energy gradient toward the locus will introduce an energetic bias that will overcome the entropic bias. Two different approaches are known to create dendrimers with an energy gradient. In one approach, Moore and coworkers developed a series of dendrimers serving both as the light-absorbing antenna and as an energy transport medium, which is the case for the dendrimers investigated in this doctoral research. In the other approach, both periphery and core are functionalized with donor and acceptor moieties, respectively. The dendritic framework is photochemically silent and acts as a transparent spacer to separate the donor groups at the periphery from the acceptor groups at the core.<sup>40,63</sup>

An example of this later approach was reported by Müllen and co-workers<sup>64,65</sup> who investigated structurally well-defined, conformationally rigid dendrimers consisting of up to three different chromophores. This “dendritic triad” includes globular polyphenylene dendrimers bearing a terrylene tetracarboxydiimide (TDI) chromophore in the center and

perylene dicarboxmonoimide (PMI) as well as naphthalene dicarboxmonoimide (NMI) chromophores at the periphery as shown in Figure 1-3. The design of the cascade system places the naphthalene chromophore at the third branch point, the perylene chromophore at the second branch point, and the terrylene chromophore at the core representing spatially the desired direction for energy transfer. These rylene chromophores were chosen since they possess excellent photostability, high extinction coefficients, and fluorescence quantum yield close to unity. The triad absorbs over the whole range of visible spectrum and shows well-separated absorption envelopes. Thus, it is possible to specifically excite distinct chromophores within the dendrimer, which helps with the investigation of vectorial energy transfer. Müllen group's work<sup>64-66</sup> clearly indicates the existence of an energy gradient and is consistent with the stepwise energy transfer from periphery to the center of the molecule.

Recently, single molecule fluorescence studies on the same triad further support the multi-step unidirectional energy transfer, including a component of direct transfer from each donor to the acceptor. Note that using a rigid polyphenylene dendrimer overcomes many possible complications due to conformational mobility. Undesired chromophore interactions such as aggregation, excimer formation, and even self quenching of dyes are minimized with a shape-persistent dendrimer.

The Müllen group's work represents the first example of a dendritic triad in which energy gradient is induced by different types of chromophores spatially and energetically distributed within the dendrimer and thus independent of the dendrimeric scaffold.

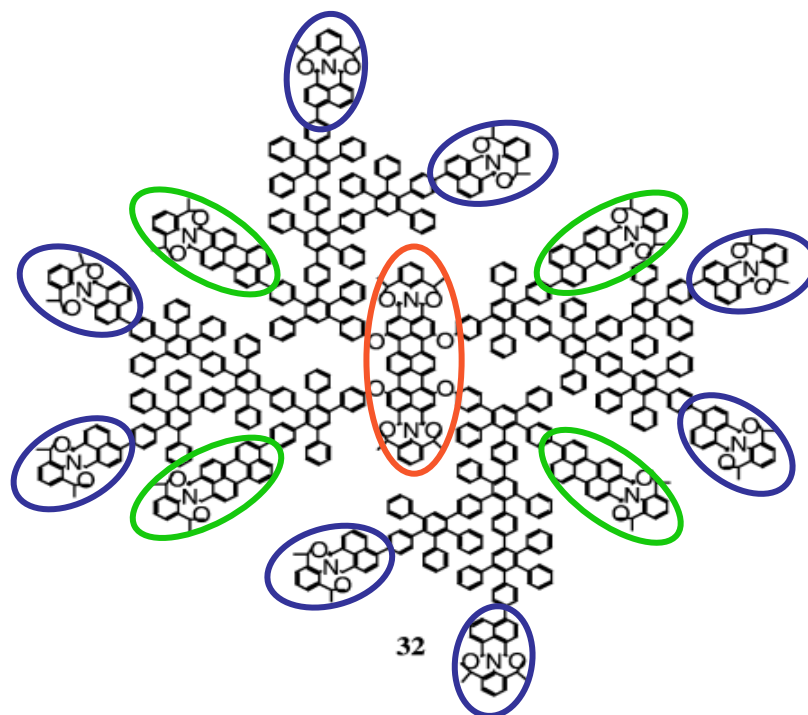


Figure 1-3. The dendritic triad. Adapted from reference<sup>64</sup>.

Shortly after, Fréchet reported the design and synthesis of a cascade light harvesting system based on a flexible dendrimer scaffold. In order to obtain the required spatial distribution, coumarin 2 and fluorol dyes were placed at the third and second branch point of a poly(aryl ether) dendrimer, respectively (Figure 1-4). The final energy acceptor consisted of a perylene derivative at the core of the dendrimer. Similar to polyphenylene dendrimers, the dendritic backbone does not participate in the energy transfer process. The steady state photophysical analysis suggested energy transfer within this system favoring a cascade route, moving from coumarin groups through intermediate fluorol units and into a final acceptor ethynyleneperylene chromophore. This system demonstrates that with proper chromophore selection, vectorial energy transfer process is generated despite the flexibility of the dendrimer.

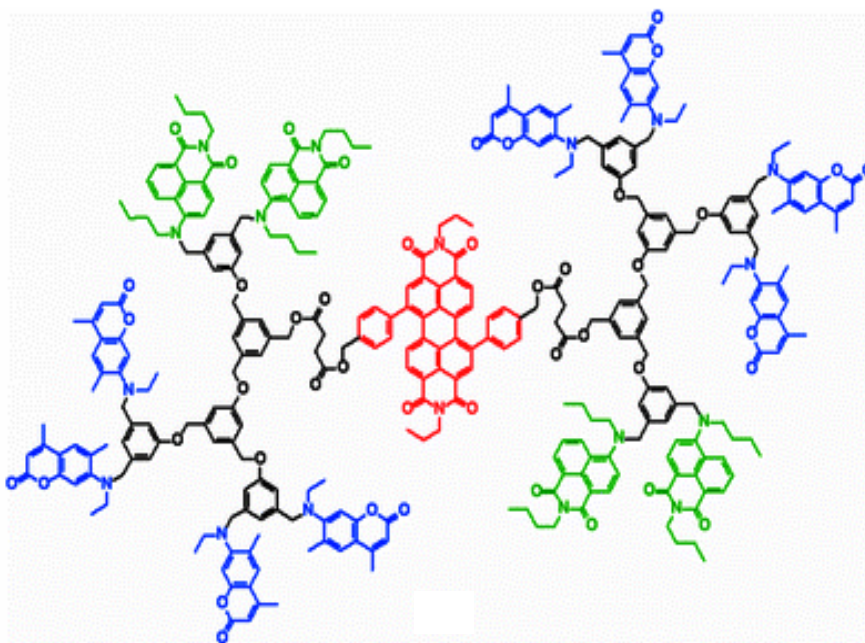


Figure 1-4. Poly(aryl ether) dendrimer functionalized with dyes. Adapted from reference<sup>67</sup>.

The dendrimers mentioned previously point out the role and necessity of an energy gradient for efficient energy transfer process as in the natural photosynthetic systems. However, for these nonconjugated dendrimers, the role of the dendritic backbone is only structural and not functional (the dendrimer backbone is just a spacer). In conjugated dendrimers, the backbone itself serves as a tool for the energy transfer. The first built-in multistep energy gradient within dendrimers was reported by Moore and coworkers using a phenylene ethynylene (PE) dendrimer, with a repeat unit conjugation length that increased with generation from periphery to the core.<sup>68-70</sup> As a result, HOMO-LUMO gaps of conjugated repeat units decrease from the exterior to the interior, generating a directional energy flow toward the core. They also investigated the PE dendrimers without a gradient, composed of phenylethynylene chains of identical lengths. These PE dendrimers are characterized as structurally symmetric due to the meta substitution of the benzene ring at each branching point. Recently, a new type of PE monodendron was

characterized as unsymmetrical since the branches extending outward were structurally nonequivalent and linked through meta and para positions on the phenyl rings. The unsymmetrical PE dendrimers also possess an intrinsic energy gradient resulting in efficient energy funneling.<sup>71</sup> The work presented in this dissertation mainly comprises the investigation of the photophysical properties and the energy transfer processes in several unsymmetrical PE dendrimers and a symmetric PE extended dendrimer. The primary photophysical characterization of symmetrical and unsymmetrical PE dendrimers is summarized in the next section.

### **Symmetrical PE Dendrimers**

Theoretical studies showed that ordered “Bethe trees” might be the optimal energy funnels.<sup>61,72</sup> With this in mind, Moore and Kopelman synthesized and investigated the photophysics of a series of phenylethynylene dendrimers.<sup>72</sup> Two families of these dendrimers, compact and extended, are characterized by symmetrical branching. The branching point is always a meta substitution of the phenyl ring leading to structurally symmetric macromolecules. Branching at para positions would grow linear chains, while branching at ortho positions would terminate the tree-like structure quickly due to steric hindrance. Thus, symmetric geometry for a large dendrimer is optimized with meta arrangement, which also permits a large degree of orientational flexibility. Deviations from planar configurations overcome the steric hindrance and enable the synthesis of higher generation dendrimers.<sup>22,73</sup>

The main difference between compact and extended dendrimers is the number of phenylene ethynylene units between consecutive branching points. In compact ones, each generational unit is composed of identical diphenylacetylene chains. The extended ones have diphenylethynylene chains around the periphery, but linear phenyleneethynylene

chains show consecutively increasing length toward the center of the molecule. Even though this seems to be a minor modification to the molecular structure, it introduces significant electronic and energetic characteristics that greatly enhance the energy funneling abilities of these systems.<sup>70</sup>

Recently, Ortiz et al. have presented a theoretical investigation of energy transfer in the nanostar molecule.<sup>74</sup> Molecular dynamics simulations have been performed to reveal the role of structural changes on the dynamics. The energy transfer rates were calculated between 2- and 3-ring chromophores using the ideal dipole approximation (IDA) and the transition density cube method (TDC). The rapid flipping of the phenyl groups at room temperature resulted in large changes in transition densities. It was shown that the traditional Förster model employing IDA was not able to reveal this dynamical effect on the transfer rates. Also, the accuracy of the IDA fouls when the size of the chromophores is comparable to the distance between them. However, the rate constants obtained with TDC were extremely sensitive to the phenyl rotation and therefore expected to yield more accurate energy transfer rates. In addition, Kleiman et al.<sup>75</sup> investigated the energy transfer in the nanostar with femtosecond degenerate pump-probe spectroscopy. They measured the recovery time of the ground state absorption of 2-ring and 3-ring chromophores. The experimental transfer rates were compared with the calculated ones using the Förster model. Even though there was a qualitative agreement, the rates were overestimated. Ortiz et al. discussed that the discrepancy between Förster model and experimental results would be improved by the use of TDC and the data from molecular dynamics.<sup>74</sup>

Theoretical calculations by Mukamel et al. indicate that meta branching electronically decouples the resonative conjugation among PE units.<sup>76-79</sup> As a result, the optical excitation is localized on each PE chain in compact and extended dendrimers. Experimental evidence for this excitonic localization can be seen by steady state spectroscopy. The absorption spectrum of any compact structure closely reproduces the spectrum of an isolated PE unit. The total absorption intensity increases monotonically with generation, but exhibits no red-shift. If excitations were delocalized over the entire dendrimer backbone, a red-shift should have been observed. Due to identical chain length of all subunits, compact dendrimers have an energetically degenerate nature, allowing the exciton to rapidly hop between neighboring localized states. An exciton initially localized on a particular PE chain will not encounter any energy gradient towards the locus. On the contrary, an entropic bias is observed which increases the probability of hopping toward the periphery. Thus, compact dendrimers do not act as energy funnels.

The extended PE dendrimers also exhibit localized electronic excitations due to branching at meta positions of phenyl rings. The difference lies in the HOMO-LUMO energy of these localized excitations. It is known that the HOMO-LUMO excitation energy of a molecule decreases with an increase in the extent of conjugation. While the single diphenylacetylene (DPA) chains around the periphery have the greatest excitation energy, this value decreases monotonically toward the center of the molecule as the chain length increases. The absorption spectra for the extended dendrimer series also exhibit a high-energy peak assigned to the shortest DPA chains, but additionally increasing red shifted peaks are observed associated with longer PE units (3- and 4-ring).<sup>80</sup> As a result, a

built-in energy gradient is observed and intramolecular energy transfer in the extended dendrimer series is well directed from periphery to the core.

The random hopping and funneling characteristics of both compact and extended PE dendrimers were investigated theoretically. Mukamel and coworkers investigated the optical properties of such systems using the Collective Electronic Oscillator (CEO) approach and the Frenkel-exciton model.<sup>76,77</sup> In parallel to the experimental results, theoretical studies have shown that optical excitations involve no charge transfer and are completely localized between linear segments. Since the meta branching disrupts the charge transfer between individual PE segments, exciton migration proceeds via Coulombic interaction and these systems can be represented by the Frenkel Exciton Hamiltonian. The linear absorption spectra of these dendrimers were calculated using the CEO approach and showed excellent agreement with the experiment. It was concluded that the linear segments can be considered as effective chromophores where optical excitations reside. Upon photoexcitation, the electron-hole pair is confined to a single chromophore, whereas its center of mass can move around representing energy migration across the molecule.

The extended PE series represent the first example of a built-in multi-step energy gradient within dendritic systems and are very efficient photosynthetic mimics. By functionalizing the core of these structures with the lower-bandgap ethynyleneperylene chromophore, an energy “sink” is introduced into the system.<sup>81</sup> The most studied extended derivative, both experimentally and theoretically, has 4 generations (2-, 3- and 4- ring PE units) and is referred as the “nanostar” (Figure 1-5a). Excitation of the nanostar backbone results in emission emanating solely from this ethynyleneperylene

dye. Hence, the PE units act as energy donors and ethynyleneperylene acts as the central acceptor. The absorption data along with the lifetime data indicate that the ethynyleneperylene unit at the focal point of nanostar has a well localized excited state. Figure 1-5b shows the energy level diagram illustrating the vibrationless electronic excitation energies of each of the localized states in the nanostar.<sup>69,82</sup> This graphic representation points out the impressive energy funneling characteristics of the nanostar.

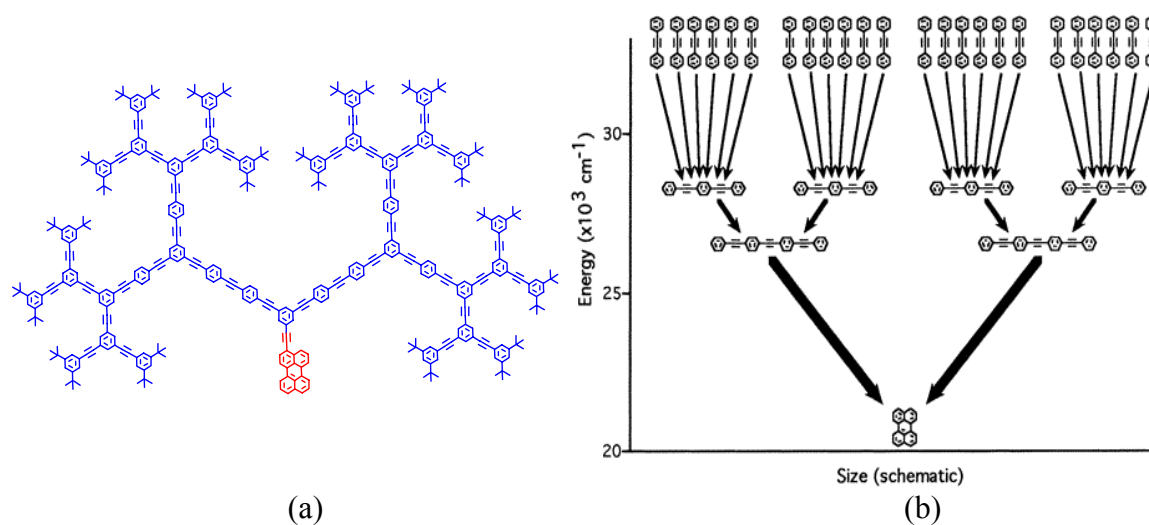


Figure 1-5. Nanostar dendrimer (a) Chemical structure (b) Energy level diagram. Adapted from reference<sup>80</sup>

Theoretically, the Mukamel group intensively investigated the nanostar molecule and computed the exciton energies, transition dipole moments, and electrostatic interactions in PE segments using the CEO method.<sup>76,78</sup> They computed linear absorption, frequency gated fluorescence spectra, and even frequency-domain pump probe signal. In addition, Tada et al. investigated photoexcited states of the nanostar and singlet excitations of linear PE units involved in the dendrimer with time dependent density functional theory and molecular orbital method.<sup>83</sup> It was concluded that the orbitals of nanostar are localized in space as well as in energy. While the steady state comparison

with these calculations implies the model of weakly coupled Frenkel excitons, the dynamics of the excited states in PE dendrimers may lead to a different picture of excitations. This issue is crucial to understand the nature of electronic excitations and further calculations have been recently carried out by Bardeen and coworkers. They reported both high-level electronic structure calculations and steady-state experiments based on the smallest building blocks of PE dendrimers.<sup>84</sup> Their emission spectral shapes, radiative lifetimes, and anisotropies change dramatically with increasing number of substituents. This yields strongly coupled diphenylethynylene units and contradicts previous findings. The excited state electronic structure was investigated theoretically using ab initio CASSCF and CASPT2 calculations and the electronic coupling was found to vary with molecular geometry. In particular, the presence of large electronic coupling in the emitting geometry was not seen for the absorbing geometry of the same molecule. In order to analyze the variability in electronic coupling, they extended their ab initio results in terms of the Harcourt model.<sup>85</sup> This model was developed to classify different interactions such as through bond, through space and charge transfer interactions between coupled chromophores. The relative roles of these three interaction terms and their dependence on meta- versus para- substitution were investigated in detail. However, the experiments in larger dendrimers do not show the spectral features (shifts) predicted in the smaller systems.<sup>70,86</sup> So, the nature of the excited states for PE dendrimers remains an open question.

In another study to address the complicated photoexcitation energy transfer between subunits of a dendritic system, a simple compact model system with one branching center was investigated by Goodson and coworkers.<sup>87,88</sup> In that study, each

component of the branching center was a conjugated linear segment. The interactions between these segments (chromophores) are strongly influenced by the electronic and structural connectivity of the branching center. Varnasvski et al. have investigated the nature of these interactions using fluorescence anisotropy.<sup>87</sup> For example, the very fast depolarization rate in a nitrogen centered triphenylamine molecule indicates strong electronic coupling between segments. In another publication by the Goodson group, fluorescence anisotropy dynamics of a system containing pyridine distyrylbenzene chromophores attached to benzene center was reported.<sup>89</sup> Their results confirmed that the benzene branching center acts as a weak coupler and electronic delocalization across the branching center is hindered by meta substitution of the chromophores. It is important to recall that phenyl is the branching center between the individual chromophores in PE dendrimers. Therefore, most of the theoretical and experimental studies are complementary in terms of verifying the localized nature of excitations for symmetrical PE dendrimers, with the exception of Bardeen's results.<sup>84,90</sup>

Our group has an ongoing collaboration with Prof. Jeff Krause and Prof. Adrian Roitberg to investigate this unique symmetric PE dendrimer nanostar. As discussed in detail in Chapter 5 of this thesis, we performed femtosecond time-resolved experiments on the nanostar. We explored the excited state dynamics by measuring the fluorescence from both the ethynyleneperylene trap (acceptor) and the dendritic backbone (donor). Broadband transient absorption following the excitation at different chromophores was also examined. In addition, room and low temperature steady-state absorption spectra of the individual PE components and the nanostar were measured and compared to theoretical calculations performed to predict the spectra.

## Unsymmetrical PE Dendrimers

Most of the dendrimers developed for light harvesting applications have symmetrical structures. As discussed in the previous section, for symmetrical PE dendrimers, the electronic communication between the periphery and the core has to go through each sub-branch. For unsymmetrical dendrimers, shortcuts exist between the periphery and the core, such that in some cases shorter PE chains are directly attached to the longest chain extending to the core. The core of the dendrimer can directly communicate with the periphery. Therefore, it is anticipated that unsymmetrical dendrimers may be better light-harvesting antenna molecules. To prove this concept, Peng and coworkers<sup>91-94</sup> reported a new class of conjugated PE dendrimers based on unsymmetrical branching which occurs at both ortho and meta positions of the branching benzene rings and leads to nonequivalent branches. Two features are crucial for unsymmetrical PE dendrimers: rapidly increasing conjugation length results in broad absorption spectra and the conjugation length increases toward the core generating an intrinsic energy gradient.

Figure 1-6 shows the structures of unsymmetrical PE monodendrons. These dendritic molecules have both ortho and meta substitution while the symmetrical ones have only meta linkage. The conjugation length of the longest chain is significantly larger compared to the meta-linked dendrimer composing of the same number of phenyl ethynylene groups. Therefore, they are expected to have different optical properties.

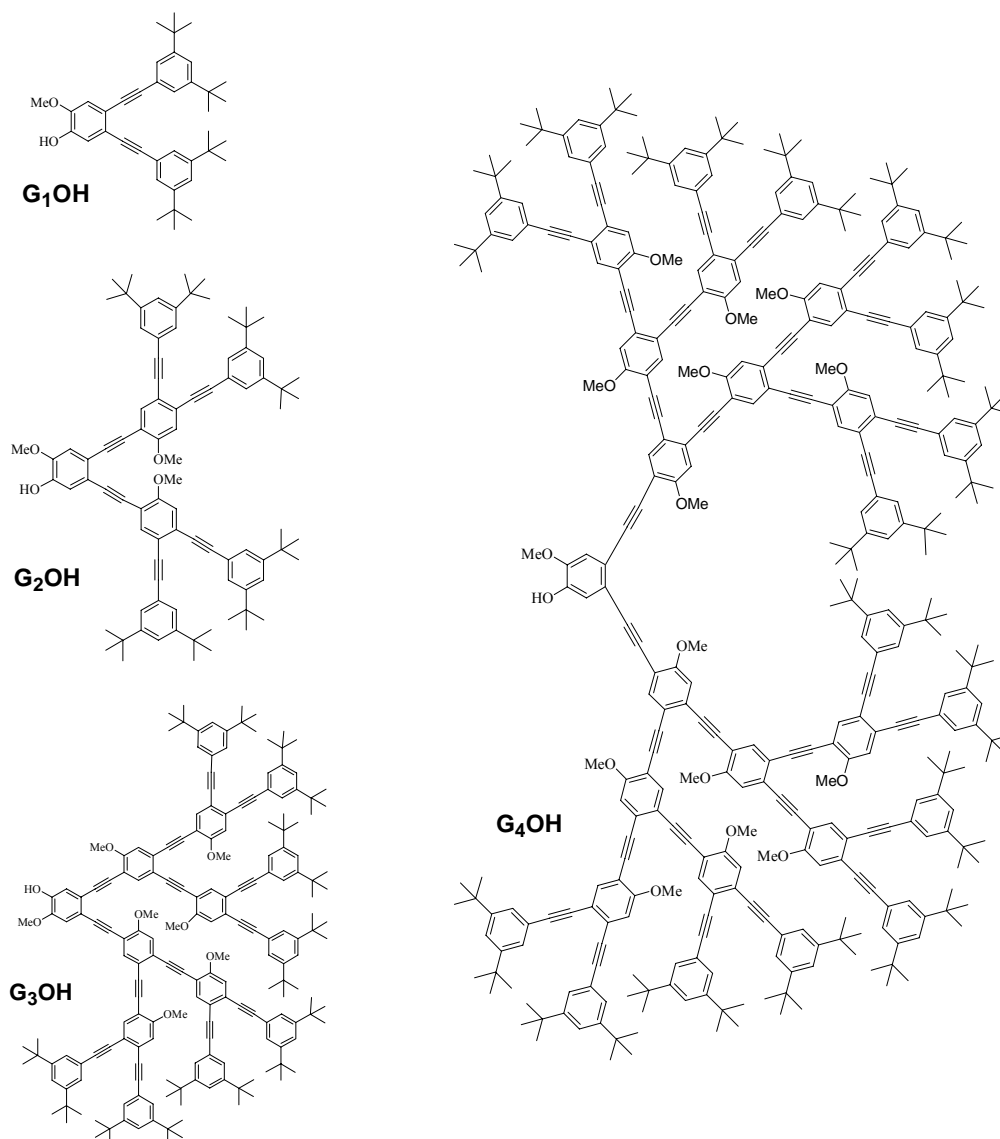


Figure 1-6. Chemical structures of unsymmetrical PE dendrimers

Figure 1-7 shows the absorption and emission spectra of G<sub>n</sub>OH (n=1-4) unsymmetrical PE dendrons. As the generation number increases, the lowest excitation energy (absorption band edge) shifts to longer wavelengths and the molar extinction coefficient increases. Even though the ortho substitution prevents the phenyl rings from having a planar geometry due to steric hindrance, the effective conjugation length clearly increases with each generation. Variable conjugation length throughout the dendrimer accounts for the much broader absorption spectrum than that of the meta-linked

symmetric analogs. This broad absorption spectrum along with direct electronic communication between periphery and the core could possibly make these types of dendrimers more efficient energy transfer funnels. As seen in the emission spectrum, fluorescence is red shifted for higher generation dendrimers. Following the photoexcitation, the energy transfer will proceed from shorter conjugation-length segments to the longest conjugated segment, thus for a given dendrimer, emission is only observed from the longest chain. The fluorescent quantum yield of  $G_n\text{OH}$  dendrimers varies from 40% up to 80% (in  $\text{CH}_2\text{Cl}_2$ ).

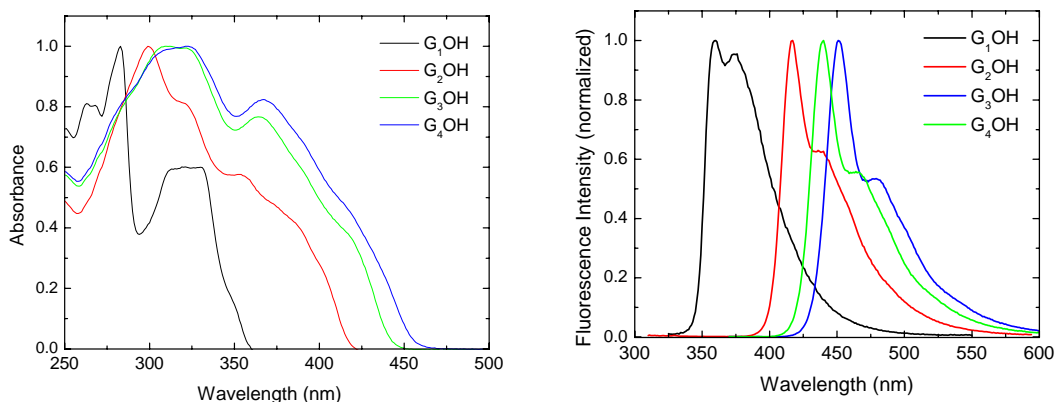


Figure 1-7. Absorption and emission spectra of  $G_n\text{OH}$  monodendrons. Adapted from reference<sup>71</sup>

Since it is hard to differentiate each segment within the unsymmetrical dendrimers, it would be hard to quantitatively evaluate the energy transfer efficiency. However, analogous to the symmetrical PE dendrimers, an ethynyleneperylene unit serving as energy trap has been attached to the focal point of the dendritic backbone. Ethynyleneperylene, having well-separated absorption from the dendrimer absorption, will help explore the excitation energy transfer. The absorption and emission spectra of  $G_n\text{Per}$  series are shown in Figure 1-8. The absorption features of perylene can be clearly distinguished from the PE backbone. The perylene bands are approximately 50 nm red-

shifted compared to the free perylene in the  $\text{CH}_2\text{Cl}_2$ , which indicates the delocalization of perylene transition dipole over the PE backbone. The fluorescence spectra of  $G_n\text{Per}$  series following 350-nm excitation is also shown in Figure 1-8b. For any given dendrimer, the emission is almost entirely from the perylene trap, which indicates very efficient energy transfer from the dendrimer backbone to the ethynyleneperylene trap. Melinger et al. presented a detailed photophysical characterization of unsymmetrical PE monodendrons in various solvents.<sup>95</sup> They reported steady-state absorption and fluorescence measurements along with the time-dependent fluorescence measurements for PE monodendrons up to fourth generation. The photophysical properties of unsymmetrical PE monodendrons were compared to those of symmetrical PE dendrimers. In addition, ultrafast degenerate pump-probe spectroscopy was applied to  $G_3\text{OH}$  and  $G_3\text{Per}$  to explore the excited state dynamics.<sup>95</sup> These initial measurements suggested that energy transfer process into the ethynyleneperylene trap occurs in a subpicosecond time scale. However, a direct measurement of the trapping time is yet to be ascertained through multi-color pump probe experiments or by measuring the time evolution of the ethynyleneperylene fluorescence with femtosecond resolution. This is one of the goals of this dissertation.

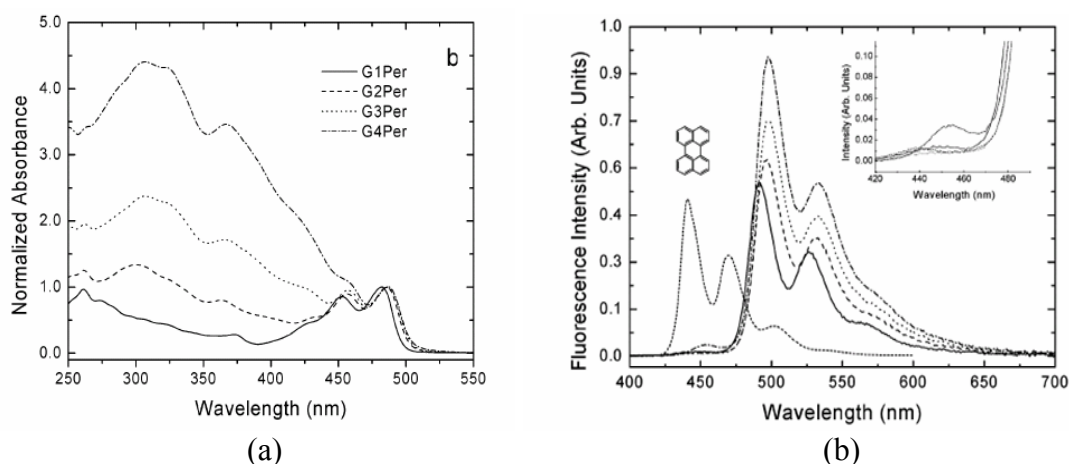


Figure 1-8. Steady state spectra of  $G_n\text{Per}$  monodendrons: absorption (a) and emission (b). Adapted from reference<sup>96</sup>

Recently, Peng and coworkers synthesized PE didendrons along with some tridendrons so that an extensive investigation is possible to establish a structure-property relationship regarding energy transfer and  $\pi$ -conjugation.<sup>97</sup> In that work, two PE monodendrons were linked by a phenyl ring at meta positions and these new structures were named as  $2G_nOH$  series. For  $2G_nPer$  dendrimers, an ethynyleneperylene unit was attached to the central benzene ring in meta position. Due to meta substitution at the core of the dendrimer, the conjugation is expected to be disrupted and an extra degree of localization might be provided between the monodendrons and/or between the monodendron and the ethynyleneperylene unit. The chemical structures of didendrons are illustrated in Figure 1-9. Through collaboration with the Peng group, we obtained the didendrons studied in this dissertation. Mainly,  $2G_nOH$  and  $2G_nPer$  ( $n=1,2$ ) are studied via both steady-state and time-resolved spectroscopic techniques in Chapter 3 and 4. Even though initial studies with unsymmetrical PE monodendrons reveal some spectroscopic evidence for the highly efficient and ultrafast energy transfer, questions remain regarding the nature of electronic excitations and related mechanisms for the transfer process. The ultrafast absorption and emission experiments designed and performed in this dissertation aim to explore these questions.

Unsymmetrical PE dendrimers are an attractive prospect as they offer a handle to obtain various extends of conjugation and help in understanding electronic structure-property relationship for better light-harvesting systems. The processes following the optical excitation in a molecule and basic energy transfer mechanisms will be explained briefly in the following section.

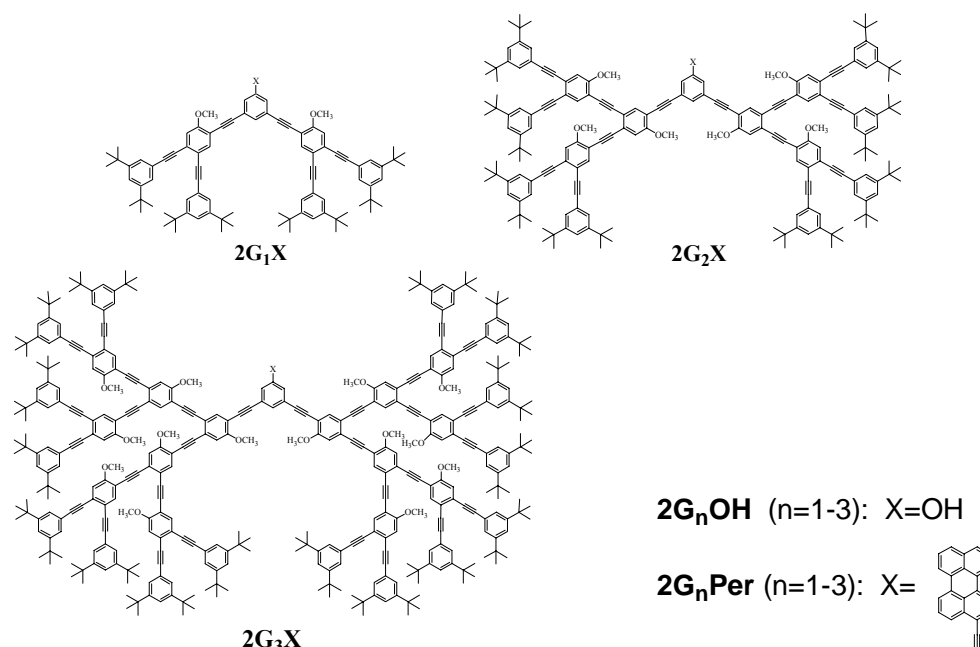
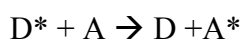


Figure 1-9. Chemical structure of PE didendrons.

### Excitation Energy Transfer

The motivation behind the work presented in this dissertation is to identify the mechanisms of intramolecular electronic excitation energy transfer in light-harvesting dendrimers and the structure-function relationship that make energy transfer very efficient in these systems. Other than self-relaxation processes, the excited states may relax to the ground state via transferring the electronic excitation to other chromophores present in the system by a bimolecular process. During this process the excited donor chromophore  $D^*$  returns to its ground state with simultaneous transfer of its electronic energy to the acceptor chromophore A:



Subsequently, the photoexcited chromophore  $A^*$  may proceed either giving a sensitized photochemical reaction or exhibit sensitized photoluminescence. Under these conditions D chromophores are termed as sensitizers while A chromophores as activators. There are mainly two conditions required for energy transfer to occur: (i) the energy of

D\* should be higher than the energy of A\*; (ii) the energy transfer process should be faster than the natural lifetime of D\*. The electronic energy transfer can be described further according to the photophysical processes that are involved in it.

### **Radiative Energy Transfer**

Radiative energy transfer is a two-step process: a photon is first emitted from the excited donor and then it is reabsorbed by the acceptor ground state:



Since the transfer mechanism is based on a radiative step (i.e. photons emitted by one chromophore are absorbed by a second chromophore), this process is named as the “trivial” case of electronic energy transfer. It does not involve the direct interaction of donor and acceptor. The most important factor that influences the process is the quantum efficiency of the donor in the spectral region where the light-absorbing ability of the acceptor is high. The trivial transfer is favored when the following conditions are met: high quantum yield of D\*, high concentration and extinction coefficient of A, and good overlap between the emission of D\* and absorption of A. This kind of energy transfer might be the dominant mechanism in dilute solutions since the dependence of energy transfer efficiency on separation distance between donor and acceptor chromophores is weak. The viscosity of the solvent does not affect the rate of radiative energy transfer.

Radiative transfer results in a decrease of the donor fluorescence intensity in the region of spectral overlap. When donor and acceptor chromophores are identical and emission and absorption overlap sufficiently, the observed fluorescence lifetime increases as a result of repeated absorption and emission (radiative trapping).

## Non-radiative Energy Transfer

Non-radiative energy transfer is a single step process that requires donor-acceptor interaction as a result of spectral overlap between donor's emission spectrum and acceptor's absorption spectrum.  $D^* \rightarrow D$  and  $A \rightarrow A^*$  transitions are isoenergetic, implying that several vibronic transitions in the donor will have the same energy as the corresponding transitions in the acceptor. Such transitions are coupled, and are in resonance as shown in Figure 1-10. For non-radiative energy transfer, the terms resonance energy transfer (RET) and excitation energy transfer (EET) are often used. If the excited state vibrational relaxation is faster than the energy transfer, and if the energy transfer is a vertical process as implied by the Franck-Condon principle, the spectral overlap can be evaluated using:

$$J = \int_0^{\infty} I_D(\tilde{\nu}) \varepsilon_A(\tilde{\nu}) d\tilde{\nu} \quad (1-1)$$

This integral is proportional to the number of resonant transitions in the emission spectrum of the donor and absorption spectrum of the acceptor as illustrated in Figure 1-10. The spectral distribution of the donor emission and the acceptor absorption are normalized to a unit area on the wave-number scale:

$$\int_0^{\infty} I_D(\tilde{\nu}) d\tilde{\nu} = \int_0^{\infty} \varepsilon_A(\tilde{\nu}) d\tilde{\nu} = 1 \quad (1-2)$$

According to this required spectral overlap condition for normalized spectra, it is clear that the magnitude of the spectral overlap is not connected to the absolute values of the oscillator strengths of the transitions that are involved in the process.

There are two different interaction mechanisms related to non-radiative energy transfer process: coulombic and exchange interactions. The coulombic interactions

consist of long-range dipole-dipole interactions and short-range multipolar interactions. The interactions due to intermolecular orbital overlap include two electron exchange (Dexter mechanism) and charge resonance interactions, which are effective in short range. The total interaction energy can be written as the sum of a coulomb term,  $U_c$  and an exchange term  $U_{ex}$ . Considering that only two electrons are involved in a transition (one on D and one on A), the energy transfer mechanisms are schematically represented in Figure 1-11. In the figure, the empty circles represent the electrons whose interactions with other electrons are assumed to be roughly constant during the energy transfer step.

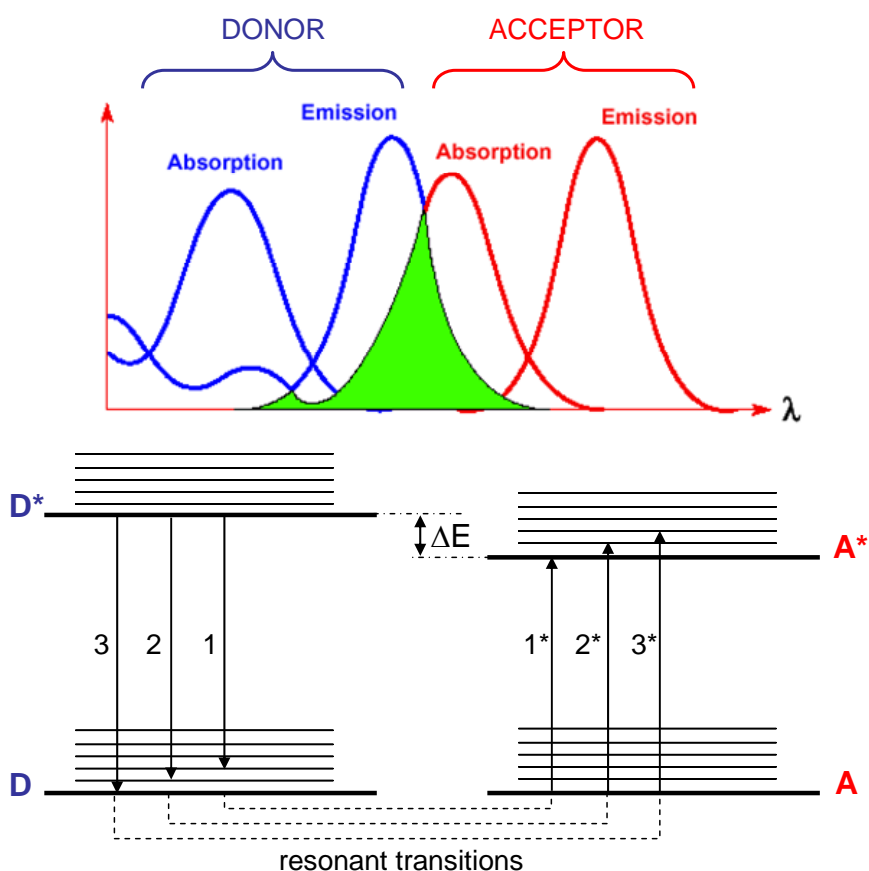


Figure 1-10. Model picture for energy transfer showing resonant transitions of donor and acceptor, and spectral overlap of donor emission and acceptor absorption.

The coulombic term corresponds to the process in which the initially excited electron on the donor (1) returns to the ground state orbital on D, while simultaneously an electron on the acceptor A (2) is promoted to excited state (Figure 1-11, top). The exchange term is represented with an exchange of two electrons between D and A, which is analogous to a moving particle transferring its energy to the other particles via collisions. Coulombic resonance interaction occurs via electromagnetic field and does not require physical contact of interacting donor and acceptor. The basic mechanism involves the induction of a dipole oscillation in A by  $D^*$ , thus the Coulombic mechanism can be effective at large distances (up to 80-100 Å). As shown in Figure 1-11(bottom), the exchange interaction represents a “double” electron substitution reaction, i.e., the electron

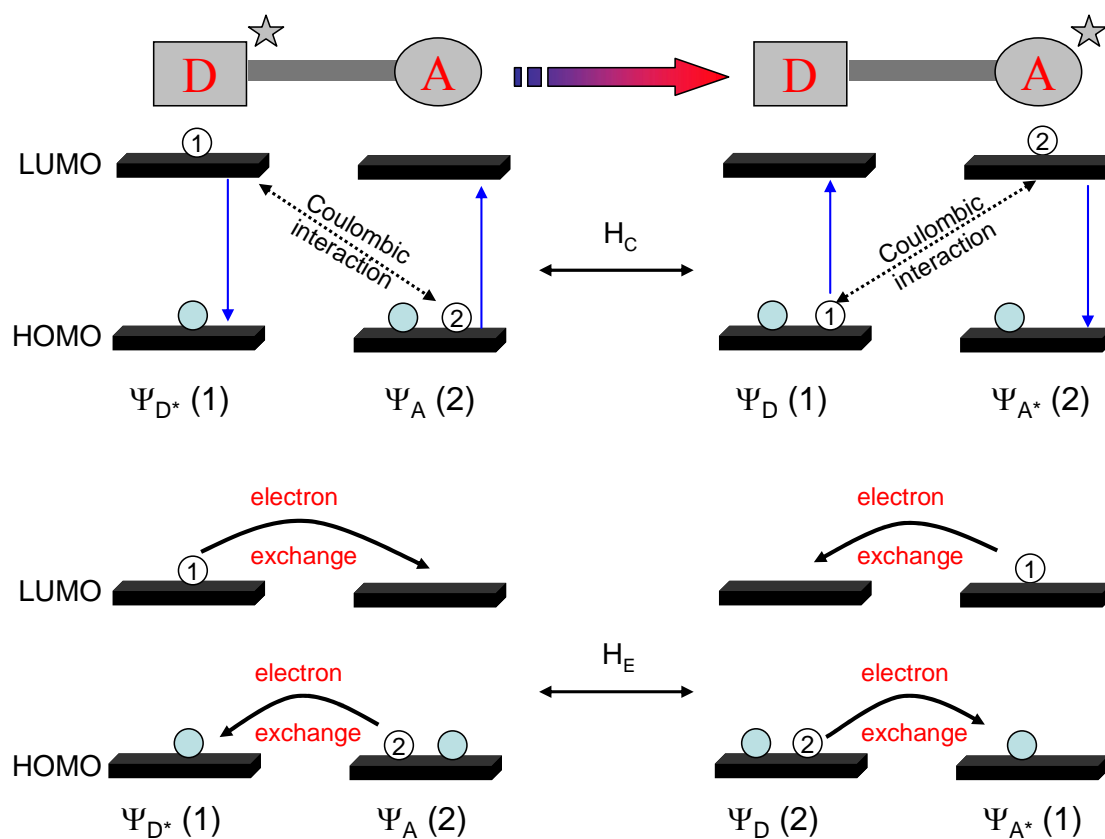
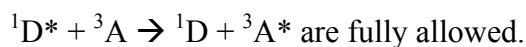


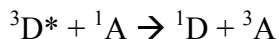
Figure 1-11. Schematic representation of energy transfer mechanism. Top: Coulombic mechanism. Bottom: Exchange mechanism<sup>98</sup>

initially on D\* jumps to A simultaneously with the jump of an electron on A to D\*. This exchange interaction occurs via overlap of the molecular orbitals requiring physical contact between donor and acceptor. The interaction is operative only at short-range (10-15 Å) because the electron density exponentially decreases outside the boundaries of molecules.

For allowed transitions on D and A (no change in spin), coulombic interaction is the predominant mechanism. Thus, singlet-singlet energy transfer such as



However, for forbidden transitions on D and A:



coulombic interaction is negligible and triplet-triplet energy transfer is only due to orbital overlap. It should be noted that for singlet-singlet energy transfer, both interactions may be involved, but in general coulomb mechanism predominates.

The interaction energy describing the coupling between the initial and final states is given by:

$$U = \langle \psi_i | H' | \psi_f \rangle \quad (1-3)$$

where  $H'$  contains the electrostatic interactions of all electrons and  $\psi_i$  and  $\psi_f$  are the electronic wavefunctions for the initial and the final excited state, respectively.

Considering that only two electrons are involved in a transition, the antisymmetrized product wave functions of the initial and final state can be written as:

$$\begin{aligned}\psi_i &= \frac{1}{\sqrt{2}}(\psi_{D^*}(1)\psi_A(2) - \psi_{D^*}(2)\psi_A(1)) \\ \psi_f &= \frac{1}{\sqrt{2}}(\psi_D(1)\psi_{A^*}(2) - \psi_D(2)\psi_{A^*}(1))\end{aligned}\quad (1-4)$$

where the numbers 1 and 2 refer to the two electrons involved. The total interaction U can be written as the sum of the Coulomb and the exchange terms:

$$U = \left\langle \frac{1}{\sqrt{2}}(\psi_{D^*}(1)\psi_A(2) - \psi_{D^*}(2)\psi_A(1)) \left| H' \right| \frac{1}{\sqrt{2}}(\psi_D(1)\psi_{A^*}(2) - \psi_D(2)\psi_{A^*}(1)) \right\rangle \quad (1-5)$$

$$U_C = \langle \psi_{D^*}(1)\psi_A(2) | H' | \psi_D(1)\psi_{A^*}(2) \rangle \quad (1-6)$$

$$U_{ex} = \langle \psi_{D^*}(1)\psi_A(2) | H' | \psi_D(2)\psi_{A^*}(1) \rangle$$

$$U = U_C - U_{ex} \quad (1-7)$$

The Coulomb term,  $U_C$ , represents the classical interaction of the charge distributions and may be expanded into multiple terms: dipole-dipole, dipole-quadrupole, etc., Dipole-dipole interaction dominates for allowed transitions:

$$U_C \approx U_{dd} = \frac{1}{4\pi\epsilon_0} \frac{\kappa\mu_D\mu_A}{R_{DA}^3} \quad (1-8)$$

where  $\mu_D$  and  $\mu_A$  denote the transition dipole moments of the two molecules ( $D^* \rightarrow D$  and  $A \rightarrow A^*$ ) and  $R_{DA}$  is the distance between the donor and the acceptor. Here, the orientation factor  $\kappa$  is defined by:

$$\begin{aligned}\kappa &= \bar{\mu}_D \cdot \bar{\mu}_A - 3(\bar{\mu}_D \cdot \bar{R}_{DA})(\bar{\mu}_A \cdot \bar{R}_{DA}) \\ \kappa &= 2 \cos \theta_D \cos \theta_A + \sin \theta_D \sin \theta_A \cos \varphi\end{aligned}\quad (1-9)$$

The vectors, angles and separation between dipoles are defined in Figure 1-12.

When  $U_{dd}$  is expressed in  $\text{cm}^{-1}$ , the transition moments are in Debye and  $R_{DA}$  is in nm.  $\varphi$  is the angle between two transition moments and  $\theta_D$  and  $\theta_A$  are the angles between each

transition moment and the vector connecting them. Considering this picture, it is clear that no interaction would be observed between perpendicularly oriented chromophores.

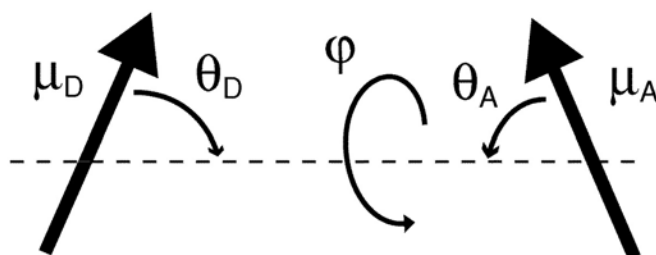


Figure 1-12. Definition of the angles used to calculate the orientation factor between the dipoles.<sup>99</sup>

The dipole-dipole approximation provides reliable estimation of the electronic coupling between point dipoles, i.e. when the donor acceptor separation is much larger than the molecular size of the donor and acceptor transition dipole moments. At short distances or when the separation is comparable to molecular dimensions (large dipole moments), the point dipole approximation is not valid, and a better description of the shape of the dipoles should also be included in the calculations. The transition moment magnitude  $\mu$  (in units of Debye) is related to the dipole strength of an absorption band, measured in media of refractive index  $n$ , according to:

$$\mu^2 \approx f = \frac{4.3 \times 10^{-9}}{n} \int \varepsilon(\bar{\nu}) d\bar{\nu} \quad (1-10)$$

Thus, the Coulomb interaction term can be related to experimentally measured quantities.

The exchange interaction is a purely quantum mechanical phenomenon and does not depend on the oscillator strengths of the transitions involved. The exchange integral

$$U_{ex} = \langle \psi_{D^*}(1) \psi_A(2) | \frac{e^2}{r_{12}} | \psi_D(2) \psi_{A^*}(1) \rangle \quad (1-11)$$

represents the interaction of charge densities separated by a distance  $r_{12}$ . Since charge densities depend on the spatial overlap of orbitals of D and A, the exchange interaction decreases exponentially with increasing internuclear distances.

The non-radiative transfer rate is basically given by Fermi's Golden Rule.

According to the Golden Rule, the rate of transition between two states is related to the magnitude of a perturbation which changes the positions or motions of particles of the initial state and reshapes the initial state so that it looks like the final state. Beyond the Born-Oppenheimer approximation, it is necessary to include the interaction between different vibrational-electronic molecular states in order to describe such transitions.

Using the time-dependent perturbation theory, the rate constant  $k_{ET}$  is formulated as:

$$k_{ET} = \frac{2\pi}{\hbar} V^2 \rho = \frac{2\pi}{\hbar} \langle \psi_i | H' | \psi_f \rangle^2 \rho \quad (1-12)$$

where  $\rho$  is the density of interacting initial and final states as determined by Franck-Condon factors, and it is related to the spectral overlap between the emission of the donor and the absorption of the acceptor in a system without inhomogeneous broadening. Using the relations for the interaction energy given above, Förster and Dexter derived expressions for the rate constant of energy transfer using the Coulomb and the exchange mechanism, respectively.<sup>100,101</sup>

Dexter's formulation points out that an exponential dependence is expected from the exchange mechanism. The rate constant for transfer can be written as:

$$k_{ET} = \frac{2\pi}{\hbar} KJ \exp(-2r_{12}/L) \quad (1-13)$$

where J is a spectral overlap integral with the normalization condition, L is the average Bohr radius and K is related to specific orbital interactions, not related to any

spectroscopic data. Thus, it is difficult to characterize the exchange mechanism experimentally.

While the nature of the interaction, whether Coulombic or exchange, is an important task to investigate, the magnitude of the interaction also needs to be explored. Förster proposed to discriminate between very weak, intermediate (weak), and strong electronic coupling depending on the relative values of the interaction energy ( $V$ ), which is the pure electronic energy difference between  $D^*$  and  $A^*$  ( $\Delta E$ ), the absorption bandwidth ( $\Delta w$ ), and the vibronic bandwidth ( $\Delta \epsilon$ ) (Figure 1-13).

**Strong coupling.** In this case, the intermolecular interaction,  $V_c$ , is much larger than the width of the individual transitions  $D \rightarrow D^*$  and  $A \rightarrow A^*$ . Then, all the vibronic subtransitions in both molecules are virtually at resonance with one another. The transfer of excitation energy is faster than the nuclear vibrations and vibrational relaxation. The absorption spectra of strongly coupled systems will be different from those of the individual components. The donor and acceptor electronic states will mix to produce

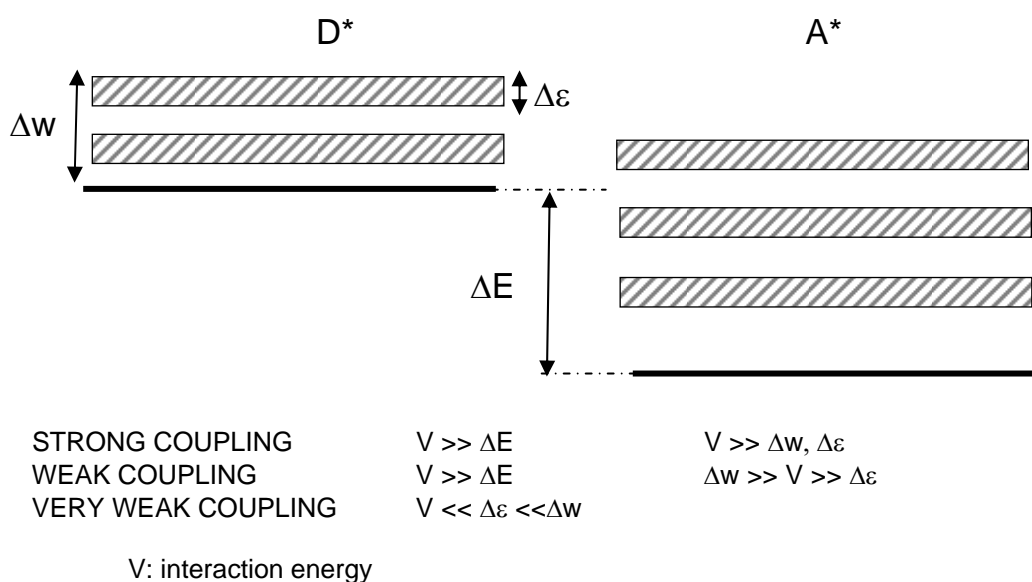


Figure 1-13: Differences between strong, weak, and very weak coupling.

**new**, delocalized states. Thus, the transfer of excitation is a coherent process and the excitation oscillates back and forth between D\* and A\*. The rate constant is derived as:

$$k_{ET} \approx \frac{4|V|}{h} \quad (1-14)$$

where V is approximated by dipole-dipole interaction. The distance dependence of V, and consequently of  $k_{ET}$ , is  $r^{-3}$ .

**Intermediate (Weak) coupling.** This is a particularly challenging case to model RET dynamics. The interaction energy, V, is larger than the width of an isolated vibronic level but much smaller than the full absorption bandwidth. Compared to the strong coupling case, the electronic excitation is more localized. On the other hand, the vibronic excitation is still delocalized and the system can be described in terms of stationary vibronic exciton states. The transfer rate is fast compared to vibrational relaxation. It is approximated as:

$$k_{ET} \approx \frac{4|V|S_{vw}^2}{h} \quad (1-15)$$

where  $S_{vw}$  is the vibrational overlap integral of the intramolecular transition  $v \leftrightarrow w$ .

Since  $S_{vw} < 1$ , the transfer rate would be slower than in the case of strong coupling.

**Very weak coupling.** The interaction energy is much lower than vibronic and absorption bandwidth. The vibrational relaxation occurs before the transfer occurs. The absorption spectra of the components are not altered. The transfer rate is given by:

$$k_{ET} \approx \frac{4\pi^2(VS_{vw})^2}{h\Delta\varepsilon} \quad (1-16)$$

The characteristic feature of this very weak coupling case is the quadratic dependence of the transfer rate on the interaction energy, as opposed to the linear

dependence found for the intermediate and strong coupling. For dipole-dipole interaction, the distance dependence is  $r^{-6}$ , whereas it is  $r^{-3}$  for the preceding cases.

Förster theory for RET is formulated for the very weak coupling limit. It is based on an equilibrium Fermi Golden Rule approach with a second-order perturbation theory treatment of the electronic coupling between donor and acceptor. The theory was established for coupling of a state to a quasi continuum of secondary states. The primary, discrete states are non-stationary and they carry all the oscillator strength. Such model allows rationalizing dynamic processes involving decay of a “stationary” state for radiationless transitions. In other words, the transfer rate occurs after vibrational relaxation. In this way, Förster model evaluates a Fermi Golden Rule expression for the RET rate, where the matrix element of interaction between excited state donor and ground state acceptor is purely electronic coupling  $V$ . Conditions of energy conservation and nuclear overlap factors, separated from the electronic coupling, relate the donor emission and acceptor absorption events:

$$k_{ET} = \frac{2\pi}{\hbar} \int_0^{\infty} d\varepsilon \sum_k \sum_l P(k)P(l) |u(\varepsilon_d^k, \varepsilon_a^k, \varepsilon)|^2 \quad (1-17)$$

where  $\varepsilon_d^k$  is the energy gap of the donor molecule,  $P(k)$  is thermal population of mode  $k$  in the excited state, and  $\varepsilon_a^k$  is the energy of the acceptor ground state. The matrix element of interaction between the excited state donor and ground state acceptor is independent of energy and can be written as:

$$u = \sum_k \sum_l P(k)P(l) |u(\varepsilon_d^k, \varepsilon_a^k, \varepsilon)|^2 = |V|^2 J(\varepsilon) \quad (1-18)$$

where  $J(\varepsilon)$  is the spectral overlap between donor emission  $f(\varepsilon)$  and acceptor absorption  $a(\varepsilon)$ , and can be written as  $J(\varepsilon) = f(\varepsilon).a(\varepsilon)$ .  $f(\varepsilon)$  and  $a(\varepsilon)$  have each been normalized to

unit area on an energy scale:  $\int f(\varepsilon)d\varepsilon = \int a(\varepsilon)d\varepsilon = 1$ . The rate constant can be rewritten as:

$$k_{ET} = \frac{2\pi}{\hbar} |V|^2 \int_0^\infty d\varepsilon J(\varepsilon) = \frac{1}{\hbar^2 c} |\bar{V}|^2 \int_0^\infty d\tilde{\nu} J(\tilde{\nu}) \quad (1-19)$$

where  $\bar{V}$  is expressed in units of  $\text{cm}^{-1}$ , and  $\tilde{\nu} = \varepsilon / 2\pi\hbar c$ . In summary, estimating a rate for RET in the weak coupling limit requires the knowledge of the electronic coupling,  $V$ , and the spectral overlap,  $J$ , between donor and acceptor transitions. The final rate equation is defined as:

$$k_{ET} = \frac{4\pi^2 J}{\hbar^2 c} |V|^2 \quad (1-20)$$

It is important to note that  $J$  in this equation is defined as  $J(\text{cm}) = \int f(\lambda)a(\lambda)\lambda^2 d\lambda$  and has units of  $\text{cm}$ .

By substituting the Coulomb interaction energy term,  $V_C$ , into the Golden Rule equation, and assuming a dipole-dipole approximation, Förster derived the final expression for energy transfer rates based on spectroscopically measurable parameters. The Förster equation is:

$$k_{ET} = \frac{9000 \ln(10) \kappa^2 \phi_D J_{DA}}{128 \pi^5 n^4 N_A R_{DA}^6 \tau_D} \quad (1-21)$$

where  $\kappa^2$  is the orientation factor of the transition dipole moments,  $\phi_D$  is donor quantum yield,  $\tau_D$  is the donor lifetime in the absence of the acceptor,  $N_A$  is Avogadro's number, and  $n$  is the refractive index of the solvent. Note that in this equation spectral overlap  $J$  is defined as:

$$J_{DA} = \int_0^{\infty} f_D(\lambda) \varepsilon_A(\lambda) \lambda^4 d\lambda = \int_0^{\infty} \frac{f_D(\tilde{\nu}) \varepsilon_A(\tilde{\nu})}{(\tilde{\nu})^4} d\tilde{\nu} \quad (1-22)$$

$f_D(\lambda)$  is the fluorescence spectrum of the donor normalized so that  $\int_0^{\infty} f_D(\lambda) d\lambda = 1$  and

$\varepsilon_A(\lambda)$  is the molar absorption coefficient of the acceptor. Hence,  $J_{DA}$  has units of  $M^{-1} \text{cm}^3$ .

At a specific distance of  $R_{DA}$ , the rate at which  $D^*$  emits light is equal to the rate at which it transfers its excitation energy to A. At this critical distance  $R_0$ , called Förster

radius, one can write  $k_{ET} = \frac{1}{\tau_D}$ , then inserting this into rate equation, and solving for  $R_0$

yields:

$$R_0^6 = \frac{9000 \ln(10) \kappa^2 \phi_D}{128 \pi^5 n^4 N_A} J_{DA} \quad (1-23)$$

$R_0$  is the donor-acceptor distance at which the probability for energy transfer is equal to

0.5. The energy transfer rate can also be written in the following form:

$$k_{ET} = \frac{1}{\tau_D} \left( \frac{R_0}{R} \right)^6 \quad (1-24)$$

The transfer efficiency is defined as:

$$\phi_{ET} = \frac{k_{ET}}{k_D + k_{ET}} = \frac{k_{ET}}{1/\tau_D + k_{ET}} \quad (1-25)$$

Using the preceding equation, the transfer efficiency can be related to the ratio  $R/R_0$  by:

$$\phi_{ET} = \frac{1}{1 + (R/R_0)^6} \quad (1-26)$$

Note that the transfer efficiency is 50% when the donor acceptor distance is equal to the Förster critical radius.

The Förster equation for RET is accurate provided that four conditions are satisfied: (i) a dipole-dipole approximation for the electronic coupling can be utilized appropriately for the donor-acceptor interaction, (ii) the donor fluorescence lifetime, emission line shape, acceptor absorption line shape, and oscillator strength are not perturbed because of interactions among donors and acceptors (weak coupling), (iii) inhomogeneous line broadening is absent in the donor and acceptor line shapes, (iv) the energy transfer dynamics is incoherent.

In this dissertation, energy transfer processes in various PE dendrimers are studied. In addition to characterizing a kinetic model for each molecule, the processes according to the strength of D-A coupling will be classified and the validity of previously used Förster approximations is tested.

### **Outline of the Dissertation**

The main scope of this work is to investigate energy transfer processes in conjugated, symmetrical and unsymmetrical phenyl ethynylene (PE) dendrimers. We have conducted experimental studies to improve the understanding of electronic structure of these molecules and its effect on the light-harvesting properties. Chapter 1 is an introduction to dendrimers and a survey of the current scientific literature regarding dendrimer photophysics. This Chapter also includes a brief introduction to energy transfer theory. Chapter 2 summarizes the experimental methods utilized to study time-resolved emission and absorption characteristics of PE dendrimers. This chapter is complemented with Appendix A, a brief description for experimental beginners on how to successfully perform these novel experiments.

Unsymmetrical generation one dendrons are investigated in Chapter 3. The excited state dynamics is studied using both time-resolved and steady state spectroscopy. In an attempt to more quantitatively analyze the results, a kinetic model is proposed.

Chapter 4 describes the excited state dynamics of generation two dendrons and we perform a comparative analysis by transient absorption and time-resolved emission spectroscopy. To explain the multicomponent rise and decays of the excited states, the basic kinetic model (described in Chapter 3) is extended to a more complex level. Apart from the initially excited state, the presence of a second state is verified via low temperature absorption and excitation anisotropy measurements. This chapter further evaluates the effect of generation on transfer rates.

In Chapter 5, we study a symmetrical PE dendrimer, namely “the nanostar” with very detailed experiments and global analysis. In contrast to unsymmetrical dendrimers, this molecule can be considered as a combination of individual chromophores with variable conjugation length. As reference compounds, 2-,3-, and 4-ring phenyl ethynylene chromophores are studied with transient absorption spectroscopy. Particular emphasis is given to recent developments in theories and the proposed kinetic model that offer physical understanding of the energy transfer.

Chapter 6 describes an independent project that we collaborated with Dr. Schanze’s group at UF. The dynamics of fluorescence quenching of a conjugated polyelectrolyte by a cyanine dye are investigated by fluorescence up-conversion and polarization resolved transient absorption. The data are analyzed with a model based on the random walk of the exciton within the polymer chain and a long-range direct energy transfer between polymer and dye.

Appendix A is provided to supplement experimental details and tricks for the upconversion technique. Appendix B gives a brief introduction to the global analysis method. The Singular Value Decomposition analysis combined with the kinetic model for each molecule is given in detail.

## CHAPTER 2 EXPERIMENTAL METHODS

The light harvesting properties of dendrimers lead to the broad investigation of energy transfer processes. It becomes important to evaluate the electronic structure of dendrimers and its effect on energy transfer mechanisms and associated dynamics. This chapter provides background information on the experimental methods employed to explore excited state dynamics of the dendrimers studied throughout this dissertation. An overview was given about the relaxation processes occurring after the photoexcitation of molecules in chapter 1. After photoexcitation, excited molecules in solution undergo various relaxation processes, which can be classified in four major categories: electronic, orientational, vibrational relaxation, and solvent relaxation.<sup>102</sup> Here, we are mainly interested in electronic relaxation processes such as transferring the excitation energy into a specific trap. Steady state absorption and fluorescence spectroscopy give some insights into the spectral composition of the dendrimers and energy transfer pathways. For better understanding of the energy transfer processes, time resolved techniques, such as transient absorption and time resolved fluorescence, are extensively used in this work.

By means of presented experimental techniques, important “ultrafast” phenomena such as energy transfer and nature of excitations in conjugated systems are studied within this dissertation.

### **Chemicals and Materials**

Throughout this dissertation, we investigate unsymmetrical conjugated phenylethynylene (PE) mono- and di-dendrons and a unique symmetrical PE structure

named the "nanostar". The detailed synthesis and structural characterizations of such conjugated PE dendrimers are reported in literature.<sup>69,70,81,82,103</sup> These dendrimers are supplied to us by our collaborators, Prof. Zhonghua Peng from the University of Missouri-Kansas City and Prof. Jeffrey S. Moore from the University of Illinois at Urbana-Champaign. They confirmed the structure and purity of our samples by thin-layer chromatography, elemental analysis, <sup>1</sup>H and <sup>13</sup>C NMR spectroscopy, and matrix-assisted laser desorption/ionization time-of-flight (MALDI-TOF) mass spectroscopy.<sup>104</sup> These samples are used as received. For steady state and time-resolved spectroscopic measurements, the dendrimer samples are dissolved in dichloromethane (CH<sub>2</sub>Cl<sub>2</sub>). The solvent is purchased from Aldrich and the purity was UV-spectroscopy grade (>99.9%). It is kept under nitrogen and used without any further purification. In order to perform steady state measurements at low temperatures, a liquid nitrogen flow cryostat is used to control the temperature in the range from 77 K to 298K. Methyltetrahydrofuran (MeTHF), purchased from Aldrich, is used as a solvent. To obtain a glassy sample, MeTHF is further purified and distilled to be anhydrous prior to each measurement.

1,2 diphenylacetylene (2-ring, DPA) is purchased from Aldrich and used as received. 1,4 bis(phenylethynyl) benzene (3-ring, para) was also purchased from Aldrich, but it is purified by recrystallization from toluene, yielding analytically pure material as determined by elemental analysis performed by Joseph Melinger at Naval Research Laboratories (NRL).<sup>105</sup> 4,4'-bis(phenylethynyl)-tolane is synthesized by Prof. Andrew Beeby's group at the Department of Chemistry, University of Durham. The sample is used as received. 1,3 (bisphenylethynyl) benzene (3-ring, meta) is synthesized in house according to procedures reported elsewhere.<sup>35</sup>

The conjugated polyelectrolyte poly(phenylene ethynylene) sulfonate (PPESO3) and the cationic dye molecule (HMIDC) used in the work presented in Chapter 6 are obtained from the group of Prof. Kirk S. Schanze at the University of Florida. The synthesis of PPESO3 has been described recently.<sup>106,107</sup> The average molecular weight,  $M_n$ , of the polymer is estimated to be 100 kDa, corresponding to about 200 monomer units. HMIDC is purchased from Aldrich and used as received. Solutions with different HMIDC concentrations are prepared and labeled according to their steady state quenching efficiency.

### **Steady State Measurements**

Steady state absorption spectra of the samples is recorded with a UV-VIS Varian-Cary 100 spectrometer. The wavelength range detected is from 190 to 2200 nm with 1 nm spectral resolution. The steady state emission spectra are measured with a Jobin-Yvon instrument (Spex Fluorolog-3) as a function of wavelength. For room temperature spectroscopic measurements, all samples are dissolved in dichloromethane. The optical density (OD) of the samples is approximately 0.2 -0.3  $\text{mm}^{-1}$  at the absorption maximum.

### **Why Time-Resolved Spectroscopy?**

Time-resolved spectroscopy is defined as “any technique that allows to measure the temporal dynamics and the kinetics of photophysical processes”.<sup>108</sup> The development of ultrafast lasers and pulse shaping techniques, among other innovations, have opened up a wide range of investigations of complex systems in chemistry, physics and biology. After interacting with a short light pulse (from milliseconds to femtoseconds), the sample under investigation will change spectroscopic properties such as energy, polarization, or phase. The fate of the ground and excited states of the system can be determined by investigating energy and charge transfer processes, coupling of electronic and vibrational

degrees of freedom, vibrational and conformational relaxation, isomerization, etc. In the case of light harvesting systems, such as the dendrimers studied throughout this dissertation, ultrafast spectroscopy is used to study energy transfer processes. These processes often take place on a (sub)picosecond time scale, which puts strict requirements for the light source to be used in these experiments. This source should provide very short light pulses with appropriate wavelengths within the electronic transitions of the system, and with suitable power and reasonable repetition rate.

Mode-locked Ti-Sapphire laser systems, such as the oscillator called Tsunami, produce less than 40 fs pulses with a very good stability. However, the pulse energies (nJ regime) is not enough for many spectroscopic measurements and the high repetition rate of 80 MHz is too fast for transient absorption techniques. In our lab, the amplification of these pulses are achieved by means of Ti-Sa Regen Amplifier (Spitfire) pumped with a Q-switched Nd:YLF laser (Evolution X). Therefore, it is possible to obtain pulses up to 0.90 mJ with 1kHz repetition rate. The output wavelength of the Regen Amplifier is centered at 790 nm, which is not suitable for many natural and synthetic light-harvesting systems. This problem is solved by employing OPAs combined with second and fourth harmonic and sum frequency techniques, which are tunable within a broad spectral region, from UV to IR (300-5000 nm).<sup>109</sup>

### **The Laser System**

To perform time-resolved experiments with femtosecond time resolution, short and intensive laser pulses with variable photon energies are required. In addition to a commercial laser system, nonlinear elements are used for our applications. Figure 2-1 shows a diagram of the laser system. The function of individual components will be discussed briefly.

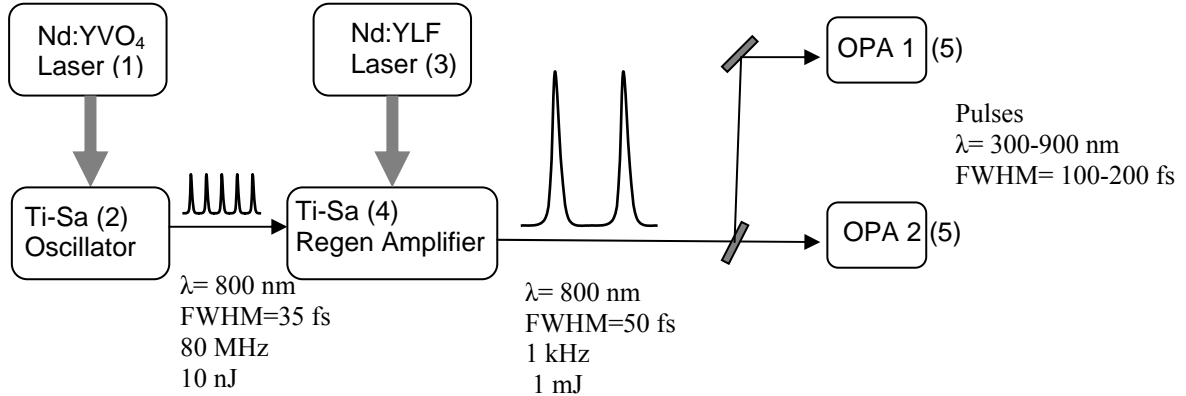


Figure 2-1. The laser system for the production of tunable femtosecond laser pulses with high energy per pulse.

(1) Millenia Vs<sup>®</sup>: The Spectra-Physics Millenia Vs uses the output from a diode laser to pump Nd<sup>+3</sup> ions doped in yttrium vanadate crystalline matrix (Nd:YVO<sub>4</sub>). An LBO crystal converts the 1064 nm light from the laser crystal to the green light, 532 nm, which becomes the output of the laser. Millenia Vs is an all solid-state CW laser, which offers near diffraction limited TEM<sub>00</sub> beam quality and ultra-low noise with an output power range from 2W to 10 W. Millenia's output pumps the mode-locked Ti-Sa Oscillator.

(2) Ti-Sa Oscillator Tsunami<sup>®</sup>: This laser, with a titanium sapphire crystal as the laser medium-called Tsunami<sup>®</sup> from Spectra Physics, provides very short (35 fs), but relatively weak laser pulses with 80 MHz repetition rate. The output spectrum is peaked at 790 nm and has ~45 nm bandwidth (FWHM). This output is the seed of our regenerative amplifier.

(3) Evolution X<sup>®</sup>: Evolution is a diode pumped (by four AlGaAs laser diode arrays), intracavity doubled Nd:YLF laser capable of producing Q-switched pulses with

average powers  $> 6$  W at 527 nm. The laser resonator is acousto-optically Q-switched at repetition rates of 1 kHz. It offers high efficiency, low maintenance, and excellent beam quality. It ideally pumps Ti-Sapphire ultrafast amplifiers, and has been optimized as a pump source for the Spitfire<sup>®</sup> regenerative amplifier system.

(4) Regenerative Amplifier Spitfire<sup>®</sup>: Ti-Sa crystal is the active laser medium, which is optically pumped by an external laser (Evolution<sup>®</sup>) and uses chirp pulse amplification to generate high intensity laser pulses centered at 790 nm. The repetition rate is set to 1 kHz. The seed pulse coming from the oscillator is first stretched temporally using a grating scheme and then inserted into a cavity using a pockels cell. The laser cavity is built in a Z form scheme. After many round trips, this pulse is amplified and released from the cavity using a second pockels cell and a thin film polarizer. The overall amplification is about  $3.3 \times 10^6$  yielding a power of 1.25 W at this point. Finally, the pulses are compressed in a similar grating arrangement to the stretcher and routinely produce pulses of  $\sim 0.85$  mJ centered at 790 nm with pulse widths around 50 fs (FWHM).

(5) Optical Parametric Amplifier (OPA): The optical parametric amplifier system, OPA-800C<sup>®</sup>, offers broad wavelength coverage from UV to mid IR with near transform limited output pulses and high pulse energies. The Spitfire amplifier output is split into two beams (50 %) and used as pumps for two independent OPA systems, providing two highly stable, inherently synchronized outputs with independent wavelength control. By proper selection of signal or idler beam, polarization direction, phase matching angle/type, and number of harmonic crystals, a range from 300 nm up to 5  $\mu$ m can be

covered completely. To obtain this wide range of wavelengths, harmonic generation of the OPA signal or idler is used.

Within the capabilities of the laser system described above, two main time-resolved experimental setups have been developed in our labs to study the excited state dynamics of light-harvesting dendrimers. The first one, Fluorescence Upconversion, is a setup that I designed and built. The second one, Transient Absorption (Pump-Probe), uses a white light super continuum as the probe. Both of these techniques and the crucial components of the setup will be explained in detail.

### **Ultrafast Time-Resolved Emission Spectroscopy**

The energy transfer processes within the conjugated dendrimers are investigated with time-resolved emission spectroscopy. For the initial studies we actually used a time-correlated-single photon counting (TCSPC) instrument, which was available in the Schanze lab (specifically for the molecules studied in Chapter 3 and 4) and the lifetime measurements for the nanostar with TCSPC were already done by Swallen et al.<sup>70</sup> This conventional method is widely used for the determination of lifetimes.

### **Time-Correlated Single Photon Counting**

When an ensemble of fluorophores is excited with a very short optical pulse, this results in an initial occupation of the excited state by  $N_0$  fluorophores. The population of the excited state will decay radiatively and/or nonradiatively to the ground state according to the following equation:

$$\frac{dN(t)}{dt} = -(k_r + k_{nr})N(t) \quad (2-1)$$

where  $k_r$  and  $k_{nr}$  are the radiative and nonradiative decay rates, respectively. The decay of the excited state population is exponential which can be written as:

$$I(t) = I_0 \exp(-t(k_r + k_{nr})) = I_0 \exp(-t / \tau_{flu0}) \quad (2-2)$$

where  $\tau_{flu0}$  is the relaxation time of the excited state. Even though this equation shows only monoexponential decay, for complex systems, the fluorescence decay becomes multi- or nonexponential. The basic principle of TCSPC experiment is that the probability of detecting a single photon at time  $t$  after pulse excitation is proportional to the fluorescence intensity at that time.<sup>110</sup> The time lag between the excitation pulse and the detected single photon is measured and the decay histogram is reconstructed from individual time lag measurements. Upon arriving a detector (e.g. PMT), a multichannel plate, or an avalanche photodiode, each emitted photon creates a reference electrical pulse that is fed to a constant fraction discriminator that triggers a time-to-amplitude converter (TAC). Meanwhile, the excited sample emits and when the detector sees the first photon from the sample, it feeds a stop pulse to the TAC. The TAC consists of a highly linear ramp voltage generator that is started by one signal and stopped by other, and delivers an output voltage whose amplitude is directly proportional to the time difference between the two signals. This TAC signal is then analyzed by an analogue-to-digital converter and one count is stored in a multichannel analyzer (MCA) for each voltage. Excitation and detection events are repeated in this way until the histogram of the number of “counts” against each time window is large enough to give a reliable decay curve of emission. It is important to note that the emitted fluorescence intensity should be low enough that the probability of detecting one photon per excitation cycle is less than unity.

The main advantages of TCSPC method are its high sensitivity and outstanding dynamic range (signal to noise: 10000/1). However, due to the electronics and the

detector, the best time resolution of the instrument is low (about 50 ps). Fairly long lifetimes, up to milliseconds, can be measured. This method was initially used to have a general idea for the emission decay rates of the dendrimers that are mainly in the nanosecond time-regime. The energy transfer process in PE dendrimers occurs in the subpicosecond time scale and therefore requires an experiment with a much better time resolution. This can be achieved with the recently developed Fluorescence Up-conversion technique.

### **Fluorescence Upconversion Technique**

The fluorescence up-conversion technique is used to measure time resolved emission dynamics with a time resolution of tens to hundreds of femtoseconds. This method was first applied by Mahr and Hirsch<sup>111</sup> and it is based on sum frequency generated by the temporal and spatial overlap of the incoherent fluorescence and an ultrafast gate pulse on a nonlinear crystal.<sup>112</sup> (It is also possible to generate a difference frequency, called down-conversion). This sum frequency is detected as a function of the time delay between the gate pulse and excitation pulse which induces fluorescence from the sample. The up-conversion technique allows the mapping of the temporal evolution of the fluorescence.

The up-conversion signal has a photon frequency given by:

$$\omega_{sum} = \omega_{gate} + \omega_{fluo} \quad (2-3)$$

implying,

$$\frac{1}{\lambda_{sum}} = \frac{1}{\lambda_{gate}} + \frac{1}{\lambda_{fluo}} \quad (2-4)$$

As illustrated in Figure 2-2a, when the gate pulse and the emission are overlapped in the nonlinear crystal, frequency mixing occurs creating an up-converted signal. The up-converted frequency is determined both by the angle between the optical axis of the crystal and the incoming beams, and by the optical frequencies of these beams. The nonlinear crystal behaves as an optical gate which is opened when the gate pulse is present in the crystal. Scanning the delay of the gate pulse relative to the excitation pulse opens this optical gate in different portions of time and the fluorescence signal is mapped out at these different time delays (Figure 2-2b).

The intensity of the sum-frequency signal is given by the convolution of the fluorescence intensity and the gate pulse intensity:

$$I_{sum}(\tau) = \int_{-\infty}^{\infty} I_{fluo}(t)I_{gate}(t - \tau)dt, \quad (2-5)$$

where  $\tau$  is the time delay between the gate beam and the fluorescence of the sample. The advantage of using this optical gating technique is that the time resolution is determined by the width of the pulses (pump and gate pulses), not by the time resolution of the detection system.<sup>113</sup>

The time resolution of the upconversion experiment is determined by the instrument response function (IRF), which is proportional to the cross correlation of the excitation pulse with the gate pulse. Operationally, the IRF is measured by angle-tuning the crystal to up-convert transmitted or scattered pump light. For very short pulses <100 fs (FWHM), crystals much thinner than 1 mm are required. The sum frequency is generated throughout the thickness of the crystal as long as the gate pulse and

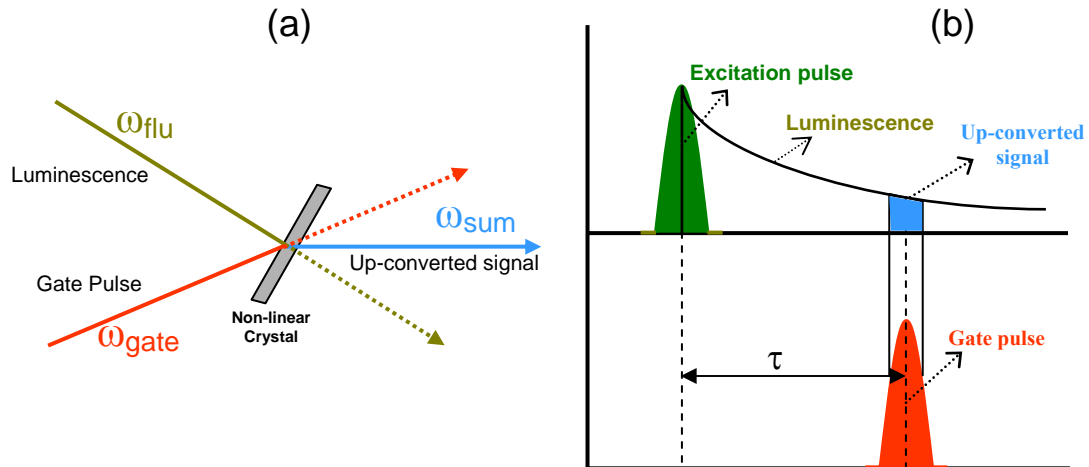


Figure 2-2. Fluorescence Up-Conversion Technique (a) Illustration of the upconversion principle (b) Up-converted fluorescence signal generated in a nonlinear crystal only while the delayed gate pulse is present

fluorescence are temporally and spatially overlapped. However, the group velocity mismatch between the fluorescence and the gate wavelengths can cause broadening of the IRF which needs to be accounted for the determination of the time resolution of the experiment. The bandwidth of the up-converted signal depends on crystal properties and on how tightly the gate pulse and fluorescence are focused on the crystal. The optical layout for our upconversion setup is explained in detail in the next section.

### Homemade Upconversion Apparatus

The experimental setup is shown schematically in Figure 2-3. In this section, we review the components together before they are separately discussed in detail. The Ti:sapphire Regenerative amplifier system provides 50 fs, 840  $\mu$ J pulses at 790 nm with 1 kHz repetition rate. This beam is split into two with 1:1 ratio. Each 420  $\mu$ J beam is independently used to pump an optical parametric amplifier (OPA 800C, Spectra Physics). The first OPA delivers the pump pulses in the UV and visible region through fourth harmonic of signal and idler, respectively. The OPA output is sent through a prism

compressor to get the shortest pulse possible, as required to investigate very fast relaxation dynamics. The polarization is controlled with a  $\lambda/2$  waveplate, and the beam is focused onto a sample with a lens ( $f=200$  mm, fused silica). The residual of the 790 nm pumping the OPA is used as the gate pulse. It passes a delay stage and finally relayed on the nonlinear crystal by a lens ( $f=300$  mm). This gate pulse is not as short as the fundamental pulse since it goes through all the optics in the OPA. The autocorrelation measurements proved that the OPA typically delivers a 120 fs gate pulse at 800 nm and its bandwidth is narrower than the fundamental 790 nm beam.

The sample is held in a 1mm rotating quartz cell (home made, 1 mm windows) to ensure sample photostability. The polarization plane of the excitation light is set to magic angle with respect to that of the gating pulse in order to examine the population dynamics without the influence of rotational diffusion of the solute molecules on the decay of fluorescence.

A pair of off-axis parabolic mirrors (A8037-207 Aluminum Uncoated Mirror, Janos Technology) collects the fluorescence and focuses the fluorescence into a nonlinear crystal. A negative focal length lens is used to magnify the fluorescence image in the nonlinear crystal. A type I phase-matching BBO crystal (0.3 mm) is chosen for the wavelength region studied here. The generated sum frequency light is then collimated and focused into the entrance slit of a 250 mm monochromator (SpectraMini). A UG11 UV cutoff filter placed in front of the monochromator minimizes the 400 nm generated on the crystal by second harmonic generation of the gate pulse. A UV sensitive photomultiplier tube (R7154, Hamamatsu) detects the signal. This electrical signal is gated by a boxcar averager SR 250, Stanford Research Systems. A personal computer is

connected to the detection system and the translational stage to control the experiment. A Labview<sup>®</sup> program was written to control the translation stage and data acquisition card.

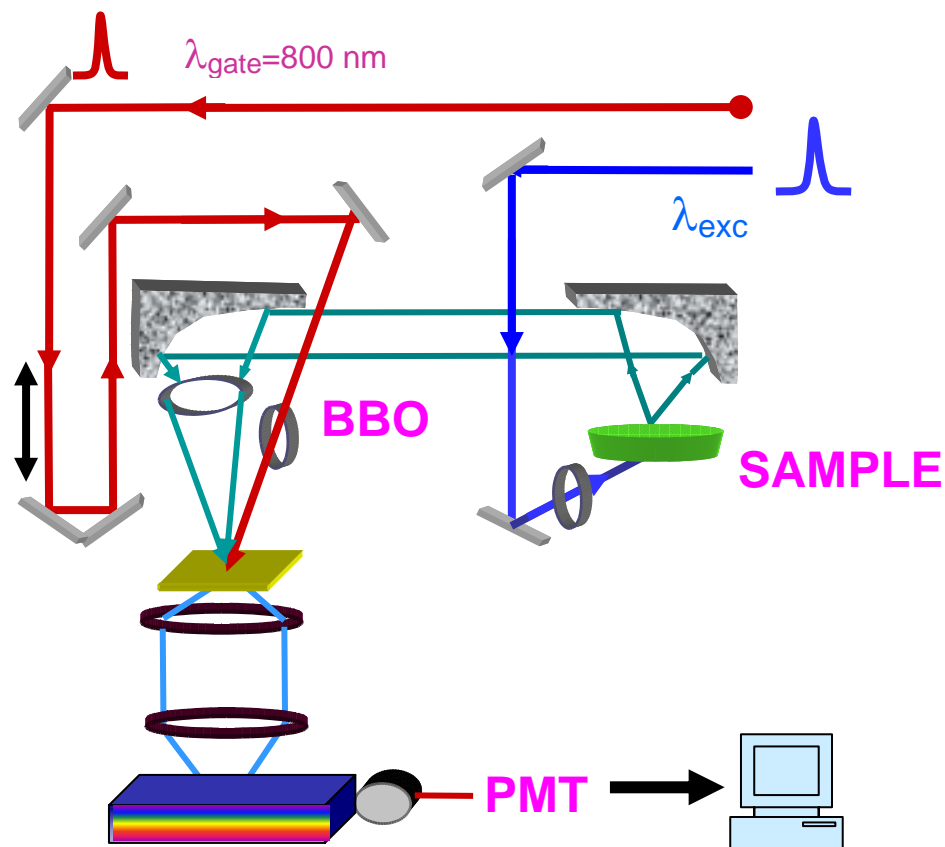


Figure 2-3. Fluorescence upconversion experimental setup.

The upconversion technique is relatively simple in principle, and has been used widely over the past decade. However, it has some crucial components, which happens to be also the most difficult to align. In Appendix A, I will explain the details of the experiment for the new users. These are mainly suggestions from an experienced graduate student who spent a lot of time designing and optimizing the upconversion setup.

### Ultrafast Transient Absorption Spectroscopy

The excited state dynamics of PE dendrimers are also investigated by ultrafast transient absorption (pump-probe) experiments. The principle of the transient absorption experiments is rather simple. At least two ultrashort laser pulses are needed. The intensive one, “pump” pulse, perturbs the sample at  $t=0$ . The probe pulse, which is delayed with respect to pump pulse, crosses the perturbed part of the sample and will probe the action of the pump pulse on the sample. The perturbation created by the pump and monitored by probe pulse can be analyzed in two ways: The modifications of the probe pulse characteristics (intensity, phase, etc.) after passing through the sample can be compared before and after the action of pump pulse. This measurement is then called the transient absorption technique. On the other hand, it is quite possible to observe the new effects created by the probe pulse itself before and after the pump pulse. Raman spectroscopy, Coherent Anti-Stokes Raman Spectroscopy (CARS), and laser-induced fluorescence are such experiments.<sup>108</sup>

Here, the changes in the absorption spectrum of a sample after being perturbed by an ultrashort pulse will be observed and measured. The absorption of the sample may increase or decrease or new absorption bands corresponding to new transitions appearing under perturbation may evolve. By changing the time delay between the pump and probe beams, it would be possible to do temporal analysis of these changes. For example, the simplest photophysical event when a molecule is interacting with a light pulse is the excitation of molecule from its ground electronic state to its first excited electronic state, followed by the return of the molecules to the ground state by fluorescence and/or internal conversion. The return of the molecules to the ground state can be monitored by

the change in transmission of a weak probe pulse through the sample as a function of delay between the pump and probe pulses.

The principle of this method is shown in Figure 2-4. At time  $t=0$ , the pump pulse excites the sample. At time  $t+\Delta t$ , the probe pulse passes through the perturbed volume of the sample ( $\Delta t$  is tunable by means of an optical delay line). The probe pulse intensity is measured. The spectral distribution of the probe is also recorded to improve the sensitivity of the measurement simultaneously in the presence and in the absence of the perturbation of the sample at each laser shot.<sup>108</sup> As shown in Figure 2-4, the probe beam is split into two equal beams; while the first partial beam crosses the pumped part of the sample, the other beam crosses the unperturbed (not pumped) part of the sample.

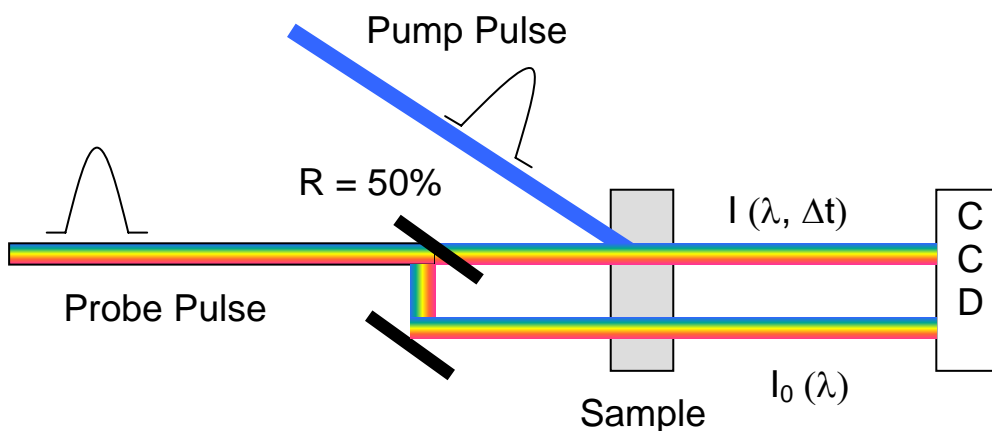


Figure 2-4. Basic principle of transient absorption experiment

These two beams are detected by a CCD. By doing so, shot to shot fluctuations of the laser power are compensated for.

Experimentally, the efficiency of the light absorption at a wavelength by a medium is characterized by the absorption or the transmission defined as:

$$A(\lambda) = \log \frac{I_0(\lambda)}{I(\lambda)} = -\log T(\lambda) \quad (2-6)$$

$$T(\lambda) = \frac{I(\lambda)}{I_0(\lambda)}$$

The detector then measures the probe pulse intensity  $I_0(\lambda)$  (no perturbation by pump) and  $I(\lambda, \Delta t)$  (sample perturbed by pump). Considering the Beer-Lambert law, one can write:

$$I(\lambda, \Delta t) = I_0(\lambda) \times 10^{-\varepsilon_\lambda N(\Delta t)l} \quad (2-7)$$

Where  $\varepsilon_\lambda$  is the absorption coefficient of the sample at wavelength  $\lambda$ ,  $N(\Delta t)$  is the population absorbing at time  $\Delta t$  at wavelength  $\lambda$ , and  $l$  is the length of the sample excited.

In fact, the optical density of the sample is measured:

$$OD(\lambda, \Delta t) = \log \frac{I_0(\lambda)}{I(\lambda, \Delta t)} = \varepsilon_\lambda N(\Delta t)l \quad (2-8)$$

The detected signal measured in the transient absorption experiments is actually the change in absorption (transmission). The detector measures the intensity of the probe beam in the presence and absence of the pump excitation as a function of time.

$$\frac{\Delta T}{T} = \frac{T_{pump} - T_{nopump}}{T_{nopump}} = \frac{\frac{I_{t,pump}}{I_0} - \frac{I_{t,nopump}}{I_0}}{\frac{I_{t,nopump}}{I_0}} = \frac{I_{t,pump}}{I_{t,nopump}} - 1 \quad (2-9)$$

Then, the change in the absorption is defined as:  $\Delta A = -\log\left(\frac{\Delta T}{T} + 1\right)$ . (2-10)

After excitation of the sample with appropriate wavelength, it is possible to follow the population dynamics at a given wavelength (single color probe is enough for such

measurement) by varying time. For a complex system, it is highly desirable to monitor the entire transient spectrum at any time delay after the excitation. Measurement of the full transient spectrum is very helpful in assignment of different absorbing units (species).

For the interpretation of the transient spectra and their relative sign and values, it must be recalled that there are three origins for the pump-probe signal: ground state bleaching, stimulated emission, and excited state absorption. When the sample is pumped within its absorption spectrum, a certain number of molecules will be excited (Figure 2-5). During the probing process if there is population in the excited state, the transmission of the sample increases and ground state bleaching is observed (negative absorption signal). Stimulated emission occurs when the probe beam stimulates the excited state molecules to return to the ground state. The detector will see more photons in the emission range of the sample, so the transmission increases resulting in a negative  $\Delta A$  signal. Note that the probability of the stimulated absorption is the same as of the

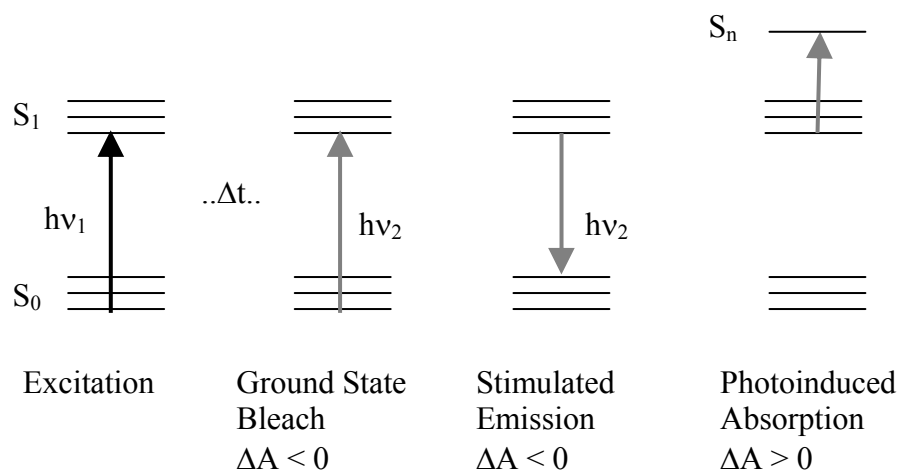


Figure 2-5. The theoretical scheme of certain signals observed as transient absorption signals.

stimulated emission at the emission wavelengths. Excited state absorption (photoinduced absorption) takes place when the excited molecules are excited to even higher electronic states by the probe pulse. This will lead to positive  $\Delta A$  signals. It is highly probable that these three different signals will spectrally overlap complicating the interpretation of the overall signal.

### **Probe Characteristics and White Light Continuum Generation**

The appropriate excitation (pump) wavelength, which depends on the absorption spectrum of the investigated system, can be generated by an OPA. The probe beam can be monochromatic or it can have a broad spectrum. In the simplest case, namely one-color (degenerate) experiments, the pump and probe pulses are split from the same initial beam and one of them is delayed with respect to the other. For two-color experiments another light source is needed to generate the required wavelength of the probe pulse. Prior to choosing the probe pulse wavelength, some preliminary studies, such as steady state spectroscopy, should have been used to characterize the sample. The probe wavelength should be in a spectral domain where it is expected that some species created by the excitation will be present in the sample at a certain time  $\Delta t$ , and will have resonant electronic transitions for that specific probe wavelength. However, it is highly informative to use a probe spectrally as broad as possible. The whole transient absorption spectrum can be measured if a multicolor probe, such as white light continuum, is used. Measuring the whole transient spectrum as a function of time will help determine the dynamics of the excited states of the system.<sup>114-118</sup> For the complex systems studied here, it was preferred to use a white light continuum as the probe pulse. How we generated this continuum will be explained briefly, but first the experimental setup will be explained.

## Experimental Setup

The experimental transient absorption setup for probing with a white light continuum is presented in Figure 2-6. The Ti:sapphire Regenerative amplifier system provides 50 fs, 840  $\mu$ J pulses at 800 nm with 1 kHz repetition rate. This beam is split into two with 1:1 ratio. Both 420  $\mu$ J beams are used to pump an optical parametric amplifier (OPA 800C, Spectra Physics). The second OPA is used to deliver the pump pulses for transient absorption experiment. The OPA is tunable in the UV and visible region (300-900 nm). Since the dendrimer systems under investigation absorb in the UV region (<400 nm), the OPA was aligned to generate UV pulses. A double-pass prism pair is used to compress these pulses. A motorized translation stage (Model No:M-415 D6, Physik Intrumente) is used to vary the time delay between the pump and probe pulse up to 1 ns. A chopper wheel is used to chop the pump beam with 10 Hz frequency in order to compare signal with and without pump.

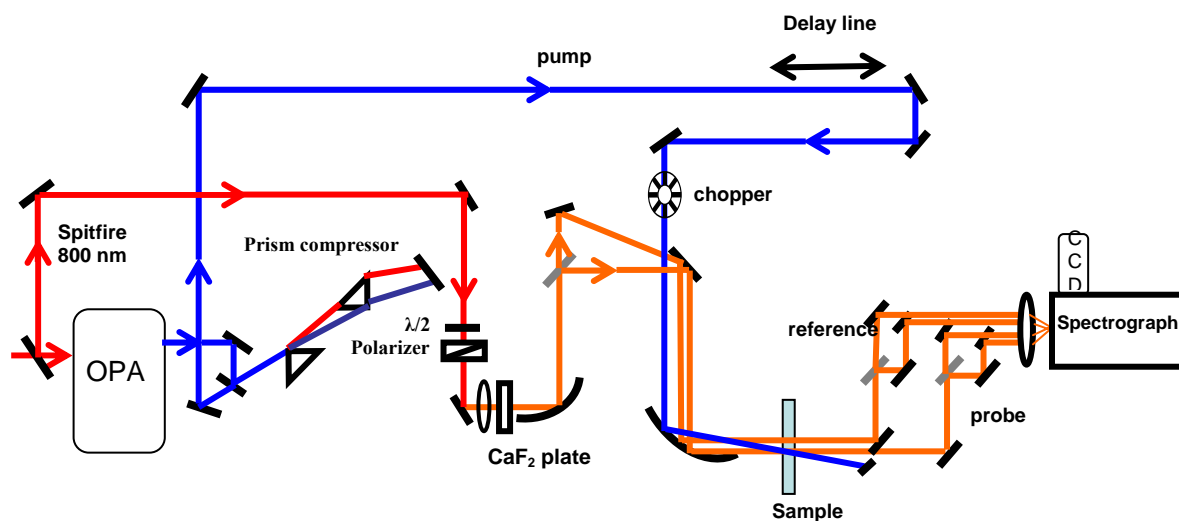


Figure 2-6. Experimental setup for transient absorption experiment probing with white light continuum. UV pump pulses are obtained from the OPA. A chopper wheel used to compare the signal with and without pump. The white light continuum is generated in CaF<sub>2</sub> window.

### **Continuum generation**

When a high peak power short pulse is focused in a (transparent) medium such as glass, water, or sapphire, a continuum of light, which may even appear as white light, is generated. The origin of this process is mainly governed by self-phase-modulation and stimulated Raman emission. The directionality of the white-light pulse makes it possible to use it as a spectrally broad probe and measure the transient absorption at different wavelengths simultaneously.

A small fraction, 3-4  $\mu\text{J}$ , of the fundamental output of the amplified laser pulse is converted to white light by focusing it into a 1mm thick  $\text{CaF}_2$  window (1" diameter, PW-1004-CFUV from CVI-laser). The  $\text{CaF}_2$  is held in a home-made rotating stage to avoid shot to shot intensity fluctuations, temperature effects. A 10 mm lens was used, and the size of the focus was about 200  $\mu\text{m}$ . The spectrum needed as a probe for the measurements on dendrimers lies in the region of 300-600 nm (absorption and emission of the system). Figure 2-7, the top curve, shows the spectrum of the white light continuum directly (without the optics necessary for the experiment) sent to the detector (CCD). As shown in Figure 2-7, the probe and reference beams have very similar spectrum. The quantity of photons (signal on the detector) and the noise evaluated by the ratio of probe/reference with and without the excitation will determine the quality of the probe pulse. Below 365 nm, the intensity of the spectrum decreases rapidly, but for a good signal quality, it is necessary to produce a spectral distribution as flat as possible. The super continuum shown in Figure 2-7 is flattened spectrally by a home made filter. This filter consists of a fused silica cuvette with 1.25 mm thick windows, filled with a mixture of dyes and polymers dissolved in dichloromethane. The total thickness of the

cuvette is 4.5 mm. Our efforts proved that the quality of the supercontinuum, its stability and spectral smoothness, depends critically on the pump pulse energy, pump beam diameter, and focusing parameters of the lens. One has to play with the distance of the lens with respect to CaF<sub>2</sub> plate (distances slightly shorter or larger than focal length) and the pump energy to obtain the optimum, spectrally broad, and smooth supercontinuum. Before using a CaF<sub>2</sub> window, we tried a sapphire plate (which is used in OPAs as a supercontinuum medium). Even though the stability was good enough, spectrally there was no light below 350 nm. Thus, we searched for a medium which will generate enough light to get some signal down to 300 nm. Our investigations suggest that a white light continuum generated in CaF<sub>2</sub> provides significantly more seed photons for shorter wavelengths ( $\lambda < 500$  nm) than the white light continuum generated in sapphire (both pumped at 800 nm). The only disadvantage is the instability of CaF<sub>2</sub> material upon

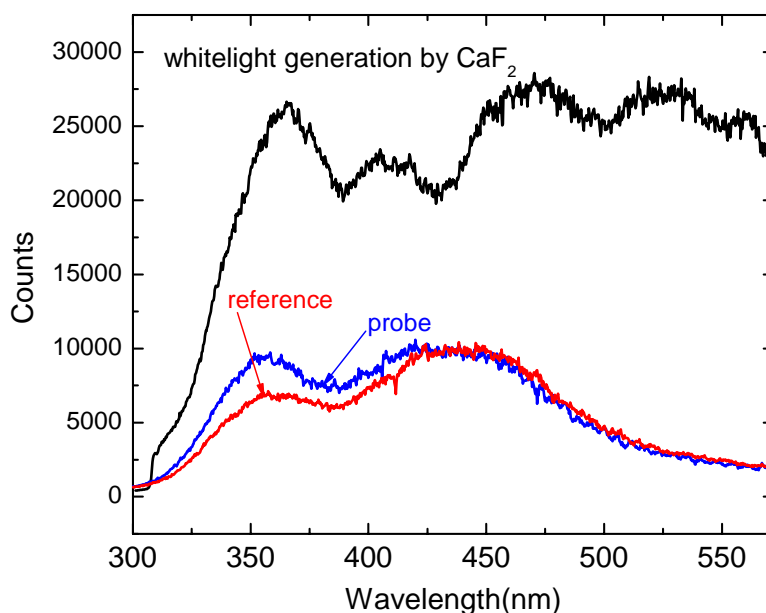


Figure 2-7. Spectrum of the white light continuum generated by CaF<sub>2</sub>. The probe (blue) and reference (red) beams used for transient absorption experiment.

focusing a short pump pulse due to its very low damage threshold.<sup>119</sup> Fortunately, by rotating the CaF<sub>2</sub> window, the problem was solved enabling the use of such white light continuum as probing beam.

The fundamental 800 nm beam used to generate white light continuum is passed through a half wave plate and a thin film polarizer is oriented at 45 degrees with respect to the pump pulse (excitation pulse for the sample) before it reaches to the CaF<sub>2</sub> medium. By doing so, the pump energy for the continuum generation is controlled and optimized. At the same time, the CaF<sub>2</sub> window is positioned at the focus of an off-axis parabolic mirror, which collects and collimates the white light continuum. The continuum is split into two equal beams: probe and reference beam\*. After passing through the sample, the probe and reference beams are split into two equal portions independently (total four continuum beams). These beams go through four Glan-Taylor polarizers aligned perpendicular and parallel with respect to the pump pulse, allowing simultaneous detection of both polarizations. In order to obtain the dynamics free from reorientation effects, the magic angle signal is calculated from parallel and perpendicular signals:

$$\Delta A_{magic} = \frac{\Delta A_{//} + 2\Delta A_{\perp}}{3} \quad (2-11)$$

The temporal evolution of anisotropy can also be obtained by evaluation of:

$$r(t) = \frac{\Delta A_{//}(t) - \Delta A_{\perp}(t)}{\Delta A_{//}(t) + 2\Delta A_{\perp}(t)} \quad (2-12)$$

---

\*Many beam splitters are not good enough for UV light down to 300 nm. Since the continuum has much less photons below 350 nm, it is vital to use the best optics for UV. I used reflective neutral density filters with OD 0.5 ( 33.3% absorption, 33.3. % transmission, 33.3 % reflection) to split probe and reference beams.

where  $\Delta A_{//}(t)$  and  $\Delta A_{\perp}(t)$  correspond to the transient absorption of the polarization oriented parallel or perpendicular to the excitation beam polarization, respectively.

The four tracks of white light are dispersed with an imaging grating monochromator (focal length 30.3 cm, 300 lines/mm). The iStar intensified CCD camera (iStar 720DH-720-25F-03, Andor Technology) is employed as the detection system. Note that, not all the probe wavelengths propagate through the optical components at the same speed (including the transparent medium used for continuum generation). Since the velocity,  $v(\lambda) = \frac{c}{n(\lambda)}$ , at which a given frequency will travel depends on the refraction index of that material at that wavelength. When using the white light continuum, it is important to account for the influence of group velocity dispersion either experimentally or numerically. If the dispersion for the continuum is well characterized, the spectra can be corrected numerically by using a home-written Labview program.

With the setup explained previously, data can be acquired in the following two ways: either time resolved measurements ( $\Delta A$  versus  $\Delta t$  plots) at a fixed probe wavelength or spectrally resolved measurements corresponding to a fixed delay between pump and probe ( $\Delta A$  versus wavelength region of the probe).

During our measurements, the signal appears earlier at shorter wavelengths than at a longer wavelength, which is a consequence of the temporal distribution of the different spectral components of the supercontinuum probe pulse, called “chirp”. The chirp of the white light continuum is determined from the delay between the signals probed at 330 nm and 560 nm, for the measurements on the dendrimers. As shown in Figure 2-8a, the chirp leads to a delay of  $\sim 520$  fs between the spectral components at 350 and 575 nm. This chirp is corrected for the time-resolved measurements analyzed in the following

chapters. Figure 2-8b also shows the signal for the DCM probed at different wavelengths. The delay here is around 570 fs. The FWHM of the Raman-like (or coherent artifacts) signal generated in such solvents (when pumped with couple of micro joules) also gives information about the time resolution of the experimental setup.

The chirp correction is done after the experimental measurements. Each data set is analyzed to get an initial estimation of the chirp and then using a labview program based on calculating dispersion of light in every refracting medium, the chirp corrected data sets are produced. This numerical correction employs the Sellmeier equation, which is an empirical relationship between the refractive index  $n$  and wavelength  $\lambda$  for a particular

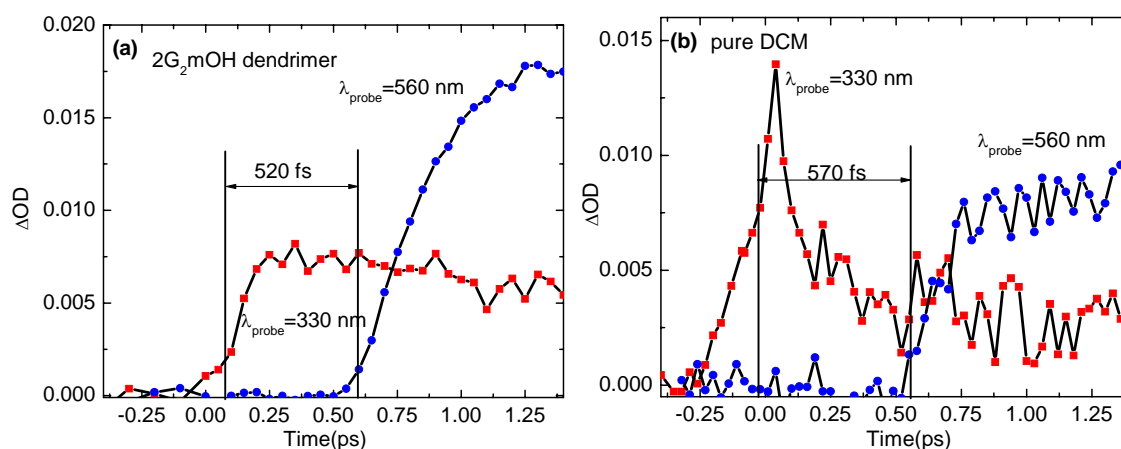


Figure 2-8. The chirp of the white light continuum determined from the delay between the signals (a) probed at 330 (squares) and 560 nm (circles) for the measurements of 2G<sub>2</sub>mOH dendrimer (b) pure dichloromethane.

transparent medium. The common form of the equation for glasses is:

$$n^2(\lambda) = 1 + \frac{B_1\lambda^2}{\lambda^2 - C_1} + \frac{B_2\lambda^2}{\lambda^2 - C_2} + \frac{B_3\lambda^2}{\lambda^2 - C_3} \quad (2-13)$$

where  $B_{1,2,3}$  and  $C_{1,2,3}$  are experimentally determined Sellmeier coefficients. Different forms of the equation are used for certain type of materials, such as crystals and common

organic solvents.<sup>120,121</sup> Chirp correction is necessary and should be done very carefully since most of the dynamics in PE dendrimers takes place in a subpicosecond time scale.

### **Time resolution of the experiment**

In general, to determine the time resolution of an experiment where two laser pulses are used, difference or sum frequency mixing between those pulses (pump and probe) is performed at the place of the sample using a very thin (50-300  $\mu\text{m}$  thick) type I BBO crystal. On the other hand, in the experiments where the white light continuum is used as the probe, the time resolution can be determined from the coherent artifact (Raman Scatter) observed in some solvents. Many basic molecular liquids and optical solids are transparent in the visible and near-UV spectral range for low intensity radiation ( $< 10^{10}$   $\text{W}/\text{m}^2$ ). However, when high power ultrashort laser pulses are applied, these media can absorb efficiently through a multiphoton absorption mechanism (two photon absorption) and Stimulated Raman Amplification (SRA).<sup>122</sup> Furthermore, a spectrally broad probe pulse, similar to white light continuum, favors efficient cross-phase modulation. Each of the signals is produced by the simultaneous action of two photons, one from the pump and the other from the probe. These artifact signals will terminate rapidly following excitation, thus their duration is directly related to the temporal width of the pump-probe cross-correlation function. This is verified by comparing duration of the coherent artifact at a specific probe wavelength with the cross-correlation measured using a single color probe mixed with the pump pulse in the BBO crystal. Simultaneous absorption of a pump photon and a probe photon gives rise to two-photon absorption, while the interchange of photons between pump and probe through a material's vibrational energy level gives rise to SRA. Moreover, the cross-phase modulation leads to

spectral modifications within the probe upon pump-induced temporal changes of the refractive index.<sup>122,123</sup>

These coherent effects are observed in many common solvents, such as, acetonitrile, methanol, water, ethanol, cyclohexane, and dichloromethane with different strength. Figure 2-9 presents typical coherent artifact signals in hexane, commonly used to measure the instrument response function. They are shown at two different wavelengths of the probe and it is obvious that the coherent artifact is getting smaller with increasing probe wavelength. The temporal width is also dependent on the probe wavelength, due to group velocity mismatch. As the probe wavelength is more distant from the pump wavelength, cross-correlation signals gets temporally broader. Such behaviors are in agreement with literature results.<sup>122</sup>

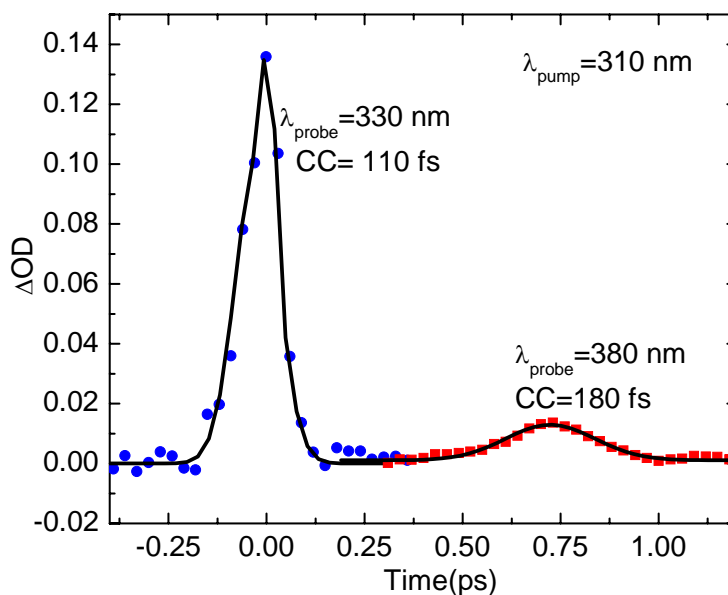


Figure 2-9. Coherent artifact of hexane solvent excited at 310 nm, probed at 330 and 380 nm.

Observing such coherent artifacts from the solvents will provoke the question, “do we have solvent contribution to the signal?” It is essential to check the solvent response at the same pump energy where the experiments are performed. In our experiments, these

measurements confirmed that there is no coherent artifact from the solvent at the pump power intensities used for excitation of the real dendrimer samples. Otherwise, the signal should be corrected for solvent contributions.

### **Concentration and Pump Pulse Energy Dependence**

For both fluorescence upconversion and transient absorption experiments, the optical density of samples is approximately  $0.2\text{-}0.3\text{ mm}^{-1}$ , yielding a concentration range of  $10^{-5}\text{-}10^{-6}$  M. All spectroscopic measurements of dendrimers at room temperature are carried out in dichloromethane (DCM). Low temperature experiments were performed in glass forming methyl-tetrahydrofuran (Me-THF). It has been shown that phenylethynylene dendrimers do not aggregate in dichloromethane despite some aggregation in solvents like isopentane (lower dielectric constant). The solvent should be anhydrous so that the dendrimer molecules can stay stable in solution for a longer period of time. The polymer experiments are performed in methanol and the samples were prepared at a concentration where steady state measurements did not show any aggregation.

Same measurements may differ from one another due to different conditions of the day that the experiment is carried out. The excitation energy, beam diameter and even the concentration of the sample might be different on a particular day. For a reliable comparison, it is important to know if and how the pump energy influences the signal. The main criterion is to check the linear region of the pump energy. As long as the molecule is excited with power in the linear regime, the shape of the signal will not change. The optimum pump energy can be determined by varying the pump pulse energy until the shape of the signal changes. For each measurement, one should calculate the number of photons absorbed per molecule. The most common problem with high energy

pulses is annihilation, which may occur when more than one photon is absorbed by a molecule. In such a case, one excited state can act as a quencher for other excitations, resulting in additional decay components in the process. Thus, to detect the dynamics associated with the studied process, the excitation intensity must be adjusted in a way that the average number of photons absorbed per molecule should be less than unity. Another scenario is the local heating of the sample leading to sample defects due to high excitation densities which can increase the proportion of the radiationless processes. The power densities for each measurement are given in the following chapters.

The photostability of the samples is another important issue. The dendrimers are not as stable as the polymer samples. Depending on the pump power, they would photobleach much faster. Rotating sample cells are used for time-resolved experiments to use the minimum sample for the maximum scan time. Absorption spectra of the investigated molecules were checked before and after each laser measurement which proves the photo stability of all compounds under the experimental conditions used in this work. All time-resolved experiments presented in this work are performed at room-temperature.

### CHAPTER 3

#### ENERGY TRANSFER IN GENERATION 1 UNSYMMETRICAL PHENYLENE ETHYNYLENE DENDRIMERS

The search for artificial light-harvesters has led to intense studies of conjugated dendritic macromolecules.<sup>36,81,124</sup> Dendrimers have potential applications in photonic devices due to their highly branched architectures and unique physical properties. With recent advances in synthetic methods,<sup>2,4,125</sup> the size, topology, flexibility, and surface chemistry of dendrimers can be controlled at the molecular level with high precision. Accurate positioning of chromophores at the core, periphery, focal point, or even at each branching point of the dendrimer can now be achieved.<sup>52,59,126</sup> For photonic applications, the dendritic architecture creates large transition dipoles due to the high number of chromophore units.

Some judiciously designed phenylene ethynylene (PE) based dendrimers show highly efficient and unidirectional energy-transfer properties.<sup>69,72</sup> Their topology suggests applications as scaffolds for light-harvesting devices. In addition, the large number of chromophore units lead to the formation of excitonic bands. These dendrimers' photophysical properties cannot be understood as simply additive properties associated with molecular orbitals on single chromophore units. In this scenario, it is essential to understand the electronic coupling,<sup>84</sup> exciton formation,<sup>72,127</sup> and energy transfer in detail.

A variety of dendritic architectures have now been synthesized, leading to unique photophysical properties. PE units coupled exclusively through *meta* or *para* substitution

on a phenyl ring lead to either compact or extended dendrimers.<sup>72</sup> These two families of dendrimers differ in the number of PE units between consecutive branching points. Compact dendrimers have a fixed-length linear unit, while extended dendrimers have a variable number of linear PE units depending on the number of branching points between the unit and the core. Both families of dendrimers have been investigated theoretically<sup>19,78,127,128</sup> and experimentally.<sup>69,75,129</sup>

In compact dendrimers, steady state experiments performed by Moore and co-workers show that the optical excitation is localized on the PE units.<sup>72</sup> The excitonic localization on individual PE units is evident by the monotonic increase in absorption intensity and the lack of spectral shift with generation number.<sup>81</sup> The extended series exhibit exciton localization on PE units of increasing length (2-,3-, 4- ring), which creates an energy funnel yielding multistep energy transfer.

Mukamel and co-workers have studied compact and extended dendrimers using a Frenkel Exciton Hamiltonian.<sup>127</sup> Applying the collective electronic oscillator model, they concluded that the electron-hole pair was confined to the linear segments between branching points. The bound Frenkel excitons are free to migrate throughout the molecule. Depending on the strength of the coupling, the migration leads to coherent or incoherent energy transfer. Absorption spectra calculated from this model are in excellent agreement with experiment.

Using time correlated single photon counting, Swallen et al<sup>130</sup> studied an extended PE dendrimer and found an instrument-limited value of about 10 ps for the energy transfer from the lowest energy chromophore in the backbone to a phenylene ethynylene perylene trap. Subsequent experiments by Kleiman et al investigated the same extended

dendrimer using femtosecond degenerate pump-probe spectroscopy and revealed a stepwise energy transfer from the shorter PE units to the longer PE chains.<sup>75</sup> These experiments indicated that some of the steps in the energy transfer occur on a subpicosecond time scale.

The novel characteristics of PE dendrimers arise from the electronic properties at the branching points. In both compact and extended dendrimers, *meta* substitutions on the phenyl rings result in broken  $\pi$ -electron conjugation in the ground electronic state. The situation in the excited state is less clear. A recent study based on a di-ethynylene phenyl unit with H or phenyl substituents shows dramatic changes in both the emission spectra and the radiative lifetimes.<sup>90</sup> The electronic structure calculations indicate that the phenyl ethynylene (H or phenyl substituted) units are strongly coupled in a relaxed geometry on the excited state.<sup>84</sup> Experiments in larger dendrimers do not show the shifts predicted in the smaller systems (see ref<sup>81</sup>, Figure 4). The extent of localization in the excited state for sizable dendrimers remains an open question.

Unsymmetrical architectures in which coupling among the PE unit occurs through *para* and *ortho* substitutions have been synthesized by Peng and co-workers<sup>96,97,131</sup> (Figure 3-1). In these dendrimers, the substitutions create combinations of PE units of variable lengths, analogous to those encountered in extended dendrimers.<sup>97</sup> Unsymmetrical branching leads to rapidly growing conjugation lengths as the generation number increases, providing a broad absorption spectral range with large molar absorptivities and high fluorescent quantum yields.<sup>95</sup> Linear conjugated segments connecting the periphery to the core suggest faster and more efficient energy transfer to the core.<sup>95</sup> Furthermore, the presence of *ortho* substitutions may allow stronger coupling

of PE units, leading to more delocalized excitation throughout the entire molecule. For these architectures, confined Frenkel excitons<sup>127</sup> might extend over regions of the molecule that includes substitutions at *ortho* positions.

Symmetric dendrimers' absorption spectra can be interpreted as the addition of building blocks, defined by the confined excitons.<sup>127</sup> The role of *ortho* substitution and exciton confinement in unsymmetric dendrimers is not as well characterized and there are still unanswered questions: Are the absorption band structures associated with exciton localization and "building blocks"? Does coherent or incoherent energy transfer occur between those localized states?

The goal of our study is to understand the exciton size and the rates of energy migration. We focus here on the characterization of intramolecular interactions and the energy-transfer mechanisms in unsymmetrical PE dendritic molecules. To investigate the extent of delocalization within the dendritic structure, we consider unsymmetrical monodendrons with multiple *ortho* and *para* substitutions. Energy transfer mechanisms are monitored by adding an ethynylene perylene trap (EPer), which acts as reporter for energy transfer.

Time-resolved photoluminescence experiments in the subpicosecond time scale are employed to follow the energy initially deposited in the dendrimer's backbone by an ultrafast pulse. A kinetic model is proposed to interpret the rise times of the fluorescence measured in unsymmetrical dendritic structures with and without an energy trap. Finally, we present an analysis of the validity of Förster model by comparing the model predictions with our experimental results.

## Materials and Methods

The synthesis of unsymmetrical dendrons is described elsewhere.<sup>96</sup> Unsymmetrical monodendrons can be covalently bonded to form larger and more symmetrical macromolecules named as di- or tri-dendrons. Here, two G<sub>1</sub> (generation 1) monodendrons are coupled to a phenyl ring in the meta positions. When the phenyl ring has an additional OH or ethynylene perylene group in the other meta position, the molecule is named 2G<sub>1</sub>-m-OH or 2G<sub>1</sub>-m-Per, respectively (Figure 3-1). The ethynylene perylene unit acts as an energy trap and is utilized to probe energy transfer dynamics. As any PE dendrimers, the molecules under investigation are quite rigid molecules that do not allow for the backfolding of any of the branches.

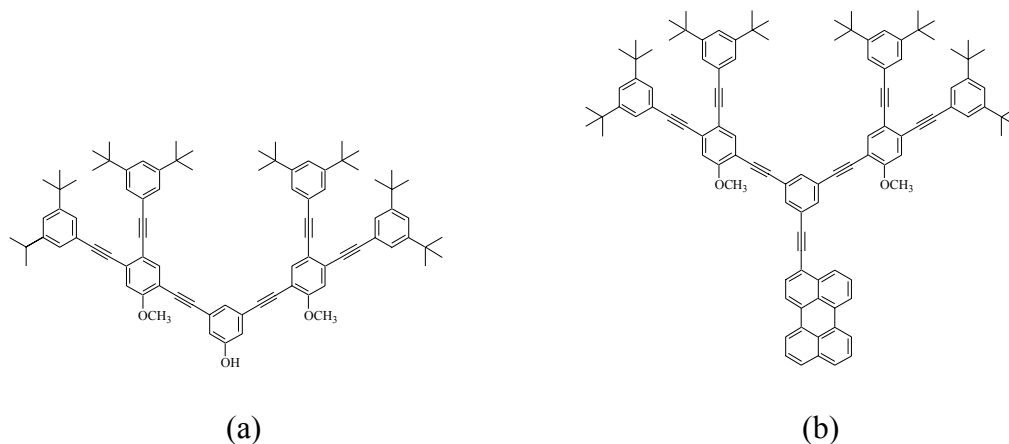


Figure 3-1. Chemical structures of generation 1 phenylene ethynylene dendrimers: (a) 2G<sub>1</sub>-m-OH (b) 2G<sub>1</sub>-m-Per.

For spectroscopic measurements, all samples are prepared in dry CH<sub>2</sub>Cl<sub>2</sub> without further purification. Absorption spectra are recorded on a Varian Cary 100 spectrophotometer. The fluorescence spectra are measured with a Jobin-Yvon instrument (Spex-Fluorolog-3). The optical density of samples used in all measurements is about 0.3 mm<sup>-1</sup>, which provides a concentration less than 10<sup>-6</sup> M to avoid any aggregation and excimer formation. All steady state measurements and transient absorption experiments

are performed in a 2 mm optical path length quartz cuvettes. In addition, a homemade rotating cell with optical path of 1 mm (for optimum time-resolution) is used for time-resolved emission experiments. The laser system, fluorescence upconversion, and transient absorption setup are described in detail in Chapter 2.

The upconversion experiment measures the temporal evolution of the fluorescence with subpicosecond resolution. It is based on the sum-frequency mixing of the molecules' emission with an ultrafast gate pulse in a nonlinear crystal. Briefly, excitation pulses are derived from an optical parametric amplifier (OPA), pumped by a commercial Ti-Sapphire laser system consisting of a Ti-Sa oscillator (Tsunami, Spectra-Physics) and subsequent amplifier (Spitfire, Spectra-Physics) with a repetition rate of 1 kHz. The fourth harmonic of the OPA output signal or idler is used to generate tunable excitation pulses in the 315 nm to 370 nm spectral region. Pump pulses of ~40 nJ with a beam diameter of 200  $\mu\text{m}$  are used to maintain a linear optical response. After all the optics in the OPA and harmonic generation processes, the UV and visible pulses accumulate group velocity dispersion, yielding longer excitation pulses and poor experimental time-resolution. To overcome this pulse lengthening we use a pair of quartz prisms to compensate the chirp.

The homemade rotating cell has a 1 inch diameter and an optical path length of 1 mm to guarantee excitation of a new sample volume with every laser shot with minimum consumption of sample. The photoluminescence is collected by two off-axis parabolic mirrors and the excitation volume is imaged onto a 300  $\mu\text{m}$   $\beta$ -BBO crystal. Usually a small portion of the regenerative amplifier beam (~30  $\mu\text{J}$ /pulse, FWHM = 60 fs) is weakly focused (50 cm focal length) and the beam diameter at the crystal is kept larger

than the imaged fluorescence. However, some modifications are necessary for experimentally challenging fluorescence wavelengths. While collecting fluorescence of 400 nm, a lot of background signal is introduced because of the sum frequency generation of 800 nm (gate beam) and its spontaneous second harmonic generation (400 nm) at the BBO crystal. With such level of background signal, it is impossible to distinguish the upconverted signal originated from the molecules studied here. Therefore, the gate beam has to be different from 800 nm. We modified the experimental setup to overcome this experimental limitation. The second harmonic of the OPA signal (630 nm and 740 nm) is used as the gate beam. However, it is still difficult to get good signal/noise with these gate beams since the intensity of SHG of the OPA signal is an order of magnitude smaller than the intensity of the 800 nm beam. The samples were excited at 315 and 370 nm using the fourth harmonic of the signal generated in the OPA. Spatially and temporally overlapped gate and collected fluorescence in the  $\beta$ -BBO crystal generates a nonlinear response signal in the UV. Colored filters (UG11) are used to remove scattered light from the excitation pulse and the second harmonic of the gate, which is also generated at the crystal. The upconverted beam is dispersed by a 0.25 m monochromator and detected with a PMT. Boxcar integration and averaging of  $10^4$  pulses per time step leads to a signal to noise ratio of about 50:1.

The time resolution of the setup was measured by detection of cross-correlation of scattered light from solvent and gate pulse. For UV excitation, the time resolution was determined to be about 225 fs.

In the transient absorption experiments as sketched in Chapter 2, a fraction of the Ti:Sa amplifier output is focused on a 1 mm CaF<sub>2</sub> plate to generate a white-light

continuum, which is used as probe and reference beams. Using a thin-film polarizer, the probe light polarization is oriented at 45 degrees with respect to the pump pulse. After passing through the sample, a Glan-Taylor polarizer splits the probe beam into its polarization components, parallel and perpendicular with respect to the pump, allowing for the simultaneous detection of both polarizations. Pump induced absorption changes of both probe polarization components are measured as a function of pump-probe time delay by modulation of the pump beam with a mechanical chopper and detection of the probe beams and a reference beam with the pump on and the pump off (to overcome shot-to-shot fluctuations) using a CCD camera equipped with a 30 cm spectrograph. For all transient absorption measurements performed here, the excitation wavelength is 315 nm. By measuring the coherent artifacts from the pure solvent (i.e. Stimulated Raman Amplification, discussed in Chapter 2), the time resolution of this setup was determined to be about 150 fs.

Data analysis involves the convolution of decay and rise time functions with the corresponding experimental IRF for each experiment. The integrity of the sample was checked before and after each set of measurements.

### **Steady State Spectroscopy**

The steady state absorption spectra of 2G<sub>1</sub>-m-OH and related monodendrons are shown in Figure 3-2. Any 2G<sub>n</sub>- didendron is composed of two G<sub>n</sub> monodendrons coupled through the meta positions of a phenyl ring. The branching center determines the strength of interactions among chromophores, which plays a key role in determining the mechanism of energy transfer. In Figure 3-2, the absorption spectrum of 2G<sub>1</sub>-m-OH, G<sub>1</sub>OH, and G<sub>2</sub>OH are compared.

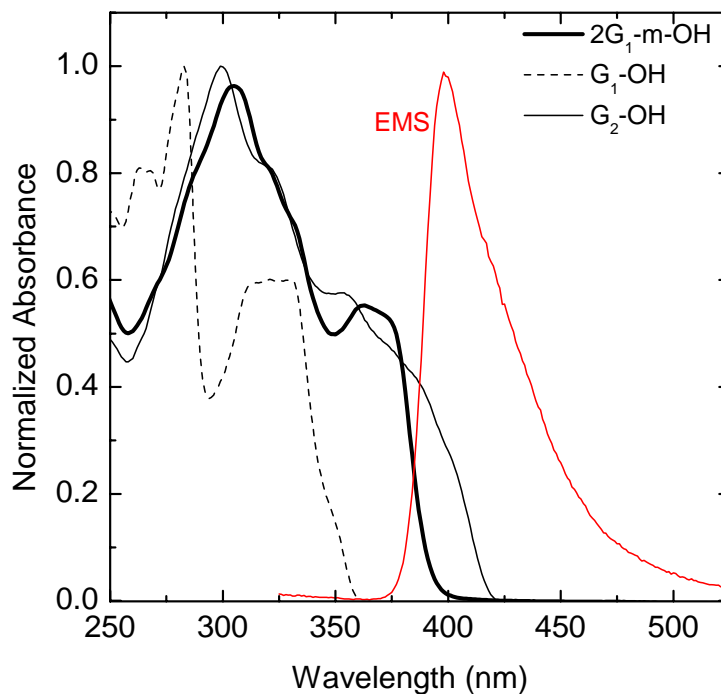


Figure 3-2. Normalized absorption spectra of —  $2G_1$ -m-OH, ---  $G_1$ -OH, and —  $G_2$ -OH in dichloromethane. Normalized emission spectrum of —  $2G_1$ -m-OH.

The absorption spectrum of  $2G_1$ -m-OH shows a 35 nm red shift compared to single  $G_1$ OH dendron.<sup>131</sup> This is due to one additional PE unit, which increases the total conjugation for the system. The absorption spectrum of  $G_2$ OH (Figure 1-6) shows more similar features, but there is a 20 nm redshift. The longest linear PE chain in  $G_2$ OH has the same number of PE units as the longest linear chain in the  $2G_1$ -m-OH. This red shift is due to more extended conjugation between the two longest linear PE units through the ortho linkage in  $G_2$ OH. Also note that the red shift here is much more pronounced compared to  $2G_2$ -m-OH versus  $G_3$ OH dendrimers (Figure 4-2).

The trap molecule, Eper, is substituted to the dendron molecule in the meta position with respect to both monodendron components. The absorption spectrum of  $2G_1$ -m-Per is a superposition of absorption spectra of  $2G_1$ -m-OH and EPer (Figure 3-3). The broad absorption feature between 300 and 400 nm corresponds to the dendritic backbone

while absorption at  $\lambda > 400$  nm is only associated with the Eper trap. Since the presence of both donor and acceptor groups within the same molecule does not lead to appearance of a new band or to differences in the ground state absorption spectrum, it can be concluded that there are no strong interactions between donor and acceptor moieties in the ground state.

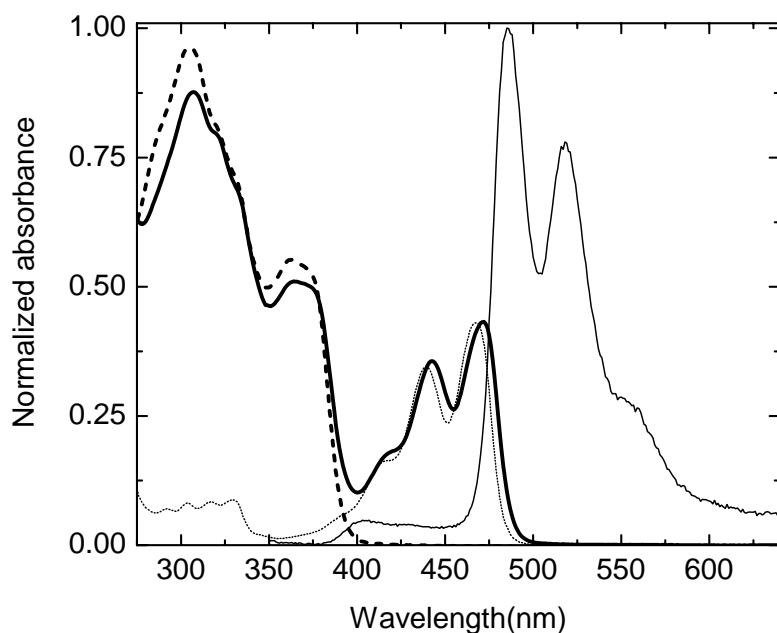


Figure 3-3. Normalized absorption spectra of ----2G1-m-OH, ...EPer, and —2G1-m-Per and fluorescence spectrum of —2G1-m-Per, excited at 315 nm.

The fluorescence of PE dendrimers attached to Eper trap is completely quenched compared to the ones without trap. In fact, after excitation at  $\lambda = 315$  nm, the emission arises entirely from the EPer unit. This is again a strong indication that within these dendrimers, the excitation energy is efficiently transferred from the dendrimer backbone to the EPer chromophore. Comparison of absorption and excitation spectra indicates ~96% efficiency for the energy transfer process.<sup>92</sup> Interestingly, at 400 nm, a small band with intensity contributions from unfunctionalized 2G<sub>1</sub>-m-OH and possibly residual

backbone emission from 2G<sub>1</sub>-m-Per is noticed in the emission spectrum. Time-resolved data will clarify its origin.

### **Time-Resolved Emission Experiments**

The fluorescence decays are measured by TCSPC and 2G<sub>1</sub>-m-OH decays with a 1.8 ns time scale, whereas 2G<sub>1</sub>-m-Per decays with the emission lifetime of EPer (2.2 ns).

Time resolved fluorescence upconversion technique is applied to measure the rise times associated with these decays. First, the dendrimer without EPer trap is studied to understand the extent of intramolecular interactions within the dendron backbone. The absorption spectrum of 2G<sub>1</sub>-m-OH has two distinguishable bands peaked at 305 and 365 nm. Since one of the goals of this study is to explore the possibility of assigning the absorption band structure to exciton localization, it is reasonable to excite 2G<sub>1</sub>-m-OH at selective wavelengths with significant contributions from each band. Therefore, the excitation wavelengths are chosen to be 315 and 370 nm. The emission is detected at backbone fluorescence of 400 nm. Note that the instrument response functions of 180-220 fs were used in the analysis of all measurements for deconvolution of data sets (IRF was routinely recorded during each measurement session).

Figure 3-4 shows no detectable excitation wavelength dependence for the subpicosecond risetime. Convolution of the IRF with the exponential rise function yields a 300 fs time constant for both excitation wavelengths, which suggests the delocalization of the initially excited state throughout the monodendrons. This risetime is definitely longer than the experimental time-resolution, meaning that it essentially takes 300 fs for the initially deposited energy to reach the lowest lying emitting state. It is thus suggested that absorbing and emitting states of the dendrimer are two different excited states.<sup>132</sup> A second component with a decay time constant of 6 ps is found in addition to the long

decay time of 2G<sub>1</sub>-m-OH (1.8 ns). This kinetic component can be attributed to vibrational relaxation in the excited state of the monodendrons, which is coupled to relaxation and reorganization of the solvation shell around the monodendrons.<sup>133</sup> The solvent molecules have to accommodate for the newly populated S<sub>1</sub> state of the whole molecule. The fluorescence is detected at the blue end of the emission at 400 nm (Figure 3-2). At fluorescence detection wavelengths close to the excitation, the vibrational relaxation will be observed as a fast decay component, whereas at longer wavelengths this decay would be seen as a risetime, since the fluorescence is detected from a state that has to be populated with this time constant. Moreover, the relative amplitude associated with 6 ps component will depend on the excitation wavelength. The excitation wavelength dependence of the 6 ps component will be explored with the kinetic analysis. If it is attributed to vibrational relaxation, its amplitude will decrease at longer excitation wavelengths.

The objective of investigating the 2G<sub>1</sub>-m-OH molecule was to understand the excitation energy transfer dynamics among the similar dendrons before the energy is transferred to a core trap. We investigate also the same dendritic structure with an EPer trap attached in meta position to the core phenyl unit. The risetime of the Eper emission is experimentally measured to follow the excitation energy migration from the initially excited state on the dendron to the final trap. Figure 3-5 shows the temporal evolution of the 2G<sub>1</sub>-m-Per fluorescence as a function of excitation wavelengths. Fluorescence is detected at the maximum emission wavelength of Eper (480 nm). Direct excitation of EPer provides the time resolution limit for fluorescence risetimes. Any risetime longer than 150 fs can be assigned to excited state dynamics.

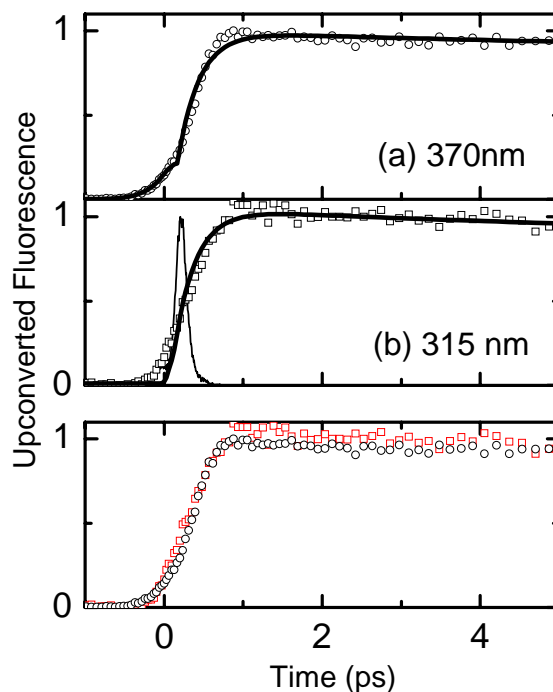


Figure 3-4.  $2G_1$ -m-OH in dichloromethane excited at a) 370 nm b) 315 nm. Upconversion signal of fluorescence is detected at 400 nm, the maximum emission wavelength of the molecule. Fitting procedures include the convolution of exponential functions from the kinetic model with the IRF. The best fit is shown as the solid line. The longest IRF function is shown in panel b. The bottom panel shows the superposition of the experimental data in panels a and b.

In addition, any different dynamics compared to what is measured in Figure 3-4 can be attributed to energy transfer to the EPer trap. Figure 3-5a and 3-5b shows the upconverted emission following excitation at 370 and 320 nm, respectively. At these excitation wavelengths, there is no residual absorption from the EPer unit. Indeed, the only mechanism responsible for EPer emission is sensitized excitation via energy transfer from the backbone. The risetimes for emission show an excitation wavelength dependence. As the excitation wavelength gets shorter (higher energy), the fluorescence risetimes become longer. Excitations at 315 nm (b) and 370 nm (a) clearly show longer risetimes (compared to both IRF and risetimes from  $2G_1$ -m-OH emission) for the

fluorescence arising from the EPer excited state, whereas the dendritic backbone ( $2G_1$ -m-OH) does not display such long risetime with excitation wavelength dependence.

As shown in the steady state spectrum, most of the  $2G_1$ -m-Per emission is from the EPer trap. However, a small band around is observed 400 nm, the same wavelength region as the emission from  $2G_1$ -m-OH. This band has contribution from unfunctionalized dendrimer ( $2G_1$ -m-OH) and residual emission from the dendritic backbone even in the presence of the trap. To confirm this assignment, the time-resolved fluorescence detected at  $\lambda=400$  nm from the  $2G_1$ -m-Per molecule has to be examined and the temporal behavior will give direct information about the energy transfer rate. As seen in Figure 3-6, a very fast risetime is followed by a fast decay, which is attributed to energy transfer from the backbone to the EPer trap. The signal does not decay to zero with the same fast time constant. The long time component corresponds to unfunctionalized  $2G_1$ -m-OH. Using the kinetic model described in the next section, the signal is simulated using the same time constants obtained from Figures 3-4 and 3-5 along with the nanosecond component corresponding to  $2G_1$ -m-OH emission lifetime. The relative contribution to the steady state emission spectrum from the  $2G_1$ -m-OH (as impurity) and the residual backbone emission can be obtained by integrating the time-resolved data. Even though the extent of unfunctionalized  $2G_1$ -m-OH of the sample is checked by Thin Layer Chromatography shows no impurity, spectroscopic measurements are more sensitive and can detect 1-2% impurity. A concentration of 1%  $2G_1$ -m-OH impurity in a solution of  $2G_1$ -m-Per yields at least 99% of the integrated fluorescence of the band peaked at 400 nm. The fast rise and decay component associated with the energy transfer can only be detected because of the ultrafast time-window probed.

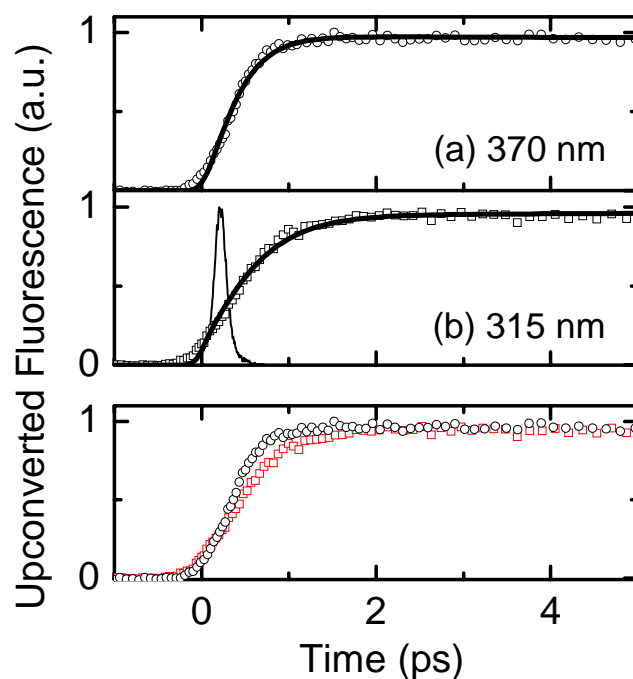


Figure 3-5. Upconversion signal of  $2G_1$ -m-Per detected at 485 nm, excited at (a) 370 nm, (b) 315 nm. The fittings correspond to the convolution of the IRF and data. The longest IRF function (at 315 nm) is shown in panel b. The bottom panel shows the superposition of the experimental data in panels a and b.

In summary, the femtosecond fluorescence measurements on generation 1 PE dendrimers exhibit subpicosecond components along with a few picoseconds ( $\sim 6$  ps) decay component. Without the Eper trap, 300 fs risetime independent of the excitation wavelength indicates the delocalization of the initially excited state while the emission occurs from a more localized state. The kinetic analysis will reveal the amplitude of each component. The 6 ps time constant and the excitation wavelength dependence of its amplitudes yield a strong argument to attribute this component to a vibrational/solvent relaxation process going on in the excited  $S_1$  state. For the  $2G_1$ -m-Per, the time-resolved fluorescence measurements along with the steady state data verify the very efficient and fast energy transfer process. The nanosecond component is straightforwardly attributed to

the fluorescence lifetime decay. The presence of these kinetic processes is also investigated with broadband transient absorption measurements.

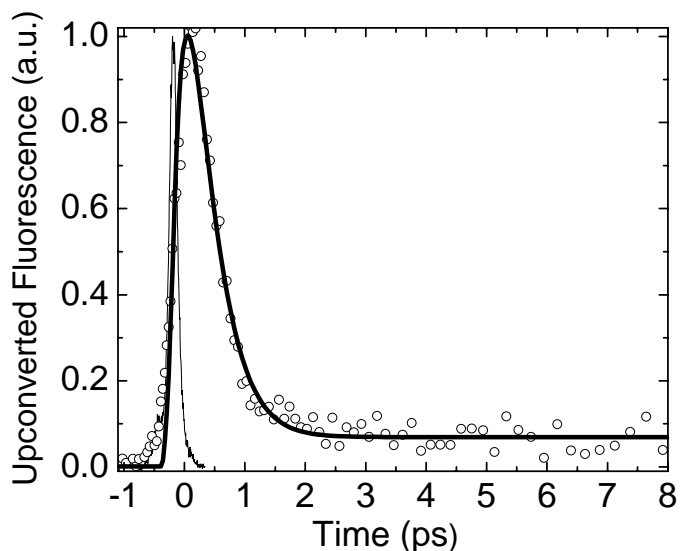


Figure 3-6. 2G<sub>1</sub>-m-Per Upconversion Signal.  $\lambda_{\text{excitation}}=315$  nm,  $\lambda_{\text{emission}} = 400$  nm. Solid line is a simulation of the  $E^*$  fluorescence with fixed time constants from previous fits. See text for the details about the model.

### Time-Resolved Broadband Transient Absorption Measurements

Before the interpretation of the transient absorption spectra, one should remember that there are three contributions to a pump-probe signal. While the excited state absorption leads to increased absorption (positive  $\Delta A$  values), both stimulated emission and ground state bleaching leads to a decrease in absorption (negative  $\Delta A$  values).

Transient absorption (TA) data for 2G<sub>1</sub>-m-OH is shown in Figure 3-7. The excitation wavelength was set to 315 nm for the measurement of transient absorption with a maximum bleach signal of  $3 \times 10^{-3}$  OD. At positive time delays, two different main components are observed. A negative signal from 300 nm to 425 nm and a positive signal beyond 425 nm are observed. Both features can be seen instantaneously after excitation (it takes 300 fs to reach the max values) and they decay on a nanosecond time

scale. The signal in the transient absorption spectrum for  $\lambda > 420$  nm is positive, so it can definitely be attributed to an excited state absorption. From the steady state studies, it is known that 2G1-m-OH has fluorescence quantum yield of 0.70 and a fluorescent lifetime of 1.8 ns.<sup>92</sup> Thus, the excited state absorption observed in the measurements reported here can be attributed to  $S_1$ - $S_n$  absorption within the 3 ring phenylethynylene chromophore.<sup>134</sup>

Since the steady state absorption spectrum ends at 405 nm and the fluorescence signal extents from 365 nm to 600 nm, the negative signal in the transient absorption spectrum can not solely be attributed to ground state bleaching. It seems reasonable to say that ground state bleach dominates the signal between 300 and 365 nm. For  $\lambda > 365$  nm, both ground state bleaching and stimulated emission are responsible for the negative absorption signal, whereas between 385 nm and 420 nm stimulated emission dominates. However, since the steady state fluorescence spectrum extends from 380 nm up to 600 nm with a maximum at 400 nm, a contribution of stimulated emission beyond 420 nm (where the positive photoinduced absorption signal dominates) is also expected. The net result of transient photoinduced absorption and stimulated emission gives rise to a large positive signal, implying that in this region the cross section for excited state absorption is larger than that for the stimulated emission.

The assignment of ground state bleaching and stimulated emission in the negative region of the transient signal needs further discussion. The maximum of the negative signal is centered at 382 nm. This is in between the maximum of the ground state absorption band (the maximum is around 372 nm at the red edge of the absorption) and the maximum of the steady state fluorescence (400 nm). Therefore, the negative signal at 382 nm is a combination of both bleach and stimulated emission. It is important to note

that the broad bleach signal reaches its maximum value within 300 fs while the peak at 382 nm still increases in amplitude. The broad bleach signal extended over the whole absorption spectrum reveals the delocalization of excitation energy on the initially excited state. The band peaked at 382 nm rises with a slower rate and shows a more localized characteristics compared to the broad bleach signal in the blue region.

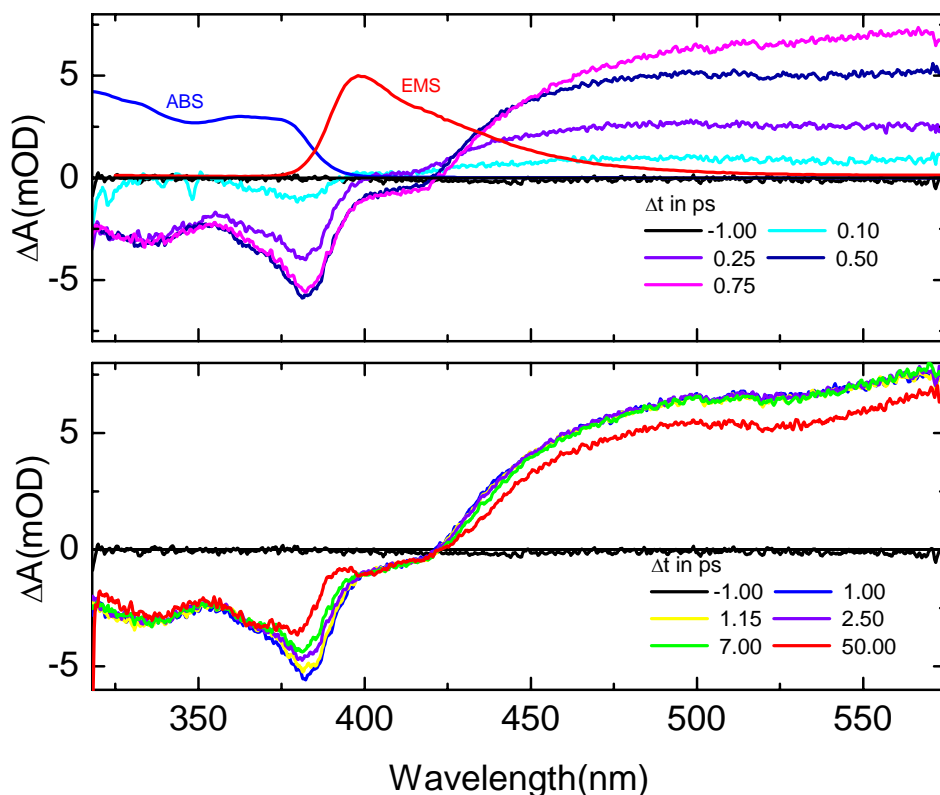


Figure 3-7. Transient absorption spectra of  $2G_1$ -m-OH molecule at different time delays, excited at 315 nm. Time delays are shown with different colors. The solid blue and red lines are absorption and emission spectrum, respectively. Top panel shows rising, whereas bottom panel shows decaying components.

The transient signals decay mainly on a nanosecond time scale. However, a kinetic analysis of the transient absorption intensities as a function of delay time at different wavelengths reveals an additional picosecond relaxation process. This relaxation process can be seen easily in Figure 3-8. The band with a maximum at 382 nm becomes narrower

due to the decrease in the stimulated emission contribution. The photoinduced absorption is observed instantaneously for the wavelengths  $\lambda > 420$  nm, and its intensity decreases along with a red shift. The intensity decrease of the 382 band and broad photoinduced absorption occurs within the same time scale. If we look at the intensity of the transient absorption signal in function of time at 382 nm and 440 nm, an additional process can be determined with time constant of 6 ps together with the nanosecond fluorescence lifetime decay. The presence of this kinetic process and its wavelength dependence was discussed in the results of upconversion experiment. This component is assigned to vibrational relaxation in the emitting excited state of the molecule. As shown in Appendix B, for the numerical analysis we had to treat this relaxation process in a different way than the raw data set, since SVD is not suitable for spectral shift, broadening or narrowing in time.

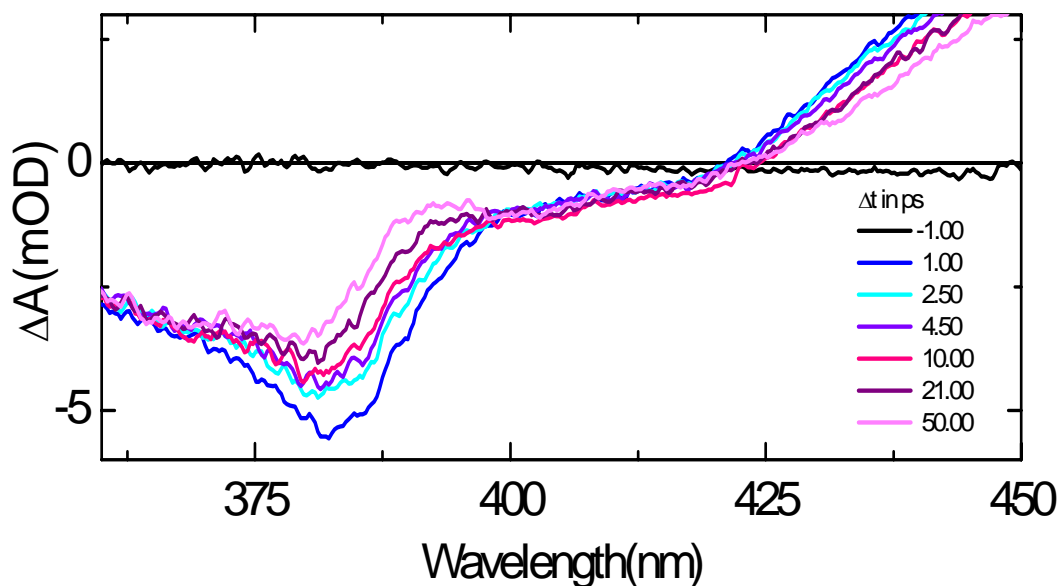


Figure 3-8. Transient absorption spectra of the 2G<sub>1</sub>-m-OH molecule at different delay times. Detailed display of the 350 nm-450 nm region.

The transient absorption spectra of 2G<sub>1</sub>-m-Per in CH<sub>2</sub>Cl<sub>2</sub> after the excitation of 315 nm are shown in Figure 3-9. Immediately after excitation, the transient absorption signal

starts evolving spectrally in the same way as the 2G<sub>1</sub>-m-OH molecule. However, this transient spectrum undergoes changes on a very fast time scale of a few hundred femtoseconds. As shown in Figure 3-9, within 1 ps, the transient signal corresponds to that expected for the ethynylene perylene (acceptor) molecule. This time evolution of the transient spectrum clearly shows the excitation energy transfer from the dendritic backbone to the trap molecule. A very small backbone bleach signal is observed at early times, but it is rapidly overcome by a new photoinduced absorption band from EPer ( $\Delta A > 0$ ). At longer wavelengths the negative signal corresponds to the bleach and stimulated emission signal from EPer.

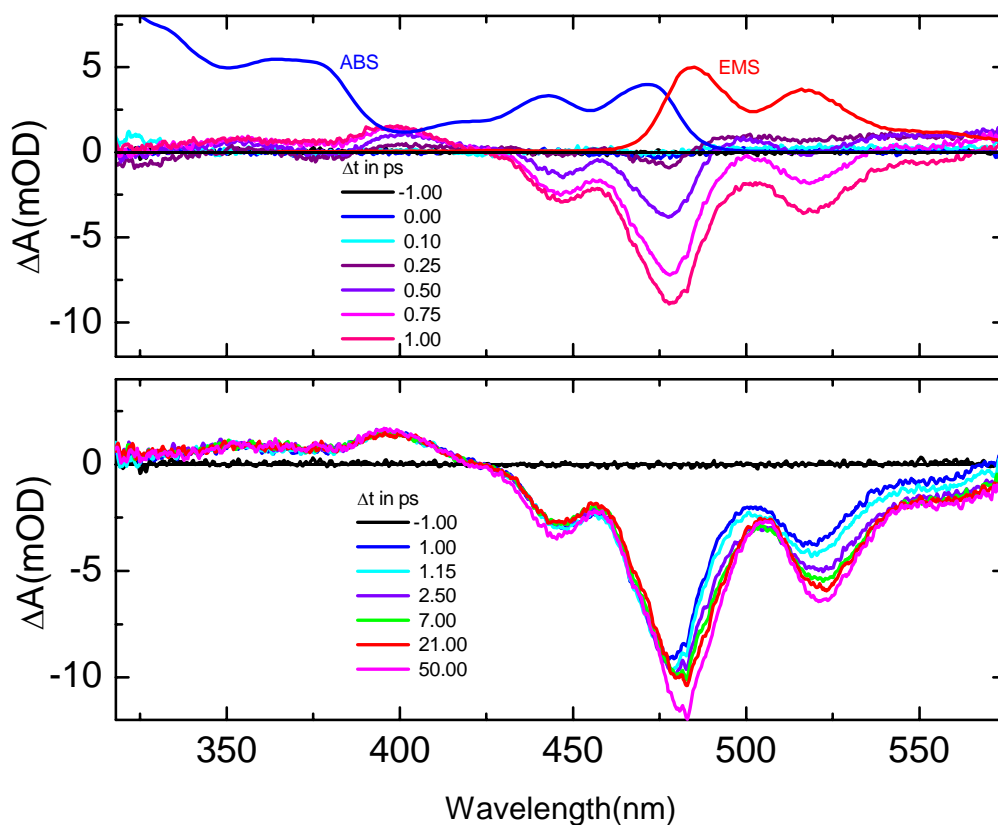


Figure 3-9. Transient absorption spectra of 2G<sub>1</sub>-m-Per at different time delays, excited at 315 nm. Top panel shows the short time scale while the bottom panel shows the long time scale. The subpicosecond energy transfer is verified with the fast ground state bleaching and fast evolution of EPer stimulated emission.

### Kinetic Model

Both time-resolved experiments reveal that the energy is efficiently transferred from the dendrons to the trap. The goal of these experiments is to understand the mechanism of this process and the extent of interaction (due to electronic coupling) between donor and acceptor moieties. The detailed analysis of both experiments will estimate the rate of energy transfer and will help understand the electronic structure of the backbone and its interaction with the trap molecule.

The data analysis is performed independently for each molecule. The fluorescence measurements are analyzed globally using a nonlinear least square fit routine from Origin Software. The broad transient absorption measurements are analyzed using the Singular Value Decomposition (SVD) algorithm from Matlab. For all molecules, a sum of exponentials will fit the data sets properly. In fact, we solve the associated differential equations of the proposed kinetic model to describe the population of each electronic state. We believe that it is crucial to apply a kinetic model instead of using a sum of independent exponentials to derive the physical meaning. Upon combination of these two analysis approaches for two different experiments, one can confirm the measurements, calculations and fit procedures.

For the 2G<sub>1</sub>-m-OH, the simplest case is considered as shown below in Equation 3-1. D is the ground state of the backbone, D\* is the initially excited state, and E\* is the emissive state of the backbone.



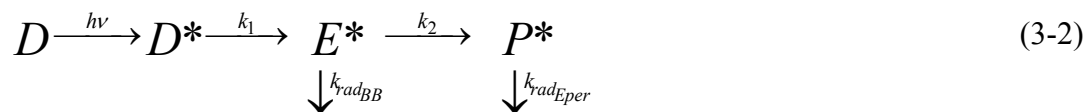
After convolution of the data with the IRF, a risetime of 300 fs was obtained from the fit to the emission data. This risetime was not dependent on excitation wavelength, which indicates the initial delocalization of excitation within the backbone. Also this relatively long risetime (not instantaneous, longer than IRF) suggests that the initially excited state undergoes a conformational relaxation before emitting. In addition to a long nanosecond decay of the fluorescence, there is a second decay component with a 6 ps time constant. The partial amplitude of this component changes as a function of excitation wavelength. When excited at 370 nm, the partial amplitude is smaller compared to the one at 320 nm. Taking into account the amplitude behavior of this kinetic component, this feature is attributed to a vibrational relaxation in the electronically excited state of the dendritic backbone. Excitation at the blue end of the spectrum (315 nm) leads to a highly excited vibrational population. This process is coupled to a relaxation and reorganization of the solvent around the chromophore as the solvent molecules have to accommodate for the newly populated  $S_1$  state of the dendrimer. At excitation wavelengths close to the blue end of the absorption band, this relaxation will be seen as a decay component with larger amplitude, whereas at longer excitations the amplitude will decrease. In similar investigations, time constant of a few picoseconds were observed and attributed to vibrational relaxation process of polyphenyl ethynylene dendrimers in organic solvents.

Spectral changes are measured as a function of delay time, and it is also possible to get kinetic information by looking into the intensity of TA signal as a function of time at particular wavelengths. In general, the transient absorption signal (both positive and negative signals) of this molecule decays with 1.8 ns time constant. There is very fast

risetime around 300 fs for both ground state bleach signal and excited state absorption signal. Considering the time dependent development of transient absorption spectrum at wavelengths between 360 nm and 435 nm, a relaxation process leading to a small red shift of the fluorescence spectrum within 6 picoseconds can be observed. This is in very good agreement with vibrational relaxation process observed in the emission experiments.

The fluorescence upconversion and transient absorption signals give complementary results. When 2G<sub>1</sub>-m-OH is excited, it takes ~300 fs for the bleach signal to evolve into the steady state absorption. This is an indication of initially delocalized excitation and this is the time scale associated with the conformational change. After the initial excitation, the vibrational cooling is observed and finally a 1.8 ns fluorescence lifetime is measured.

For the 2G<sub>1</sub>-m-Per molecule, addition of EPer trap results in a new final excited state P\*. Emission is detected from the P\* and the backbone state E\*. The simplest deactivation pathway, population transfer from the emitting state of the dendrimer backbone (E\*) to the emitting state of the EPer (P\*), is proposed. According to this model, the excitation energy is flowing to the trap molecule in a stepwise manner. Thus the vectorial nature of the energy transfer is investigated. The analysis simply involves the following scheme:



Measurements of the 2G<sub>1</sub>-m-OH fluorescence probe the E\* state directly, whereas experiments with the 2G<sub>1</sub>-m-Per probe the EPer emission (P\*) when detection is at  $\lambda =$

485 nm and backbone emission ( $E^*$ ) from 2G<sub>1</sub>-m-Per for early-time detection at  $\lambda = 400$  nm. By solving the kinetic equations for this model, one can obtain the populations of each excited state with minimum number of parameters in the fitting functions. The backbone excited state population is given by:

$$E^*(t) = \frac{k_1}{k_2 - k_1} \times [e^{-k_1 t} - e^{-k_2 t}] \quad (3-3)$$

The population of the trap excited state ( $P^*$ ) can be written as the following:

$$P^*(t) = \frac{k_1 k_2}{k_2 - k_1} \left\{ \frac{-e^{-k_1 t}}{k_1} + \frac{e^{-k_2 t}}{k_2} \right\} + 1 \quad (3-4)$$

The fluorescence lifetimes of  $E^*$  and  $P^*$  appear only as a constant offset in the model since they are on the order of nanoseconds. The preexponential factors are defined in terms of rates, which will reduce the number of free parameters, and energy transfer channels are given by characteristic times of  $(k_1)^{-1}$  and  $(k_2)^{-1}$ . The fitting results are summarized in Table 1.

Table 3-1. Fits for Time-Resolved Fluorescence Data

$\lambda_{\text{exc}}$	$\tau_1^{\&\#}$ (fs)	$\tau_2$ (fs)	$\tau_3$ (ps)
315 nm	$300 \pm 20$	$350 \pm 40$	$6 \pm 1.25$ (11%)
370 nm	$300 \pm 30$	$250 \pm 50$	$6 \pm 1.25$ (17%)

<sup>&</sup> Time constants ( $\tau_1$ ) for  $D^* \rightarrow E^*$  and ( $\tau_3$ ) for vibrational relaxation of  $D^*$  are obtained from the time-resolved fluorescence measurement of 2G<sub>1</sub>-m-OH and kept constant when fitting the 2G<sub>1</sub>-m-Per data.

<sup>#</sup> Errors correspond to  $\pm 2\sigma$

Excitation at 315 nm and 372 nm shows different dynamics. It is crucial to mention that at these wavelengths there is no direct excitation of EPer, and the emission is solely

due to energy transfer from the backbone to the trap. Excitation at 315 nm yields an energy transfer step with  $k_2^{-1} = 350$  fs, after the initial delocalization of excitation within  $k_1^{-1} = 300$  fs. At 370 nm, the fit yields a faster rate for the energy transfer,  $k_2^{-1} = 250$  fs. At this wavelength the excitation is very close to the emitting state of the dendritic backbone. However, the vibrational relaxation process measured from 2G<sub>1</sub>-m-OH molecule is not obtained when EPer is attached. This is due to very fast energy transfer to EPer. The energy transfer is faster compared to vibrational relaxation; this is already an indication that the coupling between backbone (donor) and EPer (acceptor) is beyond a very weak coupling.

When the transient absorption of 2G<sub>1</sub>-m-Per is analyzed with SVD using the same kinetic model and the very fast risetime for the bleach and photoinduced absorption are obtained. If we compare with the dynamics of 2G<sub>1</sub>-m-OH molecule, the excitation energy is transferred within 350 fs. In addition, the spectral shift within 6 ps is not observed anymore, suggesting again the energy transfer is much faster than the vibrational relaxation within the backbone.

The kinetic model proposed here is furthermore confirmed via collecting the emission dynamics of E\*(donor emitting state) in the presence of acceptor EPer. In this case the rise and decay times of the fluorescence gives direct measurement of the energy transfer process. Using the rates obtained from these fits, we predict the temporal behavior of E\*(t). Figure 3-6 shows that the experimental data agrees very well with this prediction.

Overall, the agreement between fluorescence upconversion and transient signals is excellent. We need to understand the nature of excitations and the extent of coupling between backbone and EPer.

### **Energy Transfer via Weak Coupling**

As explained in detail in Chapter 1, energy transfer can result from different interaction mechanisms. The interactions can be Coulombic and/or due to intermolecular orbital overlap. The magnitude of this interaction is very important. Briefly, in the strong coupling case, excitation energy transfer is faster than the nuclear vibrations and vibrational relaxation. The excitation energy is delocalized over donor and acceptor, the transfer of excitation is a coherent process. In the weak coupling the electronic excitation is more localized than under strong coupling. However, the system can be described in terms of stationary vibronic exciton states (vibronic excitation is delocalized). The transfer rate is faster than vibrational relaxation but slower than nuclear motions (in contrast to strong coupling). In the case of very weak coupling, the vibrational relaxation occurs before the energy transfer takes place.<sup>135</sup>

Here we report that the donor molecule (2G<sub>1</sub>-m-OH) has vibrational relaxation of 6 ps (verified by both time-resolved emission and absorption experiments). However, when the acceptor is covalently attached to this donor, the energy transfer occurs in a time scale of a few hundred femtoseconds, which is much faster than vibrational relaxation of donor. This is an indication that the donor and acceptor molecules are weakly coupled here. The interaction energy must then be smaller than the absorption bandwidth but larger than the width of an isolated vibronic level.

In the very weak coupling regime, the energy transfer rate can be evaluated using the simplest model, Förster. This model is based on the dipole-dipole approximation

which is valid when the donor-acceptor separation is much larger than the dipole sizes. For the conjugated dendrimers investigated here, this approximation is not valid, thus attempts to apply Förster theory may not yield good agreement with the experimental results. Using the excitation transfer rate in the very weak coupling limit, we will calculate the interaction energy and compare it to the values usually obtained within the Förster regime. The transfer rate in the very weak coupling limit can be calculated from

$$k_{ET} = \frac{4\pi^2}{h^2 c} J |V|^2 \quad (3-5)$$

where  $V$  is the coupling and  $J$  is the vibronic spectral overlap integral between donor and acceptor (in units of cm). The spectral overlap is a measure of the density of interacting initial and final states. The accurate calculation of the overlap integral employs the homogeneous vibronic bandwidths. Since the homogeneous bandwidths of the vibronic bands in the di-dendron are unknown, we rely on absorption and emission spectra to obtain  $J$ . The spectral density can be evaluated by using a normalized absorption spectrum -acceptor,  $a(\lambda)$ -, and normalized emission spectra –donor,  $f(\lambda)$ -,

$$J(\text{cm}) = \int_{\lambda_i}^{\lambda_f} f(\lambda) a(\lambda) \lambda^2 [\text{nm}] 10^{-7} d\lambda \quad (3-6)$$

yielding  $J = 1.187 \times 10^{-4}$  cm.

An experimentally measured transfer rate  $k_{ET} = (300 \text{ fs})^{-1}$  yields an interaction energy  $V = 155 \text{ cm}^{-1}$ . The approximation on the  $J$  calculation results on an upper limit for  $J$  and therefore, for a given experimental rate, a lower limit of the Coulombic interaction. The typical transfer rates obtained for the other dendrimer structures using Förster model are slower yielding lower interaction energies.<sup>132,136,137</sup> Thus, the interaction energy of  $155 \text{ cm}^{-1}$  is not in the very weak coupling regime.

## Conclusions

Time-resolved fluorescence and absorption dynamics of a generation 1 phenylethynylene dendron with and without energy trap are presented in this chapter . By globally analyzing the data sets from fluorescence upconversion and transient absorption measurements and comparing the results, we are able to identify and attribute various kinetic components. A 6 ps decay component observed from the 2G<sub>1</sub>-m-OH molecule is attributed to vibrational relaxation in the excited state. Since the emission detected from the longest linear PE chain in the 2G<sub>1</sub>-m-OH (3-ring PE) shows a risetime of 300 fs independent of the excitation wavelength, delocalization is noticed in the initially excited state. The presence of ortho and para substitutions in such unsymmetrical structures supports the initial exciton delocalization (unlike meta substitution). After excitation, a change in the excited state surface leads to localization, which is supported with the localized peak around 382 nm. The built-in energy gradient results in very efficient energy transfer to the EPer trap and yields a cascade mechanism. The energy transfer process occurs in sub-picosecond (250-350 fs) time scale. However, the interaction energy calculated using very weak coupling limit formulation yields a value of 155 cm<sup>-1</sup>, which is above the very weak coupling limit. Moreover, the transfer rate being faster than vibrational relaxation reduces the very weak coupling probability, thus questions the validity of Förster mechanism for the systems under investigation.

Further investigations of larger generation dendrimers will complete the map of the energy transfer pathways in the unsymmetrical PE dendrimers, and will help understand the mechanisms responsible for maintaining the highly efficient light-harvesting properties.

## CHAPTER 4

### ENERGY TRANSFER IN GENERATION 2 UNSYMMETRICAL PHENYLENE ETHYNYLENE DENDRIMERS

As described in Chapter 3, the unique unsymmetrical branching leads to rapidly increasing conjugation lengths of PE chains as the generation number is increased.<sup>131</sup> A perylene unit is attached to the focal point of dendrons to investigate the structure – property relationship regarding the energy transfer dynamics and  $\pi$ -conjugation. In one case, perylene is directly attached to the monodendrons linearly resulting in extended conjugation between the PE dendron and perylene unit.<sup>96</sup> The other case, in which two unsymmetrical PE dendrons and an ethynylperylene trap are linked through the *meta* positions of a phenyl ring, creates a new family of di-dendrons.<sup>97</sup> The *meta* substitution of the central phenyl ring disrupts the ground state  $\pi$ -conjugation, providing a degree of isolation between the monodendron backbone and the trap.

To evaluate the effect of  $\pi$ -electron delocalization on the energy transfer dynamics, we can compare the  $2G_n$ -m-Per di-dendrons with  $G_{n+1}$ Per monodendrons. Both molecules have the same total number of PE units and the same number of PE units in the longest linear chain.<sup>95</sup>

To determine the influence of the generation and size of PE dendrimers on the energy transfer process, and degree of localization, a larger di-dendron with and without ethynylperylene trap is investigated. The main focus of this study is to explore the nature of electronic excitations as well as the speed and efficiency of energy transfer. In this chapter, complementary experiments of ultrafast time resolved emission and broadband

transient absorption experiments are described. A kinetic model parallel to the one described in Chapter 3 is applied for both molecules. The energy transfer dynamics is compared to the generation one di-dendron. The unidirectional energy transfer is verified via detecting emission from an intermediate state. Finally, we present an analysis of the validity of Förster model by comparing the model predictions with our experimental results.

### Materials and Methods

The synthesis of unsymmetrical PE dendrons has been described elsewhere.<sup>97</sup> Unsymmetrical monodendrons can be combined into larger structures, leading to more symmetric macromolecules. For example, Figure 4-1a shows two G<sub>2</sub> (generation 2) dendrons coupled to a phenyl ring in *meta* positions. The phenyl ring has an additional OH group in the other *meta* position and is thus named 2G<sub>2</sub>-m-OH. The addition of an energy trap to a similar structure can be used to quantitatively probe the energy-transfer dynamics. In this case, an ethynyleneperylene unit replaces the OH group, leading to the 2G<sub>2</sub>-m-Per molecule as shown in Figure 4-1b. Even though the chemical structure seems to describe a planar molecule, the 3D modeling shown in Figure 4-1c clearly demonstrates otherwise. To obtain a reasonable picture of the room temperature structure of 2G<sub>2</sub>-m-Per, we look at Molecular Dynamics (MD) simulations performed by Roitberg and Krause.\* The system is built in Hyperchem 7.0 and run for 100 ns (T=300 K) using the program TINKER. The MM3 force field is used with the rotational barrier around the ethynylene triple bond raised to 0.6 kcal/mol to reflect experimental observables. The simulations are performed in vacuum and should be interpreted only as guides to overall

---

\* Personal communication

conformational shapes. After several nanoseconds of the MD run, a snapshot (Figure 4-1c) was taken showing the globular shape of the dendrimer. The small size of this dendrimer and its rigidity does not allow for the “fold-back” of any of the branches. In addition, the trap is completely exposed, with the dendritic structure forming a sort of “bouquet”.

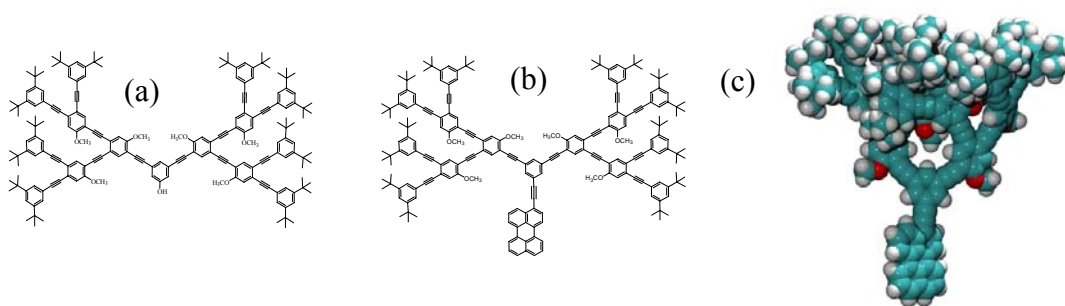


Figure 4-1. Chemical structures of phenylene ethynylene dendrimers: (a) 2G<sub>2</sub>-m-OH (b) 2G<sub>2</sub>-m-Per and (c) 3D model of the 2G<sub>2</sub>-m-Per from a MD simulation.

Steady state characterization of the di-dendrons is performed via UV-Vis absorption in a Varian-Cary 100 and emission in a Jobin-Yvon instrument (Spex Fluorolog-3). All steady state measurements are performed in the same homemade rotating cell (optical path of 1 mm), which is also used for the time-resolved emission experiments. Sample concentrations are kept below  $10^{-6}$  M to avoid any aggregation<sup>138</sup> or excimer formation,<sup>139</sup> yielding optical densities less than  $0.3 \text{ mm}^{-1}$ . Femtosecond time-resolved photoluminescence is employed to explore excited state dynamics and energy transfer. The upconversion experiment measures the temporal evolution of the fluorescence with subpicosecond resolution. It is explained in detail in Chapter 2 and additionally some brief explanation is given in Chapter 3.

The homemade rotating cell has a 1 inch diameter and an optical path length of 1 mm to guarantee excitation of a new sample volume with every laser shot with minimum

consumption of sample. The photoluminescence is collected by two off-axis parabolic mirrors and the excitation volume is imaged onto a 500  $\mu\text{m}$   $\beta$ -BBO crystal. A small portion of the regenerative amplifier beam (800 nm,  $\sim 30 \mu\text{J}/\text{pulse}$ , FWHM = 60 fs) is used as the gate pulse. Excitation pulses at variable wavelengths are obtained from the fourth harmonic generation of the OPA's signal output. The Instrument Response Function (IRF) is measured with pump scattered light, which is up-converted with the gate pulse yielding cross-correlations FWHM of 175 fs and 220 fs in the visible and UV regions, respectively.

The transient absorption measurement is performed using a whitelight continuum as the probe beam. The experimental details are explained in Chapter 2. For the molecules studied in this chapter, the excitation pulse is set to be 320 nm. The IRF is measured to be  $\sim 150$  fs. Data analysis involves the convolution of decay and rise time functions with the corresponding experimental IRF. The photostability of the sample is checked by steady state UV and emission spectroscopy before and after each time-resolved experiment.

### **Steady State Spectroscopy of Phenylene Ethynylene Dendrimers**

$G_2\text{-OH}$  is a second-generation unsymmetrical (PE) dendron and  $2G_2\text{-m-OH}$  is a dendron consisting of two  $G_2$  dendrons coupled through the *meta* positions of a phenyl ring (Figure 4-1a). It has been shown previously that the choice of site-substitution on the focal point governs the nature of the optical excitations for the entire molecule.<sup>87,127,140</sup> For the two molecules under consideration ( $2G_2\text{-m-OH}$  and  $2G_2\text{-m-Per}$ ), substitution at the focal point is the same, leading to similar steady state characteristics as shown in Figure 4-2a. The absorption spectra of  $2G_2\text{-m-OH}$  shows a 15 nm red shift compared to

the single G<sub>2</sub>-OH dendron.<sup>141</sup> This shift is due to the additional phenyl ethynylene unit, which increases the conjugation length in each individual dendron. A better comparison can be made with the steady state spectra of a generation 3 monodendron (Figure 4-2b). In the G<sub>3</sub>OH monodendron, the longest linear PE chain has the same number of PE units as the longest linear chain in the 2G<sub>2</sub>-m-OH, and their absorption spectra show similar features (bands, bandwidth, and red-shift). There is a slight red shift of G<sub>3</sub>OH over 2G<sub>2</sub>-m-OH due to some extended conjugation between the two longest linear PE units through the *ortho* linkage.

To probe the dynamics of energy transfer, EPer is added to the di-dendron molecule in the *meta* position with respect to both monodendron components. The absorption spectrum of 2G<sub>2</sub>-m-Per resembles the sum of the absorption spectra of 2G<sub>2</sub>-m-OH and EPer obtained independently as shown in Figure 4-2a. This suggests a weak ground-state coupling between the dendritic backbone and the EPer energy acceptor. From these spectra we conclude that the broad absorption feature between 300 and 430 nm corresponds to the dendritic backbone, and absorption at  $\lambda > 430$  nm corresponds to direct excitation of the EPer trap. The photoluminescence spectrum shows emission from 2G<sub>2</sub>-m-Per originating almost entirely from the EPer trap. At excitation wavelengths between 300 nm and 400 nm there is no direct excitation of EPer, and the emission is solely due to energy transfer from the backbone to the trap. This was proven by exciting 2-phenylethynyleneperylene in CH<sub>2</sub>Cl<sub>2</sub> at selected wavelengths and obtaining no emission at 485 nm (max wavelength emission of EPer). We conclude that energy transfer from the backbone to the trap is very efficient. Comparison of absorption and excitation spectra indicates ~94% efficiency for the energy transfer process.<sup>97</sup>

Interestingly, at 435 nm, we notice a small band with intensity contributions from incomplete substitution of the OH group in  $2G_2\text{-m-OH}$ <sup>97</sup> by EPer, and residual backbone emission from  $2G_2\text{-m-Per}$ . Time-resolved data will clarify the origin of this backbone fluorescence band.

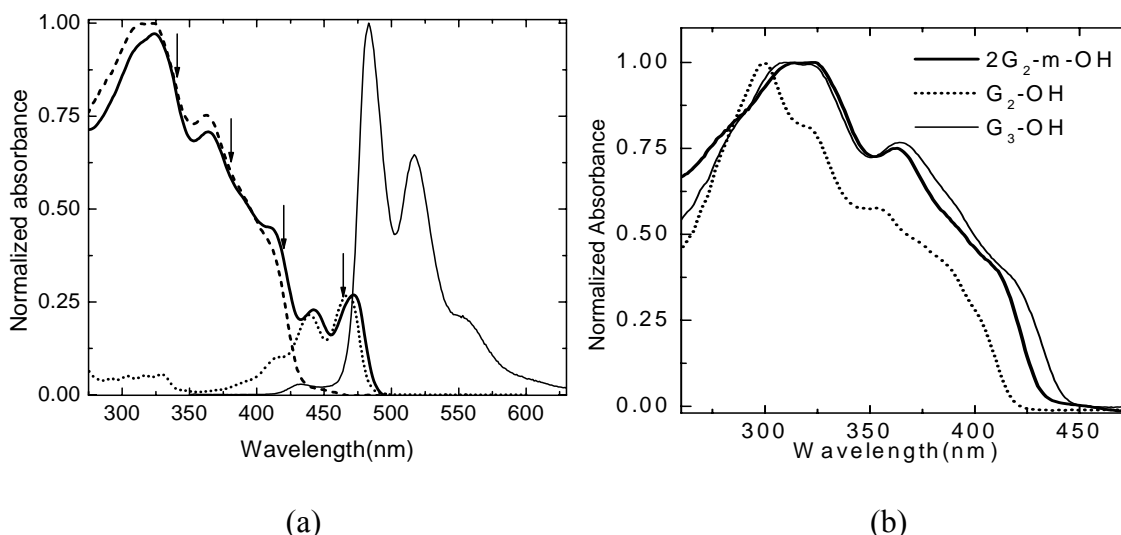


Figure 4-2. (a) Normalized absorption spectra of  $2G_2\text{-m-OH}$ , EPer and  $2G_2\text{-m-Per}$  and fluorescence spectrum of  $2G_2\text{-m-Per}$ , excited at 320 nm. (b) Normalized absorption spectra of  $2G_2\text{-m-OH}$ ,  $G_2\text{-OH}$  and  $G_3\text{-OH}$  in dichloromethane.

### Time-Resolved Emission Experiments

The fluorescence decays of  $2G_2\text{-m-OH}$  and  $2G_2\text{-m-Per}$  occur on a ns time scale and are measured by Time-Correlated Single Photon Counting (TCSPC). The fluorescence decays for these dendrimers are characterized by a single exponential decay as shown in Table 4-1. The decay for the  $2G_2\text{-m-Per}$  at 500 nm is in good agreement with that of 2-phenylethynyleneperylene emission lifetime at the same wavelength. Detection of  $2G_2\text{-m-Per}$  emission at 450 nm yields a combination of the emission lifetime of  $2G_2\text{-m-Per}$  (measured at 500 nm) and unsubstituted  $2G_2\text{-m-OH}$  whose fluorescence spectrum has a peak at 450 nm.

Table 4-1. Lifetime measurements from TCSPC

	$\lambda_{\text{excitation}}$ (nm)	$\lambda_{\text{detection}}$ (nm)	$\tau$ <sup>#</sup> (ns)
EPer	450	500	2.36±0.01
2G <sub>2</sub> -m-OH	370	450	1.83±0.01
2G <sub>2</sub> -m-Per <sup>&amp;</sup>	370	450	1.83 (52%) 2.34 (48%)
2G <sub>2</sub> -m-Per	370	500	2.34±0.01

<sup>#</sup> Errors correspond to  $\pm 2\sigma$ . <sup>&</sup> The  $\tau$ s were fixed and only the relative contributions were fitted.

The rise times associated with these fluorescence decays are measured by the femtosecond time-resolved fluorescence upconversion technique. To understand the excitation delocalization and intramolecular interactions within the di-dendron backbone, we first study the dynamics in the absence of the EPer trap.

The absorption spectrum of 2G<sub>2</sub>-m-OH has three distinguishable bands peaked at 320 nm, 363 nm and 411 nm. Exciting 2G<sub>2</sub>-m-OH at selective wavelengths (330 nm, 372 nm, and 415 nm), we seek to probe regions with considerable contributions from each band and explore the possibility of assigning the absorption band structure to exciton localization.

After excitation at the selected wavelengths, emission is detected at 435 nm corresponding to backbone fluorescence (Figure 4-2). Convolution of the instrument response function and the exponential rise function reveals a 500 fs time constant (see model below). It is important to note that the fitting involves the convolution of the IRF with the model functions and therefore the experimental time resolution is c.a. 150 fs (slightly better than the IRF FWHM).

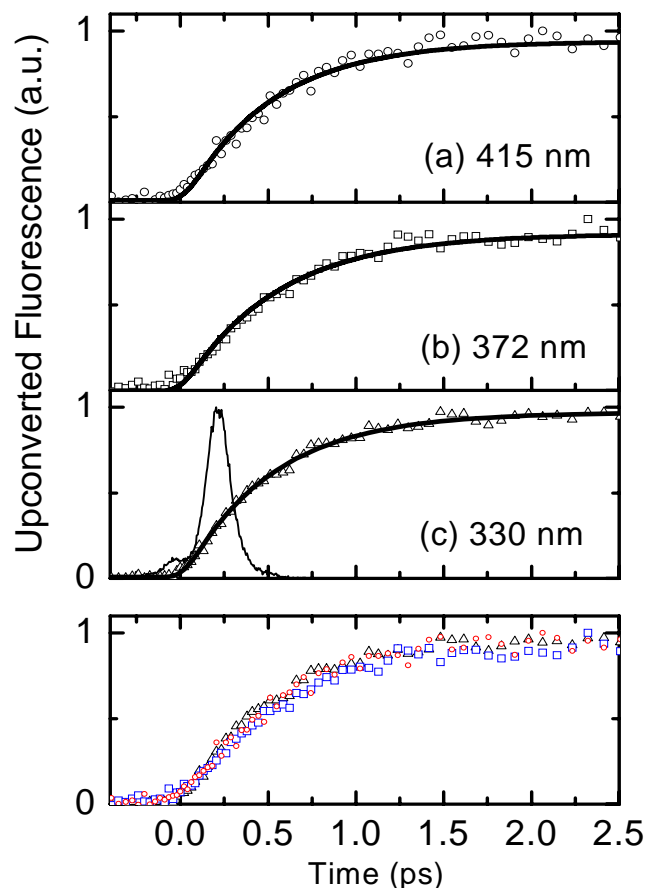


Figure 4-3.  $2G_2$ -m-OH in dichloromethane excited at a) 415 nm b) 372nm and c) 330 nm. Upconversion signal of fluorescence is detected at 435 nm, the maximum emission wavelength of the molecule. Fitting procedures include the convolution of exponential functions from the kinetic model with the IRF. The best fit is shown as the solid line. The longest IRF function is shown in panel c. The bottom panel shows the superposition of the experimental data in panels a-c.

The surprising result is the lack of rise time dependence on excitation wavelengths: the three plots in Figure 4-3 show similar rise times ( $510 \pm 20$  fs at  $\lambda = 330$  nm,  $540 \pm 30$  fs at  $\lambda = 372$  nm, and  $500 \pm 35$  fs at  $\lambda = 420$  nm). We conclude that the initially excited state must be delocalized throughout the monodendron and it takes about 500 fs to reach the lowest lying state (the emissive state).

As mentioned previously, when the EPer trap is attached to the di-dendron, a strong emission from the EPer unit is observed, which indicates efficient energy transfer. To

follow the energy migration from the initially excited state on the di-dendron backbone to the EPer trap, we measure the rise time of the EPer emission. Figure 4-4 shows the temporal evolution of the 2G<sub>2</sub>-m-Per fluorescence as a function of excitation wavelengths. The fits correspond to the convolution of exponential functions with the instrument response function (see kinetic model below). The excitation wavelengths are shown as arrows in the absorption spectrum in Figure 4-2a. Detection of the fluorescence is at the EPer maximum emission wavelength ( $\lambda = 485$  nm). Panel **a** in Figure 4-4 shows the emission response following direct excitation of the EPer trap at 465 nm. A single exponential function ( $\tau \sim 150$  fs) yields a good fit to the experimental data, which provides the time-resolution limit for fluorescence rise times. Any rise time longer than that limit can therefore be attributed to excited-state dynamics in the backbone and energy transfer to the EPer trap. Panel **b** shows excitation at  $\lambda = 420$  nm. At this excitation wavelength, in addition to backbone absorption, there is some residual absorption from the EPer unit. Indeed, there are two mechanisms for the excitation of EPer acceptor at 420 nm: *i*) absorption by the EPer moiety and *ii*) sensitized excitation via energy transfer from the backbone. To characterize these two components, we measure the photoluminescence dynamics of a solution containing only EPer in CH<sub>2</sub>Cl<sub>2</sub> after direct excitation at  $\lambda = 420$  nm. The difference in fluorescence dynamics of 2G<sub>2</sub>-m-Per and EPer can be attributed to the backbone-to-EPer energy transfer. After considering the direct excitation component, we still find that the energy absorbed by the di-dendron backbone is efficiently transferred to the EPer. This component leads to slower dynamics observed after excitation at 420 nm (panel *b*) compared to excitation at 465 nm (panel *a*).

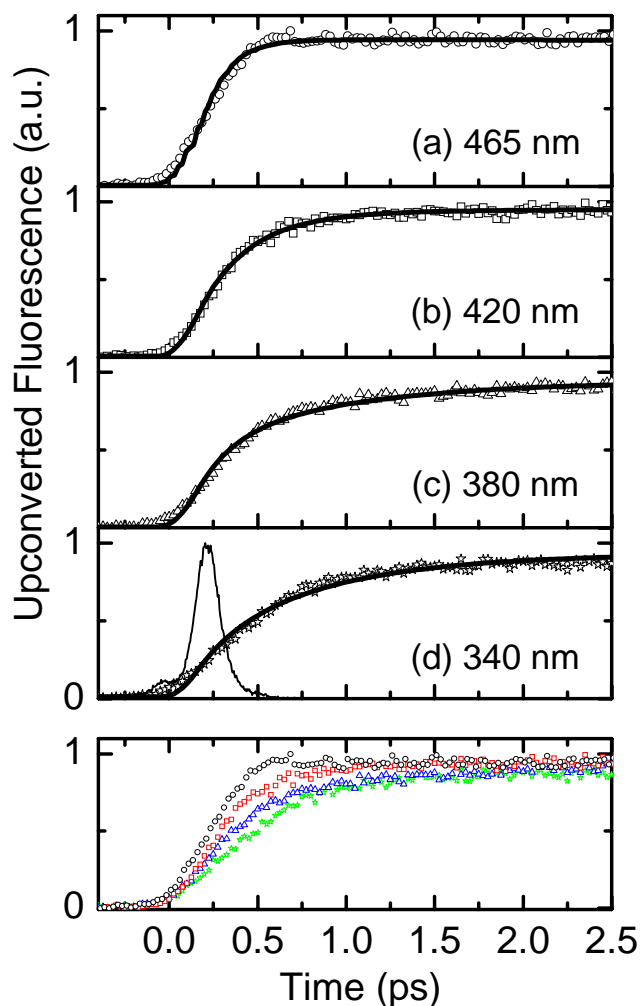


Figure 4-4. Upconversion signal of 2G<sub>2</sub>-m-Per detected at 485 nm, excited at a) 465 nm, b) 420 nm, c) 380 nm and d) 340 nm. The fittings correspond to the convolution of the IRF and the decays shown in Table 3-2. The longest IRF function (at 340 nm) is shown in panel d. The bottom panel shows the superposition of the experimental data in panels a-d.

At shorter excitation wavelengths, the fluorescence rise times become even longer. Excitations at  $\lambda = 380$  nm (panel c) and  $\lambda = 340$  nm (panel d) clearly show longer rise times for the fluorescence arising from the EPer excited state. The longer rise times correspond to energy-transfer since only backbone absorption is observed at these excitation wavelengths and 2G<sub>2</sub>-m-OH does not display any long rise times at high-energy excitation wavelengths (Figure 4-3).

The steady state fluorescence spectrum (Figure 4-2a) shows that most of the 2G<sub>2</sub>-m-Per emission (94%) derives from the EPer trap. On the blue end of the emission spectrum, a small band is centered at 435 nm, which is the same wavelength as the emission from 2G<sub>2</sub>-m-OH. This band has contribution from the unsubstituted 2G<sub>2</sub>-m-OH (as an impurity) and an additional contribution from backbone emission, even in the presence of the trap. This assertion can be confirmed by examining the time-resolved data detected at  $\lambda = 435$  nm (Figure 4-5). The temporal behavior of the fluorescence shows a very fast rise time followed by a fast decay corresponding to energy transfer from the backbone to the EPer trap. This decay time reflects the average lifetime of the excitation energy deposited in the lowest-lying state of the donor backbone. The long time component (ns) seen in Figure 4-5 corresponds to unsubstituted 2G<sub>2</sub>-m-OH. Using the kinetic model described below, we simulate this signal using the time constants obtained from Figures 4-3 and 4-4 (including a ns component corresponding to 2G<sub>2</sub>-m-OH emission lifetime). Integrating the time-resolved data yields the relative contributions to the steady state spectrum from the 2G<sub>2</sub>-m-OH impurity and the residual backbone emission.

Unsubstituted 2G<sub>2</sub>-m-OH emission accounts for more than 99% of the steady state intensity at 435 nm (impurity concentration of  $\sim 1\%$ ).<sup>†</sup> The fast decaying component corresponds to less than 1% of the steady state fluorescence; at this wavelength it can only be detected with time-resolved experiments probing in a very short time window.

---

<sup>†</sup> The purity of the sample was checked by Thin Layer Chromatography. In addition, we performed an experiment by titrating the 2G<sub>2</sub>-m-Per with 2G<sub>2</sub>-m-OH, comparing absorption and emission spectra as a function of added 2G<sub>2</sub>-m-OH. We conclude that the spectroscopy experiments are more sensitive than TLC and can detect 1-2% impurity. A concentration of 1% 2G<sub>2</sub>-m-OH yields at least 99% of the integrated fluorescence of the band peaked at 435 nm seen in Figure 4-3.

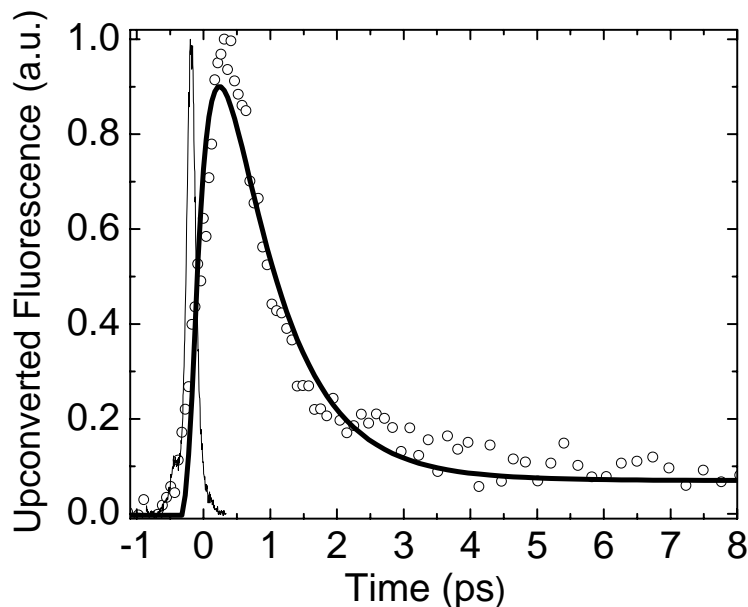


Figure 4-5. 2G<sub>2</sub>-m-Per Upconversion Signal.  $\lambda_{\text{excitation}}=320$  nm  $\lambda_{\text{emission}} = 435$  nm. Solid line is a simulation of the  $E^*$  fluorescence (equation 4) with fix time constants from Table 3-2. Inset shows steady state emission spectrum in the region of upconversion detection. See text for details.

#### Time-Resolved Broadband Transient Absorption Measurements

Transient absorption spectra of 2G<sub>2</sub>-m-OH are obtained following excitation at 320 nm. The results are shown in Figure 4-6. At positive time delays, the signal is decaying on a nanosecond time scale and it has a negative value throughout the ground state absorption range (325 nm-435 nm) along with a positive signal for  $\lambda > 435$  nm. Considering the previous steady state and single photon counting experiments,<sup>142</sup> it is known that 2G<sub>2</sub>-m-OH has quantum yield of 0.81 and a fluorescence lifetime of 1.9 ns. Since the excited state absorption observed at wavelengths  $\lambda > 435$  nm decays on a nanosecond time scale, this is attributed to an  $S_1$ - $S_n$  absorption.

When the ground state absorption spectrum of the 2G<sub>2</sub>-m-OH is compared with its transient absorption spectrum at 750 fs after the excitation, a few differences can be seen (Figure 4-6). In the former, mainly three absorption peaks are observed at 320 nm, 370

nm, and 415 nm. In the latter, the bands at 370 nm and 415 nm are 5 nm red shifted and the intensity ratio between these two bands has changed significantly. The origin of these differences between the ground state absorption spectrum and the transient absorption spectrum can be explained in the following manner. The steady state spectrum of 2G<sub>2</sub>-m-OH (Figure 4-2) shows that the ground absorption ends at 435 nm, whereas the fluorescence spectrum covers the spectral region from 405 nm to around 590 nm. As a consequence, the negative signal up to 405 nm is fully dominated by ground state bleaching. At the red edge of the absorption spectrum (420 nm), the intensity of the negative signal is larger compared to the band at 370 nm. However, the ground state absorption has almost two times smaller intensity at 420 nm. Thus, this peak has contribution from stimulated emission along with the bleach signal. Even though the stimulated emission is contributing to the transient signal in the complete fluorescence range, photoinduced absorption signal dominates beyond 435 nm.

The most significant feature of the transient spectra of 2G<sub>2</sub>-m-OH is the broad bleach signal rising within 300 fs and a more localized band at 420 nm rising independently within 750 fs. Such temporal and spectral behavior elucidates the presence of at least two electronic states within the absorption band, such that the emitting state of the molecule is different than the absorbing state. Moreover, this feature is in accordance with the slow (500 fs) risetime of the emission measured at the blue edge of the fluorescence spectrum. Due to the complete delocalization of the absorption band, it is reasonable to obtain the same risetime for any excitation wavelength.

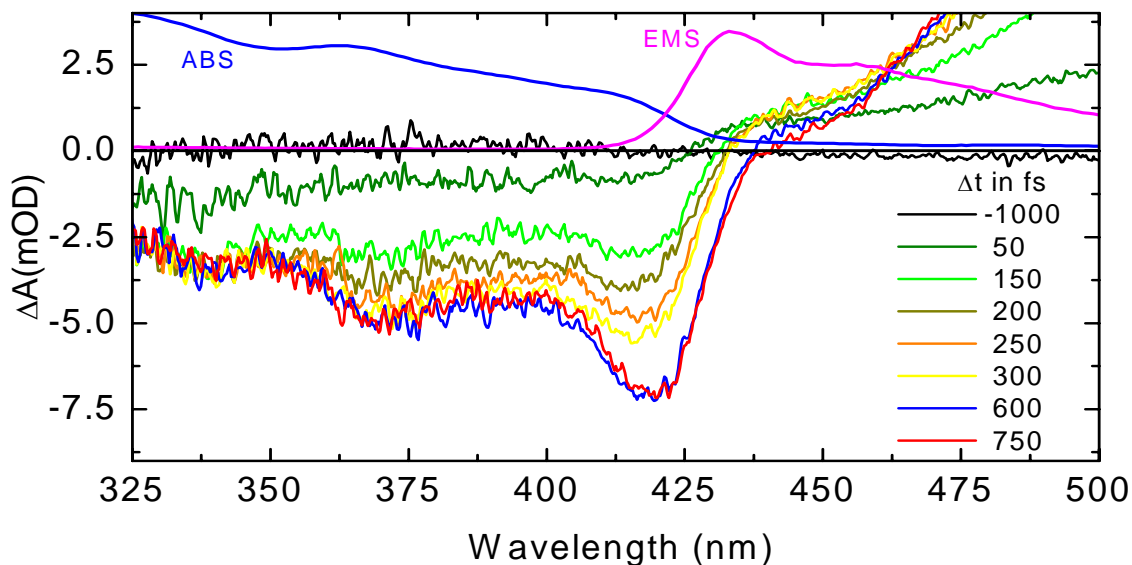


Figure 4-6. Transient absorption spectra of 2G<sub>2</sub>-m-OH at different delay times. Steady state absorption and emission are shown in solid blue and magenta colors, respectively.

It is important to note that complex signals from multiple electronic states can be mixed in the transient absorption signals. Even though time-resolved experiments give complementary results, one can argue the presence of the different electronic states. Are there really two electronic states or are we just observing some relaxation process in subpicosecond regime? To confirm our explanation, low temperature (77 K) steady state experiments are performed. Recently, it has been shown that the phenyl rings are free to rotate around the ethynylene bonds although the overall structure of PE dendrimers are quite rigid. At room temperature, the torsional barrier is of the same order as  $kT$ , and thus the rings rotate freely. At low temperature (10 K and 77 K), the rings essentially lie in the same plane. The dipole arrangement of the chromophore system is approaching planarity as the temperature is decreased. This is related to the fact that many different conformations and rotations that are possible for the molecule at room temperature in solution are not accessible at low temperature in glass forming solvents (like MeTHF).

Figure 4-7a shows the excitation spectrum of 2G<sub>2</sub>-m-OH at room temperature (red line) and at 77 K (blue line). In the spectrum measured at 77 K, new absorption peaks appear that were hidden in the broader homogenous line width at room temperature. The absorption bands are much sharper and approximately 12 nm redshifted for  $\lambda > 350$  nm. The red shift indicates the presence of a more planar geometry as the temperature is decreased. This temperature dependent change of geometry has significant effect on the transition density, which directly effects the energy transfer process. Moreover, the peak at 425 nm has more intensity and localized character at 77 K, which is very similar to the independent rise of the sharp features in the transient absorption data.

To further characterize the interactions between the chromophores and the excitation energy transfer dynamics in dendritic systems, fluorescence anisotropy is a powerful method. Anisotropy measures the orientational memory of dipoles. Any change in the transition moment during the lifetime of the excited state will cause the anisotropy to decrease. The depolarization of fluorescence might be due to transfer of excitation energy to another molecule with different orientation. Thus, using fluorescence depolarization, it is possible to observe the intramolecular excitation transfer accompanied by reorientation of the transition dipole. The different orientation of transition dipole moments are investigated with excitation anisotropy, which allows us to distinguish between electronic states. Figure 4-7b shows the excitation anisotropy measured at 77 K. There are distinctively three different regions in the excitation anisotropy spectrum. The zero anisotropy at  $\lambda < 375$  nm indicates an energy transfer from the initially excited state to the final emitting step. The nonzero anisotropy value at 425 nm verifies the existence of a second electronic state other than the absorbing state. We

also suggest that the region between 375 nm and 425 nm has contributions from both states. These steady state experiments further confirm our conclusion suggesting a localization of excitation before emission. The emission would occur from localized states while absorption is into delocalized exciton states.

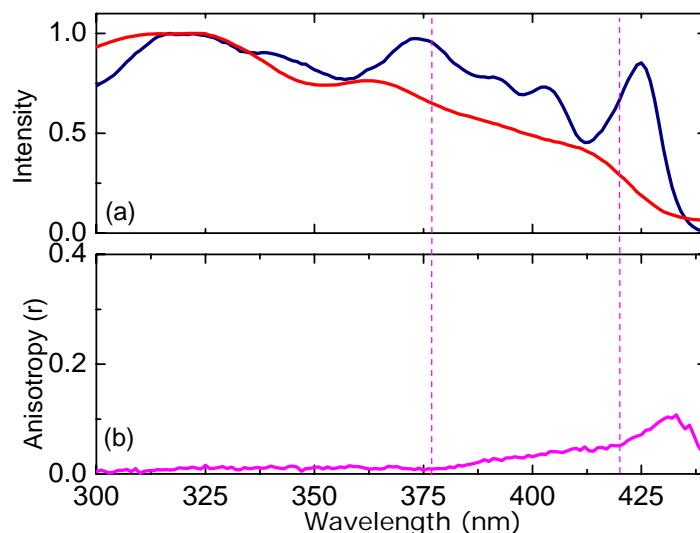


Figure 4-7. The excitation spectrum of 2G<sub>2</sub>-m-OH at 298 K (red) and 77 K (blue), emission detected at 450 nm (top). The excitation anisotropy of 2G<sub>2</sub>-m-OH at 77 K (bottom).

### Kinetic Model for Energy Transfer

Both steady state and time-resolved experiments suggest that the energy transfer efficiency from the dendrons to the trap is nearly unity. To understand the mechanism of this process and the effect of the electronic structure of the backbone, we must estimate the rate of energy transfer for each individual step. In this section, we propose a model to understand that process through an interpretation of our time-resolved emission data.

We consider the simplest case in which D is the ground state of the backbone, D\* is the initially excited state and E\* is the emissive state of the backbone:



According to this model, the  $500 \pm 40$  fs ( $k_1^{-1}$ ) rise time measured from 2G2-m-OH must be attributed to one of the two possibilities. Either the emissive state of the backbone is different from the state that is excited initially, or the initially excited state undergoes a conformational rearrangement before emitting. The insensitivity of the rise time to pump wavelength indicates delocalization of the optical excitation within the backbone prior to relaxation.

*Meta* substitution prevents the exciton from delocalizing between the backbone and the Eper unit.<sup>127</sup> Since the *meta* substitution in the core ring breaks the  $\pi$ -conjugation, we consider that the delocalization occurs within each monodendron.

The addition of the EPer trap results in a new final excited state  $P^*$ . Emission from the 2G<sub>2</sub>m-Per arises from the  $P^*$  and the backbone state  $E^*$ , depending on detection wavelength. This leads to two possible deactivation pathways for the initially excited state: direct,



or indirect,



Measurements of the 2G<sub>2</sub>-m-OH fluorescence probe the  $E^*$  state directly, whereas experiments with the 2G<sub>2</sub>-m-Per probe either the EPer emission ( $P^*$ ) when detection is at

$\lambda = 485$  nm or the backbone emission ( $E^*$ ) from 2G<sub>2</sub>-m-Per for early-time detection at  $\lambda = 435$  nm.

By solving the kinetic system of equations, we can obtain the population of each excited state with only 2 free parameters in the fitting function ( $k_2$  and  $k_3$  are free, while  $k_1$  is defined by the previous fitting to data in Figure 4-3). The backbone excited state population is given by:

$$E^*(t) = \frac{k_1}{k_2 - (k_1 + k_3)} \times \left[ e^{-(k_1 + k_3)t} - e^{-k_2 t} \right] \quad (4-4)$$

The population of the trap excited state ( $P^*$ ) includes two components, indirect (energy goes through the  $E^*$  state)

$$P_I^*(t) = \frac{k_1 k_2}{(k_2 - k_1 - k_3)} \left\{ \frac{-e^{-(k_1 + k_3)t}}{k_1 + k_3} + \frac{e^{-k_2 t}}{k_2} \right\} + \frac{k_1}{k_1 + k_3} \quad (4-5)$$

with  $(k_1 + k_3)^{-1}$  and  $(k_2)^{-1}$  as characteristics times, and direct

$$P_D^*(t) = \frac{-k_3}{k_1 + k_3} e^{-(k_1 + k_3)t} + \frac{k_3}{k_1 + k_3} \quad (4-6)$$

with  $(k_1 + k_3)^{-1}$  as the characteristic time.

The fluorescence lifetimes of  $E^*$  and  $P^*$  are on the order of ns (see Table 4-1), appearing only as a constant offset in the model. The pre-exponential factors are defined in terms of the rates (equations 4-5 and 4-6), and the relative amplitudes of the contributions for each transfer channel are given by  $k_1$  and  $k_3$ . The results are shown in Table 4-2.

To fit the data for different excitation wavelengths, we consider the relative contribution to the absorption from the EPer unit and/or backbone at, for example  $\lambda = 420$  nm. Allowing this relative contribution to become a free fitting parameter, we obtain

from the time-resolved data that  $\sim 70\%$  contribution is from straight excitation of EPer and only  $\sim 30\%$  contribution is from the excitation via energy transfer from backbone dendrons.

Table 4-2. Fits for Time-Resolved Fluorescence Data

$\lambda_{\text{exc}}$	$\tau_1^{\&\#}$ (fs)	$\tau_2$ (fs)	$\tau_3$ (fs)	Direct %	Indirect %
340 nm	$510 \pm 20$	$755 \pm 60$	$440 \pm 45$	54	46
380 nm	$540 \pm 30$	$855 \pm 60$	$305 \pm 20$	64	36
420 nm	$500 \pm 35$	$550 \pm 150$	-	-	-
465 nm	$150 \pm 20$	-	-	-	-

<sup>&</sup> Time constants ( $\tau_i$ ) for  $E^* \rightarrow P^*$  are obtained from the time-resolved fluorescence measurement of 2G<sub>2</sub>-m-OH and kept constant when fitting the 2G<sub>2</sub>-m-Per data.

<sup>#</sup> Errors correspond to  $\pm 2\sigma$

Excitation at 340 and 380 nm (panels *d* and *c* in Figure 4-4, respectively) shows different dynamics with longer rise times. At these wavelengths, there is no direct excitation of EPer and the emission is solely due to energy transfer from the backbone to the trap through both direct and indirect paths. This was proven by exciting 2-phenylethynyleneperylene in CH<sub>2</sub>Cl<sub>2</sub> at the selected wavelengths and obtaining no emission at 485 nm. Excitation at 340 nm yields the one step energy transfer (Dir) from the initially excited state with  $k_3^{-1} = (440 \pm 45)$  fs, and the indirect energy transfer (Ind) (two steps) with  $\tau_1 = (510 \pm 20)$  fs (determined from the 2G<sub>2</sub>-m-OH data) and  $\tau_2 = (755 \pm 60)$  fs ( $\tau_2$ ). The relative contribution from each path can be evaluated as

$$\text{Ind.} = \frac{k_1}{k_1 + k_3} \quad \text{and} \quad \text{Dir.} = \frac{k_3}{k_1 + k_3} \quad (4-7)$$

The results of this procedure suggest that 54% of energy accepted by the EPer is attributed to the direct path, while the contribution from the indirect, multistep pathway is 46%.

At 380 nm, the fit yields a faster rate for the direct path,  $\tau_3 = (305 \pm 20)$  fs. At this pump wavelength, the contributions from the direct and indirect channel are 64% and 36%, respectively. As the initially excited state becomes closer to resonance with the EPer transition, the contribution from the direct energy transfer pathway is more pronounced. This kinetic model reveals that for the indirect channel, the slowest step is the energy transfer from the relaxed excited state of the donor ( $E^*$ ) to the acceptor ( $P^*$ ).

A confirmation of the presence of the indirect channel is shown in Figure 4-5. This figure presents the data collected at 435 nm, a frequency at which there is residual emission from the backbone. In this case, the fast rise and decay times of the fluorescence can be predicted from the fixed values of  $\tau_1$  (from Figure 4-3) and  $\tau_2$  and  $\tau_3$ , from Figure 4-4 (including a ns component corresponding to 2G<sub>2</sub>-m-OH emission lifetime). The agreement between predicted and experimentally measured data is excellent. The rise of the signal is due to  $(\tau_1^{-1} + \tau_3^{-1})$  and its decay is given by  $\tau_2$ , thus it is the energy transfer process to the acceptor EPer that controls the fast decay of donor fluorescence.

Comparison of absorption with photoluminescence excitation spectrum indicates that the efficiency of energy transfer for the molecule investigated here is close to unity. When the energy transfer efficiency is near unity, measurement of the quantum yield comparing steady state excitation and absorption is not as accurate as using time resolved techniques. We compare the energy transfer rate (in this case from the experimental rise

time in the acceptor ( $k_{ET}^{-1}$ ) with the donor's fluorescence lifetime in the absence of the acceptor ( $\tau_o$ ) using

$$\phi_{ET} = \left[ 1 + \frac{1}{k_{ET} \tau_o} \right]^{-1} \quad (4-8)$$

where  $\phi_{ET}$  is the energy transfer quantum yield. Considering 2G<sub>2</sub>-m-OH as the donor and the EPer as the acceptor, we obtain a  $\phi_{ET} > 0.99$  which is in reasonable agreement with the value of  $\phi_{ET} \sim 0.94$  obtained from steady state measurements.

### Energy Transfer in the Weak-Coupling Limit

Mukamel and co-workers' calculations using the Frenkel exciton model<sup>127</sup> assume that *meta* substitution confines the electron-hole pair (exciton). The possibility of evaluating the coherent coupling between monomers in the 2G<sub>2</sub>-m-Per is somewhat hindered by the delocalization expected through *ortho* substituted segments. In the unsymmetrical dendrons, the *ortho* substitution is expected to have qualitatively similar characteristics as *para* substitution and thus the electron-hole pair is expected to be delocalized within each monodendron. The *meta* substitution at the core does not allow the exciton delocalization to go beyond the central phenyl group, and the exciton is confined to individual monodendrons.

Once the excitation is created, it can migrate via two pathways (direct or indirect) towards the bottom of the energy funnel. Since both donor and acceptor have allowed optical transitions with strong oscillator strength, the largest contribution to the coupling will be due to Coulombic interactions. The magnitude of the Coulombic coupling can lead to incoherent exciton migration for weak interactions or coherent exciton transfer for strong interactions.

Energy migration can be interpreted using the simplest model (Förster) that invokes very weak coupling between two point dipoles.<sup>143</sup> The “point-dipole/point-dipole” coupling approximation is valid when the donor-acceptor separation (R) is much larger than the dipole sizes. The very weak coupling is valid when the homogeneous vibronic bandwidth is larger than the dipole-dipole coupling. For the dendritic macromolecule under investigation, we evaluate the validity of each of these conditions independently.

The excitation transfer rate in the weak-coupling limit can be calculated from<sup>144</sup>

$$k_{ET} = \frac{4\pi^2}{h^2 c} J |V|^2 \quad (4-9)$$

where  $V$  is the coupling and  $J$  is the vibronic spectral overlap integral between donor and acceptor (in units of cm). The spectral overlap is a measure of the density of interacting initial and final states. The accurate calculation of the overlap integral employs the homogeneous vibronic bandwidths. Since the homogeneous bandwidths of the vibronic bands in the di-dendron are unknown, we rely on absorption and emission spectra to obtain  $J$ . The spectral density can be evaluated by using a normalized absorption spectrum -acceptor,  $a(\lambda)$ -, and normalized emission spectra –donor,  $f(\lambda)$ -,

$$J(cm) = \int_{\lambda_i}^{\lambda_f} f(\lambda) a(\lambda) \lambda^2 [nm] 10^{-7} d\lambda, \quad (4-10)$$

yielding  $J = 2.02 \times 10^{-4}$  cm.

An experimentally measured transfer rate  $k_{ET} = (750 \text{ fs})^{-1}$  yields an interaction energy  $V = 75 \text{ cm}^{-1}$ . The approximation on the  $J$  calculation results on an upper limit for  $J$  and therefore, for a given experimental rate, a lower limit of the Coulombic interaction.

Donor and acceptor spectra in the 350 nm - 450 nm (28,600 $\text{cm}^{-1}$ -22,200  $\text{cm}^{-1}$ ) range are very broad. Measuring single-molecule fluorescence, Schryver and co-workers<sup>145</sup> estimated vibronic bandwidths between 650-850  $\text{cm}^{-1}$ . Even though this number might be an overestimation of the true homogenous bandwidth, it is still very large compared to the small Coulombic interaction energy, endorsing the use of the very weak coupling model.

To understand the role of the dipole size, we again assume the Förster model and compare the result of this model with the experimental values. The critical radius  $R_0$  (the distance at which emission and energy transfer occur with equal probability) for the energy transfer step between monodendrons excited state  $E^*$  and phenyl ethynylene perylene excited state  $P^*$ , can be evaluated from

$$R_0 = 0.2108 \left[ \frac{\kappa^2 \Phi_D}{n^4} \int_0^\infty f_D(\lambda) \varepsilon_A(\lambda) \lambda^4 d\lambda \right]^{1/6}, \quad (4-11)$$

where  $\kappa^2$  is the orientation factor ( $\kappa_{\text{avg}}^2 = 2/3$ ),  $\Phi_D$  is the fluorescence quantum yield of the donor in the absence of the acceptor,  $n$  is the index of refraction of the solvent (1.4 for  $\text{CH}_2\text{Cl}_2$ ),  $f_D(\lambda)$  is the normalized fluorescence spectrum, and  $\varepsilon_A(\lambda)$  is the molar extinction coefficient of the acceptor. The overlap integral (in units of  $\text{cm}^6/\text{mol}$ ) is evaluated by taking the normalized emission spectrum of 2G<sub>2</sub>-m-OH and the absorption extinction coefficient of phenyl ethynylene perylene. With these parameter values, we find  $R_0 = 44.25 \text{ \AA}$ .

Molecular Dynamic simulations on these macromolecules provide information about the 3-D architecture of the di-dendrons (see Figure 4-1c). Despite what a 2D chemical structure sketch might suggest, the unsymmetrical dendrimers are not planar.

The 3D conformation has a somewhat rigid Y shape with only the peripheral phenyl groups rotating almost freely around the ethynylene bonds. These MD simulations allow the evaluation of the moieties' sizes, yielding  $\sim 15.5$  Å for the monodendron and  $\sim 13.5$  Å for the phenyl ethynylene perylene. The distance between the center of each monodendron and the center of the phenylethynylene perylene unit is  $\sim 17.2$  Å. If we consider that the size of monodendrons will be on the order of the dipole size, we would expect an energy transfer rate constant of  $(6.5 \text{ ps})^{-1}$ . Experimentally, the energy transfer rate constant is  $(750 \text{ fs})^{-1}$ , clearly indicating that the Förster model cannot account for this fast process. The disparity in the calculated versus measured rates is due to the sizes of the chromophores, which are very similar to the dipole-dipole distances. In a point-dipole description, the dipole is assumed to be located at the “spatial” center of each dendron. A point-dipole approximation does not account for the transition dipole density distribution which becomes an important factor when dipoles are in close proximity.<sup>128</sup>

A better treatment of the Coulombic coupling must include at least the transition dipole shape and distribution, and can be performed using the Transition Density Cube method,<sup>19,146</sup> which provides a numerical approximation to the complete Coulombic coupling.

### **Vectorial Energy Transfer in Unsymmetrical PE Dendrimers**

The cascade energy transfer is proposed to explain trap fluorescence spectra following excitation of different chromophores embedded in dendrimers. To the best of our knowledge, all evidence of the existence of energy cascades are steady state measurements providing only indirect support for the presence of the cascade. In this chapter and Chapter 3, we present a direct experimental measurement of energy migration as it goes through an intermediate state in a funnel-type dendritic structure.

Direct confirmation of the presence of the energy gradient can be obtained by following the energy as it migrates through the individual energy steps down the gradient. The process of rise and decay of the intermediate state population is followed by measuring the temporal evolution of the fluorescence at the emission wavelength of the intermediate state. This method provides an unequivocal proof of the vectorial nature of the energy transfer in a ladder-type structure.

Time-resolved fluorescence measurements of the dendrimer with and without the final energy sink led us to the 3 state (ladder) kinetic model shown in Figure 4-8.<sup>132</sup>

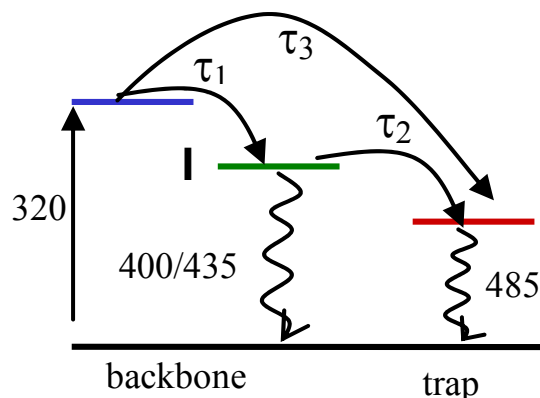


Figure 4-8. Model describing the energy ladder. The intermediate state (I) is detected at 400 nm or 435 nm. Emission from trap is at 485 nm.

The two time constants involved in the cascade process are  $\tau_1=300$ fs and  $\tau_2=350$  fs for the  $2G_1$ -mPer and  $\tau_1=510$  fs and  $\tau_2=755$  fs for  $2G_2$ -mPer. While the model for  $2G_1$ -mPer contains only the ladder mechanism, the  $2G_2$ -mPer data shows that half of the energy transfer process occurs through the ladder process, and the other half proceeds through a direct process ( $\tau_3\sim 440$  fs). The relative contributions of these two pathways have a slight dependence on excitation wavelength.<sup>132</sup>

Noteworthy in the model is the prediction of an intermediate state (I in Figure 4-8) consisting of a low-energy state of the backbone. The presence of this state leads to

efficient energy transfer after excitation at 320 nm by creating a ladder-type electronic structure which causes the vectorial energy transfer.

The model predicts that the intermediate step in the ladder-type system corresponds to the lowest-lying excited state of the backbone. Detection of fluorescence at this wavelength (400 nm and 435 nm for the 2G<sub>1</sub>-mPer and 2G<sub>2</sub>-mPer, respectively) provides direct confirmation of the cascade mechanism. As predicted, Figure 4-9 (circles) shows the data obtained after excitation at 320 nm. For both molecules, the fluorescence shows a fast rise time (though slower than our instrument response function), and a slower decay. If the model is correct, one should be able to simulate the data directly without requiring additional fitting parameters. Using the model obtained in the independent measurements of the trap fluorescence, we simulate the population transfer through this intermediate state. The convolution of the intermediate state populations with the IRF yields the solid curves in Figure 4-9.

The simulation shows excellent agreement with the experimental data obtained from the intermediate state. Note that the only variable in this simulated curve is the normalization constant ( $F_{\max}$ ). Both the decay times and the pre exponential factors are modeled as

$$F(t) = \frac{1}{F_{\max}} \left( \frac{k_1}{k_2 - (k_1 + k_3)} \times \left[ e^{-(k_1 + k_3)t} - e^{-k_2 t} \right] \right) + \text{constant} , \quad (4-12)$$

where  $k_1 = (\tau_1)^{-1}$ ,  $k_2 = (\tau_2)^{-1}$ , and  $k_3 = (\tau_3)^{-1}$  are extracted from the model and the constant corresponds to the 1.8 ns emission lifetime of 2Gn-mOH present in the sample as an impurity. Since the quantum yield for energy transfer is  $> 0.96$ , the emission from the

backbone in the presence of the sink is not observed in the steady state emission spectra, as it can only be detected only by using an extremely fast (<6 ps) time window.<sup>‡</sup>

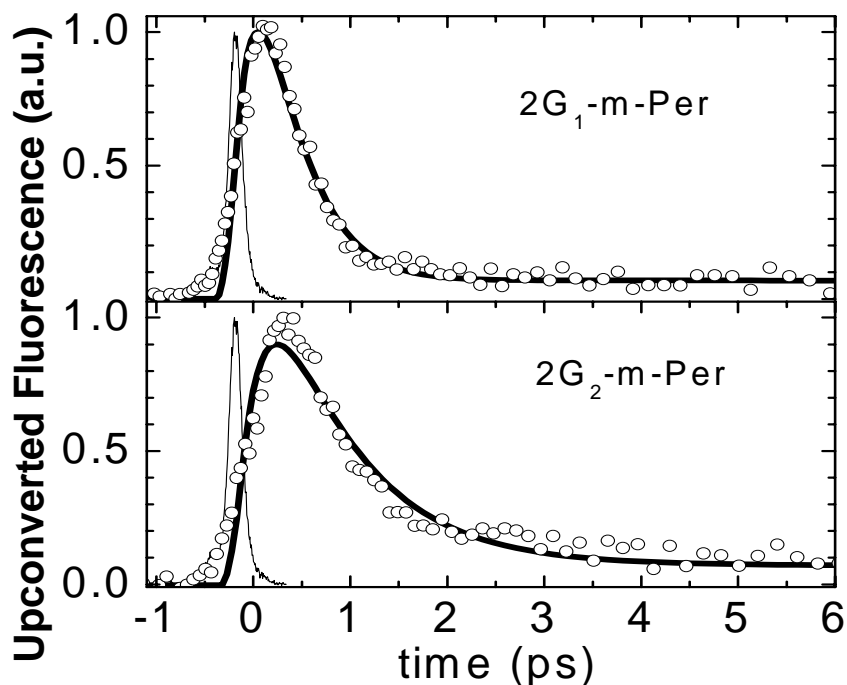


Figure 4-9. Temporal evolution of the intermediate state population followed by fluorescence up-conversion. The solid line corresponds to a simulation of the population of the excited state. The IRF is also plotted.

According to the experimental data and modeling, the cascade mechanism is present for both generations whereas the direct path is available for the generation 2 dendrimer. The energy transfer through a cascade manner and direct channel will be competing processes, but they also create a complete funnel in terms of transferring the excitation energy to a single acceptor. Despite the fact that  $2G_1$ -m-Per molecule is a less complete funnel, it transfers the energy faster than the  $2G_2$ -m-Per molecule. This is due to the relatively shorter distances between the donor (longest chain 3-ring PE unit) and EPer acceptor.

<sup>‡</sup> The purity of the sample is checked by TLC yielding better than 98% purity. Our spectroscopic methods are more sensitive than that. The limit of our emission spectrum sensitivity is ~0.5% for the concentration of  $2G_2$ -m-OH in a  $2G_2$ -m-per solution with the O.D. used in the experiment.

## Conclusions

We measured the fluorescence dynamics of a phenylethynylene di-dendron with and without an energy trap. The fast transfer dynamics yields a highly efficient light-harvester, with a subpicosecond time scale for energy transfer.

Based on steady state spectroscopy, initial studies of unsymmetrical architectures suggested that the electronic structure could be interpreted as the addition of individual building blocks. The time-resolved data presented in this work suggest that the building blocks encompass each monodendron with two possible pathways for exciton migration. The presence of a combination of *ortho* and *para* substitution leads to initial exciton delocalization within each monodendrons and the *meta* substitutions confine them there. The electronic structures of the monodendron and the trap are weakly coupled, though a more complete characterization of dipole size and shape is required to accurately simulate the transfer rates.

Linear symmetric dendrimers with phenyl ethynylene units of variable length<sup>69</sup> show energy gradients due to the localization of excitons on the different length PE units. For unsymmetrical dendrimers, the *ortho* and *para* substitutions suggest a complete initial delocalization within the monodendrons. In the 2G<sub>2</sub>-m-OH system, delocalization is found in the initially excited state as all results are independent of excitation wavelength. After excitation, a change in the excited state surface leads to localization and the formation of an energy gradient. This excited state energy gradient yields efficient multistep energy transfer in the 2G<sub>2</sub>-m-Per macromolecule. Roughly 50% of the energy transfer occurs through a multistep pathway, but the process is still completed in a subpicosecond timescale. We present here the first direct measurement of cascade energy transfer in phenyl ethynylene dendrimers. The presence of gradients makes it possible to

use larger dendrimers for light-harvesting where the intermediate states in the cascade process allow for efficient, unidirectional energy transfer.

## CHAPTER 5 ENERGY TRANSFER IN SYMMETRICAL PE DENDRIMER: NANOSTAR

Some judiciously designed phenylene ethynylene (PE) dendrimers demonstrate highly efficient and unidirectional energy transfer properties.<sup>69,95</sup> In chapters 3 and 4, the unsymmetrical PE dendrimers which include variable length of PE segments were investigated to explore the excitation energy dynamics. It was shown that the coupling among PE units occurs through para and ortho substitutions, and this leads to rapidly growing conjugation lengths as the generation number increases. Therefore, the most novel characteristic of PE dendrimers arises from the branching pattern at each generational node. As opposed to unsymmetrical dendrimers, subsequent generations are bonded at the phenyl group in meta positions in symmetrical dendrimers. This arrangement plays a crucial role in the excited state electronic structure of the dendrimers. Two series of symmetrical dendrimers have been synthesized in Moore's group. They differ in the number of PE units between consecutive branching points and were described as "compact" and "extended". In compact ones, each generational unit is composed of identical diphenylacetylene (DPA) chains. Compact dendrimers exhibit disruption of  $\pi$ - conjugation because of meta branching and they do not exhibit energy funneling due to the equal chain lengths. In the extended dendrimers, the localized excitations between meta branching points are comprised of varying excitation energies which correlate inversely with chain length. Thus, extended dendrimers serve as energy funnels directing energy towards the dendrimer focal sites.

As shown earlier, the most novel characteristic of these PE dendrimers arises from the branching pattern. While branching at para positions grows linear chains, branching only at ortho positions terminate the tree structure due to steric hindrance. The meta substitution allows a large degree of orientational flexibility and minimizes the steric hindrance between neighboring units. More importantly, the meta substitution plays a big role in the excited state electronic structure of the PE dendrimers.

The work described in this chapter is based on an extended phenylene ethynylene dendrimer known as the “nanostar” where an ethynylene perylene trap acts as an exciton trap, collecting the photoexcitations initially deposited anywhere in the dendrimer. The nanostar has a built-in energy gradient which is engineered by linking chromophore units of increasing length (2-, 3-, and 4-ring) towards the ethynylene perylene trap. This gradient provides a way of overcoming entropic effects and decreases the probability of energy dissipation to the environment.

The early experiments on the nanostar showed that the efficiency of excitation energy transfer from the peripheral groups to the core, monitored via fluorescence measurements, was nearly 100 % efficient. The energy transfer was monitored via fluorescence measurements. Using time-correlated single photon counting, Swallen et al. determined an upper limit of about 10 ps for the energy transfer from the lowest energy chromophore (4-ring) to phenylethynylene perylene trap.<sup>130</sup> For excitation at the periphery chromophores (2-ring), an upper limit of 270 ps trapping was estimated. Further experiments by Kleiman et al. investigated this energy funneling process in the nanostar for the first time with femtosecond time-resolution.<sup>75</sup> Degenerate pump-probe spectroscopy was used to preferentially measure the transients of the 2-ring and 3-ring

chromophores. A stepwise energy transfer was revealed from shorter to longer PE units. It was concluded that some of the steps in the energy transfer occurs on a subpicosecond time scale. The goal of their study was to explore the nature of excitations and degree of localization/delocalization as well as the mechanism of energy transfer. Key points are the experimental energy transfer rates and the understanding of the conjugation pattern at the branching point of the dendrimer.

Both theoretical and experimental work done so far aimed to clarify the nature of excitations and extent of coupling associated with energy transfer mechanism within these dendrimers. However, to our knowledge, the experimental investigations so far did not answer the question of whether the excitations at the periphery migrate to the ethynylene perylene through intermediate states or there are direct jumps from the periphery to the trap. In other words, are there direct and indirect energy transfer paths between the initially excited chromophores and ethynylene perylene trap?

In this chapter, we examine the nanostar molecule extensively using femtosecond time-resolved experiments. We present time-resolved fluorescence and broadband absorption studies. Our goal is to record the energy transfer process by varying the excitation energy and monitoring absorption transients and emission dynamics. The results indicate the presence of intermediate steps through the funneling process and direct paths from the initially excited states to the emitting step. Experiments show a slow trapping time for the excitation at the peripheral chromophores, while much faster transfer times are measured for 3 and/or 4 ring chromophores. The time-resolved emission detected both at the trap fluorescence and donor fluorescence wavelengths give consistent results and prove the presence of direct jumps within the cascade.

Another challenging issue with dendrimers is determination of the geometry of the molecule that can cause large variations in energy transfer properties.<sup>19,81</sup> Our collaborators Krause and Roitberg groups at UF have recently performed large scale molecular dynamics (MD) simulations for the nanostar to obtain structural information.<sup>74</sup> The interparticle interactions were modeled with an MM3<sup>147-149</sup> force field (TINKER, version 3.9) for the minimization and subsequent dynamics simulation. They found that while the overall structure of the nanostar is rigid, the phenyl rings not involved in branching are free to rotate around the ethynylene bonds. The distribution of torsion angles for the center ring of the three-ring chromophores was calculated at two different temperatures, 10 K and 300 K. The results indicated that the rings lie essentially in one plane at low temperature whereas they rotate freely at room temperature. This change in geometry was proven to have a significant effect on the transition density, and hence energy transfer rates.<sup>74</sup>

### **Materials and Methods**

The synthesis of the nanostar has been described elsewhere<sup>34,35</sup> and its chemical structure is shown in Figure 5-1. For the spectroscopic measurements, the sample is dissolved in dichloromethane where there is no excimer formation. The optical density used for transient absorption and fluorescence measurements is about  $0.3 \text{ mm}^{-1}$ . The steady state absorption of the sample was compared before and after measurement. Steady state characterization is performed via UV-Vis absorption (Varian-Cary 100) and emission in a Jobin-Yvon instrument (Spex Fluorolog-3). The laser system, fluorescence upconversion and transient absorption setup were described in detail in Chapter 2. Here we give a brief description of experiments performed.

## Transient Absorption

Absorption difference spectra are recorded with a homemade pump-probe apparatus, described in detail in Chapter 2. In brief, the output of Ti-Sapphire Regenerative Amplifier (1kHz, 800 nm, and 60 fs pulses) is used to pump an optical parametric amplifier (OPA, Spectra Physics). Pump beams at UV region with tunable central frequency in the UV region are produced in an OPA via fourth harmonic

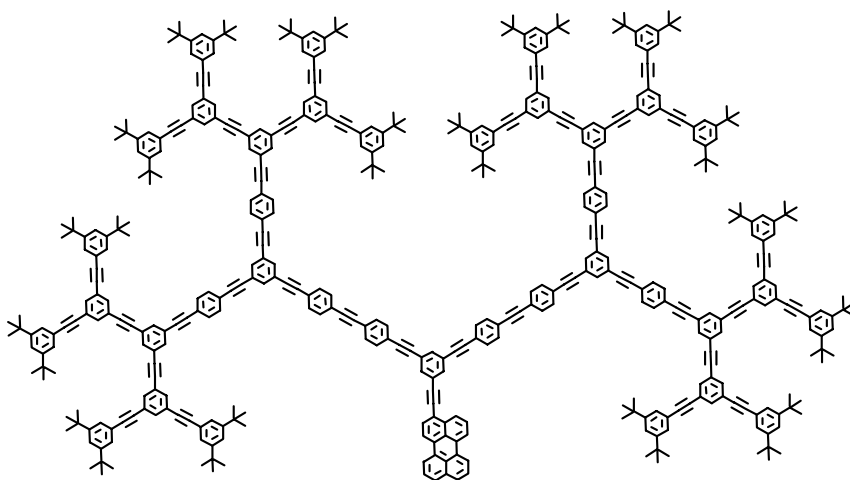


Figure 5-1. Chemical structure of nanostar dendrimer (2 dimensional sketch).

generation of the signal. Prism compression is used to reduce the pulsewidth of these UV-pulses. The excitation beam is focused on a spot with 300  $\mu\text{m}$  diameter. The energy of excitation is 30 nJ/pulse upon UV excitations. Broadband probe and reference beams are generated via focusing a small fraction of amplifier output on a 1mm  $\text{CaF}_2$  plate. Using a thin-film polarizer, the probe light polarization is oriented 45 degrees with respect to the pump pulse. After passing through the sample, a Glan-Taylor polarizer splits the probe beam into its polarization components, parallel and perpendicular with respect to the pump, allowing for the simultaneous detection of both polarizations. Pump

induced absorption changes of both probe polarization components are measured as a function of pump-probe time delay by modulation of the pump beam with a mechanical chopper and detection of the probe and a reference beams using a CCD camera equipped with a 30 cm spectrograph. The time resolution is typically 150 fs (for 310 nm, the time resolution is around 200 fs).

The data are corrected for white light group velocity dispersion and fitted globally including the convolution with the instrument response function. The optical path of samples is 2 mm and the sample is stirred with a magnet in order to refresh the sample from shot to shot. The integrity of the sample was checked before and after each set of measurements.

### **Time-resolved Emission**

Time-resolved fluorescence emission spectra are recorded with a home-built Fluorescence Upconversion setup described in detail in Chapter 2. Briefly, the pump pulses are generated within the OPA. The excitation wavelength is 310 nm, and the emission from the intermediate state of the donor and the final acceptor are detected at 380 nm and 485 nm, respectively. The gate beam is a residual 800 nm beam from the OPA. The excitation energy is 30 nj/pulse and the excitation beam is focused on a spot with 200  $\mu\text{m}$  diameter. Fluorescence is collected at magic angle with respect to the polarization of the excitation beam. The sample is placed in a spinning cell with optical path of 1 mm. The time resolution of the system is measured by detection of cross-correlation of scattered light from solvent and gate pulse. It is about 250 fs for the 310 nm excitation pump pulse (even though prism compression is used, it is hard to compress UV pulses due to much narrower bandwidth).

### Steady State Spectroscopy

The absorption and emission spectra of the nanostar in dichloromethane at room temperature is shown in Figure 5-2. The emission is almost entirely from the ethynylene perylene trap, indicating 98 % efficient excitation energy transfer.<sup>86</sup> Theoretical and experimental studies assign the peaks/shoulders near 310 nm, 352 nm, and 372 nm to the vibrationless excitonic bands of 2-, 3-, and 4- ring linear chromophores, respectively.<sup>72,75,76,86,150</sup>

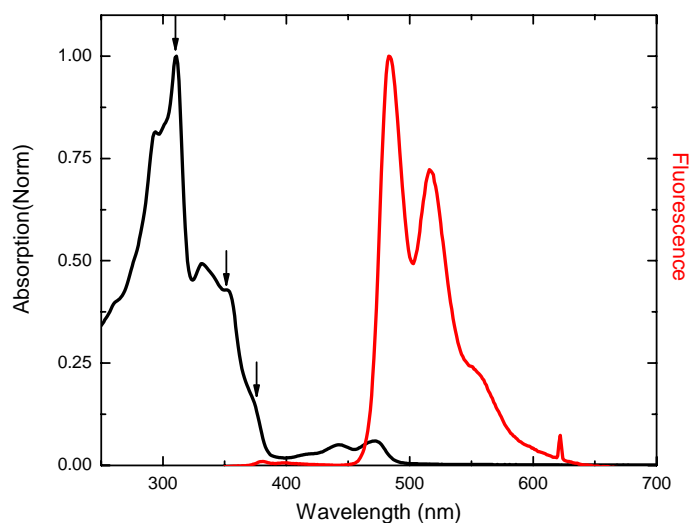


Figure 5-2. Absorption and emission spectrum of nanostar in DCM at room temperature. Arrows represent the peaks/shoulders at 310 nm, 352 nm and 372 nm.

The absorption data for all ethynylene perylene substituted dendrimers are spectrally identical to their unsubstituted dendrimer parents, with an additional absorption peak around 450 nm due to perylene moiety. Here, this indicates that phenylethynylene perylene unit has a well localized excited state, and does not perturb the electronic structure of the dendritic backbone. The high energy peak in the absorption spectrum of the nanostar at 310 nm is due to DPA chains found at the periphery of the molecule. The

longer PE chains in the interior of the molecule give rise to well-defined lower energy peaks. In order to investigate the idea of electronically decoupled PE units, due to meta conjugation, the absorption spectrum of each PE unit (2-, 3-, 4- ring) are measured and its sum is compared with the nanostar absorption. Figure 5-3a shows the absorption spectrum of independent free 2-, 3-, 4- ring PE units. The addition of these spectra, normalized to their relative number present in the nanostar, is shown in Figure 5-3b together with the experimental nanostar spectrum. These two spectra are remarkably similar. The only difference is a 12 nm overall shift, probably due to a local change in the solvent's dielectric constant. By comparing the features of individual PE rings' spectra to the features in the sum, it is reasonable to assign the region peaked at 310 nm to 2-ring absorption, the 352 nm shoulder to mostly 3-ring absorption, and 372 nm shoulder to 4-ring absorption. This can be confirmed by measuring the low temperature (10K) absorption spectrum of the nanostar.\* As shown in Figure 5-3c, the low temperature absorption spectrum of the nanostar has sharp bands corresponding to the planar configurations of the 2-,3-, 4-ring units. Altogether, these spectra reveal that in the ground state the 2-, 3-, 4-ring units are electronically decoupled.

### **Transient Absorption Spectroscopy**

Time-resolved transient difference absorption spectra of nanostar and its individual components are measured. Our aim is to compare the dynamics of individual components with the vectorial energy transfer dynamics in the nanostar. The broadband transients of the nanostar are measured after excitation at 310, 352, and 372 nm, as indicated by arrows in Figure 5-2. These wavelengths are chosen to excite preferentially the 2-ring, 3-

---

\* Personal communication from Joseph S. Melinger from Naval Research Labs

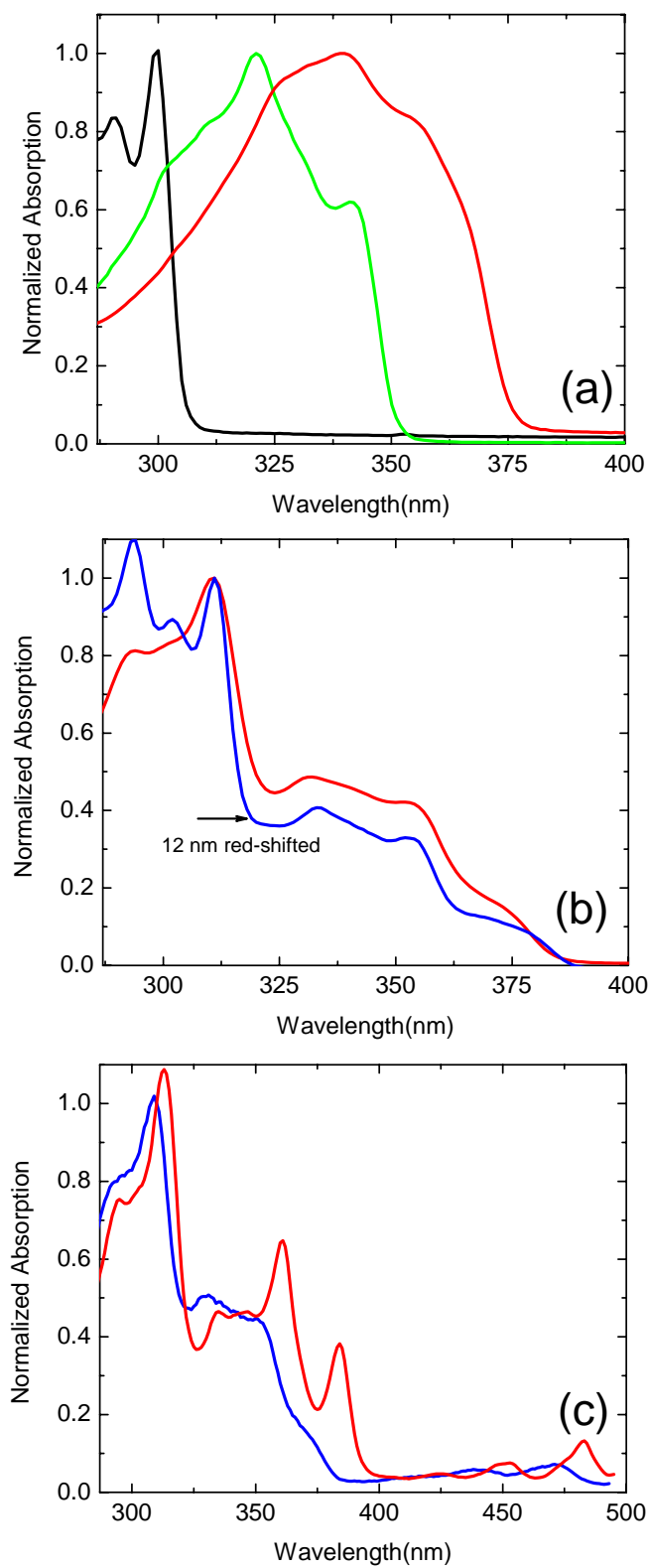


Figure 5-3. Normalized absorption spectrum of (a) 2-ring (black), 3-ring (green), and 4-ring (red) PE units (b) Nanostar absorption (red) and sum of rings' absorption at 298 K (c) nanostar absorption at 298 (blue) and 10 K (red).

ring, and 4-ring chromophores. However, the excitations are not highly selective due to overlap of vibronic transitions associated with the next longest chromophore species as shown in Figure 5-3. Results obtained from the nanostar are compared with those of model compounds: DPA excited at 305 nm and phenylethynylene perylene excited at 400 nm.

### **Model Compound DPA**

The highest peak in the absorption spectrum of nanostar at 310 nm is mostly due to absorption of peripheral 2-ring chromophores. To discuss the dynamics of the nanostar when excited at 310 nm, it is extremely informative to look into the excited state dynamics of diphenylacetylene (DPA) monomers. Hirata et al. investigated photophysical properties of DPA in various solvents by picosecond time-resolved absorption measurements.<sup>151</sup> When DPA in n-hexane was excited at 295 nm, a short-lived absorption band at 500 nm was attributed to the higher excited singlet state  $S_2$ . It was concluded that the emitting state of DPA was not the lowest excited singlet state but the short-lived  $S_2$  state. The lifetime of  $S_2$  state was estimated to be about 8 ps. Thus,  $S_2$  state is initially populated and it can return to the ground state through mainly nonradiative relaxation, or undergo internal conversion to  $S_1$  state. Then a triplet state  $T_1$  is formed via the intersystem crossing from  $S_1$  with a time constant of about 200 ps. In this chapter, we present the spectral and temporal evolution of DPA in dichloromethane after excitation at 305 nm (Figure 5-4). The steady state fluorescence spectrum peaked at 325 nm is also shown for comparison. Figure 5-4 shows very little stimulated emission starting at 320 nm and a very broad phototoinduced absorption band around 410-450 nm. This band can be assigned to a  $S_n \leftarrow S_1$  transition of DPA with a lifetime of 200 ps. At 500 nm, there is

a well distinguished photoinduced absorption band decaying with an 8 ps lifetime. This is in well agreement with the previously measured lifetime of  $S_2$  state shown by Kleiman et al.<sup>75</sup>

In Figure 5-4, bottom panel, we present the dynamics at three particular wavelengths to understand better the DPA data. In the 320-330 nm region, the initial stimulated emission

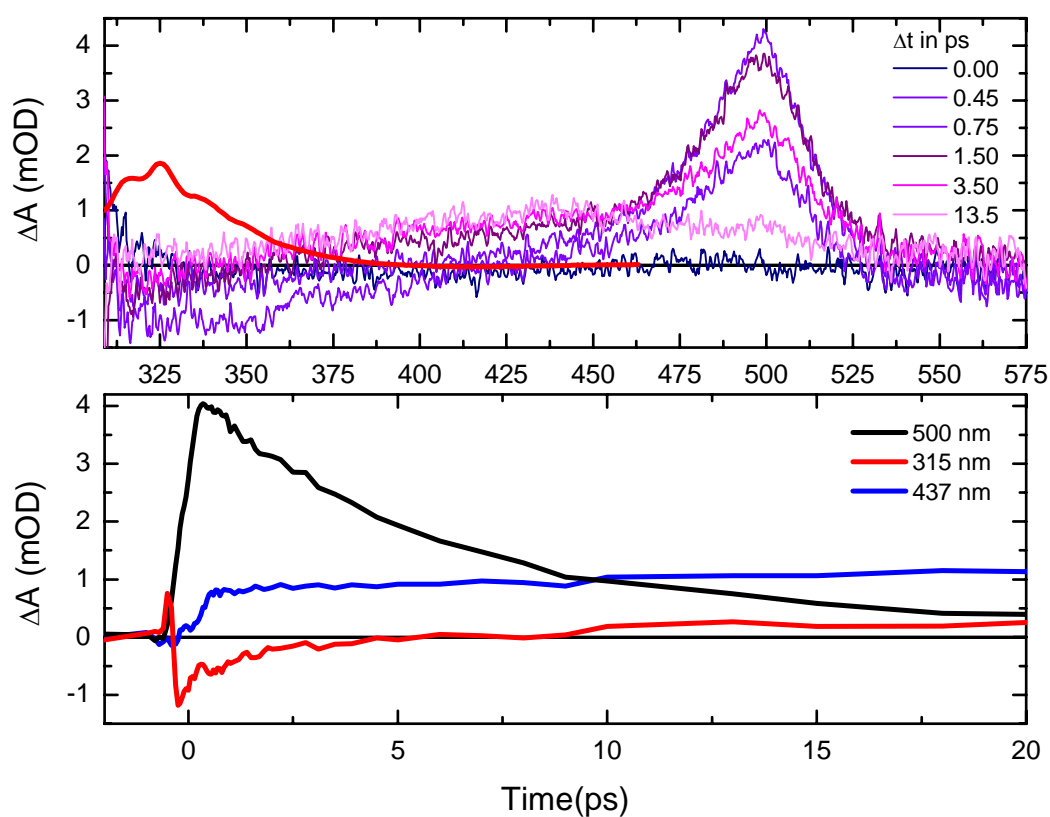


Figure 5-4. Transient absorption spectrum of model compound DPA(top), transient absorption signal as a function of time recorded at 3 different wavelengths: 315 nm (red), 473 nm (blue), 500 nm (black) (bottom).

(decreased absorption) is observed. In the 432-442 nm region, we observe the photoinduced absorption (PIA) which has a very long (hundreds of picoseconds) decay time, and finally the averaged signal between 495 and 503 nm shows the photoinduced

absorption of the  $S_2$  state with an 8 ps decay time. We will try to compare the dynamics of DPA with the nanostar dynamics when excited at 310 nm where 2-ring chromophores are excited initially.

### **Model Compound Phenylethynylene Perylene**

It was proven that the energy gradient inherent in the structure of nanostar is sufficient to supersede the entropic bias towards the periphery and absorbed light-energy is efficiently funneled to the perylene moiety.<sup>70</sup> When the excited state lifetime of phenylethynylene perylene is measured following direct excitation, it shows a precise agreement with the nanostar trap moiety. Both nanostar and isolated phenylethynylene perylene decay with a lifetime of 2.2 ns. Thus, the electronic conjugation between the dendrimer backbone and the EPer trap is broken by the meta bonding resulting in localized excitations. The knowledge of excited state dynamics of the isolated phenylethynylene perylene will be a reference point to discuss the energy transfer arising from excitation into dendritic states.

We measure the transient absorption spectra of phenylethynylene perylene in dichloromethane. The excitation wavelength was set to 400 nm and the resulting spectra are shown in Figure 5-5. At positive times, two different components can be observed. A broad positive signal extends from 325 nm to 415 nm. This feature is seen instantaneously after excitation and it decays with a nanosecond time scale. Since this broad signal is positive, it can be attributed to excited state absorption. Steady state absorption shows that the  $S_2$  state of the phenylethynylene perylene absorbs below 350 nm, we attribute this broad PIA to the  $S_n \leftarrow S_2$  absorption.

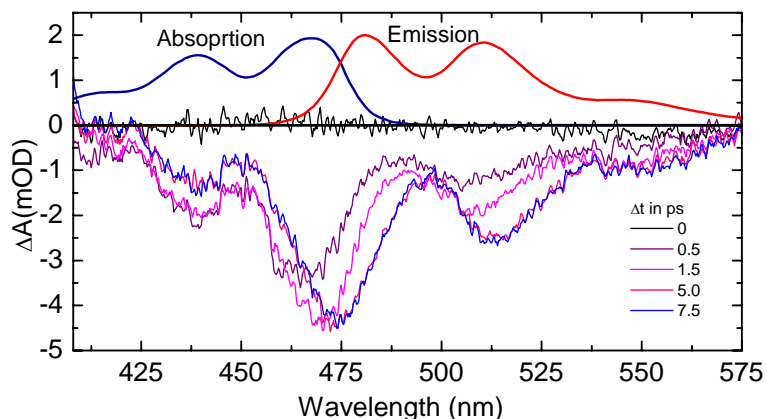


Figure 5-5. Transient absorption spectrum of the model compound phenylethynylene perylene. The steady state absorption and emission spectra are also shown.

A negative signal starting at 415 nm can be also seen following excitation. The steady state absorption spectrum ends at 500 nm and the fluorescence spectrum extends from 450 nm to 750 nm. Thus, the negative signal in the transient absorption spectrum can not solely be associated with ground state bleaching. The negative peak centered at 440 nm corresponds to the bleach signal of the  $1 \leftarrow 0$  vibronic transition of the ground state. The maximum of the negative signal is centered around 475 nm. Since this wavelength is neither at the maximum of the ground state absorption band nor at the maximum of the steady state fluorescence, we assign this peak to the sum of ground state bleaching and stimulated emission. As stated before, the transient signal from phenylethynylene perylene decays mainly on a nanosecond time scale. However, a kinetic analysis of the transient absorption intensities as a function of delay time for wavelengths around 475 nm reveals an additional picosecond relaxation process. The intensity at 465 nm decays with a 2-3 ps time constant as the intensity at 480 nm rises with the same constant. The peak at 510 nm and the shoulder around 550 nm are only due

to stimulated emission since they are further red compared to any ground state absorption band.

### **Nanostar**

To follow the energy migration from the initially excited state on the nanostar backbone to the perylene trap, transient absorption spectra following excitation at different wavelengths are monitored. The excitation wavelengths are selected to be 372 nm (4-ring PE), 352 nm (3-ring PE), and 310 nm (2-ring PE) and are shown as arrows in the absorption spectrum in Figure 5-2.

**372 nm excitation.** The nanostar in dichloromethane is excited at 372 nm with a 100 fs pulse (FWHM). The transient spectra in the 301-582 nm spectral range are shown in Figure 5-6 for several pump-probe delays. The steady state absorption and fluorescence spectra are also shown in the figure. Looking into the absorption spectrum of the 4-ring PE unit and its contribution in the whole nanostar molecule, excitation at 372 nm is mostly resonant with the 4-ring chromophores, the closest chains to the trap. Thus, dynamics associated with this excitation can be directly attributed to the energy transfer from the lowest state of the dendrimer (4-ring chromophore) to the ethynyleneperylene trap.

Looking at the time-resolved data, there are two distinct temporal windows (Figure 5-6). Following the excitation pulse at 372 nm and for time delays shorter than 350 fs, the differential optical density ( $\Delta OD$ ) is negative in the whole spectral range (Figure 5-6a). At wavelengths shorter than 400 nm, the spectra are dominated by the bleaching of the dendrimer absorption band peaked around 375 nm. For wavelengths longer than 400 nm, the negative  $\Delta OD$  values are due to bleaching signal from the ethynylene perylene trap.

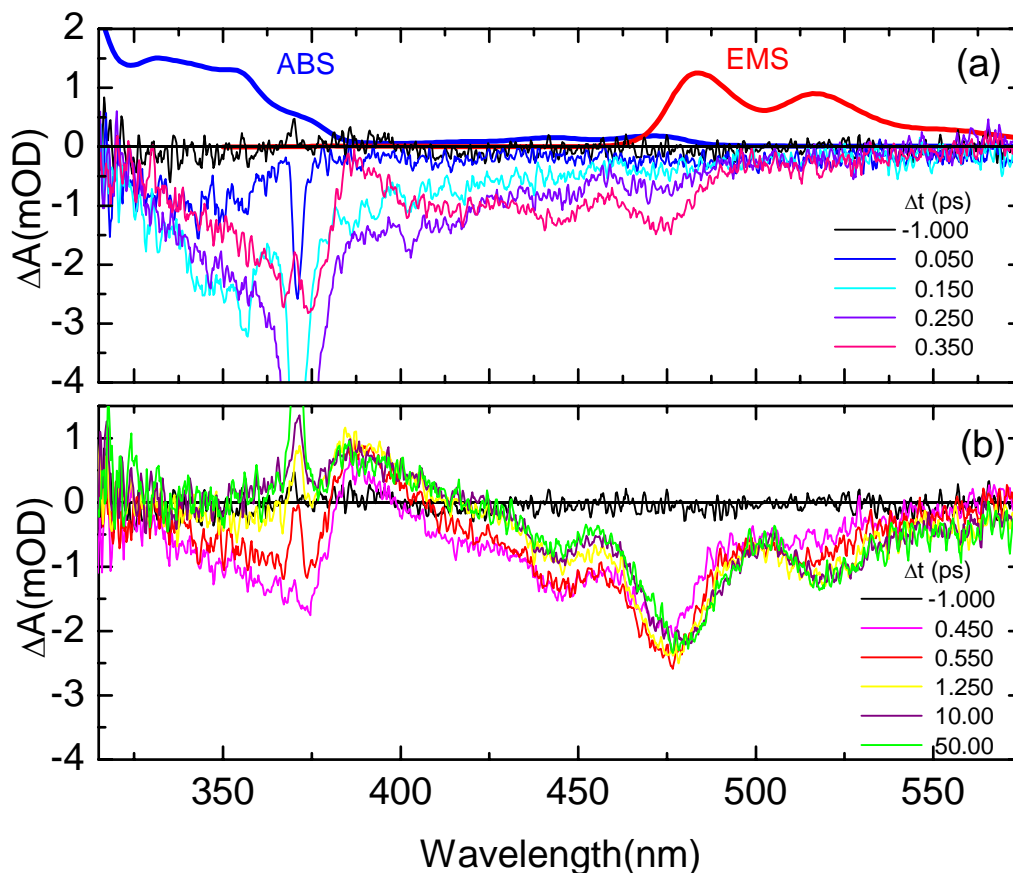


Figure 5-6. (a) Transient absorption spectrum of nanostar within 400 fs after excitation at 372 nm. (b) Long time window (0.450-50 ps). Scattered light from the excitation beam is seen at 372 nm.

At this wavelength, there is some direct excitation of the EPer, and thus the bleach signal between 400 nm and 475 nm is observed. For time delays between 450 fs and 5 ps, a fast decrease of the bleach signal for  $\lambda > 375$  nm occurs simultaneously with the rise of a photoinduced absorption band around 385 nm. At longer wavelengths, we can see that the negative signal is a combination of bleach and stimulated emission. At even longer delay times ( $\Delta t > 5$  ps), the red side of the spectrum ( $\lambda > 420$  nm) evolves to resemble to that of phenylethynylene perylene. Between 420 and 475 nm, the bleaching of perylene absorption is dominant whereas above 475 nm, stimulated emission is the only

contribution. As discussed before, the peak around 480 nm is a combination of both bleach and stimulated emission signals.

In order to determine the kinetics following the 372 nm excitation, the transient signals at two different wavelengths are shown in Figure 5-7. At 340 nm, we are solely probing the ground state bleach. This signal appears within the instrument response function and its subpicosecond decay represents the recovery time of the ground state population in the 4-ring component of the dendrimer. At 515 nm, only the stimulated emission from the ethynylene perylene trap is probed. This signal rises with the same time constant observed for the decay of the dendrimer backbone bleach. This shows that the energy transfer from the 4-ring PE segment to the perylene trap is very fast and efficient as the 4-ring PE is the closest to the perylene unit both spatially and energetically.

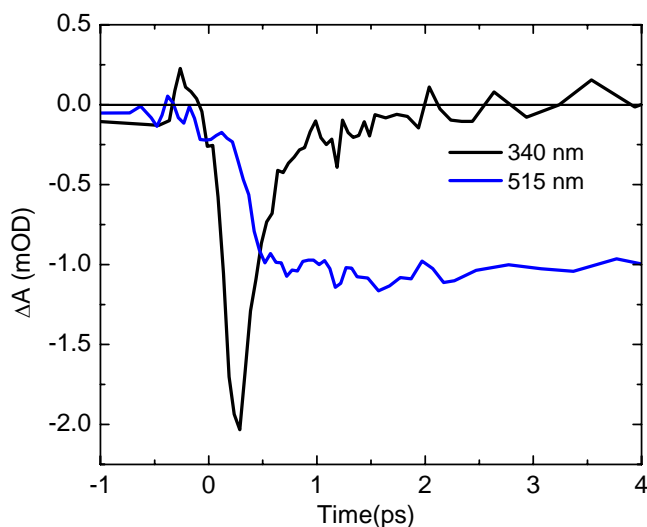


Figure 5-7. Transient absorption signal as a function of time recorded at 340 nm (black), and 515 nm (blue) following excitation at 372 nm.

**352 nm excitation.** Although the 352 nm excitation is initially considered to be specific to the 3-ring PE, the absorption studies illustrated in Figure 5-3a and 5-3b show

that the 4-ring PE also contributes to the total absorption. The 352 nm excitation is therefore resonant with both the 3-ring and 4-ring PE chromophores. Figure 5-8 shows the pump-probe spectra after excitation at 352 nm, which has similar characteristics to the 372 nm excitation spectra. The lack of bleach signal in the region of EPer absorption band (400-475 nm) demonstrates that at this excitation wavelength only the dendrimer backbone is excited, without contribution from direct excitation of EPer.

At time zero, the 352 nm excitation pulse promotes a 3-ring chromophore within the nanostar from its ground state to the  $S_1$  state. Therefore, immediately after excitation the transient spectrum of the nanostar resembles the sum of absorption spectrum of 3-ring and 4-ring PE chromophores. The excited 3-ring (or 4-ring) PE chromophore transfers its energy into the nearest 4-ring and then to the ethynylene perylene trap. At very early times ( $\Delta t < 350$  fs), the  $\Delta OD$  is negative for wavelengths shorter than 480 nm. For  $\lambda > 480$  nm, there is a positive signal which is attributed to the photoinduced absorption of the 3-ring. This broad PIA is consistent with Beeby et al.'s experiments on *para* phenylene ethynylene (3-ring namely 1,4-bis-(phenylethynyl) benzene) and with our results from the transient absorption of 3-ring and 4-ring PE units.<sup>152</sup> Such a positive signal is absent (for  $300 \text{ nm} < \lambda > 575 \text{ nm}$ ) when the molecule was excited at 372 nm. When the free 4-ring molecule is excited, there is no photoinduced absorption for  $\lambda < 575 \text{ nm}$ , which does not exclude the possibility of PIA signal being red-shifted. At longer times, this signal is masked by the stimulated emission from the ethynylene perylene trap and thus the overall signal in this region becomes negative. After a few picoseconds, the transient spectrum of the nanostar resembles that of free ethynylene perylene. Figure 5-9 shows the temporal

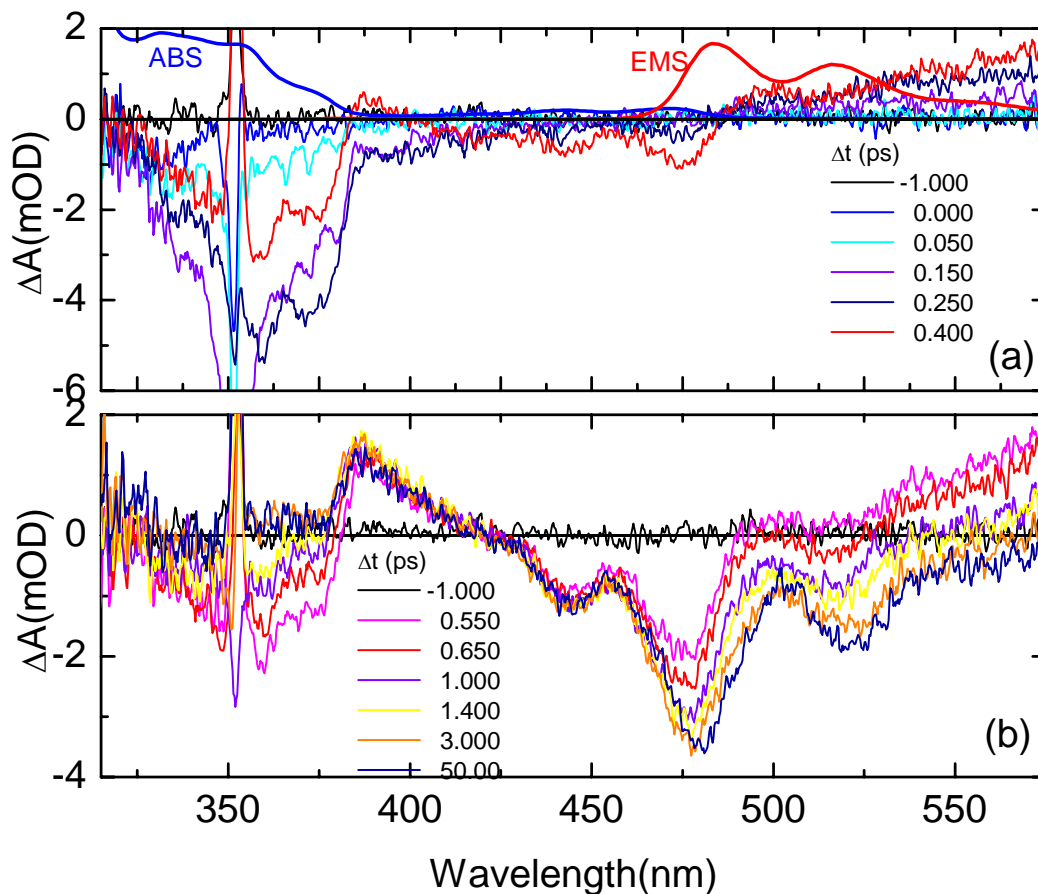


Figure 5-8. Transient absorption spectrum of nanostar after excitation at 352 nm. (a) Short time window ( $\Delta t < 450$  fs). (b) Long time window (0.550-50 ps). The scattered light from the pump beam is observed at 352 nm.

behavior in two wavelength regions: bleaching signal of the dendrimer ground state (360 nm) and stimulated emission signal from the ethynylene perylene acceptor (520 nm). The bleach signal rises instantaneously with the excitation, and decays within a couple of picoseconds. The stimulated emission signal rises with the same time constant as the bleach decays. A good correlation is observed between these two signals, indicating the vectorial energy transfer within the nanostar molecule. The energy transfer to the perylene trap at 352 nm excitation wavelength also proves to be an efficient and fast process.

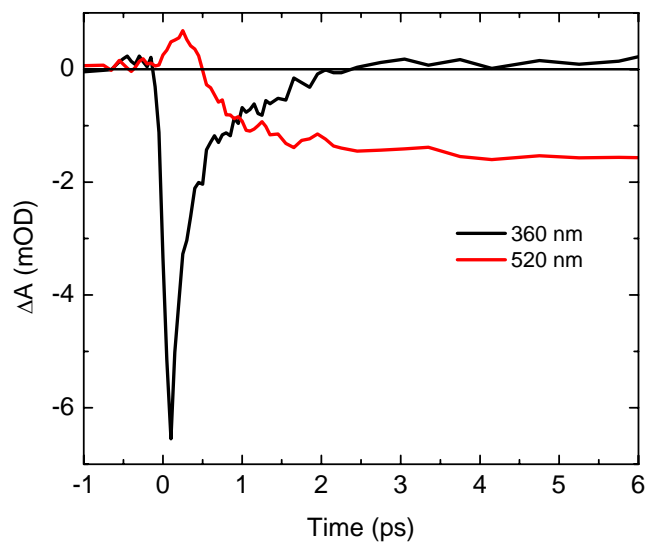


Figure 5-9. Transient absorption signal as a function of time recorded at 360 nm (black), and 520 nm (red) following excitation at 352 nm.

**310 nm excitation.** With a pump pulse spectrum centered at 310 nm, excitation energy is deposited only on the 2-ring units, which also results in energy transfer to the EPer trap. Figure 5-10a shows the pump-probe spectra along with the steady-state absorption and emission spectra. In Figure 5-10a, within the first 550 fs, the evolution of the bleach signal between 300 nm and 380 nm has better defined features resembling the steady-state absorption. Even though the initial excitation is deposited on the periphery, the absorption peaks associated with 3-ring and 4-ring PE units are observed in the transient spectrum proving the presence of cascade energy transfer. In this time window, an instantaneous photoinduced absorption signal peaked at  $\lambda = 380$  nm is observed. It is reasonable to compare this signal with the absorption of the DPA molecule shown in Figure 5-4a. DPA has a broad photoinduced absorption signal peaked at 500 nm with a lifetime of 8 ps. The signal shown in Figure 5-10a matches well with the signal obtained from the standalone DPA molecule. The instantaneous photoinduced absorption for  $\lambda > 425$  nm resembles the

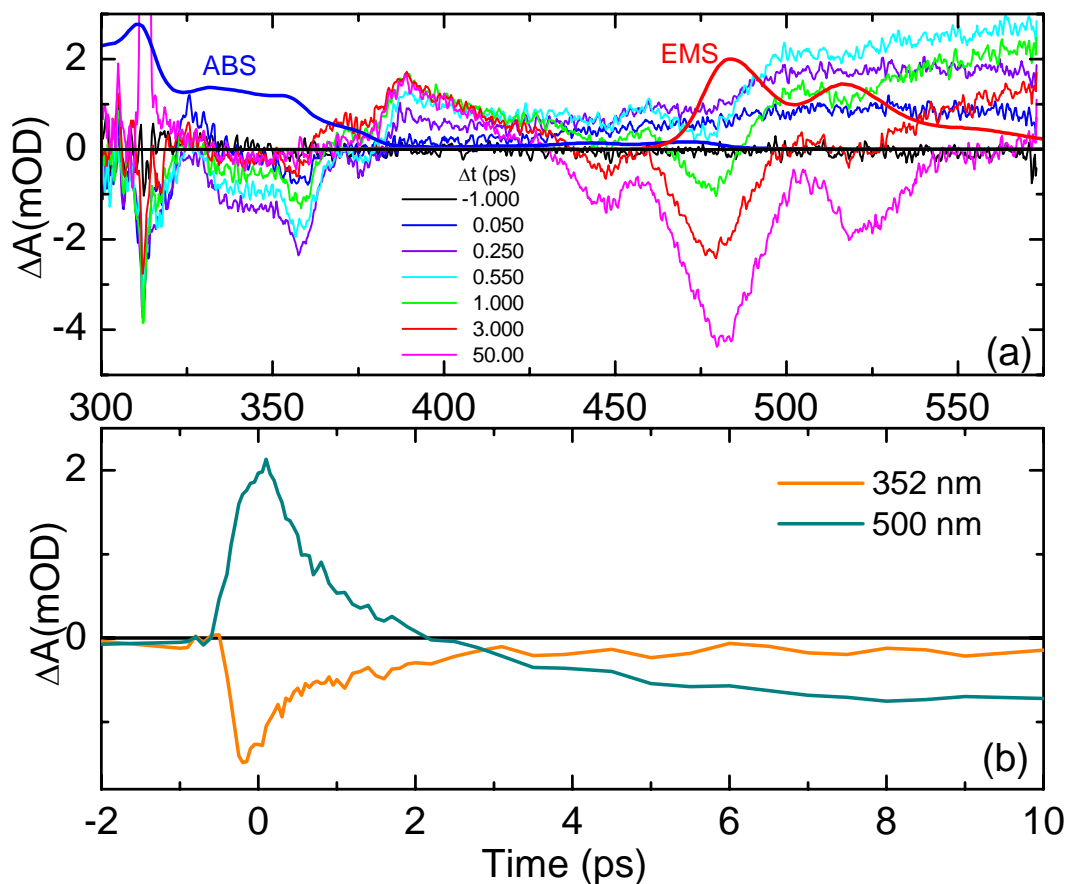


Figure 5-10. (a) Transient absorption spectrum of nanostar after excitation at 310 nm. There is scattered light from 310 pump beam (b) Transient absorption spectra as function of time recorded at 352 nm and 500 nm.

excited state absorption of DPA. This indicates that the excitation at 310 nm is localized on the peripheral 2-ring units.

The bleach signal between 300 nm and 380 nm corresponding to the dendrimer backbone absorption decays within 20 ps which is considerably slower than the previous two bleaching signals of the 4-ring and the 3-ring excitations at 372 nm and 352 nm, respectively. Simultaneously, the stimulated emission signal from the perylene trap peaked at 485 nm rises to its maximum value. At  $\Delta t = 50$  ps, the transient spectrum has almost evolved into the spectrum of phenylethynylene perylene. Here, it is obvious that

depending on the initially excited state, energy transfer can progress from a few hundreds of femtoseconds to tens of picoseconds. Figure 5-10b shows the decay of the bleach signal detected at 352 nm and the rise of the stimulated emission signal detected at 500 nm. The results obtained with broadband transient experiments are quantitatively in good agreement with the previous degenerate pump-probe investigation by Kleiman et al.<sup>75</sup>

One way to directly compare the rates of energy transfer is by looking at the rise time of the ethynylene perylene's stimulated emission. Figure 5-11 shows the kinetics of stimulated emission signal detected at 485 nm (maximum emission wavelength of perylene) following different excitation wavelengths. Since each of this excitation is proven to electronically access a specific chromophore in the nanostar, different dynamics are expected, specifically slower kinetics for periphery excitation and faster dynamics for longer segment excitation. The transient stimulated emission signal following excitation at 352 nm and 372 nm have similar time scales for the energy transfer (the risetime of 372 nm excitation is slightly faster than the 352 nm excitation, but both are in subpicoseconds regime). However, the risetime of the emission following the 310 nm excitation is considerably slower, indicating a slow energy transfer from the periphery to the core. Another important point we can derive from Figure 5-11 is the initial positive signal observed only for the 310 nm excitation. The transient of the model compound DPA showed a significant photoinduced absorption signal peaked at 500 nm. Thus, this initial positive signal is due to the localization of excitation on the 2-ring PE units.

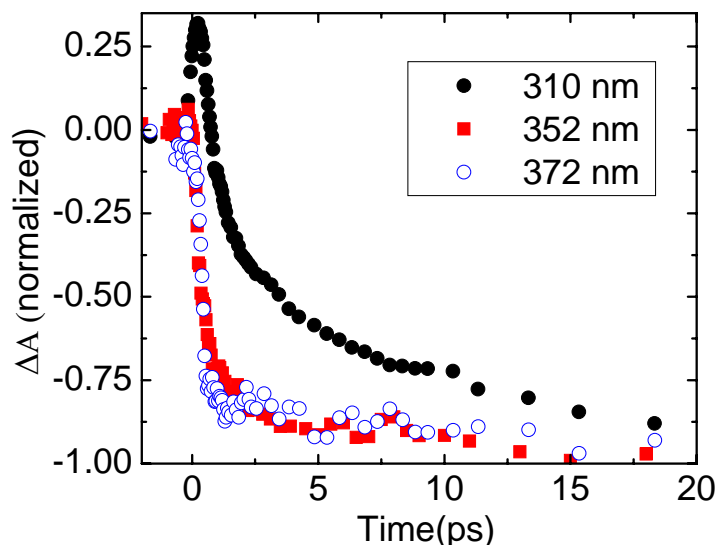


Figure 5-11. Transient absorption signal as a function of time for three different excitation wavelengths. Detection is at 485 nm, the maximum stimulated emission from the perylene trap.

### Kinetic Model for Nanostar

Both steady state and transient absorption experiments suggest that in the ground state there is no coupling between the PE segments. The meta branching results in a nearly complete loss of conjugative delocalization between the neighboring PE units. The photoinduced excitons are initially localized on a single chromophore unit. Following the excitation of an individual segment, the exciton will funnel through the accessible energy states and radiatively decay from the ethynylene perylene trap (core). To understand the kinetic phenomena associated with this process, we need to determine the rate of energy transfer for each individual step. Here, we propose a kinetic model to quantify and account for the differences in the transfer rates at three excitation wavelengths, namely 372 nm, 352 nm, and 310 nm. Figure 5-12 illustrates all possible paths yielding the vectorial transfer to the core of the molecule. A, B, and C represent the excited states 2-ring, 3-ring, and 4-ring units, respectively. P stands for the excited state of the ethynylene

perylene trap. When the kinetic equation representing the population of each excited state is solved, there are up to five exponential functions. It would be too complicated and impractical to comprehend the physical meaning of these exponential fits for the time-resolved data. Therefore, we will start with the simplest case of kinetic process, obtain the fitting parameters, and iteratively use these as constraints to analyze more complex transfer processes. For instance, the simplest process is the one step energy transfer from the 4-ring PE unit into the perylene trap when the nanostar is excited at 372 nm ( $k_3$ ). While analyzing the time-resolved data for higher energy excitation, the rates obtained from the fit to the lower energy excitations will be incorporated. By doing so, we reduce the number of variables and the data fitting becomes more informative.

#### **Model for 372 nm Excitation**

When the nanostar is excited at 372 nm, both steady state and transient absorption data revealed that only 4-ring units are initially excited. In Figure 5-12, D is the ground state of the dendrimer backbone, C is the excited state of 4-ring unit, and P\* is the excited state (emitting state) of the ethynylene perylene trap.



According to this model,  $k_3$  is the energy transfer rate from the dendrimer to the ethynylene perylene trap. The ethynylene perylene trap's radiative decay rate  $k_{rad}$  was measured via time resolved emission experiments and found to be  $(2.2 \text{ ns})^{-1}$ . While analyzing the broadband transient absorption spectra, one needs to know the population

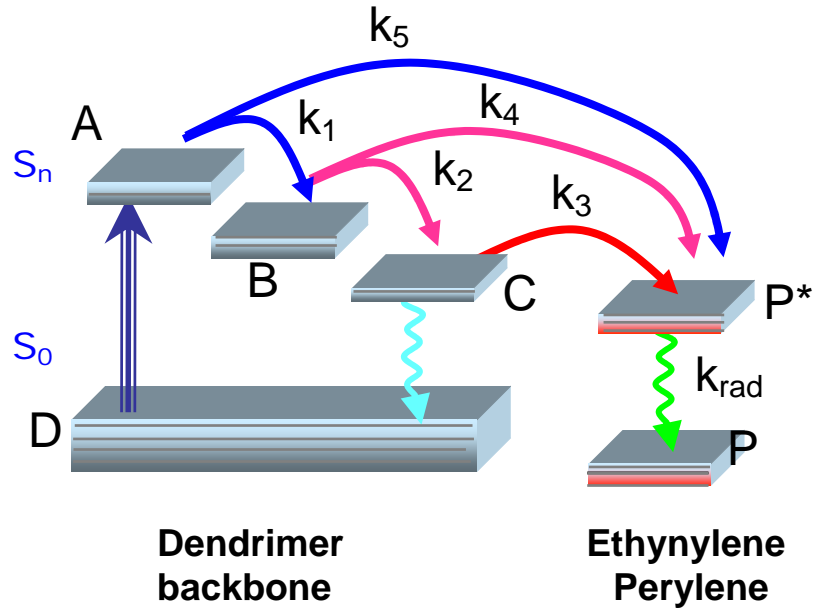


Figure 5-12. Kinetic Model proposed for the dynamics of nanostar.

of each excited state. By solving the kinetic equations for this model, the excited state population of 4-ring unit is given by:

$$C(t) = e^{-k_3 t} \quad (5-2)$$

Then, the excited state population of the ethynylene perylene follows as:

$$P^*(t) = \frac{k_3}{k_{rad} - k_3} (e^{-k_3 t} - e^{-k_{rad} t}) \quad (5-3)$$

The data measured here extend over a broad spectral range and over several orders of magnitude in time. The data sets are evaluated through Single Value Decomposition (SVD) method as explained in details in Appendix B, and the kinetic model is applied to fit both spectral and temporal evolution of the energy transfer process. The SVD analysis, reconstruction of the data in spectrum, and kinetic fits are shown in Appendix B. Since the  $k_{rad}^{-1}$  is directly measured to be 2.2 ns, the only free parameter to be determined is  $k_3$ . Using equations 2 and 3, the energy transfer time from the lowest excited state of the

dendritic backbone (C) to the ethynylene perylene core (P\*) is found to be very fast ( $k_3^{-1} = 290$  fs). This is an excellent agreement with the value obtained by Kleiman et al. from degenerate pump-probe experiments.<sup>75</sup>

### Model for 352 nm Excitation

Exciting the nanostar at 352 nm leads to initial excitation of 3-ring units. As shown in Figure 5-12, B represents the excited state of 3-ring units. There are two possible pathways that will transfer the energy from this initial state into the ethynylene perylene: direct,



or indirect,



As shown in this model,  $k_2$  is the rate of interchromophore energy transfer within the cascade (from 3- ring to 4-ring) while  $k_4$  is the direct transfer rate. The excited state population of 3-ring units is derived as:

$$B(t) = e^{-(k_2+k_4)t} \quad (5-6)$$

The population of the intermediate step C (excited state of 4-ring unit) is given by:

$$C(t) = \frac{k_2}{k_3 - (k_2 + k_4)} \times \left[ e^{-(k_2+k_4)t} - e^{-k_3t} \right] \quad (5-7)$$

Then, the population of trap excited state (P\*) includes two components, indirect where energy goes through the state C (cascade step)

$$P_I^*(t) = \frac{k_2 k_3}{(k_3 - k_2 - k_4)} \left\{ \frac{-e^{-(k_2+k_4)t}}{k_2+k_4} + \frac{e^{-k_3 t}}{k_3} \right\} + \frac{k_2}{k_2+k_4}, \quad (5-8)$$

with  $(k_2+k_4)^{-1}$  and  $(k_3)^{-1}$  as characteristic times, and direct

$$P_D^*(t) = \frac{-k_4}{k_2+k_4} e^{-(k_2+k_4)t} + \frac{k_4}{k_2+k_4} \quad (5-9)$$

with  $(k_2+k_4)^{-1}$  as the characteristic time.

Since the fluorescence lifetimes of B, C, and P\* are on the order of ns (obtained from the free molecules), they are included as constant offset terms in the model. Defining the pre-exponential factors in terms of the rates, and using the  $k_3$  obtained from the 372 nm excitation analysis leads to  $k_2$  and  $k_4$  as the only free parameters. Using equations 5-9, fitting of the data sets yields direct transfer time of  $(k_4)^{-1} = 4$  ps, and the indirect transfer with  $(k_2)^{-1} = 500$  fs. The relative contribution from each path can be evaluated as:

$$\text{Indirect} = \frac{k_2}{k_2+k_4} \quad \text{and} \quad \text{Direct} = \frac{k_4}{k_2+k_4}.$$

According to this model, 89% of energy transferred to ethynylene perylene trap is attributed to indirect, multistep path (from 3-ring to 4 ring and then to the ethynylene perylene), while the direct path contributes only 11%. As a result, the proposed model here implies that most of the energy is flowing through the cascade which includes step by step interchromophore energy transfer. Even though, only a small percentage of the initially deposited energy is flowing through the direct path, we can not neglect its contribution.

The rate constants obtained from this analysis will help to understand the degree of coupling between different size PE chromophores and the mechanism of the energy

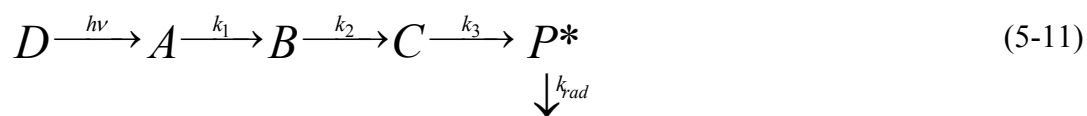
transfer. For instance, confirmation of the cascade transfer when nanostar is excited at 352 nm, definitely eliminates the strong coupling of 3 and 4 –ring units. If they were coupled, it would have been possible to fit this data set with a single step mechanism as in the case of 372 nm excitation described in the previous section. The extent of coupling/localization and energy transfer mechanism for the nanostar will be discussed in more details in the upcoming sections of this chapter.

### Model for 310 nm Excitation

2-ring chromophores in the nanostar have the highest excitation energy and they are electronically accessible via 310 nm excitation. All the possible paths shown in Figure 5-12 will be available upon this excitation. Solving the equations for this model and implementing them into the fitting procedure will be quite complicated. From the previous analysis performed for 372 and 352 excitations, the population dynamics of 3-ring (state B) and 4-ring excited states (state C) are explored in detail. Here, we need to concentrate on the population dynamics of 2-ring excited state A. In the same manner, following the excitation at 310 nm, the population on state A can flow through a cascade or can transfer directly to the ethynylene perylene trap. For the simplicity of the fitting procedure, the overall model can be reduced to a direct path:



and the cascade path:



Since  $k_2^*$ ,  $k_3$  and  $k_{\text{rad}}$  are already known, only two parameters,  $k_1$  and  $k_5$ , will need to be determined. We will use an effective  $k_2^*$  value composed of  $k_2$  and  $k_4$  measured in the previous subsection. According to this model, the excited state populations are given by:

$$A(t) = e^{-(k_1+k_5)t}, \quad (5-12)$$

$$B(t) = \frac{k_1}{k_2^* - (k_1 + k_5)} \times \left[ e^{-(k_1+k_5)t} - e^{-k_2^*t} \right], \quad (5-13)$$

$$C(t) = \frac{k_1 k_2^*}{k_2^* - (k_1 + k_5)} \times \left[ \frac{e^{-(k_1+k_5)t}}{k_3 - (k_1 + k_5)} - \frac{e^{-k_2^*t}}{k_3 - k_2^*} \right] + \frac{k_1 k_2^*}{(k_3 - k_1 - k_5)(k_3 - k_2^*)} e^{-k_3 t}, \quad (5-14)$$

and

$$P^*(t) = \frac{k_1 k_2^* k_3}{k_2^* - (k_1 + k_5)} \times \left[ \frac{-e^{-(k_1+k_5)t}}{(k_1 + k_5)(k_3 - (k_1 + k_5))} + \frac{e^{-k_2^*t}}{k_2^*(k_3 - k_2^*)} \right] + \frac{k_1 k_2^*}{(k_3 - k_1 - k_5)(k_3 - k_2^*)} e^{-k_3 t} \quad (5-15)$$

Implementing these equations into the fitting program we obtain transfer times of  $(k_1)^{-1} = 10$  ps and  $(k_5)^{-1} = 20$  ps. These energy transfer times suggest that 66% of the energy is transferred through the multistep mechanism while 33.3% of the energy can directly go to the ethynylene perylene trap. At this point it is important to recall that this model is a simplified version of what we really proposed. The 33.3 % of the energy transfer actually represents all the paths that are not included in the cascade mechanism. It is possible that 2-ring units might interact with both 4-ring units and ethynylene perylene trap other than just with 3-ring as the cascade mechanism suggests .

The overall results of the kinetic model analysis are summarized in Table 5-1. The most crucial conclusion is the slow energy transfer time when nanostar is excited at 310

nm. Even though energy transfer times are in subpicosecond regime from the intermediate chromophores, it takes 10 ps from the peripheral 2-ring PE units. Our results are in accordance with the relaxation dynamics of the same molecule measured recently via degenerate pump-probe experiment.<sup>75</sup> To our knowledge, this is the most extensive experimental investigation of the energy funneling process in the nanostar providing the time scale for each of the individual steps through a multi-step mechanism and direct jumps from the periphery to the ethynylene perylene trap with femtosecond temporal resolution. For a complete picture of this vectorial energy transfer, we also performed time-resolved emission experiments.

Table 5-1. Fits for Transient Absorption Data

$\lambda_{\text{exc}}$	$\tau_1$ (ps)	$\tau_2$ (fs)	$\tau_3$ (fs)	$\tau_4$ (ps)	$\tau_5$ (ps)	Direct %	Indirect %
372 nm	-	-	$290 \pm 20$	-	-	100	-
352 nm	-	$500 \pm 40$	290	$4 \pm 0.2$	-	11	89
310 nm	$10 \pm 1$	$550 (1/k_2^*)$	290	4	$20 \pm 3$	33.3	66.6

# Errors correspond to  $\pm 2\sigma$

### Time-Resolved Emission Experiments

The steady state photoluminescence spectrum shows emission from the nanostar originating almost entirely from the ethynylene perylene trap, and its efficiency is independent of the excitation wavelength. The energy transfer quantum yield can be estimated by comparing the absorption spectrum with the excitation spectrum while monitoring emission from the acceptor. In fact, the nanostar's normalized excitation spectrum detected at 515 nm (perylene emission region) and absorption spectrum are compared. The efficiency of energy transfer is quantified to be 98% within this molecule.<sup>70</sup>

If we take a closer look into the emission region around 380 nm, a small band consisting of emission from un-functionalized (without ethynylene perylene trap) dendrimer backbone and some residual dendritic emission (even in the presence of the trap) from nanostar is noticed. The main emission band peaked at 485 nm is solely from the ethynylene perylene trap. We detect the fluorescence both at 380 nm and 485 nm. The time-resolved emission data will clarify the origin and dynamics of each signal.

The natural electronic excited state lifetime of the nanostar is 2.2 ns, same as the lifetime of phenylethynylene perylene.<sup>70</sup> The nanostar's backbone (without the Eper trap) was measured to have a 270 ps lifetime in DCM. We performed femtosecond time-resolved fluorescence upconversion experiments to monitor the arrival time of the energy into the ethynylene perylene trap. After excitation at 310 nm, emission is detected at 485 nm (emission from P\* in Figure 5-12) and 380 nm (emission from C in Figure 5-12) corresponding to ethynylene perylene trap fluorescence and dendrimer backbone fluorescence, respectively. The dynamics obtained from these two data sets are complementary and allow us to follow the energy migration from the initially excited state on the nanostar's backbone to the ethynylene perylene trap. Figure 5-13 shows the temporal evolution of the nanostar emission at 485 nm (blue line) and 380 nm (red line). The temporal behavior of the fluorescence detected at the acceptor's emission wavelength (485 nm) shows a slow rise time (10-20 ps, the slowest rise that is measured for any PE dendrimers so far) and a nanosecond decay. On the other hand, the temporal behavior of fluorescence detected at 380 nm exhibits a subpicosecond rise and two decays one in the order of tens of picoseconds and the other on the hundreds of picoseconds. The ultrafast rise time and fast decay time are associated with the excitation

energy transfer, whereas the slower decay time corresponds to unsubstituted nanostar backbone emission. This unsubstituted backbone emission accounts for most of the steady state emission intensity at 380 nm. This emission band coincides very well with the emission from the longest chain of nanostar dendrimer, which is the 4-ring PE unit.

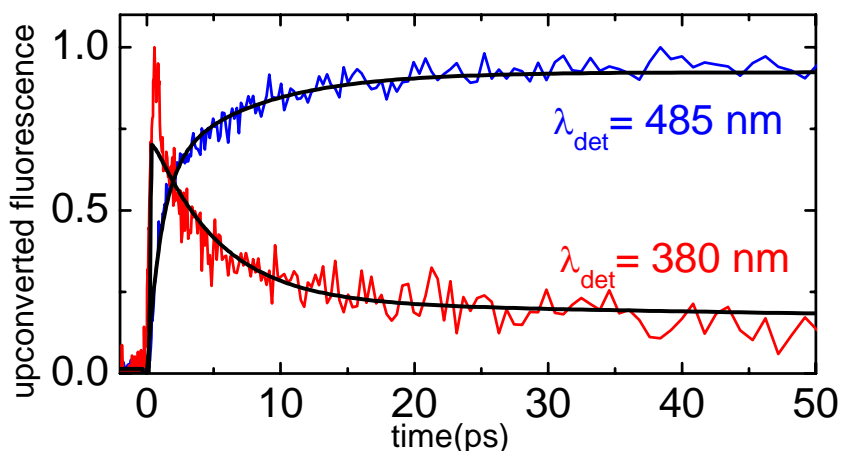


Figure 5-13. Fluorescence Upconversion signal detected at 485 nm (blue) and at 380 nm (red) following the 310 nm excitation.

The solid lines in Figure 5-13 correspond to the fits via the kinetic model solutions derived in previous section. It is important to note that what we measure here is the population dynamics of excited states C (red) and P\* (blue) given by equations 5-14 and 5-15. The fits are calculated from the convolution of these functions with the instrument response function. Exciting the nanostar at 310 nm, as discussed earlier, directly deposits the excitation energy into the 2-ring units, highest-lying state of the dendrimer backbone. Considering the transient absorption results obtained at 310 nm excitation wavelength, a stepwise energy transfer, from 2-ring to 3-ring, 4-ring, and finally to the Eper trap is expected. The fitting procedure of the emission detected at 485 nm yields mainly two risetimes, a fast component (average of  $k_2^{*-1}$  and  $k_3^{-1}$ ) in the subpicosecond time scale, and a very slow component  $\tau_{15} = 1/(k_1+k_5)$ . The fast component rises with  $\tau_{23} = 700$  fs,

while the slow component rises with  $\tau_{15} = 7$  ps time constant. These time constants are in good agreement with the time constants obtained in transient absorption analysis when excited at the same wavelength. This kinetic model reveals the presence of both direct and indirect pathway, and for the indirect (multistep) channel, the rate limiting step is the energy transfer from the peripheral 2-ring chromophores to the adjacent 3-ring chromophores.

A confirmation of the cascade mechanism concurrently with direct channels is also presented in Figure 5-13 (red line), where the emission from the intermediate state (backbone of the nanostar) at 380 nm is monitored. In this case, a very fast rise is followed by a slow decay. According to this model, the slow decay corresponds to population arriving at the emissive state C and the fast rise corresponds to the depopulation of the same state. The fit of the experimental data with equation 5-14 yields the following time constants:  $\tau_1 = 7.5$  ps,  $\tau_2 = 470$  fs,  $\tau_3 = 300$  fs and  $\tau_5 = 21$  ps. These values coincide well with the previous results obtained for ethynylene perylene emission at 485 nm. The time constants are very similar in both fits verifying the well-establishment of the predicted kinetic model. If the energy transfer was only via the cascade process, the temporal behavior of the final emitting state of the nanostar "P\*" should be exactly same as the temporal behavior of the lowest lying state of the backbone "C". However, due to direct channels from the initially excited state of the nanostar to the final trap, the data representing the population dynamics of P\* and C do not overlap completely. In addition, the long decay observed for the emission detected at 380 nm has a significant contribution from the 270 ps lifetime of the un-functionalized nanostar backbone.

We are able to fit the transient absorption data, for three different excitation wavelengths, and the fluorescence data with the same kinetic model. Thus, even though there might be some approximations for the simplicity of the fitting procedure, the proposed model provides a clear picture of the energy transfer process in this macromolecule.

Since the nanostar is a system with several chromophores absorbing light in different spectral regions and the excitation energy is localized in each chromophore, we label the electronic states independently. Unidirectional energy transfer takes place from the chromophore with the energetically highest  $S_0$ - $S_1$  transition (2-ring peripheral groups) to the chromophore with the energetically lowest  $S_0$ - $S_1$  transition (ethynylene perylene core). Considering the  $S_0$ - $S_1$  energetics, this process involves two more chromophore intermediates. If the emission spectrum of the chromophore with the highest  $S_0$ - $S_1$  transition energy overlaps with a  $S_0$ - $S_n$  absorption band of the chromophore with the lowest  $S_0$ - $S_1$  transition energy, and if both chromophores are at favorable distance and orientation, the presence of intermediate chromophores is not required for 2-ring  $\rightarrow$  EPer energy transfer. If so, distinct direct energy transfer from the periphery to the core does occur through a direct pathway. The fluorescence of 2-ring unit of nanostar overlaps with both  $S_0$ - $S_1$  and  $S_0$ - $S_2$  absorption band of ethynylene perylene, and molecular geometry optimization indicates that interchromophoric distance between these two chromophores are short enough for efficient Förster energy transfer. Since the  $S_0$ - $S_1$  and  $S_0$ - $S_2$  dipole moments of EPer are perpendicular to each other, we expect that 2-rings oriented at perpendicular position contribute to the different pathways. In addition, the intermediate 3-ring chromophore's emission has significant overlap with the  $S_0$ - $S_1$  absorption band of

ethynylene perylene. Thus, unidirectional energy transfer from 2- and 3- ring PE chromophores to the core EPer is not to be excluded and will compete with the cascade energy transfer. Considering the possibility of the direct transfer via the existence of spectral overlap, we can now assert the accuracy of the proposed kinetic model.

### Energy Transfer

The goal of the study presented in this chapter is to explore the interchromophore energy transfer process, which can result from different interaction mechanisms. The through-bond mechanism requires spatial orbital overlap, and is effective at short distances between donor and acceptor. The meta substitution between the chromophores in the nanostar disrupts the  $\pi$ -electron conjugation, thus suggesting the dendrimer molecule to be an ensemble of linear chromophores with no (weak) charge transfer between them. If such a charge transfer is completely eliminated, and linear segments are well separated, through bond mechanism is expected to be suppressed.

At donor acceptor separations beyond their van der Waals radii, the coupling is described primarily by through-space, Coulomb interaction. Both donor and acceptor chromophores in the nanostar have electronically allowed emission and absorption transitions, so the largest contribution to the coupling will be due to Coulombic interaction. Once the exciton is created, it is shown that it can migrate through a direct path and multistep path towards the acceptor molecule at the core. The strength of the Coulombic coupling will lead to coherent or incoherent exciton migration.

In the case of very weak coupling, the energy transfer rate is described by:

$$k_{ET} = \frac{4\pi^2}{h^2c} J |V|^2 \quad (5-16)$$

where  $V$  is the Coulombic coupling and  $J$  is the spectral overlap integral in units of  $\text{cm}^{-1}$ . This overlap term is calculated by using the normalized absorption spectrum of the acceptor  $-a(\lambda)-$ , and the normalized emission spectrum of donor  $-f(\lambda)$ . The resonance interaction strength,  $V$ , is calculated using the experimental transfer rates and overlap integral. Minami et al. theoretically estimated the interaction strength between the segments connected at meta positions using the Collective Electronic Oscillator approach.<sup>78</sup> The Frenkel exciton Hamiltonian was used to represent the nearest neighbor couplings, i.e. between linear segments connected by a benzene ring at the meta position.

Using equation 5-16, the interaction strength between linear segments along with the interaction of the longest segment with the perylene trap is calculated. When the longest linear segments, 4-ring units are preferentially excited at 372 nm,  $k_1 = 1/290 \text{ fs}^{-1}$  is obtained as the transfer rate ( $k_{\text{ET}}$ ). The overlap integral between the 4-ring and the ethynylene perylene is utilized as  $J$ , which is calculated to be  $9.423 \times 10^{-5} \text{ cm}^{-1}$ . In order to calculate the overlap integral, the free 4-ring chromophore is used as model for the donor, with emission spectrum red-shifted 12 nm to account for the red shift observed when the chromophore is part of the nanostar. The interaction energy between the 4-ring and the Eper is estimated to be  $V_{4\text{-pery}} \approx 176 \text{ cm}^{-1}$ . Minami et al. estimated a theoretical value of  $302 \text{ cm}^{-1}$  for the interaction between the same pair of donor and acceptor. Due to the stepwise (interchromophore) energy transfer, the excitation of the 3-ring chromophore at 352 nm results in energy transfer to the 4-ring chromophore. As noted in the analysis of transient absorption data, this transfer rate constant is determined to be  $k_{\text{ET}}(k_2) = 1/500 \text{ fs}^{-1}$ . The overlap integral between the 3-ring chromophore's emission and the 4-ring chromophore's absorption is evaluated to be  $J = 1.065 \times 10^{-4} \text{ cm}^{-1}$ . Then, the interaction

strength is estimated to be  $V_{3-4} \approx 126 \text{ cm}^{-1}$ . The same interaction was theoretically calculated to be about  $325 \text{ cm}^{-1}$ . If the peripheral 2-ring units (highest lying state of the nanostar) are excited at 310 nm, the excitation energy will be transferred to the neighboring 3-ring chromophores as the first step of the cascade mechanism. The analysis of both transient absorption and fluorescence upconversion data yields a transfer rate of  $k_{\text{ET}}(k_3) = 1/10 \text{ ps}^{-1}$ . Since the 2-ring chromophore assembly resembles a G2 phenyl-terminated monodendron, it is reasonable to calculate the spectral overlap by using the emission spectrum of the G2 phenyl terminated monodendron (structure 9 of Devadoss et al.<sup>81</sup>) and the absorption spectrum of a free 3-ring chromophore. Based on this remark, the calculations yield a value of  $J = 4.718 \times 10^{-5} \text{ cm}$ , and the interaction strength is estimated to be  $V_{2-3} \approx 45 \text{ cm}^{-1}$ . Theoretically, the interaction energy between the 2-ring and 3-ring units was calculated to be  $158 \text{ cm}^{-1}$ . In the calculations reported here, the donor and acceptor chromophores' spectra are always red-shifted  $\sim 12 \text{ nm}$  to account for the red shift observed when these chromophores are part of the nanostar. However, no change is expected for the fluorescence emission of donor G2 since it has the same periphery composition as the nanostar. In general, the values of interaction strength calculated using the experimental data are in qualitative agreement with the theoretically estimated values, even though the experiments yields 2-3 times weaker than those theoretically estimated. In a series of recent studies, Mukamel's group have computed the electronic excitations, linear absorption, pump-probe spectra, and time/frequency-gated fluorescence signals for the nanostar.<sup>76-78,150,153</sup> Redfield theory was used to describe the exciton transport. The effects of nuclear motion were incorporated through relaxation superoperators and calculated perturbatively in exciton-

phonon coupling. The fluorescence signal was computed using the Doorway-Window representation and it provided a direct probe for exciton dynamics. The frequency domain pump-probe signal is simulated as well, showing the effects of exciton coupling and excited-state absorption in the nanostar. Calculations were performed at room temperature  $T=300$  K, and the excitation pulse was tuned to coincide with the highest periphery exciton. Both simulated time-resolved fluorescence spectra and pump-probe signals for different delays indicated that within 100 ps, most of the excitation energy had reached the trap. Thus, the theoretical upper limit for energy transfer time in the nanostar is about 100 ps. The calculated rates are clearly much slower than our experimental results and the interaction energies between any chromophores are larger than the ones obtained by using our experimental findings. This difference must be related to Redfield treatment. Redfield theory is based on the assumption that the electron-phonon coupling is weaker than Coulomb coupling between the chromophores and can be applied when the relaxation of the excitonically coupled molecules is slow compared to the relaxation of surroundings. In order to test the limitations of Förster and Redfield theories, Yang et al.<sup>154</sup> used a simple system of two interacting molecules and compared the energy transfer rates obtained via both Förster and Redfield theories. It was concluded that standard Redfield theory only works well for a small energy gap between the interacting states. When the energy gap is large, the exciton states are localized on each molecule and the exciton relaxation rate reduces to the hopping rate in Förster regime. For example, in the case of relatively weakly coupled pigments (coupling strength =  $20 \text{ cm}^{-1}$ ) having similar site energies (energy gap =  $0\text{-}100 \text{ cm}^{-1}$ ), the Redfield rates can be up to 10-100 times larger than the Förster rates. Whereas, for larger energy gaps ( $200\text{-}1000 \text{ cm}^{-1}$ ), the

Redfield theory gives significantly slower rates than Förster theory. Therefore, it is expected to get faster transfer rates from our experiments compared to the simulation of the same experiments described by Redfield theory. It was emphasized that the simulations of faster relaxation lifetimes ( $\tau < 100$  ps) would question the validity of the Redfield equations and require parameters of different level of modeling (modified Redfield theory).

In summary, the relaxation times observed for excitation at 372 nm and 352 nm are considerably faster than for excitation at 310 nm. The subpicosecond ( $\tau_1 = 290$  fs and  $\tau_2 = 500$  fs) relaxations are attributed to larger electronic coupling of the corresponding chromophores. The coupling of the 4-ring chromophore and ethynylene perylene trap as well as the coupling of the 3-ring and 4-ring chromophores is much larger than any interaction of the 2-ring peripheral groups. It was discussed that the faster relaxation could be an indication of a better overlap between the emission spectrum of the donor and the absorption spectrum of the acceptor.<sup>75</sup> However, the spectral overlap obtained using the measured spectrum of free of 2-, 3-, and 4-ring chromophores (red-shifted to account for the red-shift observed when the chromophore is part of the nanostar molecule) yields very similar values. The strength of the coupling determines the rate of the transfer. In the simplest form of the Förster mechanism, the Coulomb interaction is approximated by a dipole-dipole interaction, and the density of states is expressed in terms of the shape of the donor luminescence and acceptor absorption spectrum. The energy transfer rate constant is then expressed with the equation 1-21. Using this equation, Kleiman et al. estimated  $k_{ET}$  by considering coupling of the 2-ring chromophores connected to a single 3-ring chromophore. The R values and the

orientation factors were estimated for a planar configuration. The separation,  $R$ , between the 2-ring and 3-ring chromophores ranges from 9.1 Å to 15.1 Å. The spectral overlap was estimated to be  $2.8 \times 10^{-14} \text{ cm}^6/\text{mol}$ . It was found that  $k_{\text{ET}}^{-1}$  ranges between 0.83 and 20.0 ps, depending on the position of the 2-ring chromophore at the periphery. Our experimental findings for the 310 nm excitation along with preceding results from degenerate pump-probe experiments show rough qualitative agreement with the estimated Förster rates. The uncertainties in the orientation factors and interchromophore distances has to be re-evaluated considering the globular shape of the PE dendrimers and the increase in the rotational flexibility near the dendrimer periphery. Moreover, the Förster's formulation based on the dipole-dipole approximation is questionable when the donor and acceptor molecules are closely proximate relative to molecular dimensions. More accurate expansion of the Coulomb interaction beyond the dipole-dipole level is needed for such systems. The Transition Density Cube (TDC) method, which takes advantage of modern quantum chemical calculations of excited-state wavefunctions, was developed to obtain the local interactions between the donor and acceptor transition densities. Recently, Ortiz et al. has modeled the Coulombic contribution to the energy transfer between the 2-ring and 3-ring chromophores of the nanostar using TDC method.<sup>74</sup> The MD simulations of the nanostar showed that the phenyl rings are free to rotate around the ethynylene bonds. The transition densities were calculated for both planar geometry and the off-planar geometry. While the rotation around the central angle effects the magnitude of the electronic transition dipole moment for the 3-ring chromophore, the rotation of the outer ring in the 2-ring chromophore was hindered due to bulky groups at the periphery. The energy transfer rates between the 2-ring and 3-ring

chromophores were calculated as a function of the torsion angle of the central phenyl ring of the 3-ring chromophore. The Förster formula does not explicitly depend on the torsion angle (implicit dependence through parameter  $J$ ) whereas the TDC has shown a strong dependence on torsion angle. The rate constants were almost 3 orders of magnitude different with a torsion angle of  $90^\circ$ . It was concluded that the ring rotation is a factor that must be included when modeling energy transfer in the nanostar and more accurate coupling can be calculated by reconsidering the effect of torsional angle on  $\kappa^2$  and the spectral overlap.

### Conclusions

We employed broadband transient absorption and time-resolved fluorescence experiments to investigate the complete map of the energy pathways in the nanostar. The spatial positioning of different size PE chromophores and EPer chromophore within the nanostar and their respective spectral properties make this system an efficient light-harvester, which is able to capture light over a broad spectral range and transfer it directly and in a cascade fashion to the core EPer.

Using the 372 nm excitation, a highly efficient, subpicosecond unidirectional energy transfer from the 4-ring units to the EPer core is evident. Upon 352 nm and 310 nm excitation, 3-ring and 2 ring chromophores can transfer their excitation energy either directly or in a cascade fashion. Within the nanostar, both processes are present and will compete with each other, because the emission of 2- and 3-ring chromophores overlap considerably with both the  $S_0$ - $S_1$  and  $S_0$ - $S_2$  absorption band of EPer. Based on the spectral data and our kinetic modeling, direct energy transfer takes place with 33 % probability, while the cascade mechanism accounts for 66 % of the energy reaching the final trap.

Resonant excitations with 3-ring and 4-ring chromophores result in subpicosecond energy transfer times, while the excitation of 2-ring peripheral chromophores yields transfer times of tens of picoseconds.

For the first time, independently estimated theoretical and experimental interaction energies are compared. The qualitative agreement could be improved by full treatment of Coulombic interaction using TDC and molecular dynamics. Since we are able to probe the population dynamics of intermediate states, the major outcome of the experiments presented is proving the existence of direct transfer competing with the cascade type transfer.

## CHAPTER 6

### THE ROLE OF EXCITON HOPPING AND DIRECT ENERGY TRANSFER IN THE CONJUGATED POLYELECTROLYTES

Organic semiconductors and in particular  $\pi$ -conjugated polymers have entered numerous fields of applications such as light-emitting diodes, lasers, solar cells and, recently also the important field of chemical and biological sensing. Here,  $\pi$ -conjugated polymers have proven to increase the sensitivity of fluorescence-based sensors by several orders of magnitude.<sup>155-157</sup> For biological applications, the  $\pi$ -conjugated polymers need to be soluble in aqueous environments. Recently, amplified fluorescence quenching of a water-soluble  $\pi$ -conjugated poly(phenylene vinylene) (PPV) based anionic polyelectrolyte has been demonstrated.<sup>156,157</sup> Chen *et al.* showed that quenching of a polyanionic conjugated polymer by cationic electron acceptors can be a million-fold more sensitive than the corresponding quenching of small molecules of similar structure.<sup>156</sup> The amplification of fluorescence quenching relies on the high mobility of the photoexcitations on the conjugated polymer chain, leading to the quenching of many chromophores upon the binding of a single quencher molecule<sup>155,156</sup> However, a variety of effects enhance the fluorescence quenching of conjugated polyelectrolytes (CPE's). In addition to the importance of the photoexcitations mobility along the polymer chain, quencher-induced aggregation of the polymer chain increases the number of chromophores in the direct vicinity of the quencher and enables interchain energy migration, thereby enhancing the quenching efficiency.<sup>156,158,159</sup> Furthermore, the large charge of the conjugated polyelectrolyte can lead to a local concentration enhancement of

the quencher by more than an order of magnitude<sup>160</sup>. The influence of these rather extrinsic effects raises the question, to what extent does the exciton mobility on the polymer chain contribute to the fluorescence quenching?

The rate and efficiency of intramolecular energy transfer in  $\pi$ -conjugated polymers is currently a subject of intense discussion. Recent investigations of a PPV-type conjugated polymer found the intrachain energy transfer to be slow and short-range.<sup>161</sup> This is supported by measurements and Monte-Carlo modeling of the photoluminescence anisotropy decay of MEH-PPV<sup>162</sup> and polythiophene<sup>163</sup> in dilute solution, giving a range of the energy transfer of only 6-7 conjugated segments, corresponding to about 20-30 nm. On the other hand, the enormous amplification of luminescence quenching in polymer-based sensors indicates a very efficient intramolecular energy transfer in a water-soluble PPV, extending over about 1000 monomer units.<sup>156</sup> Efficient energy transfer on conjugated polymer chains has also been found in single-molecule studies,<sup>164-166</sup> where it was suggested that the energy transfer efficiency depends strongly on the polymer chain conformation, and quenching of the complete chain is achieved only for dense conformations forming aggregated structures. In these studies,<sup>165</sup> as well as in investigations in Langmuir-Blodgett films,<sup>167</sup> a three-dimensional exciton migration was proposed to explain the high quenching efficiency. Altogether, many different mechanisms can improve or limit the quenching efficiency of fluorescence from a conjugated polyelectrolyte. A fundamental understanding of the energy transfer mechanisms in conjugated polyelectrolytes is therefore crucial for the development of reliable and sensitive polymer-based sensors.

In general, energy transfer between an excited chromophore on a polyelectrolyte chain and an acceptor molecule can occur i) by direct energy transfer (e.g. by a long-range Förster type dipole-dipole coupling) and ii) in a multi-step mechanism consisting of intrachain energy migration on the polymer chain to a site adjacent to the acceptor, followed by short-range energy transfer to the acceptor.<sup>156</sup> Furthermore, for samples in solution one has to distinguish between quenching by acceptors that are in an ionic complex with the CPE and diffusional quenching by free acceptors in the solution, where the latter becomes important at high quencher concentrations.<sup>160</sup>

Wang et al. described the fluorescence quenching of a PPV-type CPE by methyl viologen with a modified Stern-Volmer equation that accounts for static quenching by both acceptor molecules in an ionic complex with the donor and free acceptors in the solution.<sup>160</sup> The superposition of both contributions leads to an exponential rise of the quenching efficiency according to  $I_0/I = (1 + K_{SV}[Q]) \cdot \exp(\alpha V)$ , where  $I_0/I$  is given by the ratio of donor emission without and with the quencher present,  $K_{SV}$  represents the association equilibrium constant for complex formation, and  $V$  is the volume of the quenching sphere. The factor  $\alpha$  accounts for an enhanced quencher concentration in the vicinity of the CPE. The formula is derived on the assumption that the quenching is entirely *static*, i.e. much faster than the excited state lifetime of the (unquenched) donor. There is ample evidence, however, that exciton migration in conjugated polymers is active on a timescale of tens of picoseconds<sup>163,168</sup> (i.e. comparable to the excited state lifetime of most polymers). Thus, the quenching should be a *dynamic* process where the rate of energy migration on the CPE chain significantly influences the quenching efficiency.

In this work, we investigate the energy transfer dynamics from an anionic conjugated poly(phenylene ethynylene) sulfonate (PPESO3) to a cationic dye molecule (HMIDC). The chemical structures are shown in Figure 6-1. Steady state fluorescence spectroscopy reveals that formation of an ionic complex between the polymer and dye leads to efficient polymer dye energy transfer.<sup>169</sup> In order to monitor the energy transfer dynamics, femtosecond time-resolved fluorescence up-conversion is employed along with transient absorption and polarization anisotropy studies on solutions with systematically varied dye concentration.

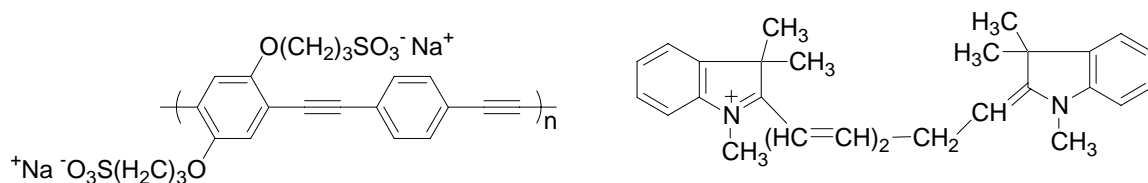


Figure 6-1. Conjugated polyelectrolytes PPESO3 (left) and cyanine dye HMIDC (right).

In addition, a numerical modeling is presented using the analytical solution of a random walk process between energetically identical and equidistant chromophores. The effects induced by energetic and conformational disorder are accounted for by a time-dependent hopping rate. Modeling of the dynamics allows us to determine the density of complexes on the polymer chain and the number of chromophores quenched by each complex formed. The individual contributions of intrachain hopping towards the acceptor and direct long-range Förster-type transfer are quantified, allowing design rules for systems with improved sensor activity to be provided.

### Steady State Experiments

The synthesis of PPESO3 has been described recently.<sup>158</sup> The molecular weight of the polymer is estimated to be  $M_n=100$  kDa, corresponding to about 200 monomer units (see Figure 6-1 for monomer repeat unit structure). HMIDC was purchased from Aldrich

and used as received. Solutions with different HMIDC concentrations were prepared and labeled according to their steady state quenching efficiency.

Steady state absorption and emission spectra of both materials in methanol solution are shown in Figure 6-2a. The emission of PPESO3 partially overlaps with the HMIDC absorption spectrum, thus enabling singlet energy transfer from the polymer to the dye. The large separation of the emission bands of the polymer and dye allows for independent measurement of donor emission and acceptor emission in time-resolved fluorescence experiments. A concentration of 34  $\mu\text{M}$  PPESO3 in  $\text{CH}_3\text{OH}$  (in polymer repeat units, PRU) was used for the time-resolved fluorescence and transient absorption experiments.

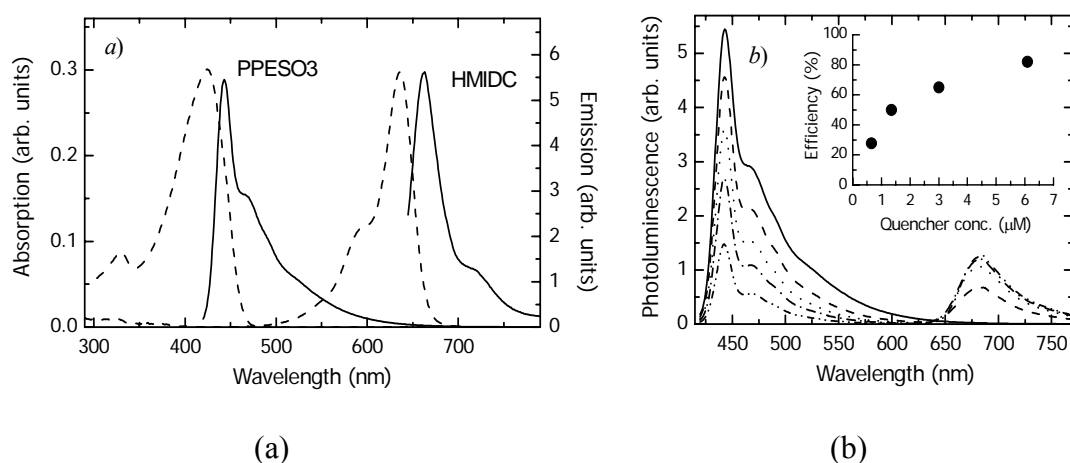


Figure 6-2. (a) Absorption (---) and emission spectra (—) of PPESO3 and HMIDC in methanol. (b) Fluorescence spectra of 10  $\mu\text{M}$  PPESO3 with added HMIDC (0 to 2.5  $\mu\text{M}$ ),  $\lambda_{\text{excitation}} = 400$  nm. Inset: efficiency of polymer (34  $\mu\text{M}$ ) quenching versus dye concentration.

Figure 6-2b shows the steady state emission spectra of PPESO3 with different concentrations of added dye. The excitation source at 400 nm exclusively excites the PPESO3 polymer. As the dye concentration is increased, the emission of PPESO3 decreases while the dye emission increases, revealing an efficient energy transfer from the photo-excited polymer to the cyanine dye. This efficient transfer process can be

attributed to a complex formation between the anionic polymer-donor and the cationic dye-acceptor.<sup>169</sup> The inset of Figure 6-2b shows the efficiency of the PPESO3 fluorescence quenching as a function of dye concentration.

### Time Resolved Fluorescence Spectroscopy

To further investigate the mechanism of PPESO3-to-cyanine energy transfer we carried out picosecond time-resolved fluorescence experiments by using fluorescence upconversion. These experiments were carried out at a fixed PPESO3 concentration (34  $\mu\text{M}$ ). HMIDC was selected as the acceptor cyanine dye, and its concentration was varied from 0 – 5  $\mu\text{M}$ . Concomitant with the time resolved experiments, parallel steady-state quenching measurements were carried out, and the fraction of the PPESO3 unquenched fluorescence ( $F_q = I/I_0$ ) for the PPESO3/HMIDC solutions are listed together with the time resolved data in Table 6-1. All of the time resolved experiments were carried out in methanol solution to minimize the influence of polymer aggregation on the observed fluorescence dynamics.

Table 6-1. Parameters Recovered from Kinetic Modeling of PPESO3 Fluorescence Decays with HMIDC in MeOH

[HMIDC] / ( $\mu\text{M}$ )	[PRU] : [Dye]	$F_q$	$A_r$	$\tau_0$ / ps	$\beta_0$	$\tau_2$ / ps	$\beta_2$
0	---	1	1	150	0.6	--	--
0.4	85:1	0.5	0.2	150	0.6	> 1500	0.25
1.2	28:1	0.25	0.41	150	0.6	760	0.25
5.0	6.8:1	0.07	0.64	150	0.6	20	0.2

[PPESO3] = 34  $\mu\text{M}$  in MeOH. Fraction of total PPESO3 fluorescence unquenched ( $F_q = I/I_0$ , where I and  $I_0$  are, respectively, the PPESO3 fluorescence intensity with and without added HMIDC quencher).

By using a laser excitation wavelength at 425 nm (the pump wavelength) it is possible to directly excite PPESO3. HMIDC was selected as the energy acceptor for these studies because it absorbs only very weakly at 425 nm, and consequently when the

425 nm pump is used to excite the PPESO3/HMIDC mixtures, excitations localized on HMIDC are created almost exclusively by energy transfer from the polymer. In addition, owing to the large wavelength separation between the fluorescence of PPESO3 ( $\lambda \approx 450$  nm) and HMIDC ( $\lambda \approx 685$  nm) it is possible to selectively observe the fluorescence dynamics for PPESO3 and HMIDC (the energy donor and acceptor, respectively).

Figure 6-3 shows fluorescence decays detected at 450 nm with 425 nm excitation for a series of solutions that contain PPESO3 and HMIDC at concentrations ranging from 0 – 5  $\mu$ M. The decay curves that are plotted in Figure 6-3 represent absolute fluorescence intensities, since were obtained under identical conditions (matched solution concentrations of PPESO3, identical pump power, and detection settings); therefore the amplitudes of the decays reflect the true relative instantaneous intensity of the time-resolved fluorescence signal from the different samples. Upon inspection of the data, two features are apparent. First, the initial amplitude of the polymer's fluorescence decay is reduced by the addition of HMIDC. Second, with increasing HMIDC concentration, the fluorescence decays more rapidly, which can be better seen in the inset of Figure 6-3, where normalized data is plotted. Taken together, these observations indicate that the PPESO3-to-HMIDC energy transfer takes place on two distinct timescales. A significant component of the transfer occurs by a pathway that is so fast that it cannot be resolved within the instrument response ( $\sim 4$  ps).

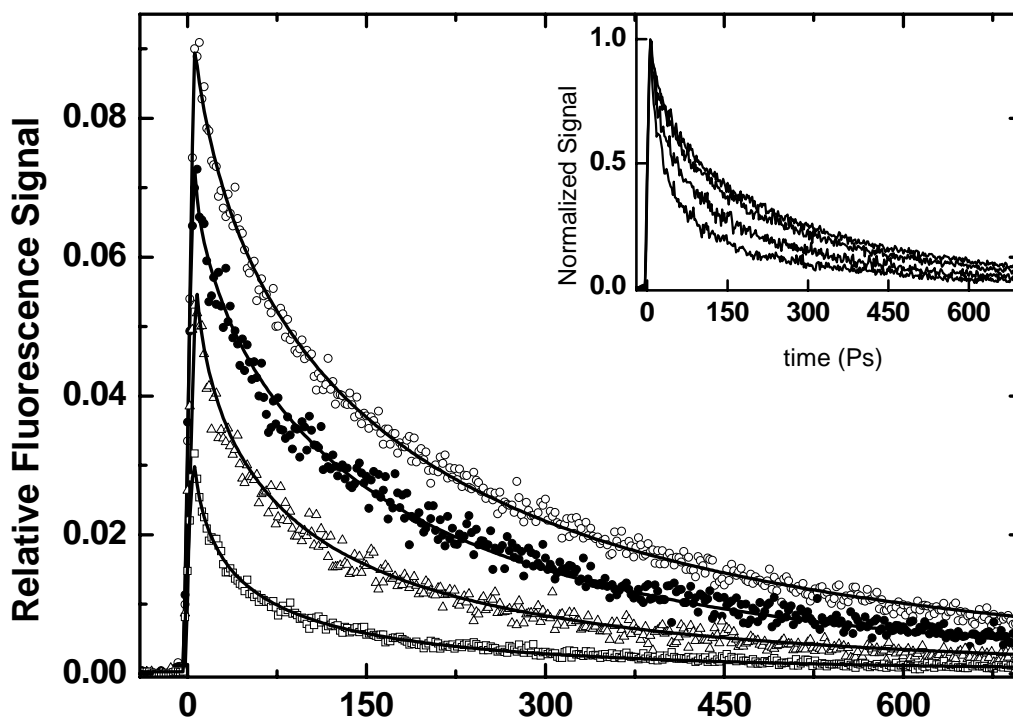


Figure 6-3. Time-resolved fluorescence of PPESO3 (34  $\mu\text{M}$ ) in MeOH for different HMIDC concentrations:  $\circ$  0  $\mu\text{M}$ ,  $\bullet$  0.4  $\mu\text{M}$ ,  $\triangle$  1.2  $\mu\text{M}$ ,  $\square$  5.0  $\mu\text{M}$ . Excitation at  $\lambda = 425$  nm, detection at  $\lambda = 450$  nm. See text for details. Inset: normalized fluorescence.

In addition, the clearly noticeable increase in the rate of the fluorescence decay with increasing HMIDC concentration (see inset, Figure 6-3) indicates that there is also a slow energy transfer process which may represent diffusion of the exciton to the HMIDC acceptor.

In order to model the decay kinetics of the PPESO3 fluorescence, both in the absence and presence of the HMIDC quencher, a stretched exponential function of the form in equation 6-1 was used:

$$I(t) = (1 - A_r) \exp\left[-\left(\frac{t}{\tau_0}\right)^{\beta_0}\right] \exp\left[-\left(\frac{t}{\tau_2}\right)^{\beta_2}\right] \quad (6-1)$$

where  $I(t)$  represents the fluorescence intensity at time  $t$ , the parameters  $\tau_0$  and  $\beta_0$  model the natural decay kinetics of the polymer (i.e., in the absence of quencher), and  $\tau_2$  and  $\beta_2$

model the dynamics of the slow energy transfer pathway. The  $\beta$  terms provide a measure of the width of the lifetime distribution ( $0 < \beta < 1$ , where the width of the distribution increases as  $\beta$  decreases). The term appearing in the pre-exponential,  $A_r$ , accounts for the reduction in the initial amplitude of the fluorescence, and it is attributed to a prompt quenching pathway (lifetime  $\tau_1$ ) which is so rapid that it cannot be resolved within the instrument response (i.e.,  $\tau_1 < 4$  ps).

The fluorescence decay of PPE-SO<sub>3</sub><sup>-</sup> in the absence of HMIDC is fitted by equation 1 with the decay time  $\tau_0 = 150$  ps and  $\beta_0 = 0.6$  ( $\tau_2 = \infty$ ). The observation of a stretched exponential decay for the polymer's fluorescence is not surprising in view of the fact that there is heterogeneity in the chromophores within the polymer chains (for example, due to a distribution of conjugation lengths caused by rotation around the Ph-C≡C bonds). In addition, studies of the fluorescence decay characteristics of phenylene ethynylene oligomers reveal complex dynamics on the 0 – 100 ps timescale associated with to solvation and conformational relaxation of the initially produced singlet exciton.<sup>170</sup> It is likely that similar processes occur in the polymer.

The decays obtained for solutions that contain HMIDC were fitted also using equation 1, holding  $\tau_0$  and  $\beta_0$  constant, and varying  $A_r$  (the amplitude of the prompt quenching pathway),  $\tau_2$  and  $\beta_2$  (the lifetime and width of the slow energy transfer pathway). The parameters recovered from the fits are collected in Table 6-1, and several trends are evident from this data. First, the amplitude of the prompt process ( $A_r$ ) increases significantly with increasing HMIDC concentration. Comparison of the value of  $A_r$  with the fraction of total emission quenched ( $F_q$ ) reveals that, on average, the prompt energy transfer process can account for more than one-half of the total

fluorescence quenching. This clearly demonstrates that a substantial component of the PPESO3-to-HMIDC energy transfer takes place on an ultrafast timescale (i.e.,  $\tau < 4$  ps). In addition to the ultrafast quenching pathway, the fits reveal that a second, slower energy transfer pathway is operative ( $\tau_2$  and  $\beta_2$ , Table 6-1). The time constant of this slow pathway decreases substantially with increasing HMIDC concentration, yet in all cases the lifetime distribution is broad as reflected by the fact that  $\beta_2$  is low (0.2-0.5).

The notion of energy transfer being active on two distinct timescales is confirmed by the temporal behavior of the HMIDC fluorescence. Figure 6-4 compares the decay kinetics of the HMIDC fluorescence for three different samples. First, excitation of a MeOH solution of pure HMIDC, with  $\lambda_{\text{exc}} = 636$  nm and  $\lambda_{\text{det}} = 663$  nm (at the maximum of the pure-dye emission), produces a fluorescence signal that rises within the instrument response and decays with  $\tau = 285$  ps (single exponential). This is the natural lifetime of the HMIDC dye in MeOH solution. Next, decays were obtained for mixtures of PPESO3 ( $c = 34$   $\mu\text{M}$ ) and HMIDC (1.2 and 5.0  $\mu\text{M}$ ). In this case the solutions were excited at 425 nm (PPESO3 absorption) with the HMIDC fluorescence detected at 685 nm. It is evident that for both solutions containing PPESO3, the decay rate of the HMIDC fluorescence is slower compared to the pure HMIDC solution ( $\tau = 1.2$  ns). The slower decay rate is believed to arise from a stabilization of the excited state of the dye upon complex formation with the PPESO3 chains. Of more interest is the fact that for both of the solutions containing PPESO3 and HMIDC, the rise of the dye's fluorescence features two distinct components. The majority of the HMIDC fluorescence signal rises with an instrument-limited response ( $\tau_1 < 4$  ps), confirming that a significant component of the PPESO3 to HMIDC energy transfer occurs on an ultrafast timescale. However, in

addition to the prompt rise component, both solutions exhibit a clearly resolved slow rise-time component, which corresponds to the slow energy transfer process resolved in the PPESO3 fluorescence decay experiments described earlier (characterized by  $\tau_2$  and  $\beta_2$ ). The solid lines shown in Figure 6-4 were generated by using the same kinetic parameters used to fit the PPESO3 decays (Table 6-1), which reinforces the hypothesis that the effect of HMIDC on PPESO3 fluorescence decay dynamics corresponds to an energy transfer process.

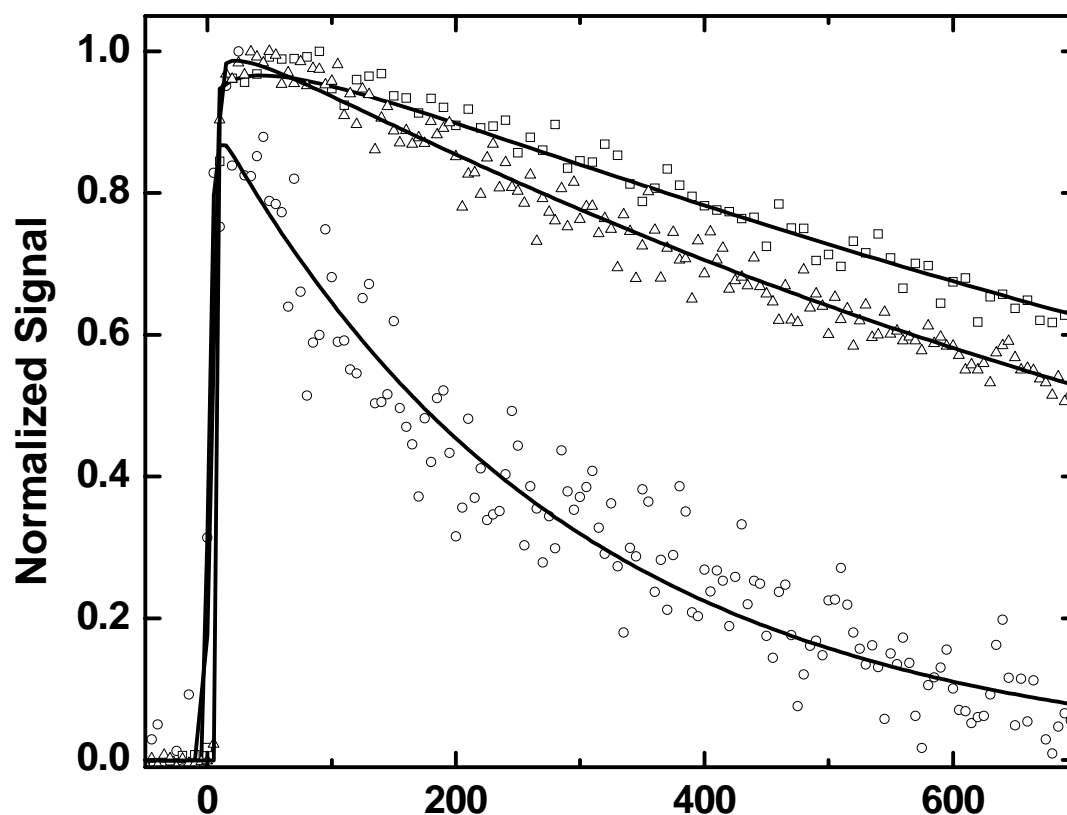


Figure 6-4. Normalized time-resolved fluorescence of HMIDC in MeOH.  $\square$  pure dye ( $\lambda_{\text{exc}} = 636 \text{ nm}$ ,  $\lambda_{\text{det}} = 663 \text{ nm}$ )  $\triangle$  HMIDC ( $1.2 \mu\text{M}$ ) + PPESO3 ( $34 \mu\text{M}$ ),  $\circ$  HMIDC ( $5 \mu\text{M}$ ) + PPESO3 ( $34 \mu\text{M}$ ). For the mixtures,  $\lambda_{\text{exc}} = 425 \text{ nm}$ ,  $\lambda_{\text{det}} = 685 \text{ nm}$ .

#### Comparison of Transient Fluorescence and Absorption Data

The fluorescence up-conversion experiments allow the study of the energy transfer dynamics from the photo-excited PPESO3 to the cyanine dye. Exciting the polymer at

425 nm and detecting the fluorescence of PPESO3 at 450 nm, allow us to follow the temporal response of the polymer's emission (Figure 6-5b). The topmost curve (0% quenching) corresponds to emission from the pure polymer in CH<sub>3</sub>OH. The other curves show the emission from the polymer in the presence of the dye for different dye concentrations. With increasing dye concentration the initial amplitude of the fluorescence decreases considerably. This amplitude reduction is assigned to energy transfer from the photoexcited PPESO3 to the dye, occurring on a timescale faster than the experimental time-resolution of about 200 fs. Additionally, at high dye concentrations leading to a steady state quenching of more than 50% (3 lower curves), the decay of the PPESO3 fluorescence becomes significantly faster, being reduced from about 250 ps for the pure polymer to 50 ps decay when 6  $\mu$ M of the cyanine dye are added (corresponding to a steady state quenching of  $\sim$ 80 %). In the following, we will refer to those quenching processes occurring much faster than the excited state lifetime of the PPESO3 as *prompt* quenching, whereas quenching taking place on the timescale of the excited state lifetime will be referred to as *gradual* quenching.

Contributions from both prompt and gradual quenching are also found in the transient absorption data, which allows monitoring the excited state population of PPESO3 and HMIDC simultaneously. The transient absorption of PPESO3 in methanol for different concentrations of cyanine dye is shown in Figure 6-5a (TA experiments are performed by Dr. Müller). Again the topmost curve corresponds to pure polymer while the other curves correspond to the TA signal in the presence of the quencher. Probing at  $\lambda=680$  nm (maximum emission of the dye), the pure polymer solution shows a positive transient absorption (an increase in the absorption of the sample).

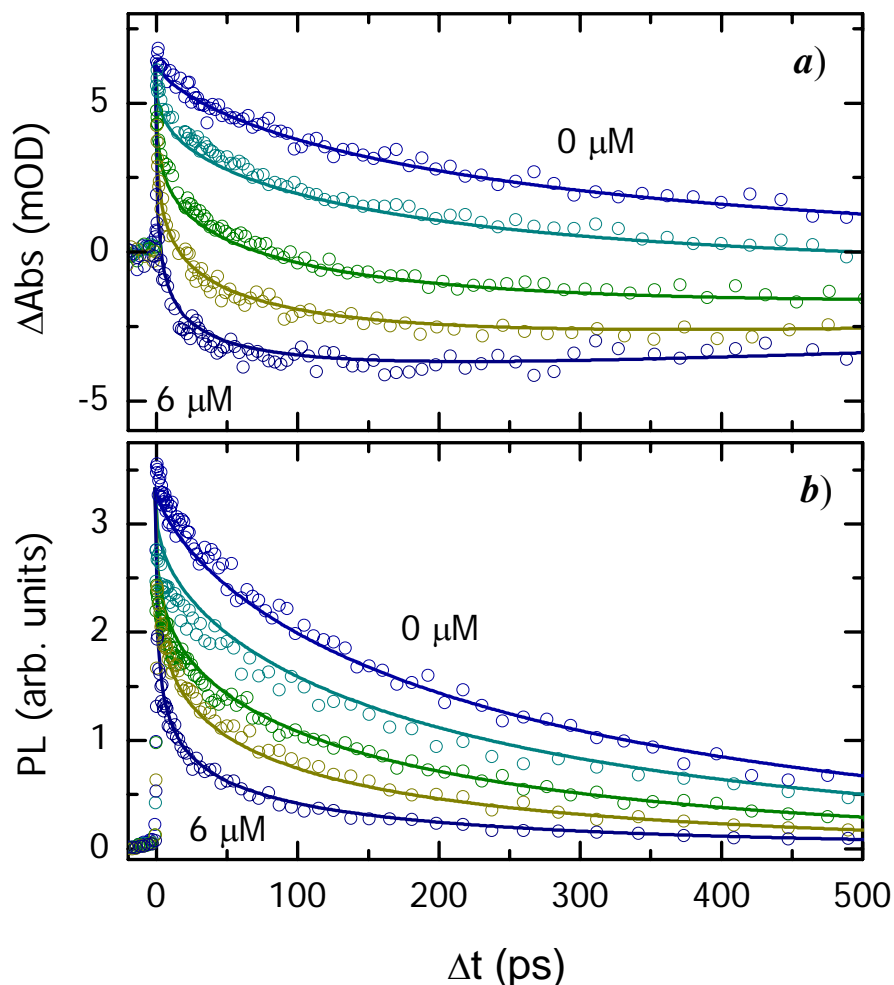


Figure 6-5. PPESO3 in MeOH for different concentrations of added HMIDC. The excitation wavelength is 425 nm. a) Transient absorption detected at a probe wavelength of 680 nm with  $[\text{HMIDC}] = 0, 0.65, 1.35, 3, \text{ and } 6 \mu\text{M}$ , and b) Up-conversion signal of fluorescence detected at 450 nm for  $[\text{HMIDC}] = 0, 0.65, 1.35, 3, \text{ and } 6 \mu\text{M}$ . Both plots present signal at magic angle. The results from the numerical calculations are shown as solid lines.

Figure 6-6 compares the time evolution of this photo-induced absorption (PIA) signal with the PPESO3 fluorescence decay. The similarity of these two curves allows us to attribute the transient absorption signal at 680 nm to absorption by the singlet exciton of PPESO3. In agreement with the fluorescence up-conversion data, the addition of HMIDC leads to a reduction of the PIA amplitude and decay time. Furthermore, in the presence of the dye the transient absorption data shows a crossover from PIA to a

negative signal (increased transmission) indicating either ground state bleaching or stimulated emission. At this probe wavelength, neither PPESO3 nor HMIDC absorb, and the polymer does not fluoresce; therefore the negative transient absorption is assigned to stimulated emission (SE) from excited HMIDC. Since direct excitation of dye molecules by the pump pulse at  $\lambda_{\text{pump}} = 425$  nm does not occur, the increase of SE with delay time reflects the energy transfer to the dye. Excitation energy leaving the polymer reduces the PIA from the PPESO3 (decrease of  $\Delta A$ ) while energy arriving on the dye enhances SE, again decreasing the measured signal  $\Delta A$ . The combination of both effects induces a strong change in the transient absorption signal and results in a high sensitivity to the energy transfer dynamics.

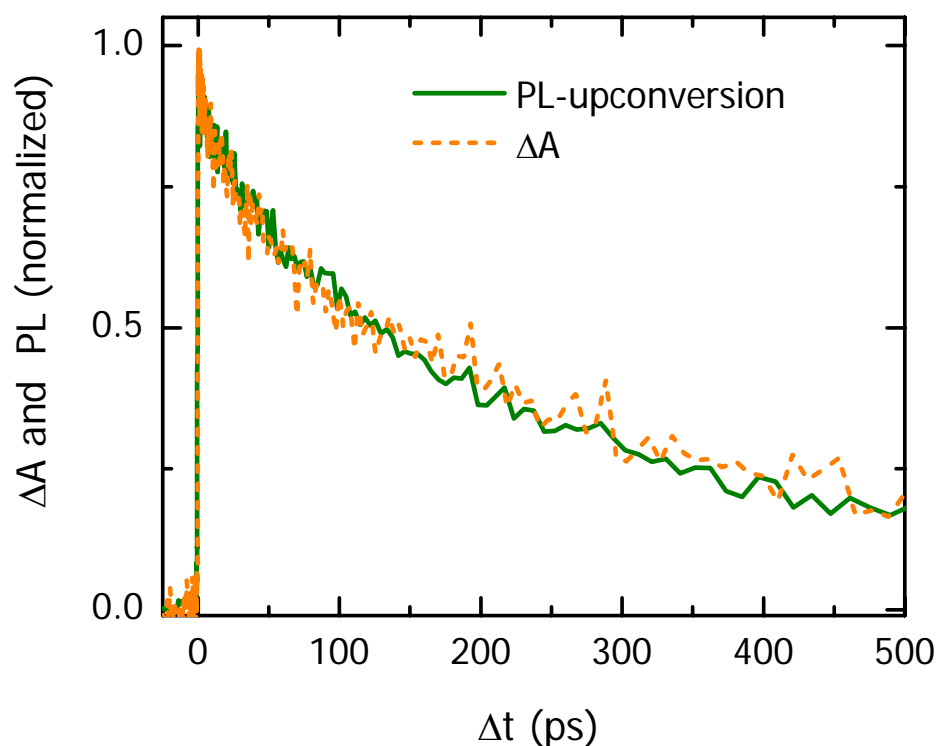


Figure 6-6. PL-upconversion (—) and  $\Delta A$ (- - -) of a pure PPESO3 solution. The signals have identical decay dynamics, showing that (i) both signals give the population of the first excited state of PPESO3, (ii) no significant energy transfer to aggregates sites with a lower radiative decay rate occurs.

### Anisotropy and Ionic Complexes

Figure 6-7a shows the anisotropy evaluated from the transient absorption data. The temporal evolution of anisotropy is obtained by evaluation of

$$r(t) = \frac{\Delta A_P(t) - \Delta A_S(t)}{\Delta A_P(t) + 2\Delta A_S(t)}$$

where  $\Delta A_P(t)$  and  $\Delta A_S(t)$  correspond to the transient absorption of the polarization oriented parallel or perpendicular to the excitation beam polarization, respectively.

The pure polymer sample features an anisotropy of  $r_0 = 0.3$  at  $\Delta t = 0$ , which is slightly lower than the theoretical value of  $r_0 = 0.4$  expected for a three-dimensional, randomly oriented ensemble of perfectly linear transition dipoles.<sup>144</sup> The reason for this lower starting value is probably an ultrafast energy transfer process occurring within the experimental time-resolution of ca 150 fs. After this initial decay, the further loss of anisotropy with time is a direct measure of the exciton hopping between conjugated segments of different orientation.<sup>163,171</sup> The large molecular weight of the polymer chain slows down the rotational diffusion, leading to an almost static orientation of the molecule on the sub-ns timescales discussed here.

The anisotropy decays within about 150 ps. A complete randomization of dipole orientations is expected to lead to  $r_\infty = 0$ , which is in contrast to the residual anisotropy of  $r_\infty = 0.05$  observed in the data. On the basis of the long-lived anisotropy decay we conclude that intrachain energy transfer on the polymer is active during the entire lifetime (250 ps) of the photoexcitations. The crossover from a fast initial decay to an extremely slow decay at larger time delays, however, indicates a significant slowdown of the hopping process with time due to energetic disorder within the CPEs, leading to trapping of the excitations.<sup>172</sup>

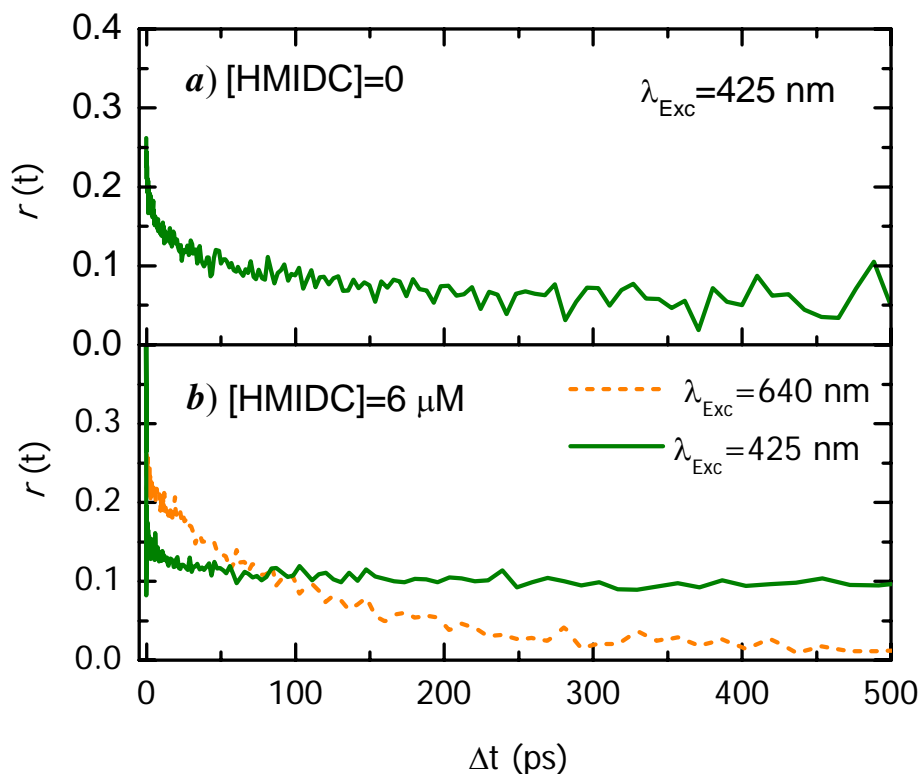


Figure 6-7. a) Time dependent loss of anisotropy for PPESO3 in CH<sub>3</sub>OH. Excitation wavelength is 425 nm (polymer absorption maximum); b) Time dependent loss of anisotropy for a solution of PPESO3 with 6  $\mu\text{M}$  of quencher, HMIDC. Excitation wavelength is 640 nm (-----) or 425 nm (—). Detection wavelength is 680 nm (measured from transient absorption) for all three curves.

Transient absorption anisotropy changes in the presence of HMIDC were examined to understand the role of HMIDC molecules complexed with the polymer vs. free dye molecules on the energy transfer. In the presence of 6  $\mu\text{M}$  of HMIDC (corresponding to  $\sim 80\%$  quenching of the steady state polymer emission) the anisotropy dynamics show a drastic change. Figure 6-7b shows the anisotropy detected after excitation with two different pump frequencies, leading either to direct or sensitized dye emission. While probing at 680 nm, which corresponds to the emission peak of the HMIDC we first excite the sample at 640 nm leading to direct excitation of the HMIDC (at this wavelength, there is no absorption by PPESO3). Consequently, under these conditions the transient

absorption signal is given exclusively by the stimulated emission of the dye, and the anisotropy calculated there from is the anisotropy of the HMIDC emission. The corresponding transient anisotropy plot in Figure 6-7b shows an initial anisotropy of  $r_o = 0.35$ , close to the theoretical expectation. The decay of the value of the anisotropy to  $r_\infty \approx 0$  shows a time constant of about 100 ps.

While still probing the dye emission ( $\lambda = 680$  nm), it is possible to investigate the anisotropy behavior after energy transfer by exciting the dye exclusively via energy transfer from the PPESO3. This is accomplished by tuning the excitation wavelength to 425 nm, where the PPESO3 absorption is high and the HMIDC absorption is negligible. Under these conditions, the time-dependent anisotropy shows an initial fast decay and then, for  $\Delta t > 50$  ps, the anisotropy of the sensitized dye emission remains about constant at a level of  $r_\infty = 0.1$ .

To understand the quenching mechanisms it is fundamental to answer the question: do free dye molecules in solution contribute to the quenching? We will first answer this question and then describe the PL-upconversion and transient absorption data quantitatively by comparing it to the results of the numerical simulation of the excitation hopping on PPESO3 chains with complexed HMIDC. An important outcome of the numerical simulations is that they provide the density of complexes along the polymer chain for the samples with different HMIDC concentrations. As we will discuss below, the computed complex density deviates significantly from expectations based on a constant complex association constant.

### Loss of Anisotropy and the Absence of Quenching by Free Dye Molecules

Figure 6-7b shows the anisotropy decay of the transient absorption signal measured on the PPESO3-HMIDC mixture. Due to the fast energy transfer to the dye, the transient absorption signal at  $\Delta t > 50$  ps is dominated by stimulated emission from dye molecules; the observed anisotropy therefore corresponds to the emission anisotropy of the HMIDC. Direct excitation of the dye leads to a high initial anisotropy of the dye emission of  $r_o = 0.35$ , decaying to  $r_\infty \approx 0$  with a time constant of about 100 ps. Any dye molecules in complex with the PPESO3 chain are expected to maintain their orientation during the timescales of interest here. Consequently, we attribute the anisotropy decay down to  $r \sim 0$  to the rotation of *free* dye molecules in solution.

Figure 6-5a shows that for the solution with highest dye concentration (6  $\mu\text{M}$ ) the energy transfer occurs very rapidly, and at  $\Delta t > 50$  ps the transfer from PPESO3 to the dye is almost complete. After completion of the energy transfer, the anisotropy of the sensitized dye emission shown in Figure 6-7b remains almost constant at  $r_\infty = 0.1$ . We conclude that the energy is exclusively transferred to dye molecules that are bound to the PPESO3 in an ionic association and cannot freely rotate, which justifies the neglect of quenching by free dye in solution. Note that this result is in contrast to previous studies on the quenching mechanism of a water-soluble poly(phenylenevinylene).<sup>160</sup>

The relatively high value of the residual anisotropy ( $r_\infty = 0.1$ ) obtained for sensitized dye molecules suggests that in the donor-acceptor complex the transition dipole moments of HMIDC molecules are aligned approximately parallel to the PPESO3 backbone. This is in agreement with the slight red-shift reported earlier<sup>159</sup> in the emission from the dye when PPESO3 is added to the solution, indicating that  $\pi$ - $\pi$  stacking

between the PPESO3 and HMIDC. The constant anisotropy of the sensitized emission from the complexed dye also shows that the polyelectrolyte chain does not significantly alter its orientation (through rotation) during the excited-state lifetime. This confirms our previous assumption that rotational diffusion of the polymer chain is much slower than the excited state lifetime and does not contribute to the anisotropy decay of photoexcitations on the polymer chain. It further implies that the sample volume in solution probed by the polyelectrolyte is much smaller than its radius of gyration, which is in contrast to previous reports.<sup>160</sup>

### Comparison of TA- and PL-upconversion Dynamics

The excitation hopping dynamics and hence the anisotropy decay can be strongly affected by the presence of energetic traps formed by interchain interactions in aggregates.<sup>173</sup> However, steady state spectroscopy provides no evidence for PPESO3 aggregates in dilute solutions in CH<sub>3</sub>OH.<sup>169</sup> This finding is corroborated by the comparison of the fluorescence-upconversion and transient absorption dynamics shown in Figure 6-6.

In polar solvents, conjugated polymers can form aggregates with radiative decay rates that differ from those of their unaggregated structures.<sup>174</sup> If aggregates are formed under the experimental conditions used in the present investigation, the energy transfer to the aggregates would be expected to change the radiative decay rate. The photoluminescence upconversion signal is given by  $PL_{up} \sim N(S_1) \cdot k_{rad}$ , where  $N(S_1)$  is the population number of excitations of PPESO3 and  $k_{rad}$  is the radiative decay rate. Assuming a time-independent cross section for the  $S_1 \rightarrow S_{n>1}$  transition, the photoinduced absorption measured in transient absorption is simply given by  $\Delta A \sim N(S_1)$ . Thus by

comparing fluorescence up-conversion and transient absorption dynamics makes it possible to determine if there is a temporal evolution in the radiative decay rate of the polymer. Since both  $PL_{UP}$  and  $\Delta A$  show exactly the same dynamics (Figure 6-6), the radiative decay rate must be constant in time. We conclude that energy transfer to PPESO3-aggregates with a lower radiative decay rate does not occur.

### Quenching Dynamics and the State Contribution

The fluorescence upconversion data shown in Figure 6-5b can be used to estimate the relative contributions of static and dynamic quenching. The temporal evolution of the fluorescence of PPESO3 in the presence of HMIDC normalized to the fluorescence of the pure CPE sample is shown in Figure 6-8. This emission ratio represents the amount of quenching at a given delay time. A ratio of 1 indicates that no quenching has occurred up to the given delay time.

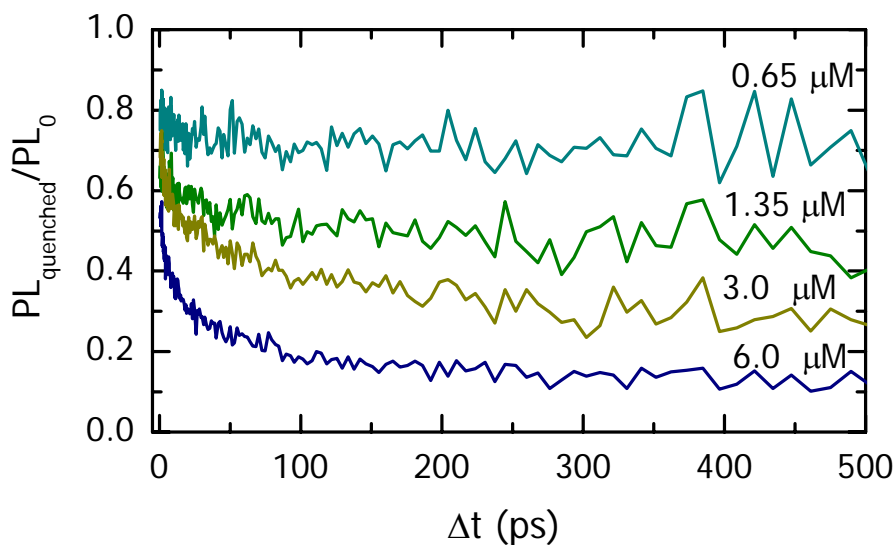


Figure 6-8. The photoluminescence yield of samples containing HMIDC, divided by the photoluminescence of the pure PPESO3 solution. The ratio is calculated from the upconversion data shown in Figure 6-5b and provides a direct description of the dynamic processes leading to quenching.

The lowest quencher concentration of  $0.65 \mu\text{M}$  corresponds to 25 % of the steady state (integrated) polymer emission being quenched by the dye acceptor. For this sample, at  $\Delta t \sim 0$  we observe a fluorescence ratio of 0.8, indicating that 20% of the emission is quenched within the experimental time resolution, therefore being regarded as static quenching. At increased delay time the fluorescence ratio appears nearly unchanged, indicating the lack of additional dynamic quenching. At increased quencher concentrations the fluorescence ratio begins to decay with time, revealing additional dynamic quenching. At the highest quencher concentration of  $6 \mu\text{M}$ , about half of the energy transfer is completed within the experimental time-resolution (static component), whereas the other half of the energy transfer occurs on a 50 ps timescale (dynamic component).

At increased quencher concentrations, the simultaneous presence of static and dynamic is expected to lead to a superlinear Stern-Volmer behavior.<sup>135</sup> Figure 6-9 shows the fluorescence signal taken from Figure 6-5b, integrated over time, and plotted versus dye concentration. This figure reveals a linear dependence of  $I_0/I$  as a function of dye concentration.

Considering a purely static quenching in a  $34 \mu\text{M}$  solution of the polymer, a fit to the Stern-Volmer equation suggests an association constant of  $\sim 7.2 \times 10^5 \text{ M}^{-1}$ . The time-resolved data allow us to draw an equivalent Stern-Volmer plot for the static component only. It is obtained by plotting the ratio of the fluorescence of the PPESO3 in the presence and the absence of dye at  $\Delta t = 0$ , also shown in Figure 6-9.

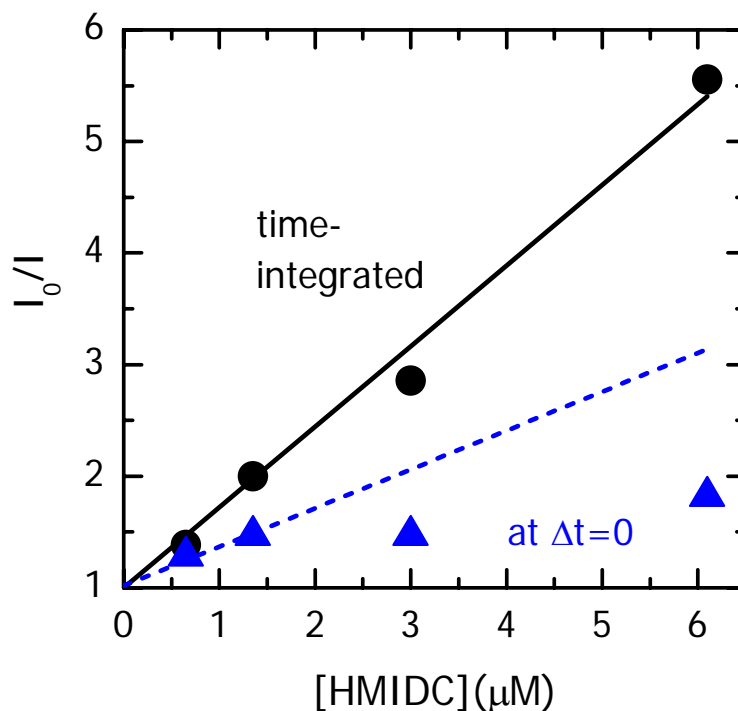


Figure 6-9. Stern-Volmer plot of the time-integrated photoluminescence (●) and the instantaneous photoluminescence ( $\Delta t=0$ , ▲) from the upconversion experiment. The instantaneous photoluminescence shows a strong saturation at quencher concentrations above 1.2  $\mu\text{M}$ .

Above a quencher concentration of  $\sim 2 \mu\text{M}$ , the quenching does not increase any further with increased HMIDC concentration. In the time-integrated Stern-Volmer plot, the saturation of the static quenching component “cancels out” the superlinear response expected from simultaneous static and dynamic quenching, and leads to an apparent linear increase of the steady-state (time-integrated) quenching with quencher concentration.

### Modeling

The quenching dynamics are affected both by the average distance between quencher complexes along the PPESO3 chain, and by the excitation hopping dynamics. In order to obtain information about the complex density on the CPE and the number of

monomers quenched by a single acceptor, numerical simulations of the intrachain excitation migration and quenching were performed by Dr. Jürgen Müller.

The quenching of mobile excitations on a one-dimensional chain with trap sites has been treated intensively experimentally and in analytical and numerical calculations.<sup>175-181</sup> Monte-Carlo simulations of the energy transfer in polythiophene and MEH-PPV found that the energy migration covers on average a region of 6 to 8 hopping steps around the originally excited conjugated segment, corresponding to a distance of about 30 nm.<sup>163,173</sup> The Förster radius  $R_0$  for energy transfer from PPESO3 to HMIDC is 49 Å.<sup>169</sup> This distance is smaller than but comparable to typical random walk distances (30 nm) indicating that direct Förster transfer can play a significant role in the energy transfer. Hence, in our numerical model, the quenching of PPESO3 photoluminescence by the complexed acceptor dye is assumed to occur *i*) due to the random walk of excitations on the polymer to the complex site, and *ii*) by a direct long range Förster-type transfer to the complexed acceptor molecules. Energy transfer to free dye molecules in solution can be excluded on the basis of anisotropy measurements as described in the results section.

The time-resolved PL-upconversion and transient absorption data are simulated. The free variables are the *disorder parameter*  $b$ , determining the excitation hopping dynamics, the average *complex distance*  $a_{\text{complex}}$ , and the *scaling factors*  $\eta_{\text{PL}}$  for the fitting of the photoluminescence -upconversion data, and  $\sigma_{\text{PPESO3}}$ , and  $\sigma_{\text{HMIDC}}$  for the fitting of the transient absorption data. Using a single set of parameters it is possible to fit the five independent PL-upconversion and transient absorption datasets.

The overall fits to all the samples with a unique set of parameters are shown as solid lines in Figure 6-5. Good agreement between the simulations and the experimental data was achieved for both the upconversion and transient absorption at all quencher concentrations. Table 6-2 summarizes the parameters used for all samples.

Table 6-2. Parameters and variables used in the numerical simulations and fitting of the time-resolved PL-upconversion and the transient absorption data.<sup>a</sup>

Fixed parameters		Variables	
$1/k_{PPESO3}^{(b)}$	250 ps	$b/kT$	0.8
$1/k_{HMIDC}^{(c)}$	1700 ps	$\eta_{PL}$	0.33
$\beta^{(\beta)}$	0.6	$\sigma_{PPESO3}$	1.47
$\tau_{hop,0}^{(d)}$	1 ps	$\sigma_{HMIDC}$	1.25
$cl^{(e)}$	6.1 nm		

<sup>a</sup> All parameters are identical for the different samples. <sup>b</sup> Obtained from the PL-upconversion of pure PPESO3 in CH<sub>3</sub>OH, <sup>c</sup> taken from ref <sup>169</sup>, <sup>d</sup> taken from ref. <sup>182</sup>, <sup>e</sup> taken from ref <sup>183</sup>

The distance between complexes formed along the polymer chain ( $a_{\text{complex}}$ ) obtained from the numeric modeling of the time-resolved quenching dynamics allows one to determine how many polymer repeat units are actually quenched by a single PPESO3/dye complex. The lowest dye concentration of  $[Q_0] = 0.65 \mu\text{M}$  leads to an integrated quenching of 25% of the polymer repeat units by forming one complex per 104 PRU (see Table 6-3). This corresponds to about 26 PRU (35.4 nm) quenched by a single complex.

Figure 6-10 shows the most important result of the simulations: the average distance between complexes on the PPESO3 chain. The left axis shows the complex distance in hopping steps ( $a_{\text{complex}}$ , in units of  $cl$ ) which is the natural unit used in the random walk simulations. By assuming a length of the conjugated segments ( $cl$ ) of about 8-9 phenylene ethynyls,<sup>183</sup> which corresponds to 4.5 polymer repeat units (PRU), the complex distance can be expressed in units of PRU (right axis in Figure 6-10). The

results of the numerical simulation range from about 23 segments (104 PRU) in the case of the sample showing the smallest overall quenching (dye concentration  $[Q] = 0.65 \mu\text{M}$  down to 6 segments (27 PRU) for the sample with the highest quenching concentration ( $[Q] = 6 \mu\text{M}$ ).

Table 6-3. Average distance between two acceptor molecules in complex with the PPESO3.

$[Q]$ ( $\mu\text{M}$ )	$a_{\text{complex}}$ (in segments)	$a_{\text{complex}}$ (in PRU) 1 segment = 4.5 PRU <sup>(a)</sup>
0.65	23	104
1.5	11	49
3	8	36
6	6	27

<sup>a</sup> These values are used to generate the curves shown in Figure 6-5. Taken from Ref. <sup>183</sup>

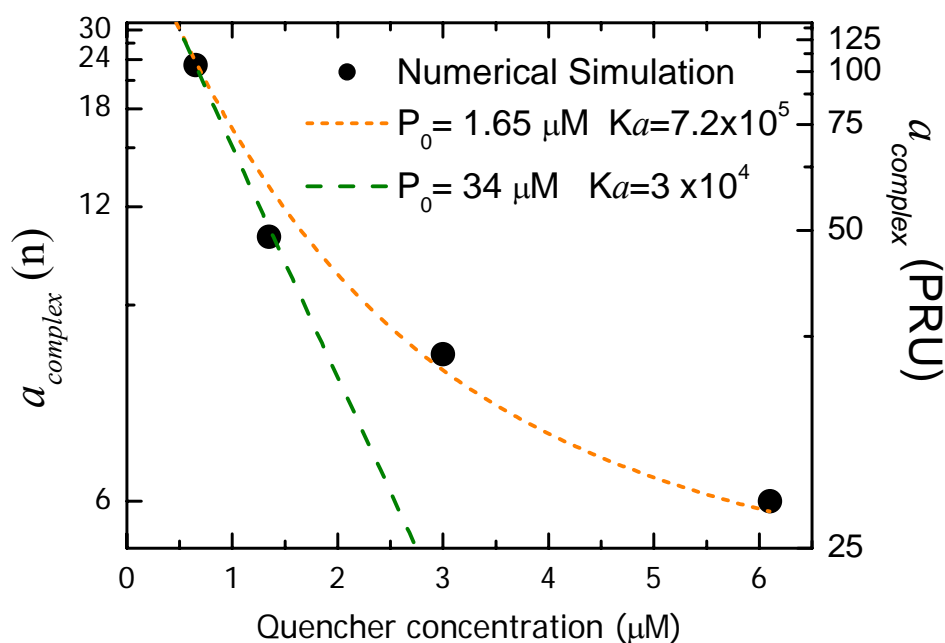


Figure 6-10. Average distance between quencher molecules complexed with the PPESO3 on a reciprocal scale as a function of the quencher concentration. The results from the numerical model are shown as solid circles (●). The linear regime (---) yields a relatively lower association constant. A good match between theory and the numerical results is achieved by using a reduced conjugated polymer concentration of  $[P_0] = 1.65 \mu\text{M}$  (---).

If we assume purely static quenching and a 1:1 PPESO3:HMIDC complex<sup>169</sup>, the distance between complex sites can also be evaluated analytically. Using the association equilibrium constant  $K_a$ , and the initial CPE and dye concentrations, we obtain the concentration of complexes in solution

$$[PQ] = \left[ \frac{[P_0] + [Q_0] + K_a^{-1}}{2} - \sqrt{\left( \frac{[P_0] + [Q_0] + K_a^{-1}}{2} \right)^2 - [P_0][Q_0]} \right] \quad (6-2)$$

where  $[P]$  and  $[Q]$  are the corresponding concentrations of uncomplexed molecules and  $[PQ]$  is the concentration of PPESO3:HMIDC complexes. This equation is derived assuming that all PRU are accessible to form PPESO3:HMIDC complexes. As shown below, this is apparently not the case for solutions with high dye concentration.

The ratio of the initial polymer concentration with the concentration of complexes,  $[P_0]/[PQ]$ , gives the average distance between the PPESO3/HMIDC complexes along the polymer chain in PRU, and is directly comparable to the complex distance  $a_{\text{complex}}$  obtained from the numerical model. Figure 6-10 compares the numerical simulation results and the ratio  $[PQ]/[P_0]$  obtained from the analytical expression for the association equilibrium. At dye concentrations below 1.2  $\mu\text{M}$ , the equilibrium equation from an assumed 1:1 PPESO3/HMIDC complex ratio leads to an approximately linear decrease of the inverse complex distance with increasing dye concentration.

Using a total polymer concentration of 34  $\mu\text{M}$ , equation 6-2 behaves linearly for  $K_a \sim 3 \times 10^4 \text{ M}^{-1}$ . This association constant is considerably smaller than the one obtained from the Stern-Volmer plot (Figure 6-9). At dye concentrations above 1.2  $\mu\text{M}$  the numerical results deviate significantly from the linear behavior predicted by a 1:1

PPESO3/HMIDC complex. The reason for this early saturation of complex formation is uncertain. It is clear from Figure 6-10 that, at high HMIDC concentrations, the number of complex formed is smaller than predicted by equation 6-2. One possibility is that at these high concentrations, more than one HMIDC molecule interacts with a given complex site. This would effectively increase the distance between complex sites. Attempts to fit the complex distance by considering complexes with different PPSO3/HMIDC ratios were unsuccessful though the simultaneous presence of complexes with one, two, or more HMIDC molecules cannot be completely ruled out.

The onset of the saturation corresponds to an average complex distance of  $\sim 30$  PRU. Given this large distance it seems unreasonable to attribute the effect to mutual electrostatic repulsion between complex sites. It is more likely that the effect arises due to formation of a loose aggregate of the PPESO3 chain, which effectively reduces the polymer surface area available to the dye in solution. Loose aggregates are defined as aggregates that contain both the polyelectrolyte and the counterions, as opposed to dense aggregates where different branches of the polymer are in Van der Waals contact.<sup>184</sup> Within these loose polyelectrolyte aggregates the electrostatic interactions between the quencher molecules might be changed. Note that the PPESO3 photoluminescence spectra clearly exclude significant electronic interchain interactions such as  $\pi$ - $\pi$  stacking of PPESO3 in dilute CH<sub>3</sub>OH solutions.<sup>169</sup>

A polymer surface reduced due to the formation of loose aggregates corresponds to an effective reduction of the polymer concentration available for complex formation with the dye. If we consider that the available concentration of PPESO3 to form complexes is smaller than the initial concentration  $[P_0]$ , we find a reasonable agreement between

equation 6-2 and the numerical modeling using an association value of

$K_a \sim 7.2 \times 10^5 \text{ M}^{-1}$  and a polymer concentration of  $[P_0] \sim 1.65 \text{ } \mu\text{M}$ . Apparently the tendency of the polymer chain to form loose aggregates lowers the quenching efficiency. In our previous studies<sup>169</sup> on the quenching of PPESO3 by cationic quenchers, we found that quencher induced aggregation of the conjugated polyelectrolytes increases the quenching efficiency significantly. In that case, it is the facilitation of the exciton dynamics through additional interchain hopping of the photoexcitations that enhances the quenching.

The modeling of the quenching dynamics allows the evaluation of the individual contributions to the energy transfer given by i) the random-walk of the excitation to the complex site and ii) direct (long-range) Förster-type energy transfer to the complex site. Figure 6-11 shows the time evolution of the integrated quenching for each mechanism for the samples quenched by 0.65 and 6  $\mu\text{M}$  HMIDC, respectively. For both samples, the random walk gives by far the largest contribution to the total energy transfer. Indeed, the random walk seems to be almost the exclusive pathway. The two contributions have distinctly different dynamics: the Förster part of the energy transfer rate is time-independent; it depends solely on the Förster radius and the complex concentration. In contrast, the random-walk mechanism is intrinsically time-dependent: the probability of an exciton to hop to a new, distinct segment, i.e. the probability of finding the quencher, decreases with time. This behavior is recognized in as a steady increase in the Förster contribution while an initial contribution followed by flat time dependence is observed for the exciton hopping mechanism.

The time dependence found in the random walk is a consequence of the quickly decreasing probability of an excitation to hop to a new, so far unvisited site. Even in the limit of a large separation of quencher sites, the probability to find a complex site decays by 75 % within only 10 hopping steps. Moreover, the decrease of the average excitation energy due to site disorder leads to a slowdown of the hopping rate by a factor of five within 10 ps. This extremely fast decay of the random-walk driven energy transfer leads to a large fraction of the energy being transferred on a timescale much faster than the

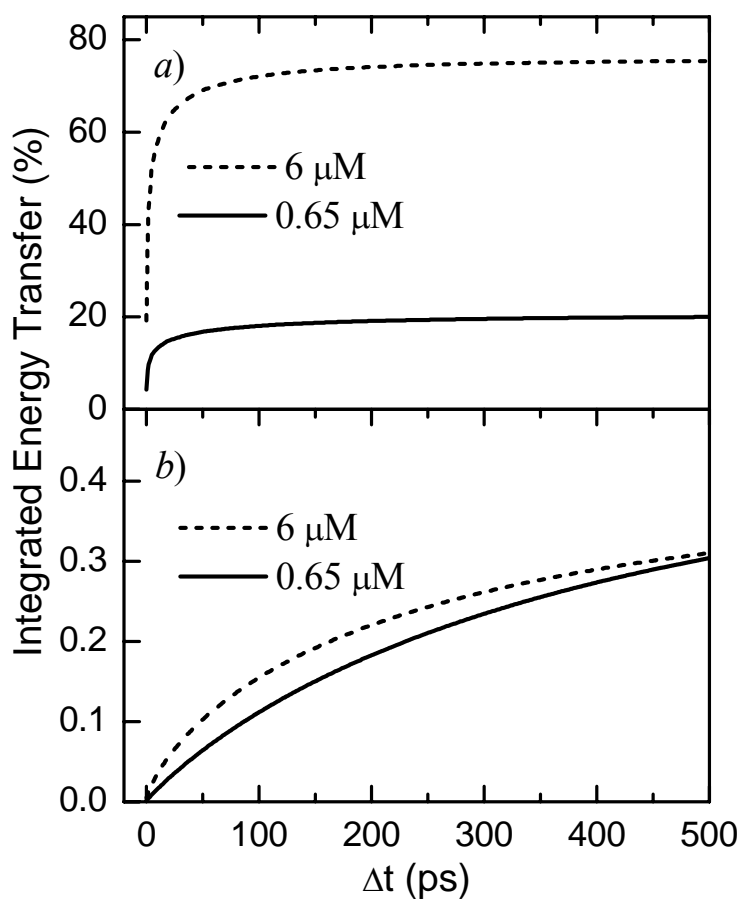


Figure 6-11. Individual contributions to the integrated energy transfer, random walk mediated (a) and direct Förster-transfer (b), versus time after excitation. For both samples (containing an acceptor concentration of  $[\text{HMIDC}] = 0.6 \mu\text{M}$ , and for  $[\text{HMIDC}] = 6 \mu\text{M}$ ), the random walk process dominates the energy transfer. The random walk driven energy transfer can be distinguished by the extremely fast decay of its transfer efficiency, leading to about 50% of the total quenching being completed within less than 1 ps.

intrinsic excited state lifetime of the donor. Accordingly, the fast excitation hopping is responsible for the dominating prompt quenching mechanism found in this material system. For example, for the high quencher concentration sample, at  $\Delta t = 5$  ps a 52 % (integrated) quenching has already occurred through the random walk of the excitations, while for the low quencher concentration sample the quenching by random walk has already reached 12%. For both samples, the contribution from the Förster mechanism is negligible on this time-scale.

The reason for the small contribution by the Förster long-range mechanism is the size of the exciton delocalization (conjugation length  $cl$ ) and its lack of time dependence. Due to the  $r^6$  dependence of the Förster mechanism, using a smaller  $cl$  parameter leads to a larger Förster contribution to the overall quenching. For example, for a  $cl$  corresponding to 4.5 PRU (8-9 rings) the numerical simulations show that at low quencher concentrations, the Förster contribution accounts for only 1.5% of the total energy transferred to the quencher. If instead we consider 3.5 PRU per conjugation length (7-8 rings), the Förster contribution rises to 25 % of the overall quenching. In the calculations presented herein we follow Kukula et al<sup>183</sup> and use 8-9 rings as the conjugation length (4.5 PRU). Though the Förster component contribution to the overall quenching is <2%, its time-independent characteristic implies that at long time-scales this mechanism is the major contributor to the quenching. However, on long time-scales Förster quenching must compete with the natural decay of the excitation, and consequently this transfer mechanism remains ineffective and it still does not contribute significantly. In conclusion, even if the  $cl$  is smaller than the 4.5 PRU used here, the

dominant mechanism responsible for the fast and effective quenching is the random walk of the excitations within the polymer chain.

As shown above, the amplification of fluorescence quenching in the PPESO3/HMIDC arises mainly from the rapid intrachain migration of excitons on the conjugated polyelectrolyte. A reduction of the site disorder would be expected to lead to significant reduction of excitation trapping, and thereby further enhance the fluorescence quenching efficiency. In our numerical model a vanishing disorder leads to a constant hopping rate. In the limiting case where a polymer could be prepared with no energetic disorder, the lowest dye concentration of  $[Q_0] = 0.65 \mu\text{M}$  would yield a fluorescence quenching efficiency of 97% instead of the 25% found experimentally. The quencher-complex concentration needed for 50% quenching decreases by a factor of five, corresponding to a dye concentration of only  $[Q_0] = 0.25 \mu\text{M}$ .

### Conclusions

The fluorescence quenching dynamics in a solution-based system have been investigated using the conjugated polyelectrolyte PPESO3 as energy-donor and the dye HMIDC as acceptor. Numerical modeling of ps time-resolved fluorescence up-conversion and transient absorption measurements was carried out on a number of samples with systematically varied quencher concentration. In general, the dynamics show that hopping of the photoexcitations to the complex sites is the dominating pathway for fluorescence quenching. Direct Förster transfer to the acceptor contributes only about 1.5 % to the total energy transfer at low quencher concentrations, and it becomes negligible at elevated quencher concentrations. Anisotropy measurements lead to the conclusion that all of the quenching occurs with dye molecules bound to the polymer

through ionic association. Simulations of the intrachain excitation migration allowed us to calculate the actual density of complexes formed between the ionic donor- and acceptor molecules. We found that at low quencher concentrations (below  $[Q_0] = 1.2 \mu M$ ) the polyelectrolyte-dye complex density scales approximately linearly with dye concentration, in accordance with the equilibrium equation for a 1:1 complex formation. At higher dye concentrations, however, a saturation of the complex density sets in. From the equilibrium equation this behavior would be expected at much higher concentrations, when the dye concentration becomes comparable to the monomer concentration of the polyelectrolyte. We suggest that the formation of loose aggregates of the polyelectrolyte leads to a strong decrease of the number of polymer sites that are available to form a complex with the dye. Since no spectroscopic signature of polyelectrolyte aggregate formation has been found, here the term ‘loose’ corresponds to aggregates with an interchain distance being too large to enable electronic interchain interactions (e.g.  $\pi$ - $\pi$  stacking), but small enough so as to prevent a steric barrier to complex formation. Satisfactory agreement of the complex densities predicted by the equilibrium equation and those calculated from the numerical simulations of time-resolved data is achieved, if the PPESO3 concentration used in the equilibrium equation is reduced by a factor of 20. The decrease of quenching efficiency induced by the formation of loose aggregates is in contrast to the increase of quenching efficiency usually found in case of the formation of dense aggregates in strongly polar solvents, where interchain migration of excitations is enabled.

The results also show that the factor limiting the fluorescence quenching efficiency is trapping of the photoexcitations on the PPESO3 conjugated polyelectrolyte. The

simulations suggest that a decrease of site disorder within the conjugated polymer chain well below  $k_B T$  should lead to an increase of quenching efficiency by a factor of 5.

## CHAPTER 7 SUMMARY AND PERSPECTIVE

Since the discovery of dendrimers first reported in 1985, there has been an immense set of developments in their synthesis, properties and applications. They represent a key stage in the ongoing evolution of macromolecular chemistry. Their success has been possible due to unique architectures with accurate positioning of chromophores. Some of the structures include numerous light-collecting chromophores that transfer their energy to a single energy “sink”. In that sense, a dendrimer is reminiscent of the architecture of natural light-harvesting complexes. To maximize the favorable energy transfer interactions, the selection of chromophores is as important as the design of each successive layer.

Conjugated dendrimers with a built-in energy gradient were studied throughout this dissertation. Our systems consist of symmetrical and unsymmetrical phenyl ethynylene (PE) dendrimers depending on the substitution at the branching point. We presented a detailed photophysical characterization of these dendrimers by both steady state and time-resolved spectroscopy. The goal of this study was to answer some fundamental questions regarding the time scale and mechanism for the energy transfer process. For example, can we attribute the absorption band structures to specific building blocks? What is the role of substitution at the branching point? Do excitations at the periphery migrate to the trap in a cascade manner, or are there direct jumps from the periphery to the trap? How can the intermediate steps be probed experimentally? What is the time scale and mechanism of the energy transfer?

Initial studies with a generation one didendron described in Chapter 3 showed that the presence of ortho and para substitutions in such unsymmetrical structures supports the initial exciton delocalization (unlike meta substitution). After excitation, a change in the excited state surface leads to localization, which is verified with the localized peak around emission wavelength. The built-in energy gradient results in very efficient energy transfer to the trap and yields a cascade mechanism occurring in a sub-picosecond (250-350 fs) time scale. Chapter 4 extended the investigation to include larger, generation two didendron which also revealed delocalization in the initially excited state. We found that while absorption is into delocalized exciton states, emission occurs from localized states. The excitation energy migrates to the trap through direct and indirect (multi-step) channels. Based on the kinetic model, almost 50% of the energy transfer occurs through the multi-step pathway, but the process is still completed in a sub-picosecond time scale. To our knowledge, we presented the first direct experimental measurement of energy migration as it goes through an intermediate state in a funnel-type dendritic structure. The process of rise and decay of the intermediate state population was observed by measuring the temporal evolution of the fluorescence at the emission wavelength of the intermediate state. This method provided an unequivocal proof of the vectorial nature of the energy transfer in a ladder-type structure. In addition, it was concluded that increasing the generation size for unsymmetrical PE dendrimers will increase and broaden the absorption while maintaining the highly efficient light-harvesting.

The symmetrical PE dendrimer was investigated with time-resolved spectroscopy as complementary to the theoretical and steady state measurements reported in the literature, and the results were described in Chapter 5. In contrast to the unsymmetrical

structures, due to meta branching, excitations are initially localized on single chromophore units, composed of 2-,3-,4- ring PE units. The transient absorption spectra following the selective excitations of these chromophores as part of the nanostar were compared with that of free PE units. Our data revealed energy transfer times from hundreds of femtoseconds to tens of picoseconds. Based on the developed kinetic model, we conclude that direct energy transfer takes place with 33.33% chance, while the cascade mechanism has 66.66% probability. We also compared our results, based on the spectral data, with theoretical calculations from the literature. We found a factor of 2-3 difference between the measured and the calculated values for the coupling strengths. This disagreement could be improved by a full treatment of Coulombic interaction using TDC and molecular dynamics.

In Chapter 6, an independent project is presented. We investigated the role of exciton hopping versus direct energy transfer mechanism within a system of conjugated polyelectrolyte and a cyanine dye. It was found that rapid intrachain energy migration towards the complex sites leads to highly efficient energy transfer, whereas the contribution from direct, long-range energy transfer is negligible.

As described in this dissertation, having an energy gradient is the key to create efficient light harvesters. For conjugated systems such as PE dendrimers, the substitution at the branching points, which actually defines the symmetry of the molecule, produce significantly different optical and photophysical properties. We showed that the extent of localization/delocalization of initial excitations depends on the conjugation, and the energy transfer times reveal the strength of the coupling between the chromophores.

The symmetrical dendrimer was proved to be a linear combination of individual PE components. Thus, comparing its dynamics with PE units of different size significantly helped to follow the energy migration. In order to identify the individual chromophores, if they exist, in the unsymmetrical structures, it is necessary to compare them with their corresponding analogs. Even though we did not have those analogs, our work based on time-resolved spectroscopy and careful model analysis explored the time scale and mechanism of the energy transfer. One of the experiments that could enhance our understanding of these systems would be fluorescence anisotropy measurements. The fluorescence anisotropy dynamics combined with isotropic time resolved and steady state spectroscopy may yield information about the interchromophore energy transfer character. The time scale of depolarization can be correlated with the excitation energy redistribution rate between the chromophores as this process is accompanied by the reorientation of the transition dipole moment. For example for delocalized excited states the energy transfer may be inferred as a coherent process and can be related to depolarization rate.

Molecular dynamic simulations performed by Krause and Roitberg groups at QTP showed that at room temperatures phenyl rings are free to rotate around the triple bonds. However, the rings lie essentially in the same plane at low temperature (77 K). This change in geometry has a significant effect on the transition density. Therefore, one of the future directions in our lab is to extend the time-resolved studies to low temperature. Another future enhancement is to use Transition Density Cube method for any dendrimer to obtain exact Coulombic interaction. Especially for unsymmetrical dendrimers, interactions among donor molecules might lead to similar characteristics as aggregated

molecular assemblies. In this case, the principles involved in the optimization of energy transfer are not revealed in a simple way by the absorption and emission spectra.

Recently, a generalized Förster theory was proposed in order to calculate rates of energy transfer in disordered molecular aggregates. In the future, modified forms of Förster can be adapted for modeling dynamics in multichromophoric dendrimers. At the present time, general design principles for efficient light harvesting structures can only be revealed by a combination of experiments and theory. Finally we hope that our discoveries presented in this dissertation open new possibilities in the design of synthetic light harvesters.

APPENDIX A  
THE FLUORESCENCE UP-CONVERSION TECHNIQUE

**The Excitation and Collection of Fluorescence**

The excitation beam is focused in one surface of the sample cell while the emission is collected from the other surface. As seen in the experimental layout (Figure 2-1), the sample is excited on the back surface. The excitation beam is aligned with a  $25^\circ$  with respect to the central axis of the off-axis parabolic mirrors so that it does not hit the parabolic mirror. First of all, this reduces the possibility of collecting and upconverting the excitation beam along with the fluorescence. Second, the time resolution is much better compared to same face excitation and fluorescence collection, since for fluorescence generated at different positions of the excitation beam, the accumulated changes in group velocity delay is compensated.

The fluorescence is collected by a pair of off-axis parabolic mirrors. The first parabolic mirror collects the fluorescence and collimates it, and the second parabolic reflector focuses the fluorescence into the crystal. The mirrors are 2" in the long axis and purchased from Janos Technology (part number, surface quality). The sample should be in the foci of the first parabolic mirror, while the BBO crystal is designed to be positioned at the foci of the second mirror. We put a pinhole where the sample is positioned and scattered pump beam was collected to check the alignment of the parabolic mirrors. The initial careful efforts to align these mirrors suggested that day to day alignment would be very hard, which will then question the reproducibility of the experiment. These two mirrors are  $90^\circ$ , meaning that the optical axis of the mirror and the

position axis of the foci are perpendicular to each other. As shown in Figure A-1,  $\theta=90^\circ$ , and the optical axis of the mirrors should be parallel to each other to image the fluorescence on the foci of the second mirror. The reflected effective focal length is 152.40 mm for both of the mirrors.

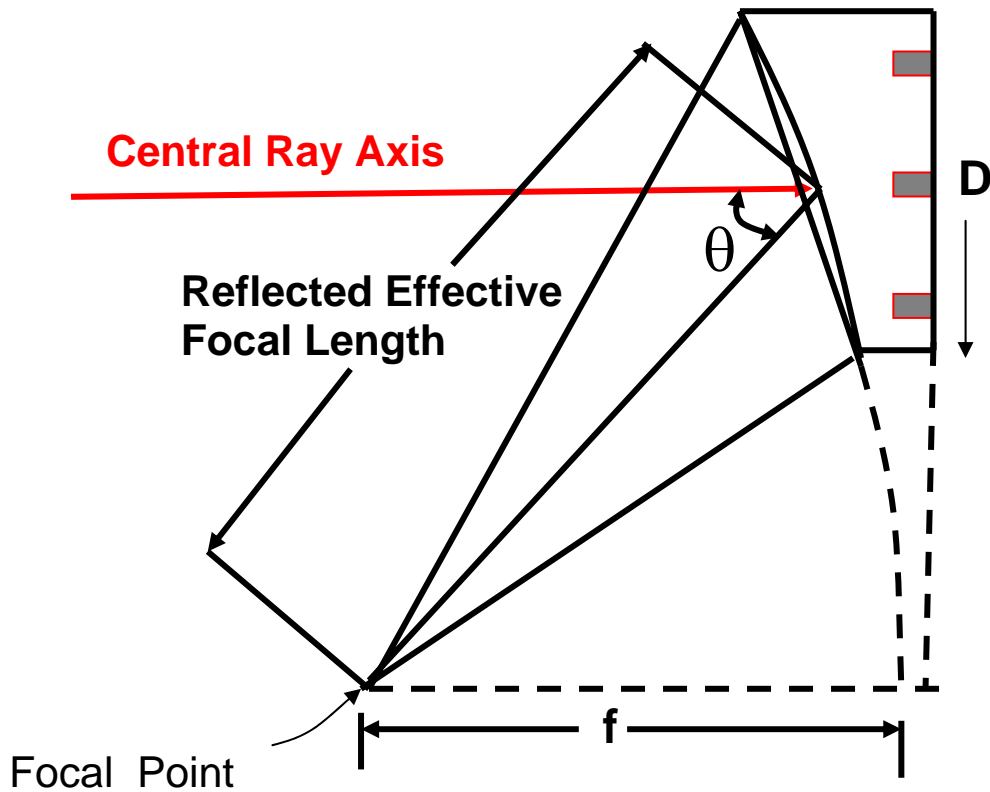


Figure A-1. Diagram of off-axis aluminum parabolic mirrors used to collect and image the fluorescence of the sample.

The position of mirrors with respect to each other is very crucial as well as their position with respect to sample and crystal. To circumvent this painful alignment, we contacted the Astronomy Department at UF, who uses very large off-axis parabolic mirrors for their research. Their expertise with such mirrors helped us to design the collection part of the experiment separately. The mirrors were pinned to homemade mounts and these mounts were pinned to an extremely flat tool plate after very careful

calculations of positioning with 0.01 mm accuracy. Once the mirrors are placed on the tool plate, they are never to be adjusted. This way, the mirrors are always aligned with respect to each other, and a lot of painful alignment time is saved. When aligning from scratch, the first step is to define the position of the sample cell. To begin, the pump beam is needed to define the location of the foci of the parabolic mirrors. It is absolutely crucial that the position of the pump beam is reproducible from one day to another. The pump beam is defined by several irises with fixed height, and they are the steady components of the setup without further adjustment. As shown in Figure A-2, three irises, separated by as large distance as possible, define the path of the pump beam. (Between the first and second irises, a waveplate and polarizer are placed). The first step each day should be aligning the pump beam through these 3 irises.

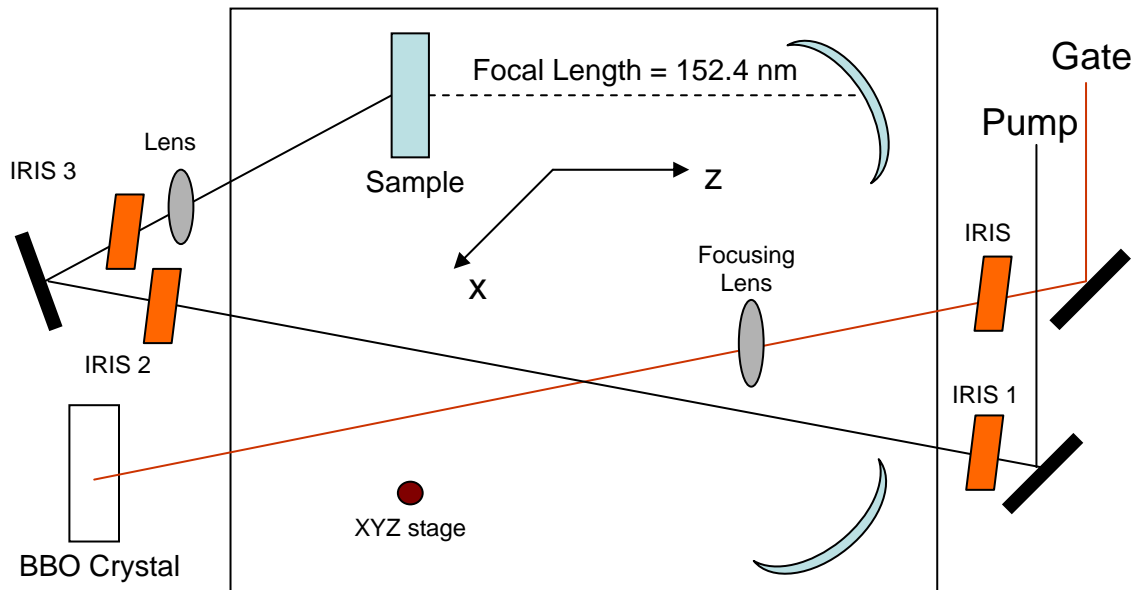


Figure A-2. Layout of the alignment beams and the collection by parabolic mirrors.

A steady mount holding a pinhole is restrained (with dowell pins) on the tool plate in a way that the pinhole would be exactly at the focus of the parabolic mirror 1 ( $f=152$  mm). At the focus of the second parabolic mirror, another pinhole in a steady (no x,y or z

adjustment) holder is placed. At this point, a quartz plano-convex lens with a focal length of 200 mm is used to pass the pump beam through the pinhole 1. The lens is mounted on a translation stage (only in z direction) and positioned to ensure that the pump beam is focused in pinhole 1, which represents the focus of the parabolic mirror 1. Using this pinhole is invaluable especially when trying to find time zero for the first time. Roughly 90% of the pump beam passes through a 100  $\mu\text{m}$  pinhole. There will be some scattered pump light at the pinhole, and the first parabolic mirror will collect and collimate it. Then the second parabolic mirror will focus the scattered light into the pinhole 2 (when you do this, please note that the collecting negative lens in the experimental setup is not in use). Basically, whatever light source is at the focus of the first mirror is imaged on the focus of the second mirror. The pump beam here does not hit the parabolic mirror and this significantly reduces the possibility of up-converting excitation beam on top of real fluorescence signal. By doing the alignment described to this point, it is ensured that the pump beam is defined and the off-axis parabolic mirrors are positioned accurately.

The next step is putting the xyz translation stage holding a mount compatible for both a pinhole and sample cell on top of the tool plate. Before doing so, the steady mount holding the pinhole at the focus of first parabolic mirror should be removed. Without changing or replacing anything else, the pinhole in the translation stage should replace the position of the previous pinhole. The xyz stage will be aligned so that the scattered light is still collected and focused on the second pinhole. The mount in the stage has been designed in a manner that the pinhole can be removed and the sample cell is easily placed in exactly the same position. Alignment of the pinhole with the translation stage guarantees that the center of the sample cell is at the focus of the mirror.

Even though the original idea was to put the nonlinear crystal at the focus of second mirror, our investigations showed that for a better phase matching the solid angle between the fluorescence and the gate beam should be smaller. Thus, a negative lens ( $f=-200$  mm) was used between the second parabolic mirror and the nonlinear crystal. The lens was mounted to a xyz stage placed on the tool plate. The upconversion crystal was placed about 350 mm apart from the mirror. This crystal can be easily replaced with a pinhole for alignment purposes, especially when overlapping the fluorescence and gate beams spatially.

One should try to find time zero for the sum frequency generation with the scattered light from the pinhole where the sample is positioned. However, in order to fine-tune the negative lens' position, a very concentrated solution of a dye molecule can be used. We usually used perylene or a very fluorescent polymer (PPE-SO<sub>3</sub>). The fluorescence that is collected and focused should be easily visible when the room lights are off. The fine-positioning of the sample cell can be adjusted so that the pump beam focuses approximately in the center of the cell. If not, there might be some scattered light from the walls of the cell, even some white light generation if the focus is really tight. Since a small volume of the sample is always excited, the fluorescence can not be accounted as a point source. When focused, the shape of the fluorescence is always a bit unclear, but there is a clear region where the fluorescence is accounted as tightly focused as possible.

So far, the pump beam and fluorescence from a real sample are aligned. The sample cell position should not be touched anymore, most critically in the z direction. Later on

you can move in x-y direction to get a better spot on the cell, or sometimes an air bubble will appear in the solution and it is best to avoid this bubble during long scans.

### **Alignment of the Gate Beam and Upconversion Crystal Phase Matching**

The alignment of the gate beam is more straightforward. The residual 800 nm beam of an OPA is used as gate (except SHG of signal used for the experiments explained in Chapter 3). It passes through a delay stage (Physik Instrumente, M-531-DD, Resolution 0.1  $\mu\text{m}$ ), a waveplate, and a polarizer. All gold mirrors are used for optimum spectrum, power and reflectivity. The gate lens ( $f=300$  mm) is placed on the tool plate. The shorter focal length gives a tighter focus, hence a greater upconversion efficiency. However, the focal area the gate beam should not be smaller than the focal volume of the fluorescence on the crystal. We obtained higher upconversion efficiency when the size of the gate beam was similar (slightly larger) to the size of fluorescence. The gate lens, also on the translation stage, should be positioned to optimize the upconversion efficiency, being careful not to focus the gate beam on the BBO crystal (if focused too tight, it will burn the crystal).

As mentioned before, the negative lens used to focus the fluorescence allows the solid angle between the gate and fluorescence to be minimized, providing the best phase-matching condition in the nonlinear crystal. Nevertheless, this angle should not be too small since this will make the spatial separation of the up-converted fluorescence and the 400 nm scattered light (from the SHG of the gate beam in the upconversion crystal) more difficult. In addition, there might be cross-correlation signals, especially when the measured fluorescence wavelength is very close to the excitation wavelength.

The pinhole is carefully placed in exactly the position as the upconversion crystal and the gate beam is aligned and focused through it. As mentioned previously, it is wise to use the pump scatter to find time zero. When the pump and gate beam foci are ensured to overlap spatially, both of them will pass through that pinhole. Then the upconversion crystal is placed (replacing the pinhole) and with a translation stage you can move it along the z axis to exactly obtain the same spatial overlap. The gate beam is vertically polarized and it controls the polarization angle of the crystal. The phase-matching angle will be optimized when the crystal is rotated around the vertical axis.

Usually the sum frequency of the pump and gate beam is visible to the eye. However, if both the crystal angle and the time zero are not known, one can approximately find the crystal angles by finding the second harmonic generation (SHG) of the pump and gate beam independently. These SHG signals should appear easily as long as they are not in the deep UV region. The phase-matching angle for sum frequency mixing is approximately in the midway between the angles for doubling of each beam. For the experiments performed for this dissertation, the pump beam was usually below 400 nm, where doubling with type I BBO crystal was not possible. Instead, when we did not know either phase-matching angle or time zero, we set the OPA output to be the same wavelength as the fluorescence and obtained SHG of that beam. This will be very useful when trying to get real signal from the sample. After the time zero is set, the OPA is aligned to produce the pump wavelength (usually only angle tuning of the crystals in the OPA is enough to switch between real pump and fluorescence wavelength). The only variable is then the phase matching angle for the pump beam. Once the mixing signal is seen or detected via the PMT, the gate beam can be tweaked, and the position of the

crystal and the delay stage can be adjusted to optimize the signal. It is important to recall that once the pump beam is aligned, it should not be adjusted.

We can summarize what has been done so far if one follows the procedure described here: First, the pump beam is aligned through the irises and the pinhole where the sample cell will also be positioned. The parabolic mirrors are never to be moved. The gate beam is tightly focused 2-3 cm after the crystal position with the pump beam and carefully overlapped with the pump using a pinhole. This pinhole is then replaced with the upconversion crystal and time zero is found scanning the delay stage. In any case, for every experiment, the phase matching angle, the spatial and temporal overlap of the beams would require a little bit of tweaking.

### **Detection of Upconverted Fluorescence**

After the upconversion crystal, there is an iris rejecting the cross-correlation and any other scattered light, such as the SHG of 800 nm. Then, a quartz lens is positioned to collimate the signal, which is always in the UV. Two UV enhanced aluminum mirrors direct the signal to the monochromator. After the crystal, one can use any filters and dielectric optics to get as many photons as possible to the detector since the time resolution is not effected by the optics after the crystal. The time resolution is only determined by the mixing process in the crystal as well as the optics before the crystal. Before the monochromator there is another lens that will focus the signal onto the entrance slit. One issue is that as the signal gets closer to the 400 nm, there will be more background due to 400 nm generated at the upconversion crystal. Even though the photons are not traveling in the direction of the signal, there will always be enough 400 nm photons reaching the detector. To minimize this contribution, we use UG-11 filters and a solar blind PMT that has only 0.01% efficiency around 400 nm.

### UV-Light Compression

For most of the experiments, the pump pulse was generated in the UV region from the fourth harmonic generation of either the signal or idler output of an OPA. The measured cross-correlation showed that the time resolution of the upconversion experiment is around 400-500 fs without any pulse compression. Despite the broad tunability of the OPA, it generates very long UV pulses with very narrow bandwidth. The width of the UV spectrum is limited by the thickness of the BBO crystal (second BBO in the OPA, 0.5 mm) due to phase matching. Having a 2-3 nm bandwidth makes it even harder to compress these UV beams, but in order to obtain an adequate amount of pump energy it is necessary to use a crystal of such a thickness. The compression of the pulses to a minimum duration is performed via UV grade isosceles fused silica prism pair (CVI, catalog Number: IB-12.4-69.1-UV). The apex angle of the prism is cut such that the angle of incidence is the Brewster angle at the incident wavelength. Thus, reflection losses for p-polarized beam are extremely small and transmission efficiency is 98 %. The OPA output between 300 and 400 nm is horizontally polarized (FHG of signal), so the loss due to prisms is minimal. This prism compressor transmits 92% of the incoming UV beam. The compressed UV pulses are used as the pump beam and the typical cross-correlation (CC) signals are measured as the sum frequency generation of pump pulse with the gate pulse. The pulse width of the gate beam is measured via autocorrelation. The values for the pulse length of the UV pump pulses can be calculated from the width of the CC signals. The value of the measured CC signal is important because it presents the time resolution of the experiment. It is possible to achieve 225 fs FWHM of CC signal when the pump beam is 310 nm. Using a prism compressor for UV pulses definitely helps with improving the time resolution of the upconversion setup.

The time-resolution of the setup is basically limited by the temporal width of the optical gating and the excitation pulses. However, for subpicosecond pulses in our system, the group velocity dispersion (GVD) induced by the nonlinear upconversion crystal and by the various optics will most probably alter the time resolution. Therefore, we try to use a thin nonlinear crystal (0.3 mm thick), along with the parabolic mirrors (instead of lenses, or any other transmitting optics) for the collection of luminescence.

## APPENDIX B DATA ANALYSIS

### **Analysis of Transient Absorption Changes**

We use broadband transient absorption spectroscopy to monitor the energy transfer towards a particular trap. Absorption change  $\Delta A$  induced by a first exciting light pulse is recorded as a function of wavelength by a second delayed probe pulse at time  $t$ . Recording the difference spectra over a long observation time (femtoseconds to milliseconds) results in a two dimensional array with many individual data points. In order to deduce reasonable information out of the raw data, models has to be used to describe the photophysical event. The model parameters such as time constants are determined by fitting the model to the experimental data points. In many cases, the reaction schemes can be simulated by a sequence of intermediate states with well-defined absorption spectra and time components. In this appendix we will discuss a numerical procedure called Singular Value Decomposition (SVD) method used for data analysis.

The absorption change defined as  $\Delta A(\lambda, t) = A(\lambda, t) - A(\lambda, 0)$  is a continuous function of the probe wavelength  $\lambda$  and the delay time  $t$ . By changing the settings of spectrometer/detector, and time delay between excitation and probing pulses, this continuous function becomes a matrix  $(A_{ij})$ , where the absorption changes at fixed probe wavelengths  $\lambda_i$  form the columns and those at fixed delay times  $t_j$  form the rows:

$$\Delta A(\lambda_i, t_j) = (A_{ij}) .$$

In a typical time-resolved absorption experiment, the matrix  $A$  will be built up of  $N_\lambda$  probe wavelengths and  $N_t$  delay times. The wavelength range used in the experiment

is from  $\sim 300$  nm to  $\sim 580$  nm with spectral resolution of 0.275 nm. In order to consider kinetics extending over several orders of magnitude, we use logarithmically-spaced time delays from  $\sim 30$  fs to 20 ps. We first plot certain rows or columns of this data matrix by a Labview program developed in our lab (by J.Mueller). Comparing different rows, one can see how the spectrum relaxes in time. The absorption difference as a function of time at a fixed wavelength can be observed by plotting a certain column of A. These two visual examinations of the data (especially with the mentioned Labview program) provide the experimentalist with a first guess on the involved processes, i.e. time constants, spectral characteristics. These visually obtained results are then supported and expanded by SVD.

SVD is a powerful matrix technique that filters out experimental noise and identifies the independently evolving transient species from the difference spectra. We use the SVD algorithm in MATLAB. The data matrix  $(A_{ij}) = \Delta A(\lambda_i, t_j)$  is decomposed into the product of three matrices

$$A=U.S.V^T$$

Where U and V are orthogonal matrices of dimensions  $N_\lambda \times N_t$  and  $N_t \times N_t$ , respectively. S is an  $N_t \times N_t$  square diagonal matrix, containing the singular values. Each of these values determine s how much the corresponding columns of U and V contribute to the reconstruction of A. For an intuitive understanding of SVD, note that U and V are the matrix eigenvectors for  $AA^T$  and  $A^T A$ , respectively. The singular value of A are the square roots of shared eigenvalues E of  $AA^T$  and  $A^T A$ , which are the diagonal elements of S. The mathematical relationships follow as:

$$AA^T = U.E.U^T,$$

$$A^T A = V \cdot E \cdot V^T, \text{ and}$$

$$S = E^{1/2}.$$

$N_\lambda \times N_\lambda$  matrix  $AA^T$  contains overlap of kinetic vectors for all pairs of wavelengths, while  $N_t \times N_t$  matrix  $A^T A$  contains time-pairwise overlap of spectral vectors. Thus, the columns of  $U$  contain the minimal set of orthonormal basis for the row space of  $A$ . Likewise, the columns of  $V$  contain the orthonormal basis for the column space of  $A$ . Hence, SVD identifies the mathematically independent bases of data, spectrally in  $U(\lambda)$  and temporally  $V(t)$ . We select the usable components of  $U(\lambda)$  and  $V(t)$  and determine the number of components contributing to the set of spectra from the magnitudes of the singular values of  $A$  (diagonal elements of  $S$ ). In the absence of measurement noise, the number of independent components would equal the number of non-zero singular values. However, all singular values are non-zero in the real experimental data. In most cases the magnitude of singular values, combined with the evaluation of shapes of the corresponding column vectors of  $U$  and  $V$  will provide enough information to find the number of components. If this is not the case, certain statistical tests can be applied to find the number of components.

It has to be pointed out that SVD is a purely mathematical method for determining the number of independent vectors in a matrix. As a result, chemically different species that have either equal spectra or equal kinetics will show up as one component. Another remark that should be made is that SV is in principle not suited for components whose spectra shift and/or broaden in time.

We first identify the dominant singular values, which could be an extremely difficult decision. The number of dominant singular values determines the number of

time constants used to describe the data. For example, during the SVD analysis of 2G<sub>1</sub>-m-OH molecule, it was hard to decide the number of singular values. The initial visualization of the data with Labview, and a simple, yet very useful, technique reported for the inspection of two dimensional data sets from transient absorption spectroscopy helped to obtain reasonable starting information for further numerical treatment. We observed a 5-6 ps vibrational relaxation component resulting in a spectral shift. This component is removed from the data set. When SVD is applied again on the new data set, it reveals reasonable number of singular values. Thus, we only have two relevant SVD components for 2G<sub>1</sub>-m-OH data: column vectors U<sub>1</sub> and V<sub>1</sub> associated with singular value S<sub>11</sub>, and column vectors U<sub>2</sub> and V<sub>2</sub> associated with singular value S<sub>22</sub>. Thus, we can reduce the A matrix and express it as the following:

$$\Delta A(\lambda, t) = U_1 \cdot V_1^T + (S_{22}/S_{11}) U_2 \cdot V_2^T$$

We apply a kinetic model, which has well-defined population dynamics for each state. The time constants are obtained and we can reconstruct the noise-filtered absorption spectra at any delay time. We try to minimize the difference between the reconstructed data via the model, and the actual data in two dimensions.

The following section shows the SVD analysis of the molecules investigated through this dissertation and the difference absorption spectra at any delay time is reconstructed using the kinetic models proposed in Chapters 3,4 and 5 for the relevant molecules.

**2G<sub>1</sub>-m-OH**

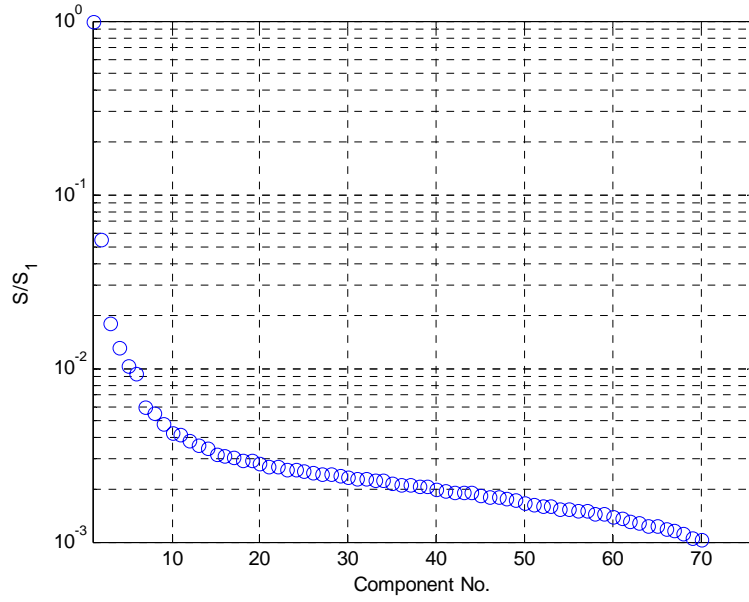


Figure B-1. Singular values

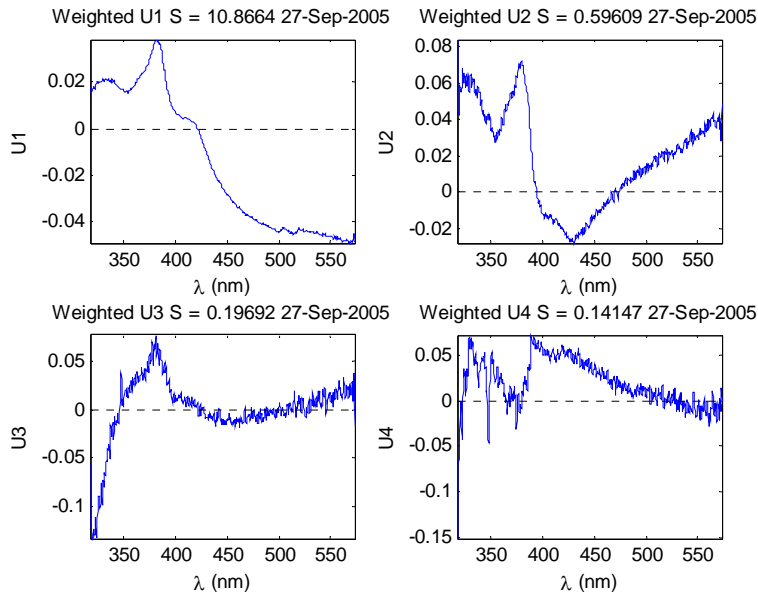


Figure B-2. Transient spectra of SVD output.

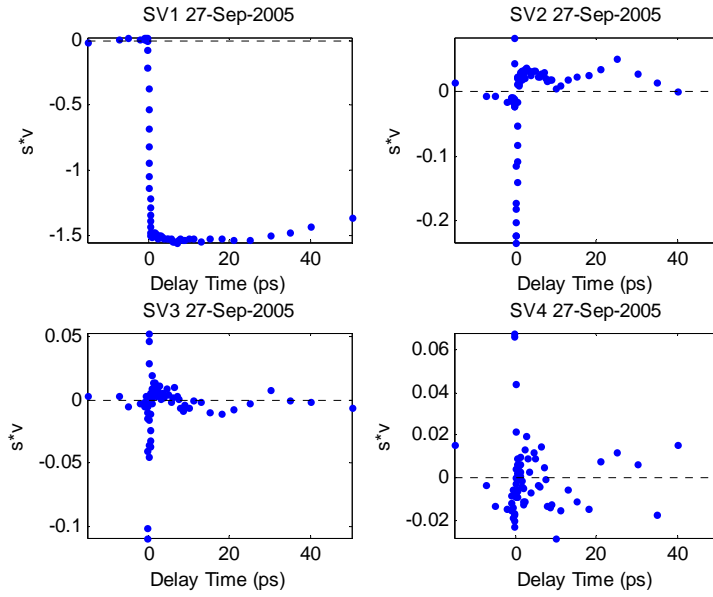


Figure B-3. Dynamics of SVD output.

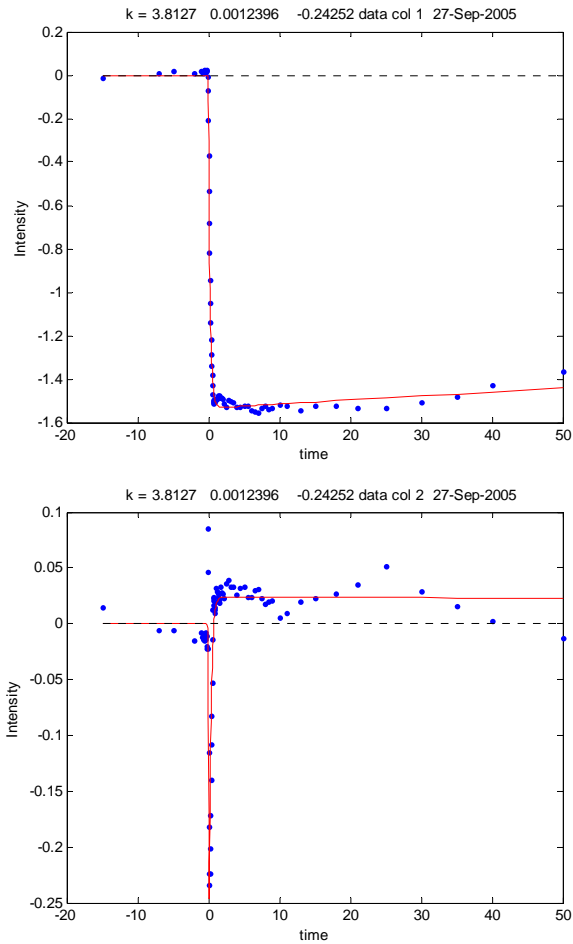


Figure B-4. Model fits for the relevant components with large singular values.

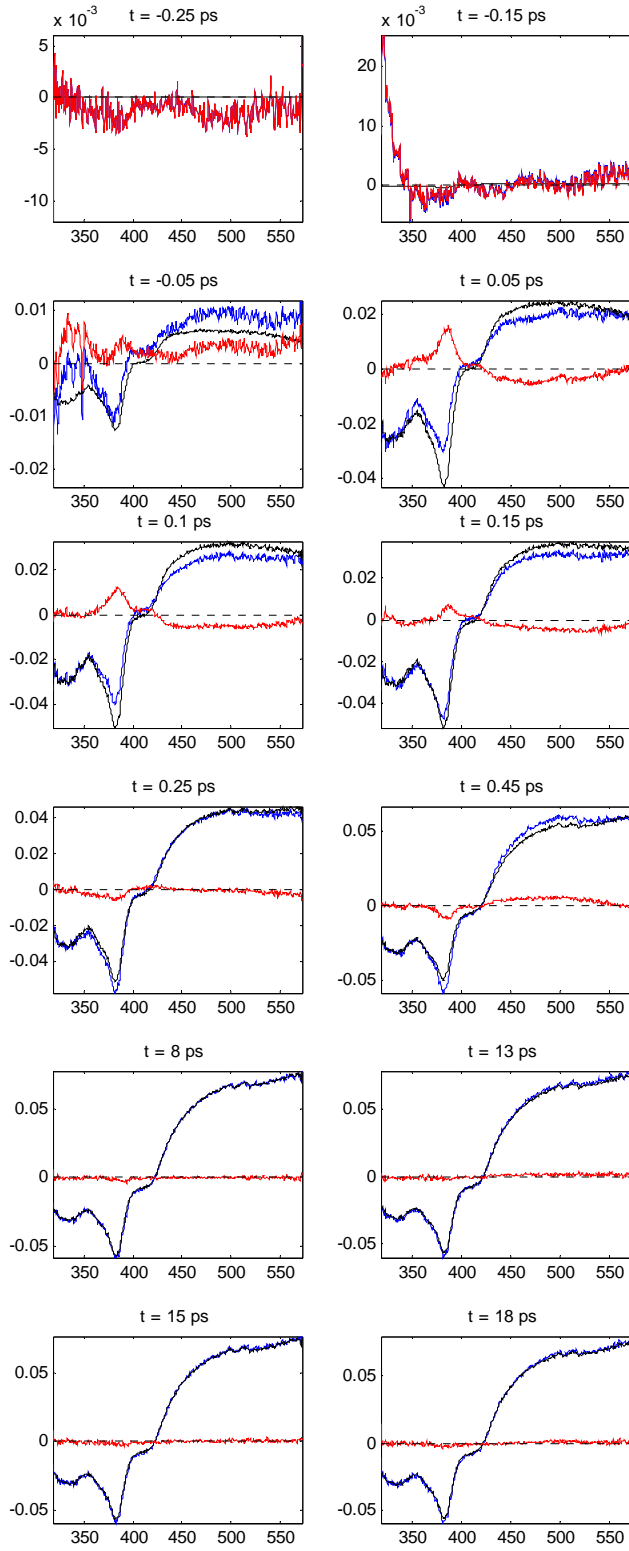


Figure B-5. Reconstructed versus real  $\Delta A$  as a function of wavelength.

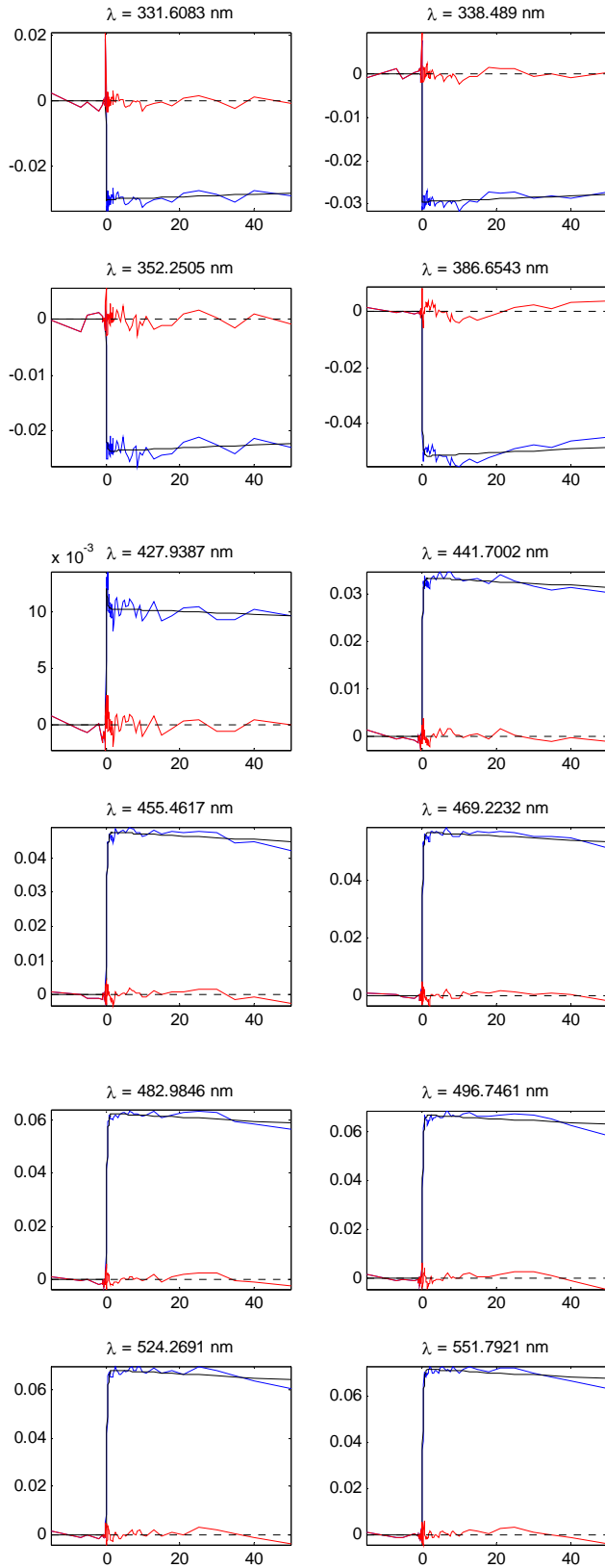


Figure B-6. Reconstructed versus real  $\Delta A$  as a function of time.

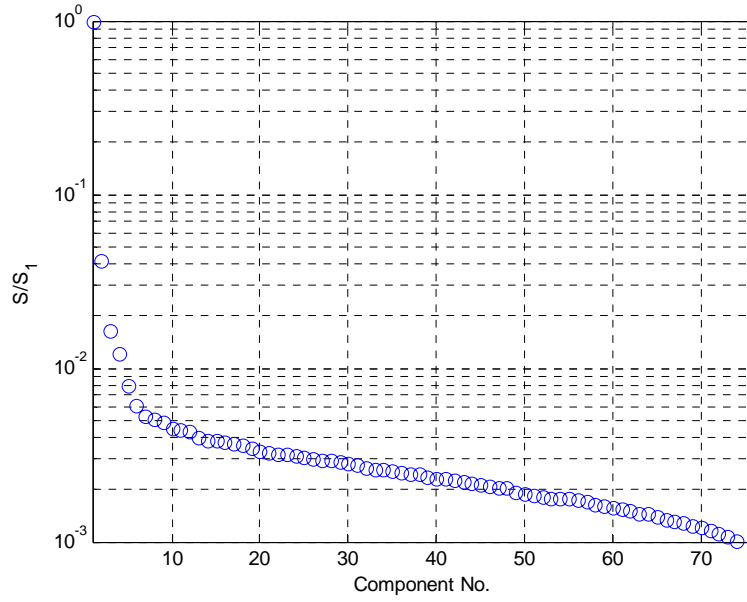
**2G<sub>2</sub>-m-OH**

Figure B-7. Singular values

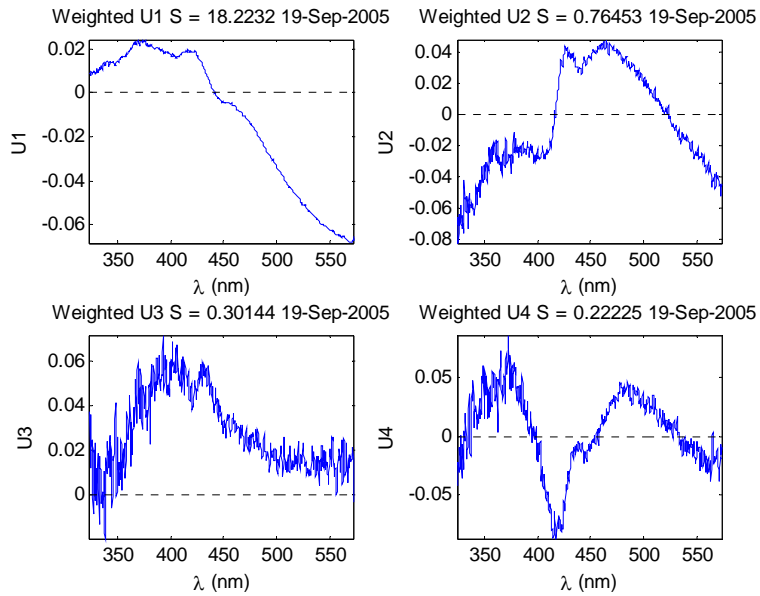


Figure B-8. Transient spectra of SVD output.

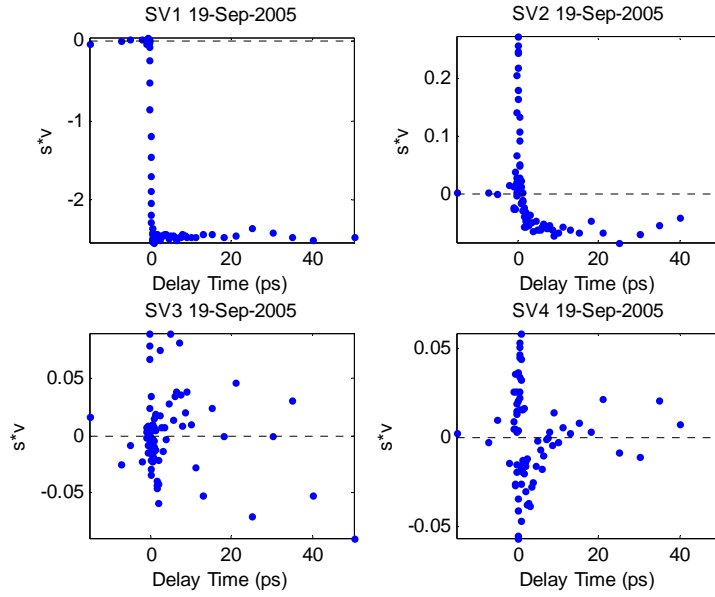


Figure B-9. Dynamics of SVD output.

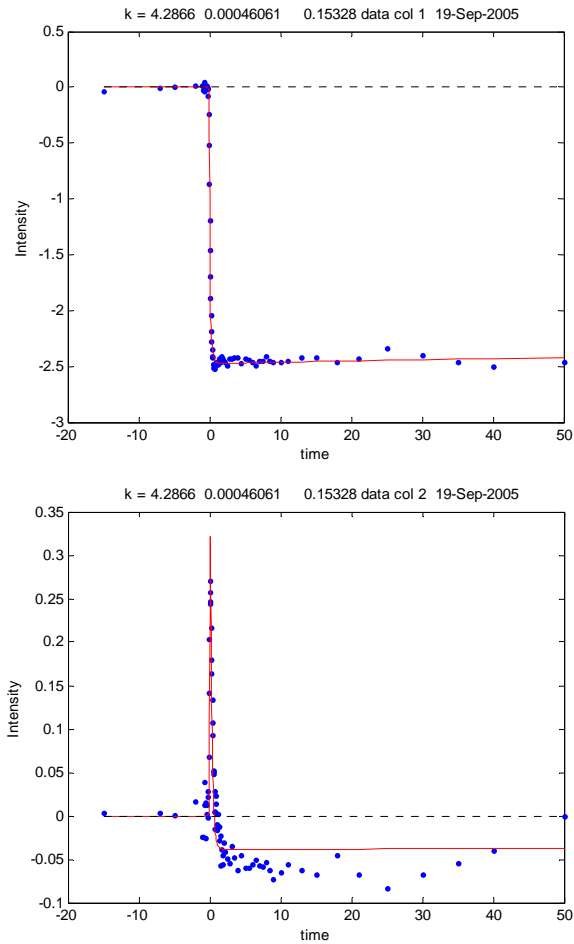


Figure B-10. Model fits for the relevant components with large singular values.

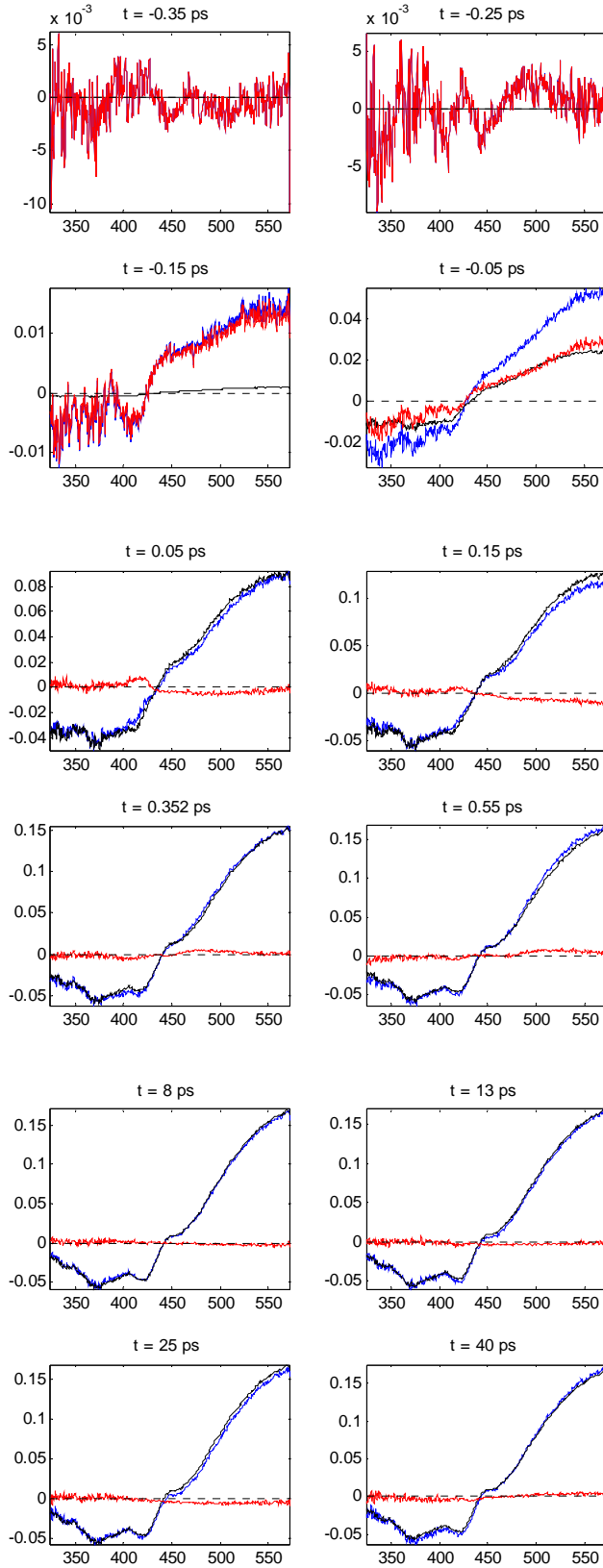


Figure B-11. Reconstructed versus real  $\Delta A$  as a function of wavelength.

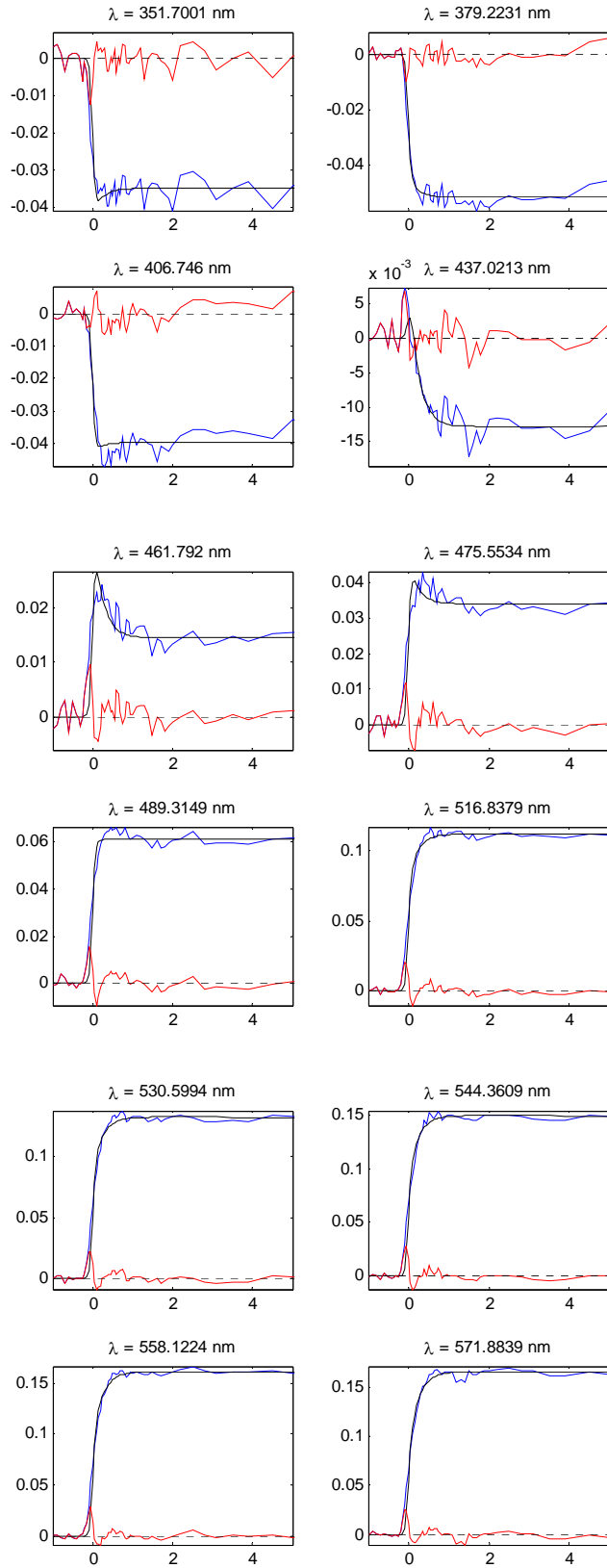


Figure B-12. Reconstructed versus real  $\Delta A$  as a function of time.

## Nanostar Excited at 310 nm

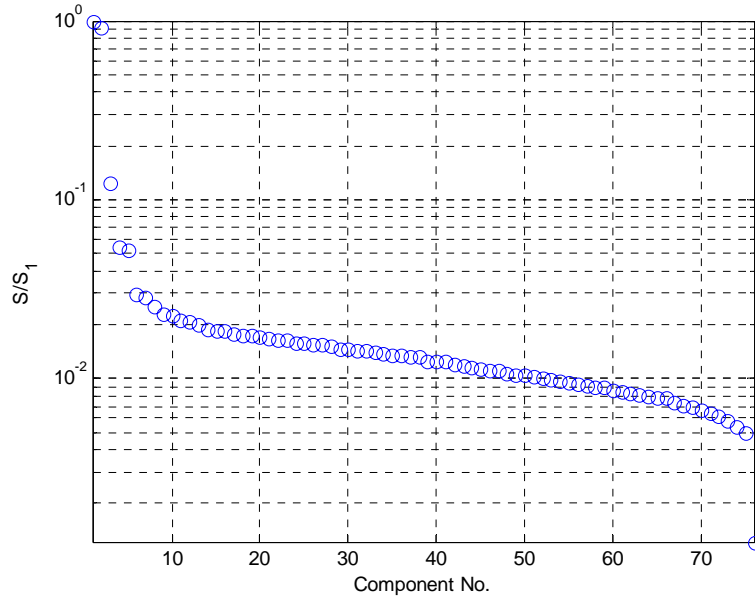


Figure B-13. Singular values

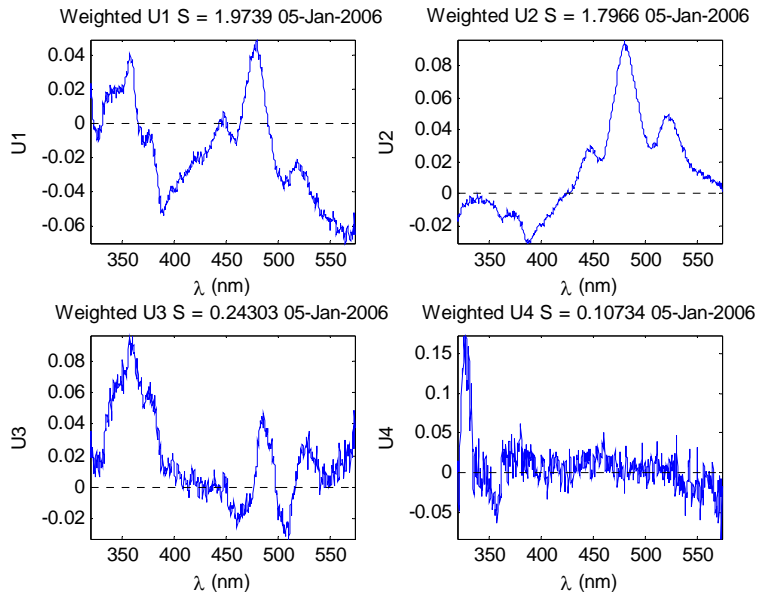


Figure B-14. Transient spectra of SVD output.

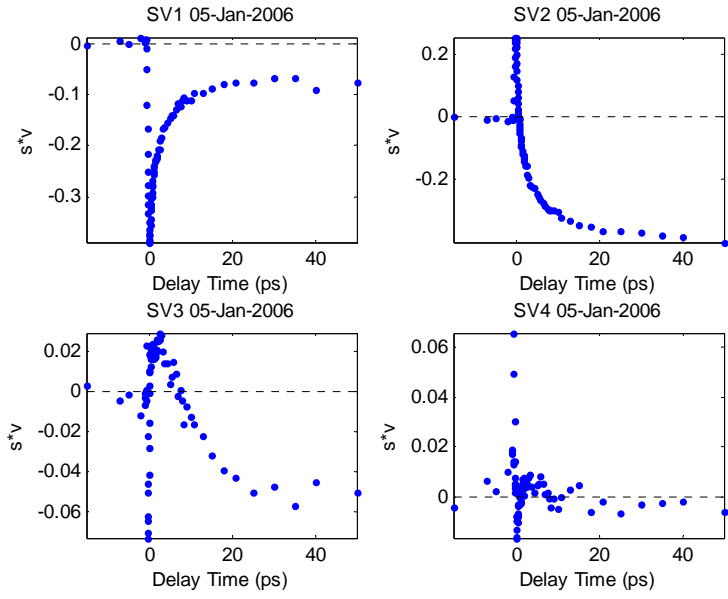


Figure B-15. Dynamics of SVD output.

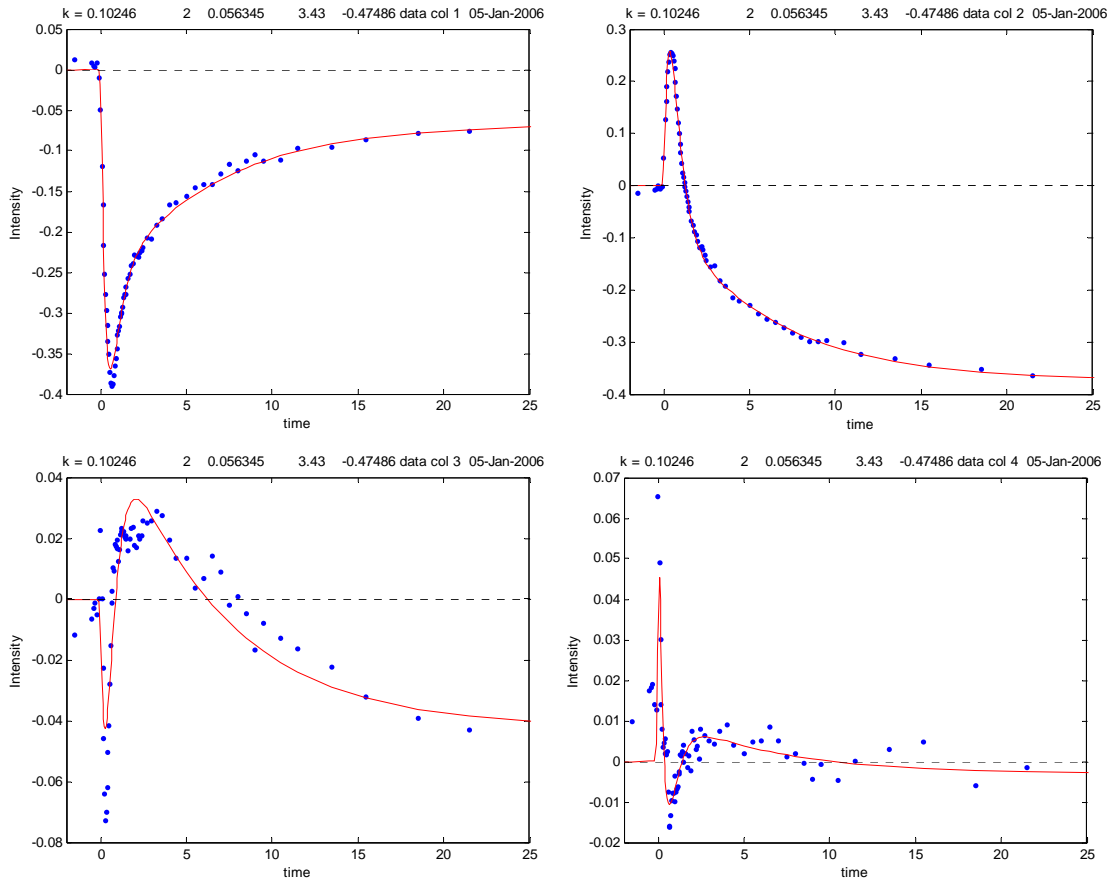


Figure B-16. Model fits for the relevant components with large singular values.

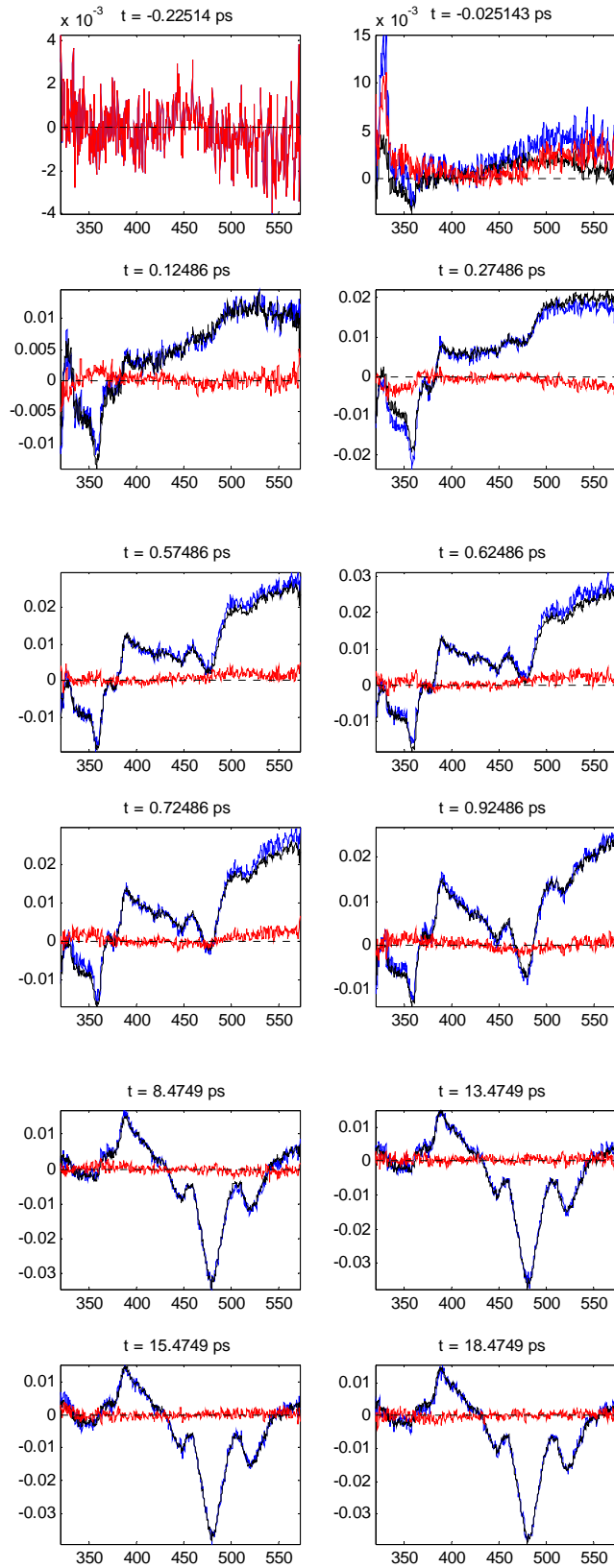


Figure B-17. Reconstructed versus real  $\Delta A$  as a function of wavelength.

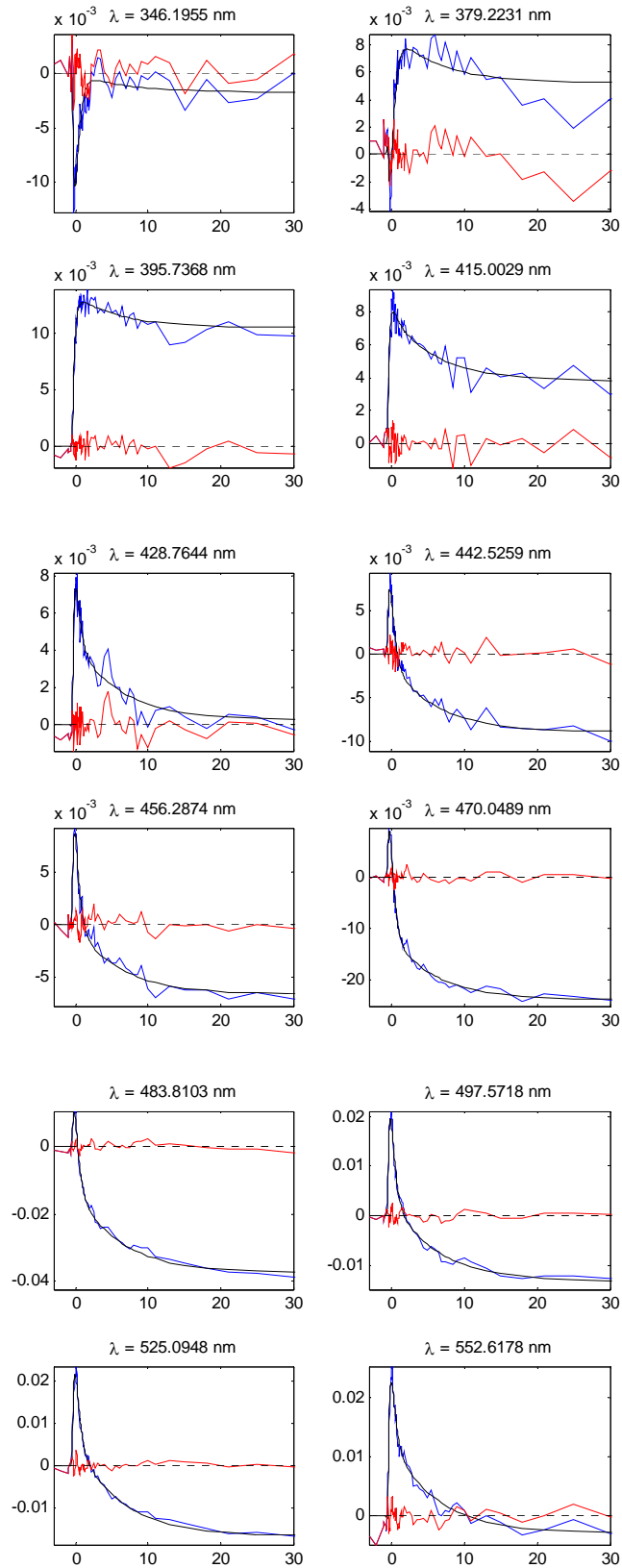


Figure B-18. Reconstructed versus real  $\Delta A$  as a function of time.

## LIST OF REFERENCES

- (1) Tomalia, D. A.; Naylor, A. M.; Goddard, W. A., III. *Angewandte Chemie* **1990**, *102*, 119.
- (2) Frechet, J. M. J. *Science* **1994**, *263*, 1710.
- (3) Newkome, G. R.; Moorefield, C. N. *Comprehensive Supramolecular Chemistry* **1996**, *10*, 777.
- (4) Newkome, G. R.; Moorefield, C. N.; Vogtle, F. *Dendrimers and Dendrons: Concepts, Syntheses, Applications*, 2nd ed.; Wiley-VCH: New York, 2001.
- (5) Flory, P. J. *Journal of the American Chemical Society* **1952**, *74*, 2718.
- (6) Flory, P. J. *Principles of Polymer Chemistry*, Cornell University: Ithaca, 1953.
- (7) Buhleier, E.; Wehner, W.; Voegtle, F. *Synthesis* **1978**, 155.
- (8) Tomalia, D. A.; Dewald, J. R. Dense star polymers having two dimensional molecular diameter; United States patent application 85-757546, 1986
- (9) Tomalia, D. A.; Baker, H.; Dewald, J.; Hall, M.; Kallos, G.; Martin, S.; Roeck, J.; Ryder, J.; Smith, P. *Macromolecules* **1986**, *19*, 2466.
- (10) Tomalia, D. A.; Baker, H.; Dewald, J.; Hall, M.; Kallos, G.; Martin, S.; Roeck, J.; Ryder, J.; Smith, P. *Polymer Journal* **1985**, *17*, 117.
- (11) Newkome, G. R.; Yao, Z.; Baker, G. R.; Gupta, V. K. *Journal of Organic Chemistry* **1985**, *50*, 2003.
- (12) Woerner, C.; Muelhaupt, R. *Angewandte Chemie* **1993**, *105*, 1367.
- (13) de Brabander-van den Berg, E. M. M.; Meijer, E. W. *Angewandte Chemie* **1993**, *105*, 1370.
- (14) Hawker, C.; Frechet, M. J. *Journal of the Chemical Society, Chemical Communications* **1990**, 1010.
- (15) Hawker, C. J.; Frechet, J. M. J. *Journal of the American Chemical Society* **1990**, *112*, 7638.

- (16) Newkome, G. R.; Moorefield, C. N.; Vogtle, F. *Dendrimers*, Wiley-WCH: New York, 2001.
- (17) Bosman, A. W.; Janssen, H. M.; Meijer, E. W. *Chemical Reviews* **1999**, *99*, 1665.
- (18) Tomalia, D. A.; Baker, H.; Dewald, J.; Hall, M.; Kallos, G.; Martin, S.; Roeck, J.; Ryder, J.; Smith, P. *Polymer Journal* **2002**, *34*, 132.
- (19) Ortiz, W.; Roitberg, A. E.; Krause, J. L. *Journal of Physical Chemistry B* **2004**, *108*, 8218.
- (20) Grayson, S. M.; Frechet, J. M. J. *Chemical Reviews* **2001**, *101*, 3819.
- (21) Moore, J. S.; Xu, Z. F. *Macromolecules* **1991**, *24*, 5893.
- (22) Moore, J. S. *Accounts of Chemical Research* **1997**, *30*, 402.
- (23) Morgenroth, F.; Berresheim, A. J.; Wagner, M.; Mullen, K. *Chemical Communications* **1998**, 1139.
- (24) Morgenroth, F.; Kuebel, C.; Muellen, K. *Journal of Materials Chemistry* **1997**, *7*, 1207.
- (25) Morgenroth, F.; Reuther, E.; Muellen, K. *Angewandte Chemie, International Edition* **1997**, *36*, 631.
- (26) Hawker, C. J.; Wooley, K. L.; Frechet, J. M. J. *Journal of the Chemical Society, Perkin Transactions 1: Organic and Bio-Organic Chemistry (1972 - 1999)* **1993**, 1287.
- (27) Mattei, S.; Seiler, P.; Diederich, F.; Gramlich, V. *Helvetica Chimica Acta* **1995**, *78*, 1904.
- (28) Stevelmans, S.; Hest, J. C. M. v.; Jansen, J. F. G. A.; Van Boxtel, D. A. F. J.; de Berg, E. M. M.; Meijer, E. W. *Journal of the American Chemical Society* **1996**, *118*, 7398.
- (29) Jansen, J. F. G. A.; Meijer, E. W.; de Brabander-van den Berg, E. M. M. *Journal of the American Chemical Society* **1995**, *117*, 4417.
- (30) Jansen, J. F. G. A.; de Brabander van den Berg, E. M. M.; Meijer, E. W. *Science (Washington, D. C.)* **1994**, *266*, 1226.
- (31) Jansen, J. F. G. A.; de Brabander-van den Berg, E. M. M.; Meijer, E. W. *Recueil des Travaux Chimiques des Pays-Bas* **1995**, *114*, 225.
- (32) Naylor, A. M.; Goddard, W. A., III; Kiefer, G. E.; Tomalia, D. A. *Journal of the American Chemical Society* **1989**, *111*, 2339.

- (33) Kawa, M.; Frechet, J. M. J. *Chemistry of Materials* **1998**, *10*, 286.
- (34) Xu, Z.; Moore, J. S. *Acta Polymerica* **1994**, *45*, 83.
- (35) Xu, Z. F.; Kahr, M.; Walker, K. L.; Wilkins, C. L.; Moore, J. S. *Journal of the American Chemical Society* **1994**, *116*, 4537.
- (36) Adronov, A.; Frechet, J. M. J. *Chemical Communications* **2000**, 1701.
- (37) Frechet, J. M. J. *Macromolecular Symposia* **2003**, *201*, 11.
- (38) Frechet, J. M. J. *Journal of Polymer Science, Part A: Polymer Chemistry* **2003**, *41*, 3713.
- (39) Aida, T.; Jiang, D. L.; Yashima, E.; Okamoto, Y. *Thin Solid Films* **1998**, *331*, 254.
- (40) Hofkens, J.; Latterini, L.; De Belder, G.; Gensch, T.; Maus, M.; Vosch, T.; Karni, Y.; Schweitzer, G.; De Schryver, F. C.; Hermann, A.; Mullen, K. *Chemical Physics Letters* **1999**, *304*, 1.
- (41) Weil, T.; Wiesler, U. M.; Herrmann, A.; Bauer, R.; Hofkens, J.; De Schryver, F. C.; Mullen, K. *Journal of the American Chemical Society* **2001**, *123*, 8101.
- (42) Crooks, R. M.; Zhao, M.; Sun, L.; Chechik, V.; Yeung, L. K. *Accounts of Chemical Research* **2001**, *34*, 181.
- (43) Brunner, H. *Journal of Organometallic Chemistry* **1995**, *500*, 39.
- (44) Lee, J.-J.; Ford, W. T. *Journal of the American Chemical Society* **1994**, *116*, 3753.
- (45) Crooks, R. M.; Ricco, A. J. *Accounts of Chemical Research* **1998**, *31*, 219.
- (46) Larsen, J.; Brueggemann, B.; Polivka, T.; Sundstroem, V.; Aakesson, E.; Sly, J.; Crossley, M. J. *Journal of Physical Chemistry A* **2005**, *109*, 10654.
- (47) Larsen, J.; Andersson, J.; Polivka, T.; Sly, J.; Crossley, M. J.; Sundstroem, V.; Akesson, E. *Chemical Physics Letters* **2005**, *403*, 205.
- (48) Hu, X.; Damjanovic, A.; Ritz, T.; Schulten, K. *Proceedings of the National Academy of Sciences of the United States of America* **1998**, *95*, 5935.
- (49) Denti, G.; Campagna, S.; Serroni, S.; Ciano, M.; Balzani, V. *Journal of the American Chemical Society* **1992**, *114*, 2944.
- (50) Balzani, V.; Campagna, S.; Denti, G.; Juris, A.; Serroni, S.; Venturi, M. *Accounts of Chemical Research* **1998**, *31*, 26.

- (51) Balzani, V.; Ceroni, P.; Gestermann, S.; Gorka, M.; Kauffmann, C.; Maestri, M.; Vogtle, F. *Chemphyschem* **2000**, *1*, 224.
- (52) Balzani, V.; Ceroni, P.; Juris, A.; Venturi, M.; Campagna, S.; Puntoriero, F.; Serroni, S. *Coordination Chemistry Reviews* **2001**, *219*, 545.
- (53) Balzani, V.; Vogtle, F. *Comptes Rendus Chimie* **2003**, *6*, 867.
- (54) Balzani, V.; Ceroni, P.; Maestri, M.; Vicinelli, V. *Current Opinion in Chemical Biology* **2003**, *7*, 657.
- (55) Balzani, V.; Ceroni, P.; Maestri, M.; Saudan, C.; Vicinelli, V. Luminescent dendrimers. Recent advances. In *Dendrimers V: Functional and Hyperbranched Building Blocks, Photophysical Properties, Applications in Materials and Life Sciences*, 2003; Vol. 228; pp 159.
- (56) Jiang, D.-L.; Aida, T. *Journal of the American Chemical Society* **1998**, *120*, 10895.
- (57) Vogtle, F.; Gorka, M.; Hesse, R.; Ceroni, P.; Maestri, M.; Balzani, V. *Photochemical & Photobiological Sciences* **2002**, *1*, 45.
- (58) Gilat, S. L.; Adronov, A.; Frechet, J. M. J. *Abstracts of Papers of the American Chemical Society* **1997**, *214*, 42.
- (59) Gilat, S. L.; Adronov, A.; Frechet, J. M. J. *Angewandte Chemie-International Edition* **1999**, *38*, 1422.
- (60) Serin Jason, M.; Brousmiche Darryl, W.; Frechet Jean, M. J. *Chemical communications* **2002**, 2605.
- (61) Bar-Haim, A.; Klafter, J.; Kopelman, R. *Journal of the American Chemical Society* **1997**, *119*, 6197.
- (62) Bar-Haim, A.; Klafter, J. *Journal of Luminescence* **1998**, *76-7*, 197.
- (63) Adronov, A.; Gilat, S. L.; Frechet, J. M. J.; Ohta, K.; Neuwahl, F. V. R.; Fleming, G. R. *Journal of the American Chemical Society* **2000**, *122*, 1175.
- (64) Weil, T.; Reuther, E.; Mullen, K. *Angewandte Chemie, International Edition* **2002**, *41*, 1900.
- (65) Weil, T.; Reuther, E.; Beer, C.; Muellen, K. *Chemistry--A European Journal* **2004**, *10*, 1398.
- (66) Cotlet, M.; Vosch, T.; Habuchi, S.; Weil, T.; Muellen, K.; Hofkens, J.; De Schryver, F. *Journal of the American Chemical Society* **2005**, *127*, 9760.

- (67) Serin, J. M.; Brousmiche, D. W.; Frechet, J. M. J. *Chemical Communications (Cambridge, United Kingdom)* **2002**, 2605.
- (68) Swallen, S. F.; Shi, Z. Y.; Tan, W. H.; Xu, Z. F.; Moore, J. S.; Kopelman, R. *Journal of Luminescence* **1998**, 76-7, 193.
- (69) Shortreed, M. R.; Swallen, S. F.; Shi, Z. Y.; Tan, W. H.; Xu, Z. F.; Devadoss, C.; Moore, J. S.; Kopelman, R. *Journal of Physical Chemistry B* **1997**, 101, 6318.
- (70) Swallen, S. F.; Kopelman, R.; Moore, J. S.; Devadoss, C. *Journal of Molecular Structure* **1999**, 485-486, 585.
- (71) Melinger, J. S.; Pan, Y.; Kleiman, V. D.; Peng, Z.; Davis, B. L.; McMorro, D.; Lu, M. *Journal of the American Chemical Society* **2002**, 124, 12002.
- (72) Kopelman, R.; Shortreed, M.; Shi, Z. Y.; Tan, W. H.; Xu, Z. F.; Moore, J. S.; BarHaim, A.; Klafter, J. *Physical Review Letters* **1997**, 78, 1239.
- (73) Moore, J. S.; Xu, Z. *Macromolecules* **1991**, 24, 5893.
- (74) Ortiz, W.; Krueger, B. P.; Kleiman, V. D.; Krause, J. L.; Roitberg, A. E. *Journal of Physical Chemistry B* **2005**, 109, 11512.
- (75) Kleiman, V. D.; Melinger, J. S.; McMorro, D. *Journal of Physical Chemistry B* **2001**, 105, 5595.
- (76) Tretiak, S.; Chernyak, V.; Mukamel, S. *Journal of Physical Chemistry B* **1998**, 102, 3310.
- (77) Chernyak, V.; Poliakov, E. Y.; Tretiak, S.; Mukamel, S. *Journal of Chemical Physics* **1999**, 111, 4158.
- (78) Minami, T.; Tretiak, S.; Chernyak, V.; Mukamel, S. *Journal of Luminescence* **2000**, 87-9, 115.
- (79) Mukamel, S.; Tretiak, S.; Wagersreiter, T.; Chernyak, V. *Science* **1997**, 277, 781.
- (80) Kopelman, R.; Shortreed, M.; Shi, Z.-Y.; Tan, W.; Xu, Z.; Moore, J. S.; Bar-Haim, A.; Klafter, J. *Physical Review Letters* **1997**, 78, 1239.
- (81) Devadoss, C.; Bharathi, P.; Moore, J. S. *Journal of the American Chemical Society* **1996**, 118, 9635.
- (82) Shortreed, M. R.; Shi, Z. Y.; Kopelman, R. *Molecular Crystals and Liquid Crystals Science and Technology Section a-Molecular Crystals and Liquid Crystals* **1996**, 283, 95.
- (83) Tada, T.; Nozaki, D.; Kondo, M.; Yoshizawa, K. *Journal of Physical Chemistry B* **2003**, 107, 14204.

- (84) Thompson, A. L.; Gaab, K. M.; Xu, J. J.; Bardeen, C. J.; Martinez, T. J. *Journal of Physical Chemistry A* **2004**, *108*, 671.
- (85) Harcourt, R. D.; Scholes, G. D.; Ghiggino, K. P. *Journal of Chemical Physics* **1994**, *101*, 10521.
- (86) Shortreed, M. R.; Swallen, S. F.; Shi, Z.-Y.; Tan, W.; Xu, Z.; Devadoss, C.; Moore, J. S.; Kopelman, R. *Journal of Physical Chemistry B* **1997**, *101*, 6318.
- (87) Varnavski, O. P.; Ostrowski, J. C.; Sukhomlinova, L.; Twieg, R. J.; Bazan, G. C.; Goodson, T. *Journal of the American Chemical Society* **2002**, *124*, 1736.
- (88) Varnavski, O.; Samuel, I. D. W.; Palsson, L. O.; Beavington, R.; Burn, P. L.; Goodson, T. *Journal of Chemical Physics* **2002**, *116*, 8893.
- (89) Ranasinghe, M. I.; Murphy, P.; Lu, Z. K.; Huang, S. P. D.; Twieg, R. J.; Goodson, T. *Chemical Physics Letters* **2004**, *383*, 411.
- (90) Gaab, K. M.; Thompson, A. L.; Xu, J. J.; Martinez, T. J.; Bardeen, C. J. *Journal of the American Chemical Society* **2003**, *125*, 9288.
- (91) Pan, Y. Synthesis and optical properties of unsymmetrical conjugated dendrimers, *Ph.D. Dissertation*, University of Missouri, 2002.
- (92) Pan, Y.; Lu, M.; Peng, Z.; Melinger, J. S. *Journal of Organic Chemistry* **2003**, *68*, 6952.
- (93) Pan, Y.; Peng, Z.; Melinger, J. S. *Tetrahedron* **2003**, *59*, 5495.
- (94) Xu, B.; Lu, M.; Peng, Z. *Abstracts of Papers, 221st ACS National Meeting, San Diego, CA, United States, April 1-5, 2001* **2001**, PMSE.
- (95) Melinger, J. S.; Pan, Y. C.; Kleiman, V. D.; Peng, Z. H.; Davis, B. L.; McMorro, D.; Lu, M. *Journal of the American Chemical Society* **2002**, *124*, 12002.
- (96) Pan, Y. C.; Peng, Z. H.; Melinger, J. S. *Tetrahedron* **2003**, *59*, 5495.
- (97) Pan, Y. C.; Lu, M.; Peng, Z. H.; Melinger, J. S. *Journal of Organic Chemistry* **2003**, *68*, 6952.
- (98) Turro, N. J. *Modern Molecular Photochemistry*, 1978.
- (99) Scholes, G. D. *Annual Review of Physical Chemistry* **2003**, *54*, 57.
- (100) Forster, T. *Ann. Physik* **1948**, *2*, 55.
- (101) Dexter, D. L. *Journal of Chemical Physics* **1953**, *21*, 836.

- (102) Fleming, G. R. *International Series of Monographs on Chemistry, Vol. 13: Chemical Applications of Ultrafast Spectroscopy*, Oxford University: Oxford, 1986.
- (103) Pan, Y. C.; Lu, M.; Peng, Z. H.; Melinger, J. S. *Organic & Biomolecular Chemistry* **2003**, *1*, 4465.
- (104) Peng, Z.; Pan, Y.; Xu, B.; Zhang, J. *Journal of the American Chemical Society* **2000**, *122*, 6619.
- (105) Beeby, A.; Findlay, K.; Low, P. J.; Marder, T. B. *Journal of the American Chemical Society* **2002**, *124*, 8280.
- (106) Pinto, M. R.; Kristal, B. M.; Schanze, K. S. *Langmuir* **2003**, *19*, 6523.
- (107) Tan, C.; Atas, E.; Mueller, J. G.; Pinto, M. R.; Kleiman, V. D.; Schanze, K. S. *Journal of the American Chemical Society* **2004**, *126*, 13685.
- (108) Rulliere, C. *Femtosecond Laser Pulses: Principles and Experiments, 2nd Edition*, Springer: Verlag, 2004.
- (109) Schweitzer, G.; Xu, L.; Craig, B.; DeSchryver, F. C. *Optics Communications* **1997**, *142*, 283.
- (110) O'Conner, D. V.; Phillips, D. *Time-Correlated Single-Photon Counting*, 1988.
- (111) Hirsch, M. D.; Marcus, M. A.; Lewis, A.; Mahr, H.; Frigo, N. *Biophysical journal* **1976**, *16*, 1399.
- (112) Kahlow, M. A.; Jarzeba, W.; DuBruil, T. P.; Barbara, P. F. *Review of Scientific Instruments* **1988**, *59*, 1098.
- (113) Barbara, P. F.; Kang, T. J.; Jarzeba, W.; Kahlow, M. *Proceedings of SPIE-The International Society for Optical Engineering* **1988**, *910*, 124.
- (114) Kovalenko, S. A.; Dobryakov, A. L.; Ruthmann, J.; Ernsting, N. P. *Physical Review A: Atomic, Molecular, and Optical Physics* **1999**, *59*, 2369.
- (115) Kovalenko, S. A.; Ernsting, N. P.; Ruthmann, J. *Chemical Physics Letters* **1996**, *258*, 445.
- (116) Kovalenko, S. A.; Ruthmann, J.; Ernsting, N. P. *Journal of Chemical Physics* **1998**, *109*, 1894.
- (117) Kovalenko, S. A.; Schanz, R.; Farztdinov, V. M.; Hennig, H.; Ernsting, N. P. *Chemical Physics Letters* **2000**, *323*, 312.
- (118) Ernsting, N. P.; Kovalenko, S. A.; Senyushkina, T.; Saam, J.; Farztdinov, V. *Journal of Physical Chemistry A* **2001**, *105*, 3443.

- (119) Huber, R.; Satzger, H.; Zinth, W.; Wachtveitl, J. *Optics Communications* **2001**, *194*, 443.
- (120) Lozhkarev, V. V.; Freidman, G. I.; Ginzburg, V. N.; Khazanov, E. A.; Palashov, O. V.; Sergeev, A. M.; Yakovlev, I. V. *Laser Physics* **2005**, *15*, 1319.
- (121) Ghosh, G. *Applied Optics* **1997**, *36*, 1540.
- (122) Lorenc, M.; Ziolk, M.; Naskrecki, R.; Karolczak, J.; Kubicki, J.; Maciejewski, A. *Applied Physics B: Lasers and Optics* **2002**, *74*, 19.
- (123) Ekvall, K.; van der Meulen, P.; Dhollande, C.; Berg, L. E.; Pommeret, S.; Naskrecki, R.; Mialocq, J. C. *Journal of Applied Physics* **2000**, *87*, 2340.
- (124) Adronov, A.; Robello, D. R.; Frechet, J. M. J. *Journal of Polymer Science Part a-Polymer Chemistry* **2001**, *39*, 1366.
- (125) Tomalia, D. A.; Naylor, A. M.; Goddard, W. A. *Angewandte Chemie-International Edition* **1990**, *29*, 138.
- (126) McElhanon, J. R.; McGrath, D. V. *Journal of the American Chemical Society* **1998**, *120*, 1647.
- (127) Tretiak, S.; Chernyak, V.; Mukamel, S. *Journal of Physical Chemistry B* **1998**, *102*, 3310.
- (128) Ortiz, W.; Krueger, B. P.; Kleiman, V. D.; Krause, J. L.; Roitberg, A. E. *Journal of Physical Chemistry B*, **2006** *in press*.
- (129) Ranasinghe, M. I.; Hager, M. W.; Gorman, C. B.; Goodson, T. *Journal of Physical Chemistry B* **2004**, *108*, 8543.
- (130) Swallen, S. F.; Zhu, Z. G.; Moore, J. S.; Kopelman, R. *Journal of Physical Chemistry B* **2000**, *104*, 3988.
- (131) Peng, Z. H.; Pan, Y. C.; Xu, B. B.; Zhang, J. H. *Journal of the American Chemical Society* **2000**, *122*, 6619.
- (132) Atas, E.; Peng, Z.; Kleiman, V. D. *Journal of Physical Chemistry B* **2005**, *109*, 13553.
- (133) De Belder, G.; Jordens, S.; Lor, M.; Schweitzer, G.; De, R.; Weil, T.; Herrmann, A.; Wiesler, U. K.; Mullen, K.; De Schryver, F. C. *Journal of Photochemistry and Photobiology a-Chemistry* **2001**, *145*, 61.
- (134) De Schryver, F. C.; Hofkens, J. *Abstracts of Papers of the American Chemical Society* **2001**, *221*, U288.

- (135) Lakowicz, J. R. *Principles of Luorescence Spectrosocopy*, 2<sup>nd</sup> ed.; Kluwer Academic/Plenum Publishers: New York, 1999.
- (136) Neuwahl, F. V. R.; Righini, R.; Adronov, A.; Malenfant, P. R. L.; Frechet, J. M. J. *Journal of Physical Chemistry B* **2001**, *105*, 1307.
- (137) Schweitzer, G.; Gronheid, R.; Jordens, S.; Lor, M.; De Belder, G.; Weil, T.; Reuther, E.; Muellen, K.; De Schryver, F. C. *Journal of Physical Chemistry A* **2003**, *107*, 3199.
- (138) Davis, B. L.; Melinger, J. S.; McMorrow, D.; Peng, Z. H.; Pan, C. Y. *Journal of Luminescence* **2004**, *106*, 301.
- (139) Swallen, S. F.; Kopelman, R.; Moore, J. S.; Devadoss, C. *Journal of Molecular Structure* **1999**, *486*, 585.
- (140) Varnavski, O.; Menkir, G.; Goodson, T.; Burn, P. L. *Applied Physics Letters* **2000**, *77*, 1120.
- (141) Melinger, J. S.; Davis, B. L.; McMorrow, D.; Pan, C. Y.; Peng, Z. H. *Journal of Fluorescence* **2004**, *14*, 105.
- (142) Pan, Y.; Lu, M.; Peng, Z.; Melinger Joseph, S. *The Journal of organic chemistry* **2003**, *68*, 6952.
- (143) Förster, T. *Modern Quantum Chemistry*; Academic Press: New York, 1965; Vol. 3.
- (144) Valeur, B. *Molecular Fluorescence: Principles and Applications*, First ed.; Wiley-VCH: Weinheim, 2002.
- (145) Hofkens, J.; Cotlet, M.; Vosch, T.; Tinnefeld, P.; Weston, K. D.; Ego, C.; Grimsdale, A.; Mullen, K.; Beljonne, D.; Bredas, J. L.; Jordens, S.; Schweitzer, G.; Sauer, M.; De Schryver, F. *Proceedings of the National Academy of Sciences of the United States of America* **2003**, *100*, 13146.
- (146) Krueger, B. P.; Scholes, G. D.; Jimenez, R.; Fleming, G. R. *Journal of Physical Chemistry B* **1998**, *102*, 2284.
- (147) Lii, J. H.; Allinger, N. L. *Journal of the American Chemical Society* **1989**, *111*, 8566.
- (148) Lii, J. H.; Allinger, N. L. *Journal of the American Chemical Society* **1989**, *111*, 8576.
- (149) Allinger, N. L.; Yuh, Y. H.; Lii, J. H. *Journal of the American Chemical Society* **1989**, *111*, 8551.

- (150) Tortschanoff, A.; Mukamel, S. *Journal of Physical Chemistry A* **2002**, *106*, 7521.
- (151) Hirata, Y.; Okada, T.; Mataga, N.; Nomoto, T. *Journal of Physical Chemistry* **1992**, *96*, 6559.
- (152) Beeby, A.; Findlay, K. S.; Low, P. J.; Marder, T. B.; Matousek, P.; Parker, A. W.; Rutter, S. R.; Towrie, M. *Chemical Communications (Cambridge, United Kingdom)* **2003**, 2406.
- (153) Kirkwood, J. C.; Scheurer, C.; Chernyak, V.; Mukamel, S. *Journal of Chemical Physics* **2001**, *114*, 2419.
- (154) Yang, M.; Fleming, G. R. *Chemical Physics* **2002**, *282*, 163.
- (155) Zhou, Q.; Swager, T. M. *Journal of the American Chemical Society* **1995**, *117*, 12593.
- (156) Chen, L. H.; McBranch, D. W.; Wang, H. L.; Helgeson, R.; Wudl, F.; Whitten, D. G. *Proceedings of the National Academy of Sciences of the United States of America* **1999**, *96*, 12287.
- (157) Wang, D. L.; Gong, X.; Heeger, P. S.; Rininsland, F.; Bazan, G. C.; Heeger, A. J. *Proceedings of the National Academy of Sciences of the United States of America* **2002**, *99*, 49.
- (158) Tan, C. Y.; Pinto, M. R.; Schanze, K. S. *Chemical Communications* **2002**, 446.
- (159) Tan, C. Y.; Atas, E.; Muller, J. G.; Pinto, M. R.; Kleiman, V. D.; Schanze, K. S. *Journal of the American Chemical Society* **2004**, *126*, 13685.
- (160) Wang, J.; Wang, D. L.; Miller, E. K.; Moses, D.; Bazan, G. C.; Heeger, A. J. *Macromolecules* **2000**, *33*, 5153.
- (161) Nguyen, T. Q.; Junjun, W.; Doan, V.; Schwartz, B. J.; Tolbert, S. H. *Science* **2000**, *288*, 652.
- (162) Grage, M. M. L.; Zaushitsyn, Y.; Yartsev, A.; Chachisvilis, M.; Sundstrom, V.; Pullerits, T. *Physical Review B* **2003**, *67*.
- (163) Grage, M. M.-L.; Pullerits, T.; Ruseckas, A.; Theander, M.; Inganas, O.; Sundstrom, V. *Chemical Physics Letters* **2001**, *339*, 96.
- (164) VandenBout, D. A.; Yip, W. T.; Hu, D. H.; Fu, D. K.; Swager, T. M.; Barbara, P. F. *Science* **1997**, *277*, 1074.
- (165) Huser, T.; Yan, M.; Rothberg, L. J. *Proceedings of the National Academy of Sciences of the United States of America* **2000**, *97*, 11187.

- (166) Muller, J. G.; Lemmer, U.; Raschke, G.; Anni, M.; Scherf, U.; Lupton, J. M.; Feldmann, J. *Physical Review Letters* **2003**, *91*.
- (167) Levitsky, I. A.; Kim, J. S.; Swager, T. M. *Journal of the American Chemical Society* **1999**, *121*, 1466.
- (168) Herz, L. M.; Silva, C.; Friend, R. H.; Phillips, R. T.; Setayesh, S.; Becker, S.; Marsitsky, D.; Mullen, K. *Physical Review B* **2001**, *64*.
- (169) Tan, C. Y.; Alas, E.; Muller, J. G.; Pinto, M. R.; Kleiman, V. D.; Schanze, K. S. *Journal of the American Chemical Society* **2004**, *126*, 13685.
- (170) Sluch, M. I.; Godt, A.; Bunz, U. H. F.; Berg, M. A. *Journal of the American Chemical Society* **2001**, *123*, 6447.
- (171) Gaab, K. M.; Bardeen, C. J. *Journal of Physical Chemistry B* **2004**, *108*, 4619.
- (172) Scheidler, M.; Cleve, B.; Bassler, H.; Thomas, P. *Chemical Physics Letters* **1994**, *225*, 431.
- (173) Grage, M. M. L.; Wood, P. W.; Ruseckas, A.; Pullerits, T.; Mitchell, W.; Burn, P. L.; Samuel, I. D. W.; Sundstrom, V. *Journal of Chemical Physics* **2003**, *118*, 7644.
- (174) Kamalov, V. F.; Struganova, I. A.; Yoshihara, K. *Journal of Physical Chemistry* **1996**, *100*, 8640.
- (175) Rosenstock, H. B. *Journal of the Society for Industrial and Applied Mathematics* **1961**, *9*, 169.
- (176) Montroll, E. W. *Journal of Mathematical Physics* **1969**, *10*, 753.
- (177) Fitzgibbon, P. D.; Frank, C. W. *Macromolecules* **1982**, *15*, 733.
- (178) Klafter, J.; Blumen, A.; Zumofen, G. *Journal of Statistical Physics* **1984**, *36*, 561.
- (179) Palszegi, T.; Mollay, B.; Kauffmann, H. F. *Journal of Chemical Physics* **1998**, *108*, 7023.
- (180) Scheidler, M.; Lemmer, U.; Kersting, R.; Karg, S.; Riess, W.; Cleve, B.; Mahrt, R. F.; Kurz, H.; Bassler, H.; Gobel, E. O.; Thomas, P. *Physical Review B* **1996**, *54*, 5536.
- (181) Kauffmann, H. F.; Mollay, B.; Weixelbaumer, W. D.; Burbaumer, J.; Riegler, M.; Meisterhofer, E.; Aussenegg, F. R. *Journal of Chemical Physics* **1986**, *85*, 3566.
- (182) Beljonne, D.; Pourtois, G.; Silva, C.; Hennebicq, E.; Herz, L. M.; Friend, R. H.; Scholes, G. D.; Setayesh, S.; Mullen, K.; Bredas, J. L. *Proceedings of the National Academy of Sciences of the United States of America* **2002**, *99*, 10982.
- (183) Kukula, H.; Veit, S.; Godt, A. *European Journal of Organic Chemistry* **1999**, 277.

(184) Nomula, S.; Cooper, S. L. *Macromolecules* **2000**, *33*, 6402.

## BIOGRAPHICAL SKETCH

Evrin Atas was born on October 2, 1978 in Igdir, Turkey, where she spent her childhood until she started elementary school. After attending Haydarpasa Anatolian High School for 4 years, she began her undergraduate studies in the Fall of 1996 at Bilkent University, Department of Chemistry in Ankara, Turkey. With an intense physical chemistry education and a special interest in spectroscopy, she came to the University of Florida, Department of Chemistry in the Fall of 2000 to begin doctoral studies under the supervision of Professor Valeria Kleiman in the area of ultrafast laser spectroscopy of dendrimers and conjugated polymers. Her professional career as a Ph.D. will begin as a post-doctoral fellow with Professor Amit Meller at the Rowland Institute, Harvard University. She will then move to the Department of Biomedical Engineering, Boston University.